SCUOLA DI DOTTORATO
UNIVERSITÀ DEGLI STUDI DI MILANO-BICOCCA

Dipartimento di / Department of

Physics “G. Occhialini”

Dottorato di Ricerca in / PhD program Physics and Astronomy Ciclo / Cycle XXXV

Curriculum in Plasma Physics and Biophysics

First principle based integrated modelling in support of the Divertor Tokamak Test facility design

Cognome / Surname Casiraghi Nome / Name Irene

Matricola / Registration number: 722191

Tutore / Tutor: Dr. Paola Mantica, ISTP—CNR

Coordinatore / Coordinator: Prof. Stefano Ragazzi

ANNO ACCADEMICO / ACADEMIC YEAR **2021/2022**

There is something fascinating about science.
One gets such wholesale returns of conjecture
out of such a trifling investment of fact.

— Mark Twain —

Life on the Mississippi

Contents

Introduction

The deepening energy crisis, which recently hit the world economy and Europe in primis, has spotlighted the need of reliable energy supplies.
A strategic plan for the electrical power production should include a mix of low environmental impact sources not relying on continuous restocking in order to avoid disruptions in the supply chain. Due to the intermittent nature of the renewable sources and to their low power density, other energy sources that are readily available are required to bear the energy demand baseload.
In this framework, controlled thermonuclear fusion acquires great relevance, as it would provide an energy source devoid of the risk associated with nuclear fission power plants and of the high environmental impact of fossil fuels.
The future fusion power plant fuel, a deuterium–tritium mixture, is virtually unlimited. Particularly, deuterium is a naturally occurring hydrogen isotope that can be extracted from seawater, while tritium can be produced within the reactors from lithium, which is widely available in the Earth's crust. Being the fusion fuel almost evenly distributed all over the world, the thermonuclear fusion is an engaging perspective decoupled from international geopolitical instabilities.
Nevertheless, electricity generation via thermonuclear fusion is a huge challenge due to the extremely high temperatures needed to fuse together nuclei. The deuterium–tritium mixture in plasma state must be heated up to about ten times the temperature of the Sun nucleus to sustain fusion reactions and must be properly confined. Plasmas can be confined exploiting suitably designed magnetic fields. The tokamak (toroidal chamber with magnetic coils) is the magnetic confinement device which has provided the best performance so far.

In the last decades, great progresses have been achieved in terms of scientific and technological knowledge, and a roadmap has been defined to re-

alise future fusion power plants for wide deployment. The next key step in the roadmap is ITER, an experimental reactor under construction in France within a worldwide collaboration. Its main goal is to demonstrate the scientific and technological feasibility of fusion as an energy source, obtaining for the first time an energy gain factor significantly larger than one. As a following step, the realisation of the demonstration plant DEMO is planned to produce electrical power by fusion. The operating conditions of DEMO and future reactors require plasma–facing components able to cope with huge power fluxes in the range of 10–20 $\mathrm{MW/m^2}$.
The Divertor Tokamak Test facility (DTT) was recently included in the roadmap to develop and test heat and particle exhaust strategies relevant for DEMO. The project is located in Italy and mainly financed by the Italian governement, with support by EUROfusion for what concerns the divertor. The DTT facility was proposed for the first time in 2015 and is now at an advanced stage of design, with construction already started at the ENEA Research Center in Frascati. The realisation of the first plasma in DTT is scheduled by the end of 2028, to guarantee that the DEMO engineering design can proceed with a mature enough alternative exhaust strategy on time, according to the European roadmap planning.

This PhD thesis concerns the first–principle based integrated modelling of plasma discharges in different DTT operational scenarios, an essential tool to support the machine design and the elaboration of its scientific work programme. The thesis makes use of the most advanced available integrated modelling tools, which have been developed within a worldwide effort over the last 30 years, and particularly within dedicated projects in EUROfusion. The models used have been validated against data from various tokamaks, reaching a degree of confidence that now allows to adopt a predict–first approach for future experiments. Including self–consistently the state–of–art modules for transport, heating, fuelling, and magnetic equilibrium in the simulations, we can predict the core plasma profiles, whilst matching as well as possible the separatrix parameters with those provided by SOL simulations is a crucial aspect to achieve edge–core integration. Therefore, an iterative work has been carried out to reach a consistent core–edge–SOL modelling. Finally, the integrated simulations have to be tested against the electromagnetic control system capabilities, to guarantee their feasibility in DTT.

CHAPTER 1

Nuclear fusion

1.1 Nuclear fission and fusion

Since the mass of a stable nucleus is lower than the sum of its component masses, the nucleus binding energy B of a general nuclide ${}^{A}_{Z}X_{N}$ is calculated as

$$B = \underbrace{\left[Zm_p + Nm_n - \underbrace{\left(m_{{}^{\mathrm{A}}_{\mathrm{Z}}\mathrm{X}_{\mathrm{N}}} - Zm_e \right)}_{m_{\mathrm{nucl}}} \right]}_{\text{mass defect}} c^2$$

where Z is the atomic number, A is the mass number, N is the neutron number, m_p is the proton mass, m_n is the neutron mass, m_e is the electron mass, m_{nucl} is the nucleus mass, and c is the speed of light in vacuum.[1]

Experimental values of the binding energy per nucleon B/A as a function of the mass number A are plotted in figure 1.1. We note that the most tightly bound nucluei correspond to the ^{56}Fe iron isotope ones.
In exoenergetic nuclear reactions, the reagent binding energy is larger than the product one and this energy difference $\left(m_{\mathrm{reagents}} - m_{\mathrm{products}}\right) c^2$ is released as kinetic energy. Hence, it is possible to gain energy through two processes:

- the **nuclear fission**, in which a heavy nucleus ($A > 56$) splits into two lighter nuclei;
- the **nuclear fusion**, in which two light nuclei ($A < 56$) fuse together into a heavier nucleus.

[1] The total electron binding energy is neglected, since the atomic mass energies are in the order of $(1\,\mathrm{GeV} \cdot A)$ while the electron binding energies are in the range 10–100 keV.

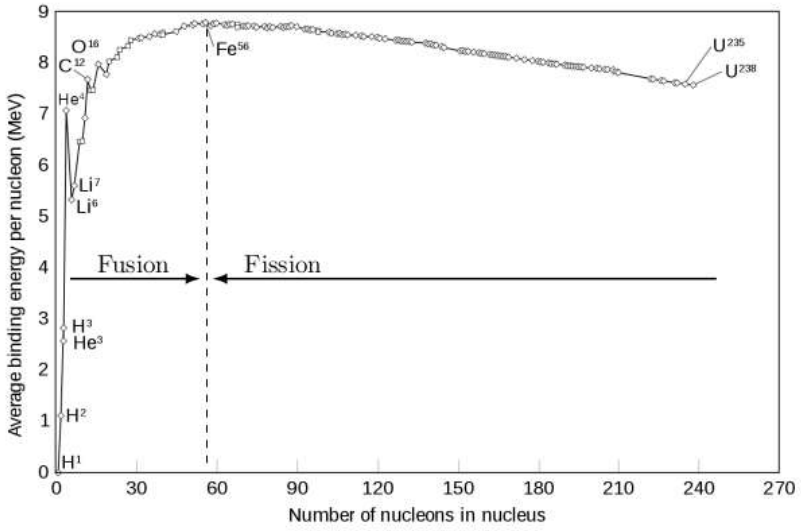

Figure 1.1: Binding energy per nucleon B/A as a function of A.

Nowadays several fission power plants operate all around the world, but they are always associated with the entailed risks of chain reactions and with the radioactive waste management issue. Moreover, the availability of required heavy radioactive elements is limited. These reasons make fission less enticing than fusion.
Unfortunately, a fusion power plant does not exist at present. The fusion inhibition by the Coulomb barrier between the reagent nuclei indeed represents a disadvantage to be faced. Since a large amount of thermal energy is needed to overcome the nuclei mutual repulsion, we refer to this process as thermonuclear fusion.

1.2 Thermonuclear fusion

In order that two nuclei have the opportunity to fuse together, they must to be close enough that the strong nuclear force prevails over the Coulomb force due to their positive charge.
The tunnel effect allow a particle to overcome the potential barrier even if its energy is lower than the maximum value of the potential. So, thanks to the quantum–mechanical effects, fusion reactions have a good probability to occur at much lower temperatures ($\sim 10\,\mathrm{keV}$) than the classical expectations ($> 100\,\mathrm{keV}$). The typical cross section shape is shown in figure 1.2.

Nevertheless, a very large amount of thermal energy in the order of 10 keV has to be supplied to the nuclei. Hence, in controlled thermonuclear fusion

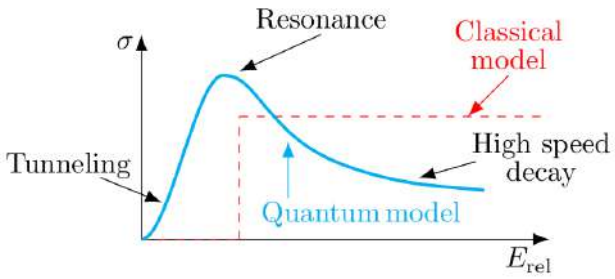

Figure 1.2: Quantum cross section σ for a fusion reaction as a function of relative kinetic energy E_{rel} of nuclei.

reactors on Earth, extremely high temperatures are reached. In these conditions the fusion fuel is in the state of plasma, also known as the fourth state of matter in addition to the solid, liquid, and gaseous ones.
A plasma is an ionised gas mainly composed by positive charged ions and negative charged electrons which exhibits the collective behaviour of shielding out external electric fields for distances larger than some Debye length λ_D, defined as

$$\lambda_D := \left(\sum_s \frac{q_s^2 \, n_{\sigma 0}}{\varepsilon_0 \, k T_s} \right)^{-1/2}$$

where k is the Boltzmann's constant, ε_0 is the vacuum dielectric constant, and s is a general plasma species characterised by a particle charge q_s, an initial density $n_{\sigma 0}$, and a temperature T_s.

Performances of a thermonuclear fusion reactor are affected by the used plasma species and by operational conditions. Therefore, it is crucial to choose wisely the employed fusion fuel also based on the related fusion reaction rate depending on temperature and density values.

1.2.1 Fusion reactions and reaction rates

The most suitable fusion reactions

$$\begin{aligned} \mathrm{D} + \mathrm{D} &\longrightarrow \mathrm{n} + {}^3\mathrm{He} + 3.27\,\mathrm{MeV} \\ \mathrm{D} + \mathrm{T} &\longrightarrow \mathrm{n} + {}^4\mathrm{He} + 17.6\,\mathrm{MeV} \\ {}^3\mathrm{He} + \mathrm{D} &\longrightarrow \mathrm{p} + {}^4\mathrm{He} + 18.3\,\mathrm{MeV} \end{aligned} \tag{1.1}$$

have been investigated to select the best choice for a future thermonuclear fusion power plant.
It would be convenient to have a large amount of released energy as well as a

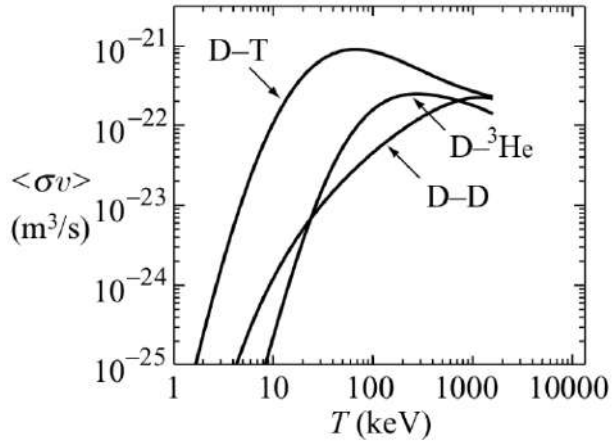

Figure 1.3: Reactivity $\langle \sigma v \rangle$ of the candidate fusion reactions as a function of the plasma temperature.[2]

neutron (not subjected to magnetic confinement) among reaction products, while it is disadvantageous to use tritium as reagent because of its poor availability. However, to identify which is the best reaction to exploit, the reaction rates of candidates have to be compared.

The reaction rate is the number of reactions per unit of volume and per unit of time. In view of the energy production goal, plasma conditions have to be optimised in order to increase as much as possible the reaction rate. Considering a plasma with only two ion species, the reaction rate is

$$\frac{\#\text{ reactions}}{\text{time} \cdot \text{volume}} = n_1 n_2 \langle \sigma v \rangle$$

where n_1 and n_2 are the two ion densities, $v \equiv v_{\text{rel}} = |\boldsymbol{v}_1 - \boldsymbol{v}_2|$ is the relative velocity, and the reactivity $\langle \sigma v \rangle = \langle \sigma v \rangle (T)$ depends on the plasma temperature T.

Since the reactivity and the density product are independent, they can be maximised separately. Figure 1.3 shows the reactivity of the candidate fusion reactions (1.1) as a function of T.[1] Clearly, using a mixture of deuterium and tritium as fusion fuel is the best choice, inasmuch it ensures the highest reactivity at lower temperatures. Therefore, the fusion reaction selected for future fusion power plants is

$$\boxed{\mathrm{D} + \mathrm{T} \longrightarrow \mathrm{n} + {}^4\mathrm{He} + 17.6\,\mathrm{MeV}}$$

On the other hand, to maximise the reaction rate, the product of reagent nuclei densities $n_1 n_2 = n_D n_T$ should be increased as much as possible within

feasibility limits, provided the same plasma temperature is reached. However, for a given ion density $n_D + n_T$, different ratio of n_D/n_T could be used in the mixture. By definition, the condition $\mathrm{d}\left(n_\mathrm{D} n_\mathrm{T}\right)/\mathrm{d}n_\mathrm{T} = 0$ needs to be fulfilled to find the maximum value of $n_\mathrm{D} n_\mathrm{T}$. Exploiting the quasi–neutrality of plasma, we can rewrite $n_\mathrm{D} n_\mathrm{T} \simeq \left(n_e - n_\mathrm{T}\right) n_\mathrm{T} = n_e n_\mathrm{T} - n_\mathrm{T}^2$ and solve the condition

$$n_e - 2n_\mathrm{T} = 0 \implies n_\mathrm{T} = n_e/2 \implies n_\mathrm{D} = n_e - n_\mathrm{T} = n_e/2 \implies n_\mathrm{D} = n_\mathrm{T}$$

finding out that a mixture with 50 % of tritium and 50 % of deuterium allow us to obtain more reactions and hence more fusion power with equal total ion density.

1.2.2 Neutron and α particle energies

The energy $W = 17.6\,\mathrm{MeV}$ released during the fusion reaction is converted into kinetic energy and spitted between the neutron and the ^{4}He nucleus, also called α particle.

Since the reagent kinetic energies are in the order of keV while the product kinetic energies are in the order of MeV, a null initial momentum $\left(\boldsymbol{p}_D + \boldsymbol{p}_T\right) = \left(m_D \boldsymbol{v}_D + m_T \boldsymbol{v}_T\right)/2 = 0$ can be assumed. Under this hypothesis, the total momentum conservation and the conservation of energy imply respectively that $m_\alpha v_\alpha - m_n v_n = 0$ and $W = E_n + E_\alpha$ with $E_n = \left(m_n v_n^2\right)/2$ and $E_n = \left(m_\alpha v_\alpha^2\right)/2$.

$$\begin{cases} v_\alpha = m_n v_n / m_\alpha \\ W = E_n + \left(m_\alpha v_\alpha^2\right)/2 \end{cases} \implies W = E_n + \frac{m_\alpha}{2}\frac{m_n^2 v_n^2}{m_\alpha^2} \implies W = E_n\left(1 + \frac{m_n}{m_\alpha}\right)$$

$$\implies \quad E_n = \frac{m_\alpha}{m_\alpha + m_n} W \simeq \frac{4m_n}{4m_n + m_n} W = \frac{4}{5} W \qquad \text{e} \qquad E_\alpha \simeq \frac{1}{5} W$$

Therefore

$$\boxed{E_n = 14.1\,\mathrm{MeV}} \qquad \text{and} \qquad \boxed{E_\alpha = 3.5\,\mathrm{MeV}}$$

are obtained.
Through collisions, alpha particles contribute to the plasma heating. The kinetic energy of neutrons, which are slowed down in the fusion device blanket surrounding the plasma, is converted into heat and in turn this thermal energy could be transformed into electrical energy.

Table 1.1: Estimated availability of fusion fuel.

Energy Resource	Estimated energy availability [GJ]	Estimated fuel availability at the present consumption rate [y]
Deuterium (oceans)	10^{22}	10^{10}
Lithium (oceans)	10^{19}	10^{7}
Lithium (land)	10^{16}	10^{4}

1.2.3 Fuel availability

The natural hydrogen, which can be extracted from the H_2O, includes the deuterium with an isotopic abundance of about 0.015 %. On Earth, thanks to the huge seawater amount, a deuterium availability of about ten billion years is evaluated.

On the other side, there are only trace amounts of natural tritium produced by the interactions between Earth's atmosphere and cosmic rays. Hence, a mechanism to generate tritium within fusion reactors has been developed. Natural lithium (7.6 % of ^{6}Li and 92.4 % of ^{7}Li), embedded in the breeding blanket, intercepts neutrons coming from the fusion reactions. The interaction between lithium and neutrons through two possible reactions

$$\mathrm{n} + {}^6\mathrm{Li} \longrightarrow \mathrm{T} + {}^4_2\mathrm{He} + 4.8\,\mathrm{MeV}$$
$$\mathrm{n} + {}^7\mathrm{Li} \longrightarrow \mathrm{T} + {}^4_2\mathrm{He} + \mathrm{n} - 2.5\,\mathrm{MeV}$$

leads to the tritium production. The availability threshold of 10 000 years estimated for the land Lithium is overstepped by the lithium reserves in oceans which at the current energy consumption rate could supply Li for around 10 million years, as summarised in table 1.1.

It is very useful to compare fuel reserves of various existing energy sources with those of elements required in fusion reactors. The temporal availability estimations reported in table 1.2 refer to the current world consumption rate of $\sim 6 \times 10^{11}$ J/y.[1]
Among fossil fuels, the coal is the longest–term resource with an evaluated availability of about half a millennium.
The classical fission power plants are usually based on uranium 235, while only the rarest fast–neutron reactors employ uranium 238. The future generation of fission plants called breeder reactors, which use primarily uranium 238 and Thorium 232, could significantly extent the life of the fission energy source.

Table 1.2: Estimated availability of various fuels.[1]

Energy Resource	Estimated energy availability [GJ]	Estimated fuel availability at the present consumption rate [y]
Coal	3×10^{14}	500
Oil	2×10^{13}	30
Natural gas	2×10^{13}	30
^{235}U	1×10^{13}	20
^{238}U and ^{232}Th	1×10^{16}	20 000
Li (to produce T)	10^{16}–10^{19}	10^{4}–10^{7}

The renewable energies, such as wind and solar ones, are potentially unlimited resources. Unfortunately, since they typically are non–constant and have low energy densities, they need to be supported by other power sources. Observing the competitor availabilities, it is clear why the fusion challenge is so attractive from an energetic perspective.

1.3 Plasma confinement

A key point of a fusion device is its capability to confine plasma to safeguard the machine walls against the high thermal conductivity of the ionised gas at temperatures of about hundreds of millions Celsius degrees.[2]
Plasma could be confined with three methods:

- gravitational confinement;
- inertial confinement;
- magnetic confinement.

The gravitational confinement, exploited by stars thanks to their huge masses, is inoperable on the Earth obviously.
In inertial fusion devices, a fuel pellet is hit by very focused and powerful energy impulses emitted by an extremely intense power source, typically by high power lasers. The pellet surface is ablated because of the incident power and is radially expelled outward. Due to the resulting inward radial force, the pellet is mightily compressed adiabatically, its temperature and density arise, and the fuel fusion is obtained.

[2]The most refractory materials have relatively low thermal resistance limits.

The third confinement method is based on the employment of high and specially designed magnetic fields to confine the charged particles of the plasma. Nowadays, the research in the nuclear fusion field is mainly focused on the magnetic confinement machines, since they present the best achieved results.

1.4 Magnetic confinement

An equilibrium can be reached exploiting a magnetic field to confine the plasma particles.
Let us examine a completely ionised plasma with S particle species subjected to a magnetic field $\boldsymbol{B}$ and an electric field $\boldsymbol{E}$. The number of particles, the atomic number, the temperature, the density, the mean velocity, and the current density of a general species σ are respectively called N_σ, Z_σ, T_σ, n_σ, $\boldsymbol{v}_\sigma = N_\sigma^{-1} \sum_j^{N_\sigma} \boldsymbol{v}_{\sigma_j}$, and $\boldsymbol{J}_\sigma := Z_\sigma e\, \boldsymbol{v}_\sigma n_\sigma$, where e is the proton charge and $Z_e = -1$ is assumed for electrons.
The total force $\boldsymbol{F}$ acting on the plasma is the sum of the the kinetic pressure force, all the electric forces, and all the Lorentz forces for particles of each σ species. So, the total force $\boldsymbol{F}$ acting on the plasma per unit of volume V is

$$\begin{aligned}
\frac{\boldsymbol{F}}{V} &= -\boldsymbol{\nabla} P + \frac{1}{V} \sum_{\sigma=1}^{S} \left(\sum_{j=1}^{N_\sigma} Z_\sigma e \boldsymbol{E} + \frac{1}{V} \sum_{j=1}^{N_\sigma} Z_\sigma e\, \boldsymbol{v}_{\sigma_j} \times \boldsymbol{B} \right) = \\
&= -\boldsymbol{\nabla} P + \sum_{\sigma=1}^{S} \left(\frac{N_\sigma}{V} Z_\sigma e \boldsymbol{E} + \frac{N_\sigma}{V} Z_\sigma e\, \boldsymbol{v}_\sigma \times \boldsymbol{B} \right) = \\
&= -\boldsymbol{\nabla} P + e\, \boldsymbol{E} \sum_{\sigma=1}^{S} n_\sigma Z_\sigma + \sum_{\sigma=1}^{S} \boldsymbol{J}_\sigma \times \boldsymbol{B} \simeq \\
&\simeq -\boldsymbol{\nabla} P + \boldsymbol{J} \times \boldsymbol{B}
\end{aligned}$$

where we assumed the quasi–neutrality $\sum_{\sigma=1}^{S} n_\sigma Z_\sigma \simeq 0$ in the last step and where $J = \sum_{\sigma=1}^{S} \boldsymbol{J}_\sigma$ is the plasma current density.
Therefore, the configuration is at the equilibrium ($\boldsymbol{F} = 0$) when

$$\boxed{\boldsymbol{J} \times \boldsymbol{B} = \boldsymbol{\nabla} P} \tag{1.2}$$

We notice that the same conclusion would be reached regardless the presence or lack of the electric field.

The β concept

A parameter frequently used to define the efficiency of a magnetic field to confine a plasma is the β factor. To introduce the β concept, let us suppose to have a null or constant electric field and rewrite the plasma current density in terms of $\boldsymbol{B}$, thanks to the fourth Maxwell's equation, as follows

$$\boldsymbol{\nabla} \times \boldsymbol{B} = \mu_0 \boldsymbol{J} + \mu_0 \varepsilon_0 \cancelto{0}{\frac{\partial \boldsymbol{E}}{\partial t}} \qquad \Longrightarrow \qquad \boldsymbol{J} = \frac{1}{\mu_0} \boldsymbol{\nabla} \times \boldsymbol{B}$$

where μ_0 is the vacuum magnetic permeability. Therefore

$$\boldsymbol{J} \times \boldsymbol{B} = -\frac{1}{\mu_0} \left[\boldsymbol{B} \times (\boldsymbol{\nabla} \times \boldsymbol{B}) \right] = -\frac{1}{\mu_0} \left[\frac{1}{2} \boldsymbol{\nabla} \big(B^2 \big) - (\boldsymbol{B} \cdot \nabla) \boldsymbol{B} \right]$$

is obtained.[3] Substituting this expression in (1.2), we find the pressure balance equation

$$\frac{1}{\mu_0} \left[(\boldsymbol{B} \cdot \nabla) \boldsymbol{B} - \frac{1}{2} \boldsymbol{\nabla} \big(B^2 \big) \right] = \boldsymbol{\nabla} P \implies \underbrace{\frac{1}{\mu_0} (\boldsymbol{B} \cdot \nabla) \boldsymbol{B}}_{\text{magnetic field term}} \underbrace{-\boldsymbol{\nabla} \left(P + \frac{B^2}{2\mu_0} \right)}_{\text{pressure term}} = 0$$

Two terms appear in the equilibrium condition:

- a **magnetic field term** which is null for a uniform magnetic field;
- a **pressure term**, sum of the kinetic and the magnetic pressure.

We notice that, although $\boldsymbol{B}$ is uniform, the configuration equilibrium could be reached thanks to the balance of kinetic pressure with magnetic pressure. The β factor defined as

$$\boxed{\beta = \frac{P}{B^2/(2\mu_0)}}$$

indicates the efficiency of the magnetic confinement. In fusion plasmas high values of densities and temperatures, and hence of pressure, are reached; so intense magnetic fields are required too. Nevertheless, since the costs increase with field magnitude, a large β parameter reveal a good configuration capable of confining high pressure plasma with a relatively low B.

[3] The following vector identity has been used

$$\boldsymbol{\nabla}(\boldsymbol{A} \cdot \boldsymbol{B}) = \boldsymbol{A} \times (\boldsymbol{\nabla} \times \boldsymbol{B}) + \boldsymbol{B} \times (\boldsymbol{\nabla} \times \boldsymbol{A}) + (\boldsymbol{A} \cdot \nabla) \boldsymbol{B} + (\boldsymbol{B} \cdot \nabla) \boldsymbol{A}$$

$$\Rightarrow \quad 2 \left[\boldsymbol{B} \times (\boldsymbol{\nabla} \times \boldsymbol{B}) \right] = \boldsymbol{\nabla} \Big(B^2 \Big) - 2 (\boldsymbol{B} \cdot \nabla) \boldsymbol{B}$$

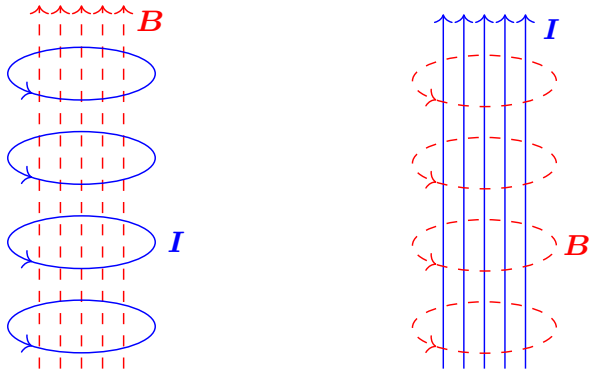

(a) Theta pinch. (b) Zeta pinch.

Figure 1.4: Simple magnetic confinement systems. The dashed red lines represent the magnetic field lines, while the solid blue ones represent the current which produces the magnetic field.

1.4.1 Linear magnetic configurations

The simplest magnetic confinement devices are the linear magnetic configurations, which include:

- the theta pinch;
- the zeta pinch;
- the magnetic mirror.

The pinch configurations, whose sketches are shown in figure 1.4, take their names from the direction of the electric current $\boldsymbol{I}$ generating the magnetic field. Clearly, it is natural to use cylindrical coordinates in linear magnetic configurations.
In a typical theta pinch device, which is basically a solenoid, the current flows in circular coaxial coils producing an approximately uniform magnetic field in the plasma along the coil axis $\boldsymbol{B} \simeq B\hat{\boldsymbol{z}}$. Although the theta pinch configuration is stable under both kink and sausage perturbations, the particles are very quickly lost as it lacks any sort of axial confinement.
In an ideal zeta pinch, the axial current density $\boldsymbol{J} = J_z(r)\hat{\boldsymbol{z}}$ flows in a limitless plasma column producing an azimuthal magnetic field $\boldsymbol{B} = B_\theta(r)\hat{\boldsymbol{\theta}}$. The attractive force arising between parallel currents tends to squeeze the plasma column. When this pinching force and the opposite kinetic pressure force are balanced, the so–called equilibrium pinch is achieved and the plasma reaches stationary conditions. Close magnetic field lines entail a more efficient magnetic confinement of plasma in zeta pinch systems ($\beta_{\max} \approx 2$) than in theta

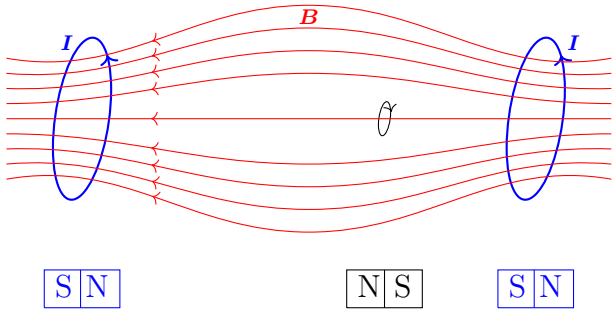

Figure 1.5: Sketch of the simplest version of a magnetic mirror. Intuitively, the coils and a test charged particle can be thought as magnets.

pinch ones ($0 \leq \beta \leq 1$). Nevertheless, in zeta pinch devices any pressure perturbation is amplified by the magnetic field reaction and hence this intrinsic instability against perturbations makes the zeta pinch configuration unsuitable for fusion purposes.
The magnetic mirror, depicted in figure 1.5, is an evolution of the theta pinch idea where the charged particles can be reflected thanks to a non null magnetic field gradient along the direction of field lines. The particle loss at the device extremities is partially solved. Defining the pitch angle θ_p of a particle as the angle between its velocity $\boldsymbol{v}$ and the magnetic field $\boldsymbol{B}$ in the point of minimum field, the criteria which a charge has to fulfil to be reflected in the magnetic mirror is

$$\sin\theta_p > \sqrt{\frac{B_{\min}}{B_{\max}}} = \sin\theta_c \tag{1.3}$$

where θ_c is the critical pitch angle. Charges with a pitch angle large enough are confined inside the magnetic mirror, while the others can escape from the device. Unfortunately, the fraction of particles in this loss cone is non negligible for a good fusion configuration candidate.

Summarising, a fusion reactor can not be a linear device because of stability or confinement deficiencies. Hence, starting from the theta pinch concept, it was devised to bend the magnetic field lines into themselves to obtain closed lines, i.e. a toroidal shape, to improve stability and confinement.

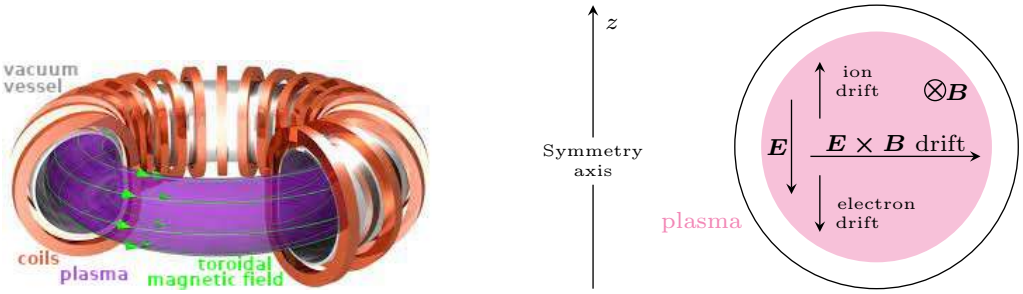

(a) Toroidal configuration.

(b) Poloidal section with particle drifts.

Figure 1.6: (a) The simplest toroidal configuration (figure courtesy of C. Brandt [3]). (b) Poloidal section and particle drifts in the simplest toroidal configuration.

1.4.2 Toroidal magnetic configurations

The simplest toroidal configuration, depicted in figure 1.6(a), has a sequence of magnetic coils arranged to form a torus with each coil in a specific poloidal plane to produce a toroidal magnetic field $\boldsymbol{B} = B\hat{\boldsymbol{\theta}}$ with θ indicating the toroidal angle.
According to the Ampère theorem, we have

$$\oint_{\Gamma} \boldsymbol{B} \cdot \mathrm{d}\boldsymbol{l} = \mu_o I_{\mathrm{tot}} \quad \Longrightarrow \quad 2\pi R B = \mu_0 I N$$

where Γ is a circumference of radius R concentric with the torus and internal to it, I_{tot} is the total current passing through Γ, N is the number of coils, and I the current flowing in the coils. Since the toroidal magnetic field intensity is inversely proportional to the toroidal radial coordinate R

$$\boxed{B(R) = \frac{\mu_0 I N}{2\pi R}} \tag{1.4}$$

there is a force due to the magnetic field gradient $\boldsymbol{F}_{\boldsymbol{\nabla} B} = -\mu \boldsymbol{\nabla} B$.
Since a charge q subject to a force $\boldsymbol{F}$ in a magnetic field $\boldsymbol{B}$ has a drift velocity $\boldsymbol{v}_d = \boldsymbol{F} \times \boldsymbol{B} / \left(qB^2\right)$, in a toroidal configuration the plasma particles experience a velocity drift due to the magnetic field gradient

$$\boldsymbol{v}_{\boldsymbol{\nabla} B} = -\mu \frac{\boldsymbol{\nabla} B \times \boldsymbol{B}}{qB^2} = -\mu \frac{|\boldsymbol{\nabla} B|}{qB} \left(-\hat{\boldsymbol{R}} \times \hat{\boldsymbol{\theta}}\right) = \mu \frac{|\boldsymbol{\nabla} B|}{qB} \hat{\boldsymbol{z}}$$

along the torus axis. Particularly, the positive charged ions move in $\hat{\boldsymbol{z}}$ direction, while the negative charged electrons move in $-\hat{\boldsymbol{z}}$ direction. Therefore,

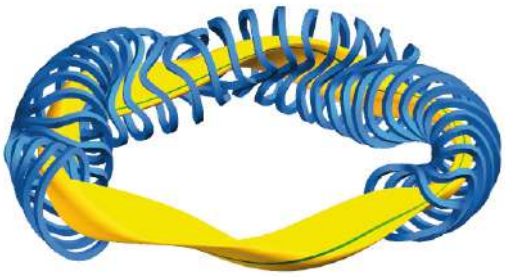

Figure 1.7: Wendelstein 7–X stellarator design where the plasma is drawn in yellow surrounded by some magnet coils in blue and with an example magnetic field line in green. Figure courtesy of Max–Planck Institut für Plasmaphysik.

a vertical electric field $\boldsymbol{E} = -E\hat{\boldsymbol{z}}$ is generated. The related electric force $\boldsymbol{F_E} = q\boldsymbol{E}$ causes a radial drift velocity independent of particle charge sign

$$\boldsymbol{v_{E\times B}} = \frac{\boldsymbol{E}\times\boldsymbol{B}}{B^2} = \frac{E}{B}\left(-\hat{\boldsymbol{z}}\times\hat{\boldsymbol{\theta}}\right) \qquad \Longrightarrow \qquad \boxed{\boldsymbol{v_{E\times B}} = \frac{E}{B}\hat{\boldsymbol{R}}}$$

called $\boldsymbol{E}\times\boldsymbol{B}$ drift velocity, which push all the plasma outward. A scheme of drifts is illustrated in figure 1.6(b). Hence, a basic toroidal magnetic device as in figure 1.6(a) does not improve enough the confinement.

To reduce the $\boldsymbol{E}\times\boldsymbol{B}$ drift, a magnetic field with helicoidal field lines rolled around torus surfaces can be used. Thus, the drift due to the magnetic field gradient and the resulting electric field produced by the charge separation is sometimes in $\hat{\boldsymbol{z}}$ direction an sometimes in $-\hat{\boldsymbol{z}}$ direction. Two different device kinds are able to created the desired helicoidal field lines:

- stellarators;
- tokamaks.

Stellarators, devised in the 1950s by the American physicist Lyman Strong Spitzer, employ non–planar magnetic coils specifically designed to achieve the helicoidal field lines. They always work in a stationary operational regime, but an extremely high precision in the magnetic coil realisation is required. Figure 1.7 displays a stellarator design sketch.
The fusion research has shelved stellarators for many years, but recently a revival of interest was aroused in these devices and the new Wendelstein–7X stellarator, realised at Greifswald in Germany and become operational in the 2015, has presented the first promising results. Nonetheless, stellarators has

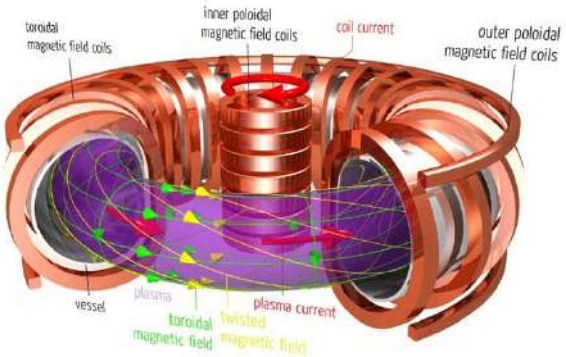

Figure 1.8: Tokamak design sketch (figure courtesy of C. Brandt [3]).

fallen behind compared to the tokamaks and nowadays their performances are still worse.

1.5 Tokamaks

Tokamaks, devised in 1951 by the Soviet physicists Igor Tamm and Andrej Sacharov, have been studied for long as thermonuclear fusion devices. Tokamak is a syllabic acronym of "toroidal chamber with magnetic coils".

In tokamaks, a toroidal magnetic field $\boldsymbol{B}_T$ and a poloidal magnetic field $\boldsymbol{B}_P$ contribute to produce a total magnetic field with helicoidal field lines, as required. A set of planar coils arranged as in the simplest toroidal configuration of figure 1.6(a) generate the toroidal component $\boldsymbol{B}_T$, while a plasma current I_{pl} flowing toroidally in the tokamak produces the poloidal field $\boldsymbol{B}_P$. This needed plasma current is achieved exploiting a suitable $f.e.m.$ and the conductor properties of the plasma. The $f.e.m.$ is induced according to the Faraday–Neumann–Lenz law $f.e.m. = -\mathrm{d}\Phi(\boldsymbol{B})/\mathrm{d}t$ by a suitable variable magnetic field flux $\Phi(\boldsymbol{B})$, which can be generated by a time varying current in a solenoid placed along the torus symmetry axis. Particularly, to obtain a constant I_{pl}, the current in the central solenoid has to vary linearly in time. In other words, plasma behaves as the secondary circuit of a transformer with the central solenoid as primary circuit. Figure 1.8 shows the typical tokamak design. Every magnetic field line belongs to a torus surface and is wrapped around it. Thus, in a tokamak the concentric torus surfaces are both the magnetic and the flux surfaces.

Since the toroidal magnetic field intensity is inversely proportional to the toroidal radial coordinate R, two plasma regions can be identified: the outer Low–Field Side (LFS), where the density and temperature gradients are parallel to the toroidal magnetic field gradient, and inner the High–Field Side

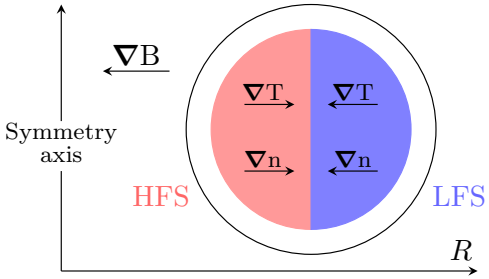

Figure 1.9: High–Field Size (HFS) and Low–Field Side (LFS), with typical directions of the density and temperature gradients in the plasma (poloidal section view).

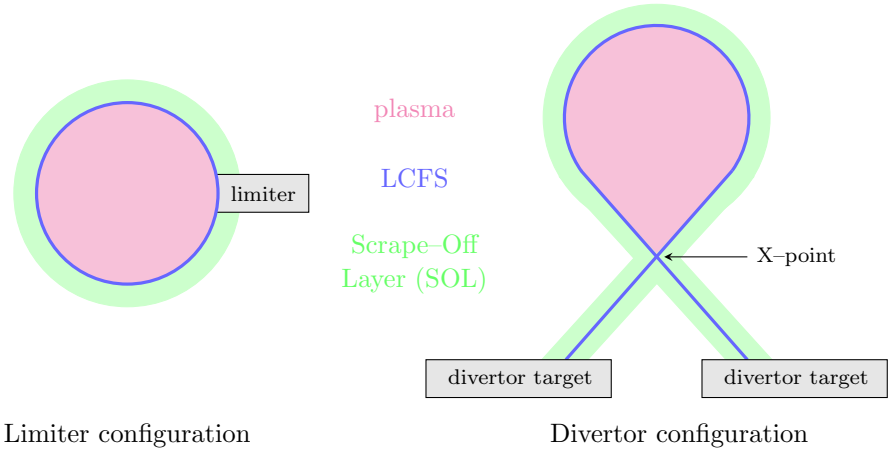

Figure 1.10: Limiter and divertor configurations schematically.

(HFS), where the density and temperature gradients have opposite sign with respect to the toroidal magnetic field gradient. These region are sketched in figure 1.9.

Without auxiliary heating systems supporting the plasma current, tokamaks are intrinsically non stationary, since the current in the central solenoid has to be varied in order to have the poloidal magnetic field required to confine the plasma. To operate in a stationary regime, very energy–consumptive techniques to drive the plasma current are required.

To protect the vacuum vessel of a tokamak from extremely high thermal loads coming from plasma, it is possible to use limiter or divertor configurations, sketched in figure 1.10. Limiters are protective components inserted within the vessel and constantly in contact with the plasma. In this configuration, the Last Closed Flux Surface (LCFS) is determined by the intersection between magnetic field lines and material structures of limiters. In the di-

vertor configuration, the magnetic surfaces are reshaped to create a LCFS with an X–point called the separatrix which separates the closed magnetic surfaces inside from the d magnetic surfaces and the open magnetic surfaces outside. The region with open magnetic surfaces is called Scrape–Off Layer (SOL). In this region, charged particles coming from the plasma core are collected on a target structure called divertor in a region separated from the plasma, ensuring better performances than with limiter configuration.

Nowadays, the biggest operating tokamak is the Joint European Torus (JET)[4], an EURATOM experiment sited at Abingdon in the UK.
The construction of a larger tokamak called International Thermonuclear Experimental Reactor (ITER)[5] at Cadarache in France is in progress (first plasma scheduled for December 2025). ITER is a worldwide cooperative project involving the European Union, China, India, Japan, South Korea, Russia, and the United States, whose main goal is to prove that the fusion power can be significantly larger than the injected thermal power.
Nevertheless, the baseline strategy planned for ITER of testing a conventional metal divertor will be unsuitable for higher thermal loads. Hence, some alternative strategies have to be developed and tested in view of the operating conditions of the DEMOnstration power plant (DEMO) and of future reactors. Thus, studying the controlled power and particle exhaust from a fusion reactor has been selected one of the central research topics of the European Fusion Roadmap.[6, 7]
To address this issue, the new Divertor Tokamak Test facility (DTT)[8, 9, 10] was planned and is being built at Frascati in Italy. This PhD project concerns the integrated modelling work of the main plasma scenarios of DTT.

1.5.1 Important parameters in tokamaks

In tokamaks, it is useful to define a set of cylindrical coordinates (R, φ, z), as shown in figure 1.11(a). The toroidal radius coordinate R is often substituted by another equivalent radial coordinate, such as the poloidal one r displayed in figure 1.11(b).

Aspect ratio

To characterise a specific device, it is important the ratio between the major radius R_0 and the minor radius a of the tokamak, called aspect ratio $A \coloneqq R_0/a > 1$.
The inverse aspect ratio $\varepsilon \coloneqq r/R_0 < 1$ is also used as parameter of a certain magnetic surface. A cylindrical approximation can be used sometimes, but on the condition that $\varepsilon \ll 1$.

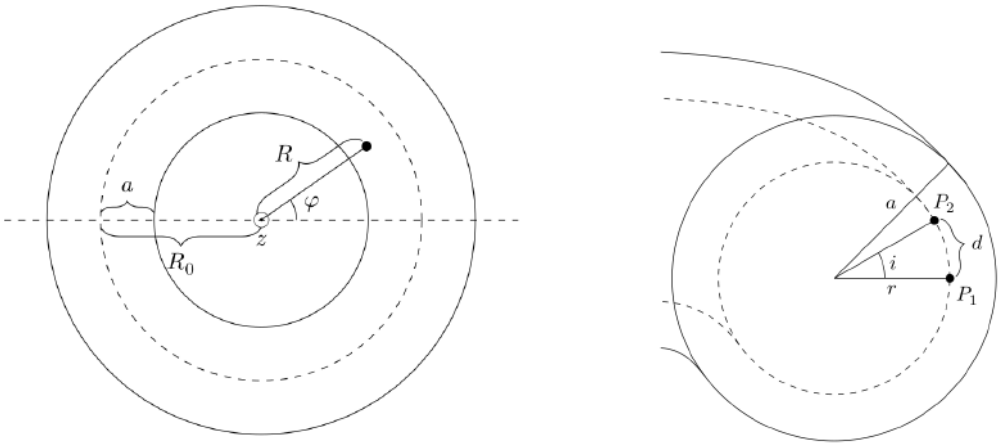

(a) Torus top view.

(b) Poloidal section view.

Figure 1.11: Coordinates and main geometrical parameters in a tokamak.

Rotational transform, safety factor, and magnetic shear

As long as we consider the simplest toroidal configuration of figure 1.6, the circular magnetic field lines close on themselves after a whole toroidal turn. The poloidal magnetic field added in the tokamak configuration twists the field lines around the flux surfaces leading the lines to no longer close in one toroidal turn.
Let us follow a field line which intersects a given poloidal section, displayed in figure 1.11(b), in P_1 and after one turn in P_2. The length d of the circumference arc between P_1 and P_2 divided by the poloidal radial coordinate r of the circumference is called rotational transform $i \coloneqq d/r$. The rotational transform is typically small since $B_P \ll B_T$ and hence i is approximately the poloidal angle variation in one toroidal turn of the field line. The rotational transform can be associated with the toroidal and poloidal magnetic field intensities, using cylindrical approximation shown in figure 1.12. In this approximation, the ratio B_P/B_T equals the ratio between the poloidal displacement in a toroidal turn d and the toroidal circumference length $2\pi R_0$

$$\frac{B_P}{B_T} = \frac{d}{2\pi R_0} \qquad \Longrightarrow \qquad d = 2\pi R_0 \frac{B_P}{B_T} \qquad \Longrightarrow \qquad i = \frac{2\pi R_0}{r} \frac{B_P}{B_T}$$

The $q \coloneqq 2\pi/i$ parameter called safety factor and the magnetic shear s

$$\boxed{q = \frac{r}{R_0} \frac{B_T}{B_P}} \qquad \text{and} \qquad \boxed{s \coloneqq \frac{r}{q} \frac{\mathrm{d}q}{\mathrm{d}r}}$$

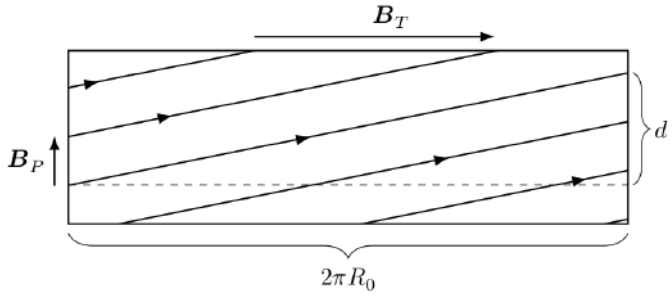

Figure 1.12: Flux surface with field lines in cylindrical approximation.

are more frequently used.
If q is rational, then the magnetic field line closes on itself after n turns. Otherwise, the magnetic field maps all its magnetic surface. On a surface with rational q the magnetohydrodynamic (MHD) instabilities could cause a confinement loss, since perturbations generate stationary waves amplified every n turns.
Large values of q generally guarantee a higher MHD stability, while magnetic shear values are important for the turbulent transport stability.

Larmor radius and Larmor frequency

When a charge q with mass m moving with velocity $\boldsymbol{v}$ in a uniform and constant magnetic field $\boldsymbol{B}$, then the particle motion equation is

$$m\frac{\mathrm{d}\boldsymbol{v}}{\mathrm{d}t} = q\boldsymbol{v}\times\boldsymbol{B}$$

and hence the kinetic energy is constant

$$\frac{\mathrm{d}}{\mathrm{d}t}\left(\frac{1}{2}m\boldsymbol{v}\cdot\boldsymbol{v}\right) = \frac{1}{2}m\left(\boldsymbol{v}\cdot\frac{\mathrm{d}\boldsymbol{v}}{\mathrm{d}t}+\frac{\mathrm{d}\boldsymbol{v}}{\mathrm{d}t}\cdot\boldsymbol{v}\right) = m\boldsymbol{v}\cdot\frac{\mathrm{d}\boldsymbol{v}}{\mathrm{d}t} = \boldsymbol{v}\cdot(q\boldsymbol{v}\times\boldsymbol{B}) = 0\,.$$

The charged particle moves with an helicoidal trajectory around the magnetic field lines with a radius r_L and a cyclotron frequency ω_L, respectively called Larmor radius and Larmor frequency, equal to

$$r_L = \frac{mv_\perp}{|q|B} \qquad \text{and} \qquad \omega_L = \frac{|q|B}{m} \tag{1.5}$$

where $v_\perp$ is the velocity component perpendicular to the magnetic field.

Energy confinement time

The thermal energy confinement time, defined as ratio between the plasma thermal energy and the heating power provided to the plasma particles $\tau_{E_{\text{th}}} := E_{\text{th}}/P_{\text{heat}}$ is a key parameter of a thermonuclear fusion device.[4]
It is the time spent by energy to travel from the plasma centre to the edge, i.e. to cover a distance $\sim a$. Hence, according to the random walk model, it is proportional to

$$\tau_{E_{\text{th}}} \propto \frac{a^2}{\chi}$$

with χ heat diffusion coefficient.
Obviously, in a tokamak we aim to minimise particle and heat diffusion by various strategies to confine plasma and energy for as long as possible. Another way to increase the thermal energy confinement time is to enlarge the fusion device, but this strategy costs a lot.

1.5.2 Particle orbits in a tokamak

In a tokamak, the intensity of the magnetic field in first approximation is $B \approx B_T = B_0 R_0/R$, since $B_T \gg B_P$. Therefore, along a general helicoidal field line, the magnetic field magnitude B changes. It entails that charge trajectories can include turning points where charges are reflected by the non null field gradient, such as in the magnetic mirror configuration. These particles, snared between two toroidal angles, are called trapped particles. The other plasma charges, called passing particles, twist for many toroidal turns in the tokamak.

To distinguish trapped particles from passing particles, the condition (1.3) is applied once more. Rewriting $R = R_0 + r\cos\theta$ as inferred by figure 1.13(a), the toroidal field can be rewritten as a function of the surface inverse aspect ratio and of the poloidal angle θ coordinate $B = B_0/(1 + \varepsilon\cos\theta)$, sketched in figure 1.13(b). Thus, a charge in a tokamak is a trapped particle if its pitch angle fulfils the condition $\sin\theta_p > \sqrt{B_{\min}/B_{\max}} = \sqrt{(1-\varepsilon)/(1+\varepsilon)}$. Hence, the number of trapped particles is larger close to the plasma edge than in plasma centre.

In a collisionless plasma, without taking into account drifts, the gyrocentre of a passing particle travels along an helicoidal field line and hence the its trajectory projection on a poloidal plane is simply a circumference. Nevertheless, a velocity drift $\boldsymbol{v}_{\text{D}}$ due to both the magnetic field gradient and

[4] The thermal energy is simply calculated as integral of plasma pressure over its volume, while the heating power is the integral of the energy flux over the plasma surface.

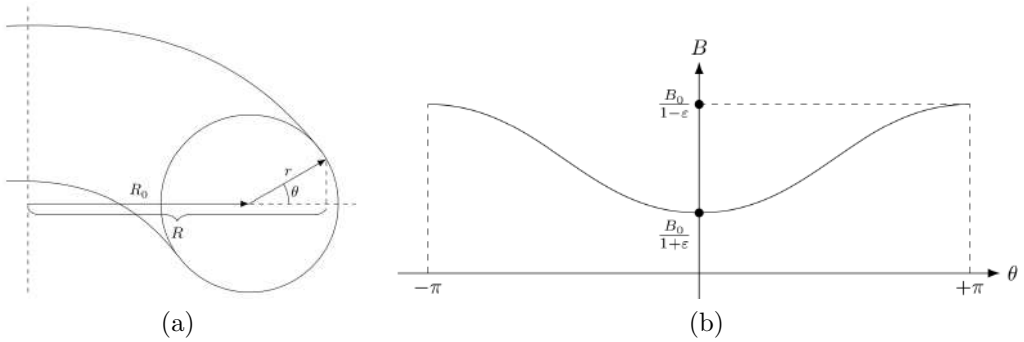

Figure 1.13: (a) Magnetic surface identified by the poloidal radius r. (b) Magnetic field magnitude as a function of the poloidal angle θ for a general magnetic surface with inverse aspect ratio ε.

the centrifugal force shifts the circumference of $\Delta_{\text{pass}} = v_{\text{D}}/\omega$, where ω is the poloidal rotation frequency. With an isotropic particle velocity distribution, the orbit displacement Δ_{pass} can be approximated as

$$\Delta_{\text{pass}} \approx r_L \cdot \frac{B_T}{B_P}\frac{r}{R} \approx r_L \cdot q$$

Thus, without collisions, the orbit shift of passing particles is of the order of some Larmor radius, i.e. is quite small since the ion and electron Larmor radii in a fusion plasma are of the order of 1 cm and 1 mm respectively.

The trapped particles have a gyrocentre trajectory with two turning points, placed on the same magnetic surface, where the toroidal motion direction is reversed. Even in this case, the velocity drift intervenes shifting the orbits. Particularly, during a back and forth loop it moves both outward and inward. The resulting gyrocentre motion projected on the poloidal plane is shown in figure 1.14 for all combination of magnetic field directions and for a positive particle. Due to this peculiar shape, trapped particle gyrocentre trajectories are also called banana orbits. Every banana orbit reaches the maximum displacement $\Delta_{\text{trap}}^{\max} \approx r_L\, q/\sqrt{\varepsilon}$ from the turning point surface in the equatorial plane.

Therefore, since $\Delta_{\text{pass}}/\Delta_{\text{trap}}^{\max} \approx \sqrt{\varepsilon} < 1$, in a tokamak the passing particles are better confined than the trapped particles.

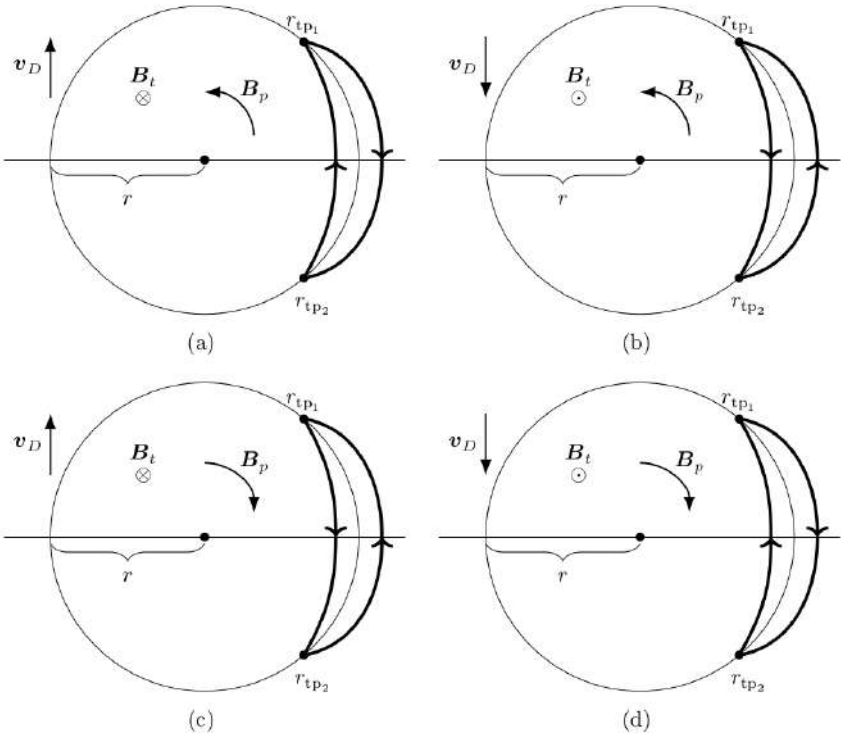

Figure 1.14: Projection on the poloidal plane of the possible orbits of the guiding centre of a positive trapped particle.

1.6 Energy balance in a fusion reactor

In order to determine the conditions of density, temperature, and energy confinement time of the fusion fuel to be reached in a thermonuclear fusion power device to achieve an output power much larger than the input power $P_{\text{out}} \gg P_{\text{in}}$, it is crucial to write the energy balance of the reactor.

The energy conservation equation for a general fluid

$$(3/2)\frac{\partial p}{\partial t} + \frac{3}{2}\boldsymbol{\nabla}\cdot(p\boldsymbol{V}) + p\,\boldsymbol{\nabla}\cdot\boldsymbol{V} + \boldsymbol{\nabla}\cdot\boldsymbol{\Gamma} = \sum_j S_j$$

can be also used for small plasma volume V with pressure p and diffusion energy flux $\boldsymbol{\Gamma}$, where $\boldsymbol{V}$ heads outward and all equation terms dimensionally are power densities.

On the left side of the equation, the first addend constitutes the internal energy density variation in time of the fluid, which is null in a stationary state. The convective term is the second one, describing the net flux energy density flowing for convection outside of the volume, and is null for core plasma in tokamaks and stellarators where the magnetic surfaces are closed. The third added represents a power density gain or a loss due to a fluid compression or expansion; this term is also null in a stationary state. The diffusive term is the fourth one and describes the power density loss for diffusion; although we were able to dominate the turbulences, it could never be null due to the non null density gradient. On the right side of the equation, there is the sum of all other power density wells or sources to be included in the energy balance.

In a tokamak in stationary state, the fluid energy conservation equation simply is $\boldsymbol{\nabla}\cdot\boldsymbol{\Gamma} = \sum_j S_j$, which integrated over all volume to obtain a global balance becomes

$$\int \boldsymbol{\nabla}\cdot\boldsymbol{\Gamma}\,\mathrm{d}V' = \int \sum_j S_j\,\mathrm{d}V'$$

For S_j terms constant over all the plasma volume, the mean diffusive term is given by the sum of all and only gain and loss sources

$$\frac{1}{V}\int \boldsymbol{\nabla}\cdot\boldsymbol{\Gamma}\,\mathrm{d}V' = \sum_j S_j$$

The diffusive term can be regarded as loss term and included in the sum

$$\sum_k S_k = 0 \qquad \text{with } S_D \coloneqq -\frac{1}{V}\int \boldsymbol{\nabla}\cdot\boldsymbol{\Gamma}\,\mathrm{d}V'$$

where the sum index change underlines the inclusion of the diffusive well. The sum contributions are divided into:

- **heat sources** including
  - $S_\alpha \longrightarrow$ fusion α particle heating
  - $S_H \longrightarrow$ all other additional heating
- **heat sinks** including
  - $S_D \longrightarrow$ diffusive term
  - $S_B \longrightarrow$ Bremsstrahlung emissions

All these power loss and gain terms S_k are dimensionally power densities.

S_α term

As mentioned in section 1.2.2, the energy of the α particles contribute the the plasma heating. If we assume that alpha particles provide all their energy to the plasma before leaving the system, then S_α can be simply calculated as product of a single α particle energy E_α and the fusion reaction rate $S_\alpha = E_\alpha \cdot n_D n_T \langle\sigma v\rangle$. With a mixture composed of 50 % deuterium and 50 % tritium, we have

$$S_\alpha = E_\alpha \cdot \frac{n_e^2}{4} \langle\sigma v\rangle$$

where quasi–neutrality $n_e \simeq n_D + n_T = n_D/2 = n_T/2$ has been used. Since the plasma pressure is $p = n_e k T_e + n_\mathrm{D} k T_\mathrm{D} + n_\mathrm{T} k T_\mathrm{T} = 2 n_e k T$ according to the perfect gas law, S_α can be expressed in terms of p

$$S_\alpha = E_\alpha \cdot \left(\frac{p}{2kT}\right)^2 \frac{\langle\sigma v\rangle}{4} \quad \Longrightarrow \quad S_\alpha = \frac{E_\alpha}{16} \frac{p^2}{(kT)^2} \langle\sigma v\rangle$$

where T is the plasma temperature at the equilibrium and $\langle\sigma v\rangle = \langle\sigma v\rangle (T)$.

S_H term

Both the Ohmic heating due to the plasma current and any additional power densities due to external auxiliary heating systems are included in the S_H term.

S_D term

With the divergence theorem, the mean diffusive term can be written as

$$S_D = \frac{1}{V}\int_V \boldsymbol{\nabla}\cdot\boldsymbol{\Gamma}\,\mathrm{d}V' = \frac{1}{V}\int_S \boldsymbol{\Gamma}\cdot\mathrm{d}\boldsymbol{A}$$

where S is the closed surface around the plasma volume V.
This term can be simply evaluated as

$$|S_D| = \frac{3p}{2\tau_E}$$

where $\tau_E = \tau_E(p,T)$ is the experimental value of the energy confinement time.

S_B term

Power losses due to the Bremsstrahlung emission associated with particle collisions are described by the S_B term. All collisions $(i-j)$ between two plasma species with densities n_i and n_j and atomic numbers Z_i and Z_j, contribute to S_B as follows

$$\left|S_{B_{i,j}}\right| \propto n_i n_j Z_i Z_j \sqrt{kT}$$

In the simplest plasma with only a single element, three $S_{B_{i,j}}$ terms corresponding to the collision between $(e-e)$, $(i-i)$, and $(e-i)$ have to be taken into account.[5] For non relativistic electrons, $S_{B_{e,e}}$ is null. Furthermore we can observe that $S_{B_{i,i}} \ll S_{B_{e,i}}$, since $S_{B_{i,i}}/S_{B_{e,i}} = (a_e/a_i)^2\,(m_e/m_i)^2 \sim 10^{-6}$, and we can neglect $S_{B_{i,i}}$. Hence the Bremsstrahlung term can be identified with only $S_{B_{e,i}}$

$$|S_B| \propto n_e n_i Z_e Z_i \sqrt{kT} \simeq n_e^2 \sqrt{kT} = \frac{p^2}{4(kT)^2}\sqrt{kT} = \frac{p^2}{4(kT)^{3/2}}$$

Power density balance

The power density balance $S_\alpha + S_H - |S_D| - |S_B| = 0$ which explicitly is

$$\boxed{\frac{E_\alpha}{16}\frac{p^2}{(kT)^2}\langle\sigma v\rangle(T) + S_H - \frac{3}{2}\frac{p}{\tau_E} - \frac{c_B}{4}\frac{p^2}{(kT)^{3/2}} = 0} \tag{1.6}$$

relates three fundamental variables: pressure p, temperature T, and energy confinement time τ_E.

[5] Here we use $Z_e = 1$.

1.7 Operating regimes

Three fusion reactor operating regimes can be distinguished.

- In the **ideal ignition regime**, auxiliary heating systems are not used ($S_H = 0$) and the energy confinement time is unlimited ($\tau_E = +\infty$).
- In the **non ideal ignition regime**, auxiliary heating systems are not used ($S_H = 0$), but the energy confinement time is limited ($\tau_E < +\infty$).
- In the **power amplification regime**, auxiliary heating systems are required ($S_H \neq 0$).

Let us discuss these regimes briefly.

Ideal ignition regime

Actually, since the diffusive term is always non null, the utopian ideal ignition regime cannot be reached but it establishes a threshold. The power density balance (1.6) in this regime is

$$\frac{E_\alpha}{16}\frac{p^2}{(kT)^2}\langle\sigma v\rangle - \frac{c_B}{4}\frac{p^2}{(kT)^{3/2}} = 0 \quad \Longrightarrow \quad \frac{E_\alpha}{4}\frac{\langle\sigma v\rangle}{(kT)^{1/2}} - c_B = 0 \quad \Longrightarrow$$
$$\Longrightarrow \quad \sqrt{kT}\,\langle\sigma v\rangle(T) = \frac{4c_B}{E_\alpha} = const. \quad \Longrightarrow \quad kT = 4.4\,\mathrm{keV}$$

For $kT > 4.4\,\mathrm{keV}$ plasma is warmed up by the α particle heating, while for $kT < 4.4\,\mathrm{keV}$ plasma cools down because of the predominant Bremsstrahlung effect. Thus the ideal ignition imposes a lower limit for the plasma temperature.

Non ideal ignition regime

The power density balance (1.6) in this regime is

$$\frac{E_\alpha}{16}\frac{p^2}{(kT)^2}\langle\sigma v\rangle - \frac{c_B}{4}\frac{p^2}{(kT)^{3/2}} - \frac{3}{2}\frac{p}{\tau_E} = 0 \quad \Longrightarrow \quad p\tau_E = \frac{k_D T^2}{k_\alpha\langle\sigma v\rangle - k_B T^{1/2}}$$

where the coefficient were called k_D, k_α, and k_B for the sake of brevity. As displayed in figure 1.15(a), when $p\tau_E \geq k_D T^2/(k_\alpha\langle\sigma v\rangle - k_B T^{1/2})$, the ignition is reached, i.e. the plasma self–sustains without auxiliary heating system contributions.
The ignition curve minimum for a D–T plasma is reached at $T \approx 15\,\mathrm{keV}$, as

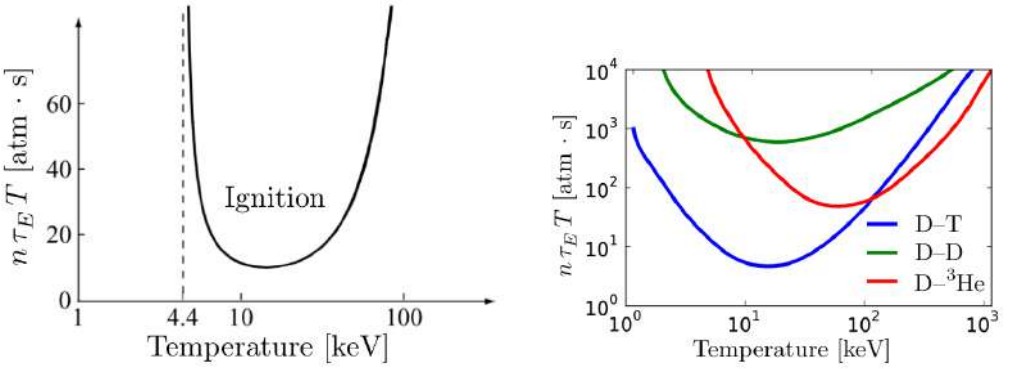

(a) (b)

Figure 1.15: Triple product as a function of the plasma temperature. (a) Figure from [2]. (b) Figure courtesy of D. Strozzi.

highlighted by the figure 1.15(b). Since working close to this minimum allows to reduce diffusive and Bremsstrahlung losses, ITER has been designed to operate at around $T \approx 15\,\text{keV}$, even if the maximum D–T reaction rate is reached at a higher temperature ($\sim 70\,\text{keV}$). The Lawson criterion on the triple product $n\tau_E T$

$$\boxed{n\tau_E T \geq 3 \times 10^{21}\,\text{m}^{-3}\text{s}\,\text{keV}}$$

is often used to express the ignition condition at the curve minimum.

Power amplification regime

The plasma current is essential in a tokamak to produce the poloidal magnetic field needed to confine plasma. Due to the Joule effect, it implies an Ohmic heating and hence a non null heating term $S_H \neq 0$. Therefore, tokamaks intrinsically cannot work in an ignition regime. Nevertheless, in a future fusion reactor the ignition is not required for the energy production, because it will be enough to amplify the input power.
In the power amplification regime, the ignition is not reached but the net energy balance is positive.

1.8 Fusion energy gain factor Q

In the power amplification regime, the net thermal output power $P_{\text{out}} - P_{\text{in}}$ is larger than the heating input power P_{in}, i.e. the fusion energy gain factor Q defined as

$$Q := \frac{P_{\text{out}} - P_{\text{in}}}{P_{\text{in}}}$$

is larger than 1. The total output thermal power is $P_{\text{out}} = (S_n + S_B + S_D)\, V$, where the neutron heating power density S_n can be written as a function of the α particle power density $S_n = (E_n/E_\alpha) S_\alpha \simeq 4 S_\alpha$. The heating input power is simply $P_{\text{in}} = S_H V$, where $S_H = S_D + S_B - S_\alpha$ from the energy balance. Hence the gain factor is

$$Q = \frac{[(4S_\alpha + S_B + S_D) - (S_D + S_B - S_\alpha)]\, V}{S_H} = \frac{5 S_\alpha}{S_H}$$

Since the numerator equals the fusion power density $S_{\text{fus}} := S_\alpha + S_n \simeq 5 S_\alpha$, the fusion energy gain factor ca be written as

$$Q = \frac{P_{\text{fus}}}{P_{\text{heat}}}$$

with $P_{\text{fus}} := S_{\text{fus}} V$ and $P_{\text{heat}} \equiv P_{\text{in}} = S_{\text{H}} V$.
When $Q = 1$, the power released by fusion reactions is equal to external heating power and the breakeven is reached. As stated above, in the power amplification regime $1 < Q < +\infty$, while ignition regime $Q = +\infty$. A gain factor $Q \simeq 30$–40 was evaluated to guarantee a competitive price to the fusion energy production.

The fraction of the α heating

$$f_\alpha := \frac{S_\alpha}{S_\alpha + S_H} \quad \Longrightarrow \quad f_\alpha = \frac{Q S_H/5}{Q S_H/5 + S_H} = \frac{Q}{Q+5}$$

quantifies the α particle contribution to the total heating. In the ignition regime $f_\alpha = 1$, while in the power amplification regime $0.17 < f_\alpha < 1$. When α particles contribute less than $\sim 17\,\%$ to the plasma heating, then $P_{\text{fus}} < P_{\text{heat}}$.

So far, the highest gain factor of $Q = 0.65$ ever achieved was reached in a JET plasma in 1997, with a corresponding α heating fraction of $11\,\%$. The breakeven is planned to be overtaken in ITER, with $f_\alpha = 0.67$ and $Q_{\text{ITER}} = 10$ ($P_{\text{fus}} = 500\,\text{MW}$ from $P_{\text{heat}} = 50\,\text{MW}$) at the full performance. For the first time, a burning plasma will be obtained in a tokamak allowing the researchers to experiment the power amplification regime.

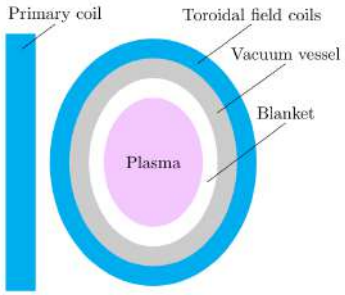

Figure 1.16: Sketch of a poloidal section of a conceptual tokamak reactor.

1.9 Power plant structure

Figure 1.16 shows a simplified poloidal section scheme of a conceptual tokamak reactor, highlighting the different layers that make it up.

As discussed above, the energetic neutrons coming from the fusion reactions are slowed down in the breeding blanket surrounding the plasma. Their kinetic energy is converted into thermal energy and then removed by a suitable fluid coolant. A blanket thickness in the range of 0.6–1.0 m allows to absorb most of the neutrons, shielding the magnetic coils and the other external components from them. Furthermore, in the blanket the reactions between embed lithium atoms and incoming neutrons produce tritium to fuel the reactor.[6]

The blanket is the internal lining of the vacuum vessel, a hermetically sealed steel toroidal vessel that creates a high–vacuum environment for the plasma. The vacuum vessel also protects the magnetic coils against thermal load and radiation damages.

In future fusion reactors, such as ITER and DTT, superconducting magnets will be used in place of the conventional magnetic coils employed so far in tokamaks. More intense magnetic fields and induced currents can be achieved consuming less power than with classical coils.

A cryostat surrounding both the vacuum vessel and the magnetic coils provides the ultra–cool environment required by magnets to acquire the superconducting properties. Particularly, the stainless steel cryostat of ITER, which will be the largest high–vacuum pressure chamber ever built, will use supercritical helium to chill magnets at a temperature of 4 K.

The coolant fluid that removes thermal energy from the blanket goes through a heat exchanger, where some water is heated up and evaporates. In a turbine the resulting steam is subject to an expansion, then is condensed

[6] Neutron multipliers, such as lead or beryllium, are used to increase the breeding ratio.

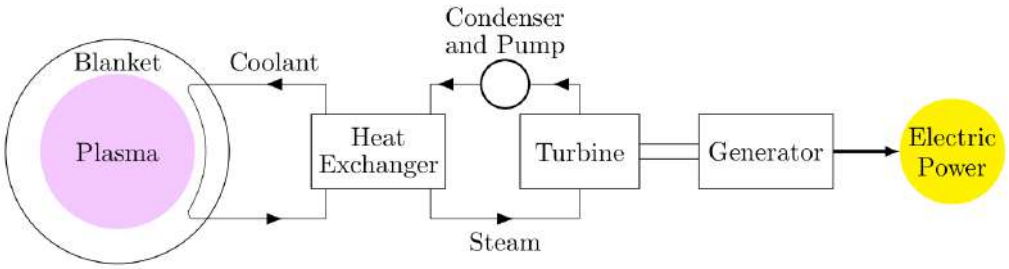

Figure 1.17: Design of a future thermonuclear fusion power plant.

again and pumped back the heat exchanger to restart the cycle. At the end, a generator transforms the rotation energy of the turbine into electric energy. In figure 1.17, the scheme of the electricity production process in a fusion reactor is sketched.

CHAPTER 2

The Divertor Tokamak Test facility

2.1 The DTT main task

The fusion community identified some crucial challenges to be faced on the path towards fusion electricity. The "European Research Roadmap to the Realisation of Fusion Energy"[7], finalised and approved by EUROfusion General Assembly in 2018, outlines the following eight missions.

1. **Plasma regime of operation** $\longrightarrow$ Plasma scenarios in tokamak configuration have to be developed, combining theory–based models and experiments, to increase the success margin of ITER and to fulfil requirements of DEMO and of future commercial power plants.

2. **Heat–exhaust system** $\longrightarrow$ Huge power amounts leaving reactor plasmas have to be properly exhausted via the divertor region and the main chamber wall. Nowadays, the heat exhaust management strategies designed for DEMO and future power plants still represent a tough experimental and theoretical challenge.

3. **Neutron tolerant materials** $\longrightarrow$ Materials able to withstand huge 14 MeV neutron fluxes for long periods preserving their physical properties suitably and exhibiting reduced activation are needed for future fusion reactors.

4. **Tritium self–sufficiency** $\longrightarrow$ To minimise the tritium storage, breeding, and extraction systems efficient enough to ensure the tritium self–sufficiency are mandatory in DEMO and in fusion power plants. Studies

on the test blanket module installed on ITER will drive the design of an effective technological solution for future breeding blankets.

5. **Implementation of the intrinsic safety features of fusion** $\longrightarrow$ Although the thermonuclear fusion has intrinsic safety features, their implementation has to guarantee an inherent passive resistance to incidents and a minimum tritium content in components extracted to be properly disposed of.

6. **Integrated DEMO design and system development** $\longrightarrow$ Fusion technologies, plasma parameter requirements, improved materials, and all involved systems have to be blended coherently into an all–embracing integrated DEMO design.

7. **Competitive cost of electricity** $\longrightarrow$ To let the thermonuclear fusion be attractive as future energy source, a competitive electricity cost must be reached. Thus, devising strategies to reduce capital and operational costs as much as possible and adopting also a long–term economical perspective is crucial in the reactor design.

8. **Stellarator** $\longrightarrow$ A further development of the stellarator configuration is planned in order to make this research line mature enough to envisage a stellarator power plant as alternative to tokamak reactors.

The Divertor Tokamak Test facility fits into the second mission framework, since it is a key facility dedicated to study power exhaust issues.
A large amount of particle and power exhaust from a fusion reactor has to be handled and the plasma facing components (PFC) have to cope with extremely high heat and particle fluxes.

The baseline approach for the attainment of this second mission plans to operate in a full metal PFC environment with a conventional single null divertor (with only one X–point) and to reduce the thermal loads on the divertor targets thanks to a sufficient edge radiative dissipation. A seeding gas can be used to enlarge the radiative power enough to reach detached plasma conditions. This strategy, currently used in some existing tokamaks, will be also adopted by ITER to investigate its extrapolability to DEMO and future fusion power plants, where power fluxes in the range of 10–20 $\mathrm{MW/m^2}$ are foreseen. Since this baseline approach may be unsuitable for these extreme operating conditions, exploring and developing in parallel up to a sufficient level of maturity alternative exhaust strategies is crucial to mitigate this risk. Various magnetic configurations (double null, single null with negative triangularity, snowflake, quasi–snowflake, X–divertor, and super–X configurations) as well as the employment of liquid metal targets are being tested.

DTT is optimised to analyse heat exhaust systems at parameters as relevant as possible for DEMO working conditions, to extend the performance of plasma facing materials and to prove the technical feasibility of alternative solutions. In addition to different advanced magnetic configurations, liquid metal technologies based on either capillary porous systems or boxes/pools systems will be also developed in this fusion device.

The DTT design is advanced but will be kept flexible with regard to the choice of the divertor until 2023, when the outcome of the work conducted under the EUROfusion PEX (Plasma EXhaust assessment panel) group will be available to drive the best choice for the divertor. To guarantee that the DEMO engineering design can proceed with a mature enough alternative exhaust strategy on time, according to the European roadmap planning, the realisation of the first plasma in DTT is scheduled by the end of 2028.

2.2 The DTT project

The DTT project was proposed in 2015 by several Italian institution researchers in collaboration with scientists from various international labs (including KIT in Germany, CEA IRFM in France, CRPP–EPFL in Switzerland, FOM–DIFFER in the Netherlands, IPPLM in Poland).[11]
In 2019, a revised project version [8] was published and the DTT Consortium was established as legal entity. Hitherto the DTT Consortium Partners are:

- Agenzia nazionale per le nuove tecnologie, l'energia e lo sviluppo economico sostenibile (ENEA) [2019]
- Consorzio di Ricerca per l'Energia, l'Automazione e le Tecnologie dell'Elettromagnetismo (CREATE) [2019]
- Ente Nazionale Idrocarburi (ENI) [2020]
- Consiglio Nazionale delle Ricerche (CNR) [2021]
- Consorzio RFX [2021]
- Istituto Nazionale di Fisica Nucleare (INFN) [2021]
- Politecnico di Torino [2021]
- Università degli Studi della Tuscia [2021]
- Università degli Studi di Milano–Bicocca [2021]
- Università degli Studi di Roma Tor Vergata [2021]

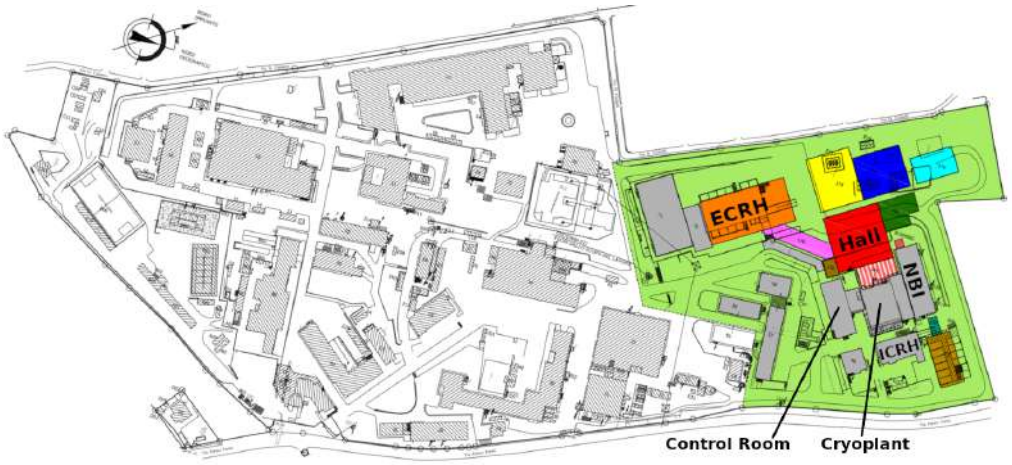

Figure 2.1: Map of the whole ENEA Frascati Research Center, where the DTT area is highlighted in green and new facilities are coloured (from [12]).

Currently, the DTT Consortium is led by Prof. Francesco Romanelli.
In addition to these scientific and managerial partnerships, other subjects and institutions are also involved officially as DTT stakeholders:

- EUROfusion with scientific collaborations and a financial contribution up to 60 million € for the divertor system;
- Ministero dello Sviluppo Economico (MISE) with a financial contribution of 40 million €;
- Ministero dell'Istruzione, Università e Ricerca (MIUR) with a financial contribution of 40 million €;
- Regione Lazio with a financial contribution of 25 million €;
- The European Investment Bank with a long–term loan of 250 million € (conceded within the EU Juncker Plan) granted to ENEA;
- China with scientific collaborations up to a value of 30 million €.

The construction of the facility at the ENEA Research Center in Frascati (Italy) already started. The project includes both the recovery and redevelopment of existing buildings and the construction of new ones, as shown in figure 2.1. Moreover, the big procurement for the superconducting strand has been assigned and in the last months the DTT working team has grown and reinforced.

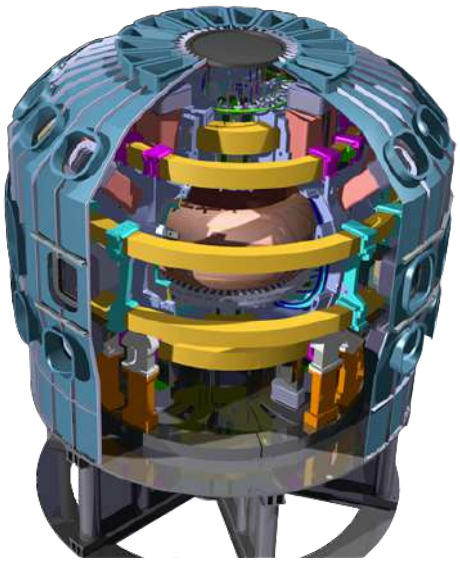

Figure 2.2: The DTT device (from [10]).

2.3 The DTT main parameters

The DTT device is a superconducting tokamak with D–shaped poloidal cross section, as depicted in figure 4.1, to study deuterium plasma discharges in high performance regimes.

The machine design is currently ongoing and some important parameters changed in the last years. Some results of this PhD project also led to major review of the machine, such as the decision to enlarge the device as described in the following chapters. The values reported here are referred to the present design.

The characteristics of DTT were chosen to make it ITER and DEMO relevant, so that exhaust solutions could be extrapolated to a reactor–grade plasma. Bearing in mind the requirement of a strong compatibility with the operating conditions in DEMO, DTT is designed to be a bulk–edge integrated experiment with a reactor relevant bulk. Therefore, the DTT dimensionless physical parameters should be as close as possible to the ITER and DEMO ones. It is not possible to simultaneously preserve all these quantities, and hence DTT has been scaled down following the so called "weak scaling" described in [13].

The main DTT parameters are compared in table 4.1 with those of ITER and DEMO. We can observe that these tokamaks, notwithstanding the substantially different sizes, were designed to have the same aspect ratio A.

Since the P_{sep}/R parameter, where P_{sep} is the power exiting through the

Table 2.1: Main parameter comparison amongst the DTT, ITER, and EU DEMO future devices.[12, 14, 15, 16, 17]

	DTT	ITER	EU DEMO
R [m]	2.19	6.2	9.1
a [m]	0.70	2.0	2.93
A	3.13	3.1	3.11
I_{pl} [MA]	5.5	15	19.6
B_{tor} [T]	5.85	5.3	5.7
P_{tot} [MW]	45	150	460
P_{sep}/R [MW/m]	15	14	17
λ_q [mm]	0.7	0.9	1.0
Pulse length [s]	100	400	7600

separatrix, is recognised as a key metric for the extent of the exhaust issue in a tokamak, geometry and auxiliary power coupled to the plasma have been chosen to guarantee a value of $P_{\mathrm{sep}}/R = 15\,\mathrm{MW/m}$ similar to those foreseen for ITER and DEMO.

2.4 Operational programme of DTT

An ambitious programme spread over a period of several years ($\geq$ 25 years) has been planned for the DTT operations. A schematic planning of the experimental programme split in operational phases is shown in figure 2.3.

In the initial phases a SN magnetic configuration is used. The goal of the first phase is to realise and install the machine components and to test the first plasmas. From the first phase to the third phase, the total additional power provided by the auxiliary heating systems will be progressively increased up to the maximum of the full performance scenarios. During these phases, plasma current and toroidal magnetic field values will also be increased. The phase 3 is dedicated to test alternative solutions (both advanced magnetic configurations and liquid metal divertors).

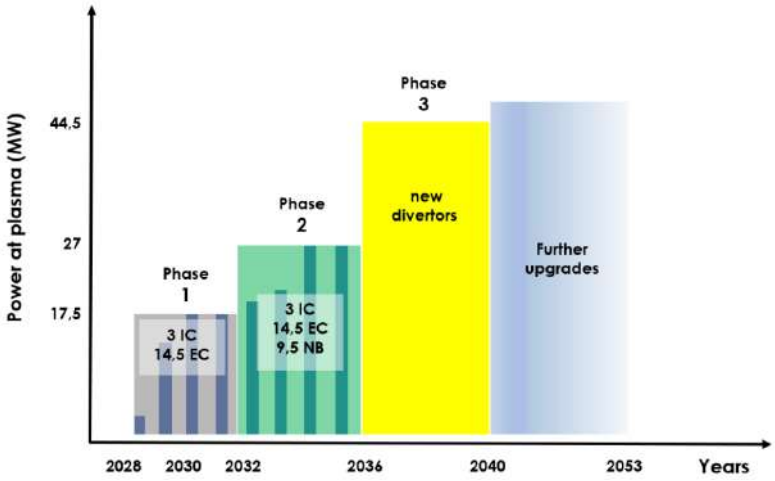

Figure 2.3: Schematic planning of the DTT operational phases (from [12])

2.5 Plasma heating in DTT

Plasma temperatures of $\sim 10^8$K are required in fusion devices to guarantee that D–T reactions occur frequently enough. Thus, a large amount of plasma heating is required and the inherent Ohmic heating due to the plasma current is insufficient. Hence, some additional heating systems are typically employed. They can be based on the injection into the plasma of fast neutral particles or of radio frequency waves at a plasma resonance frequency (electron or ion Larmor frequencies or lower hybrid frequency).
In DTT three auxiliary heating systems will be progressively realised and installed on the machine:

- the Electron Cyclotron Resonance Heating (ECRH) system;
- the Ion Cyclotron Resonance Heating (ICRH) system;
- the Neutral Beam Injection (NBI) system;

This PhD project contributed significantly to define the definitive heating mix for the DTT full performance scenario, which was rediscussed with respect to the original options proposed in [8]. As described in [18] and in chapter 4, the power distribution amongst the three systems and the choice of NBI energy were optimised. In this chapter, the main features of the final version of the heating systems are briefly described.

2.5.1 Ohmic heating

Since the plasma has a non null resistivity η mainly due to the collisions between electrons and ions, the toroidal current I_{pl} heats the plasma by Joule effect. The resulting Ohmic power density is $Q_{\text{Ohm}} = \eta J^2$, where J is the plasma current density. The plasma resistivity in a tokamak is

$$\eta = \underbrace{\frac{e^2 \ln\Lambda}{3\pi^{3/2}\varepsilon_0^2 m_e}\left(\frac{m_e}{2kT_e}\right)^{3/2}}_{\eta_S} \cdot \frac{Z_{\text{eff}}}{\left(1-\sqrt{a/R_0}\right)^2} \qquad \Longrightarrow \qquad \eta \propto T_e^{-3/2}$$

where η_S is the Spitzer resistivity of a pure hydrogen plasma, e is the proton charge, m_e is the electron mass, ε_0 is the vacuum dielectric constant, k is the Boltzmann constant, $\ln\Lambda \coloneqq \ln\left(\lambda_D/b_{\pi/2}\right)$ is the Coulomb logarithm with λ_D Debye length and $b_{\pi/2}$ collisional impact parameter for a $\pi/2$ scattering[1], a is the minor radius, R_0 is the major radius, Z_{eff} is the effective charge defined as the averaged charge of all ions

$$Z_{\text{eff}} \coloneqq \frac{\sum_j n_j Z_j^2}{\sum_j n_j Z_j} \simeq \sum_j n_j Z_j^2 / n_e$$

used to characterise the plasma impurity content.

Since the dependence of the Ohmic power on the electron temperature is $P_{\text{Ohm}} \propto T_e^{-3/2}$, the Ohmic heating significantly contributes at the beginning of the plasma discharge when T_e is still relatively low, but then it becomes quite inefficient at fusion relevant temperatures. The operational range of the central solenoid in inducing plasma current, which limits the plasma discharge duration, also limits the Ohmic heating contribution.

As shown in next chapters, in DTT scenarios an Ohmic power of the order of 1 MW has been assessed and therefore it weakly impacts the total heating and the plasma kinetic profiles.

2.5.2 Ion Cyclotron Resonance Heating

Through a ICRH system, suitable electromagnetic waves at a plasma ion species cyclotron frequency are injected into the plasma to heat it via resonance effects. The cyclotron frequency of a species σ is simply its Larmor frequency $\omega_{\text{L}\sigma} \equiv \omega_{\text{c}\sigma} = q_\sigma B/m_\sigma$ defined in (1.5). Since it depends on the magnetic field magnitude B approximatively inversely proportional to R, the

[1] The collisional impact parameter for a $\pi/2$ scattering is $b_{\pi/2} = e^2/\left(4\pi\varepsilon_0 m_e v_e^2\right)$.

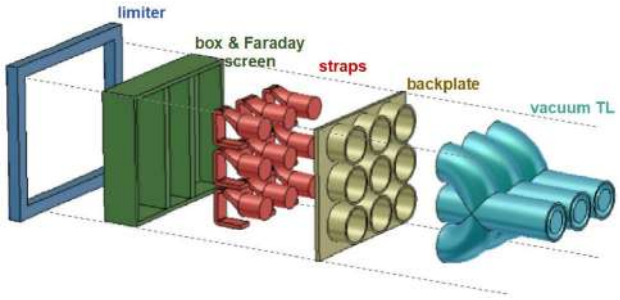

Figure 2.4: ICH coupler and part of the vacuum transmission line (from [12]).

power deposition of a general cyclotron resonance heating system is localised around a certain radius depending on the frequency. The ion cyclotron frequency of ions with atomic number Z_i and mass m_i is $\omega_{ci} = Z_i eB/m_i$. Actually, varying the IC antenna frequency, it is possible to couple to a main ion species or to a minority ion species or even to the electrons if the plasma contains multiple ion species.
The ICRH is used in the so–called minority scheme when its frequency is tuned to be resonant with the Larmor motion of a minority ion species, inserted into the plasma in small concentration with respect to the main ions. Thus the minor species particles absorb most of the ICRH power, becoming ICRH fast ions. Then, electron and main ions are heated up by these energetic particles via collisions.

The ICRH system of DTT is designed to operate in the radio frequency (RF) range of 60–90 MHz, with a duty cycle comprised of pulses of 50 s every 3600 s at maximum performance. At full field operational point, the fundamental harmonic cyclotron resonances of ^{3}He and H minorities are located on–axis when the ICRH frequency is respectively 60 MHz and 90 MHz. The first harmonic cyclotron resonance of the main D can also be exploited to have a central power deposition using the ICRH system at 60 MHz.
The DTT ICRH system is devised in modular units placed in equatorial ports and each module is based on a pair of three–strap antennas, which couple the RF power to the plasma. To better cope with abrupt coupling changes because of L–H transitions or ELMs, the two antennas of a single module are fed in parallel.[2] Two integrated transmitters and one transmission line (TL) are associated to each antenna. An integrated transmitter is a RF power generator including all units required to convert the electrical AC into RF power. Figure 2.4 displays the ICRH coupling structure and part of the vac-

[2]The L–H transitions are plasma transitions from a Low confinement mode (L–mode) to High confinement mode (H–mode). ELMs is the acronym for Edge Localised Modes.

uum transmission line of DTT.
Two ICRH modules, i.e. 4 RF antennas, are included in the DTT full power scenario. The installation of first and second modules are respectively scheduled for the initial phase and for the third phase of the DTT operational programme. The installed power for each antenna is 2 MW. Typical efficiencies for transmission lines and antenna coupling are 80 % and 90 %. Hence, to assess conservatively the ICRH power provided to the plasma, an efficiency of 0.75 can be supposed, leading to a ICRH coupled power of about 1.5 MW per antenna.

2.5.3 Electron Cyclotron Resonance Heating

The ECRH heating systems launch electromagnetic waves into the plasma but at the cyclotron frequency of plasma electrons $\omega_{ce} = eB/m_e$. Compared to the ICRH technique, the ECRH systems require much higher frequencies (of the order of 100 GHz) and hence their wave generation and transmission systems are more challenging.
DTT will be equipped with one of the largest ever made ECRH plants, which has been designed starting from the ECRH technologies developed for ITER, Wendelstein–7X, and JT–60SA[19] fusion devices, aiming at high reliability and robustness.

The DTT ECRH system is designed to operate at a frequency of 170 GHz, with a duty cycle comprised of pulses of 100 s every 3600 s at maximum performance. It will include up to 32 gyrotrons, equally split in 4 clusters, with an installed power of 1 MW from each gyrotron.[3] To each cluster a specific transmission line is associated. The installation of the first ECRH cluster is scheduled for the initial phase, while the other clusters will be installed in the following phases according to the DTT operational programme. Every cluster is composed by 8 gyrotrons: two upper (UP) beams, three equatorial bottom (EQB) beams, and three equatorial top (EQT) beams, depending on the access port.
The ECRH system includes the high voltage and auxiliary power supplies, the RF power sources, the transmission lines, the launcher systems, and the vacuum systems for lines and launchers.

The high voltage power supply (HVPS), whose design was derived from the ITER system, polarises the gyrotron electrodes with the needed high DC voltages. The HVPS system of DTT will count up to 16 HVPS sets to feed 32 gyrotrons (16 gyrotron pairs). Each HVPS set includes one main power

[3]To increase the total supplied power, this option might still undergo a change: the last cluster might be composed by gyrotrons with 1.2 MW of installed power.

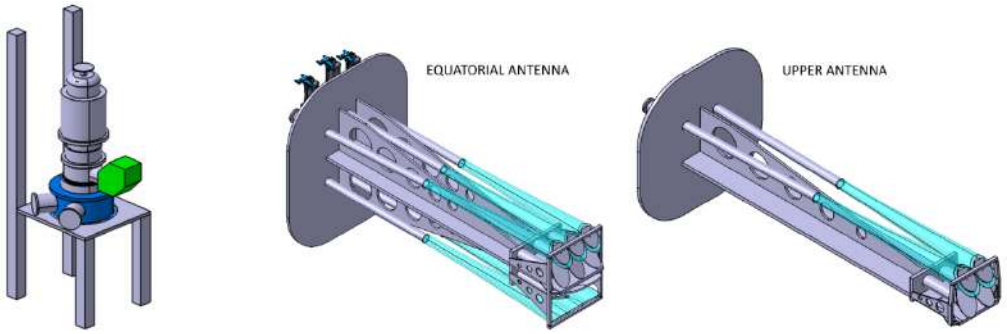

(a) Gyrotron. (b) Equatorial and upper port ECRH antennas.

Figure 2.5: (a) A sketch of a gyrotron with the matching optical unit in green and the He–free magnet in blue (from [12]). (b) Sketches of equatorial and upper port ECRH antennas (from [12]).

supply unit, which polarises the cathodes of two gyrotrons negatively with respect to the collector assumed at the ground potential, and two body power supply units, which polarise the body of gyrotrons positively.

DTT will be equipped with diode (or triode) gyrotrons with collector potential depression working at $(170 \pm 0.3)\,\mathrm{GHz}$ with an efficiency $\geq 40\,\%$ (achieving a nominal output power $\geq 0.98\,\mathrm{MW}$) and provided with a He–free cryo–magnet. In order to avoid magnetic disturbances, DTT gyrotrons have to maintain a mutual distance of at least 5 m and to stay at about 50 m from the tokamak centre. The gyrotron source includes matching optic unit, which transforms the the gyrotron output into a fundamental transverse electromagnetic Gaussian beam ($\geq 98\,\%$ TEM_{00} mode purity). The gyrotron Gaussian output beams are then transmitted by an evacuated quasi–optical multi–beam transmission line to the ECRH antennas. In figure 2.5(a) a DTT gyrotron sketch is displayed. A single transmission line is designed to be able to handle up to 1.5 MW of power, in view of possible gyrotron power upgrades in the future.

The 8 launchers of an ECRH cluster are arranged in 2 different antennas placed in the same tokamak sector: an antenna with 2 launchers hosted in the upper port and an antenna with 6 launchers hosted in the equatorial port. To improve as much as possible the system flexibility, every launcher is independently steerable, since it includes a fixed mirror for beam shaping and a movable (both poloidally and toroidally) plane mirror faced to the plasma for directing the beam by a steering mechanism. In the equatorial antenna two linear modules of three launchers are placed symmetrically with respect to the equatorial plane, while the upper antenna is provided with a single module of two launchers. Figure 2.5(b) shows the design of the two types of

the DTT EC antennas. Constraints on the launching mirror dimensions are imposed by the port opening amplitude and by the steering ranges.

2.5.4 Neutral Beam Injection

Another method to heat the plasma consists in injecting a beam of energetic neutral particles into the fusion device. In this technique, very fast neutral atoms are fired by a Neutral Beam Injection (NBI) system, collide with plasma particles, and are ionised mostly through processes of charge exchange or of impact ionisation with an ion or an electron, depicted as follows

$$\begin{aligned}
&\text{Charge exchange:} && X_{\text{en}} + H^+_{\text{th}} \longrightarrow X^+_{\text{en}} + H_{\text{th}} \\
&\text{Ion impact ionisation:} && X_{\text{en}} + H^+_{\text{th}} \longrightarrow X^+_{\text{en}} + H^+_{\text{th}} + e^-_{\text{en}} \\
&\text{Electron impact ionisation:} && X_{\text{en}} + e^-_{\text{th}} \longrightarrow X^+_{\text{en}} + e^-_{\text{th}} + e^-_{\text{en}}
\end{aligned}$$

where subscripts $_{\text{en}}$ and $_{\text{th}}$ identify the energetic particles of the beam species and the thermal particles of plasma species respectively. The cross sections of these reactions depend on the beam energy, as shown in figure 2.6, and the electron impact ionisation cross section also depends on the electron temperature. Charge exchange dominates at relatively low NBI energies ($\lesssim 100\,\text{keV}$ for a hydrogen beam, $\lesssim 200\,\text{keV}$ for a deuterium beam), while at larger beam energies the ion impact ionisation prevails over the other processes, and at even higher beam energy ($\gg 1\,\text{MeV}$) the electron impact ionisation doninates.

Regardless of which process is dominant, the generated fast ions X^+_{en} and electrons e^-_{en} are charged particles and thus are confined by the tokamak magnetic field. They are subjected to a series of Coulomb collisions transferring part of their energy to the plasma until being thermalised. In this way, the NBI power is provided to the plasma. The supplied power P_{NBI} is split between electrons and ions according to the following expression

$$P_{\text{NBI}} = \underbrace{m_b A_D \frac{2E_b\sqrt{m_e}}{3\sqrt{2\pi}T_e^{3/2}}}_{P_{\text{NBI}_e}} + \underbrace{m_b A_D \frac{m_b^{3/2}}{2\sqrt{2E_b}m_i}}_{P_{\text{NBI}_e}}$$

where m_b is the beam particle mass, $A_D \coloneqq (ne^4 \ln\Lambda)/(2\pi\varepsilon_0^2 m_b^2)$, and E_b is the beam energy.
Moreover, an important feature of NBI systems is their current drive capability and central fuelling.

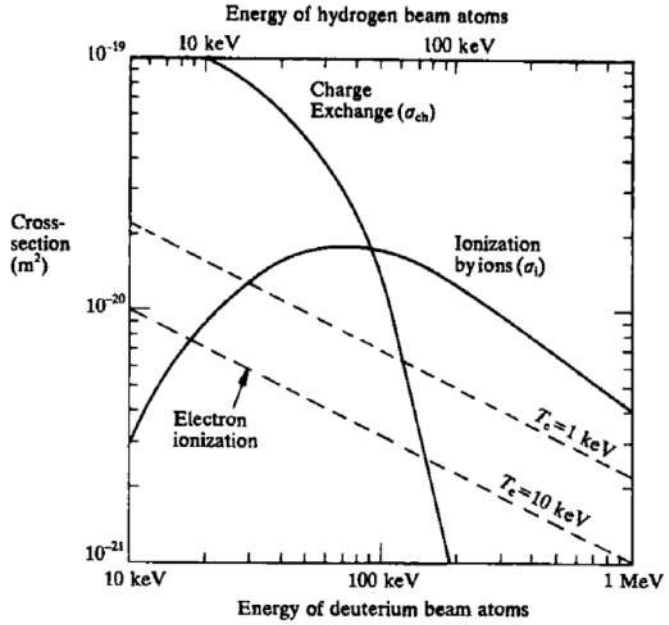

Figure 2.6: Cross sections for charge exchange and ion impact ionisation, and effective cross section $\langle \sigma_e v_e \rangle / v_b$ for electron impact ionisation processes, as functions of the neutral beam energy (from [1]).

The beam intensity I_b decreases progressively with its penetration x into the plasma as follows

$$\frac{\mathrm{d}I_b}{\mathrm{d}x} = -n \left(\sigma_{cx} + \sigma_i + \frac{\langle \sigma_e v_e \rangle}{v_b} \right) I_b$$

where $n = n(x)$ is the plasma density, σ_{cx} is the charge exchange cross section, σ_i is the ion impact ionisation, σ_e is the electron impact ionisation, v_e is the thermal electron velocity, and v_b is the beam particle velocity.

The neutral beam is produced by a line with an ion source, an accelerator, and finally a neutraliser (eventually coupled with a deflector magnet). The classical NBI system is based on a positive ion source, but this conventional method does not allow to achieve beams with enough energy to penetrate up to the plasma centre in high density fusion devices.[4] Since using negative ion sources allows to have more energetic neutral beams, negative ion based NBI (NNBI) systems will be installed on future reactors as well as in DTT.[5]

[4]The typical decay length of a classical deuterium NBI at 100 keV in a plasma with density $n \approx 10^{20}\,\mathrm{m}^{-3}$ is about 30 cm.

[5]The ITER NBI will have a beam energy of ~ 1 MeV.

Particularly, to reach a central power deposition during the flat–top plasma discharge phase, a NNBI system at high energies $E > 300\,\mathrm{keV}$ must be used in DTT, due to the high densities. During early current ramp–up, late current ramp–down, and low current scenarios the employment of the NBI system must be cautiously evaluated, in order to avoid shine–through risks.

The definitive design of the DTT NBI system, sketched in figure 2.7, features only one injector of deuterium neutrals with 510 keV of energy and 10 MW of injected power. It mainly includes an ion source, an accelerator, a gas neutraliser, an electrostatic residual ion dump, a calorimeter, and a large pumping system. The beam source is air–insulated, so that it is more accessible and a single large bushing is not required to connect the transmission line to the vacuum vessel (VV).

The DTT ion source which generates a current of D^- ions is a radio frequency source kept at high voltage of $-510\,\mathrm{kV}$, whose design is derived from the NBI systems developed for SPIDER, MITICA, and ITER.[20, 21]

In the accelerator, the D^- ions are then extracted by an extraction grid at $-500\,\mathrm{kV}$ and accelerated by a sequence of three grids, each made of 4 copper segments, respectively at $-333\,\mathrm{kV}$, $-166\,\mathrm{kV}$, and ground potential. The accelerated D^- ion beam is transformed into a neutral beam with an efficiency $\lesssim 60\,\%$ by the neutraliser. The residual ions which remain after the neutraliser are dumped by the residual ion dump. Finally, the calorimeter allows to measure the beam power. The beam line components (the neutraliser, the residual ion dump, and the calorimeter) adopted in DTT are ITER–like too. The beam line components are contained in a vacuum vessel, which also supports the accelerator and the ion source. Differently from ITER, the DTT NBI vacuum vessel will be equipped with only small flanges for pumping, diagnostics, cooling water, D_2 gas, and electric bias, in order to reduce weight and cost. The maintenance of the beam line components will be done through the large circular flange that becomes accessible removing the beam source. To maintain a pressure inside the NBI vacuum vessel lower than $2 \times 10^{-4}\,\mathrm{mbar}$, a vacuum pumping system based on turbomolecular pumps placed on the vessel side walls and Non–Evaporable Getter (NEG) pumps located on the upper and lower vessel faces is foreseen.

In DTT the NBI will also be used in support of beam–based diagnostics: the motional Stark effect diagnostic for magnetic field measurements and the charge exchange diagnostic for spatially resolved ion measurements.

More details of the DTT NBI beamline conceptual design are reported in section 6.5.

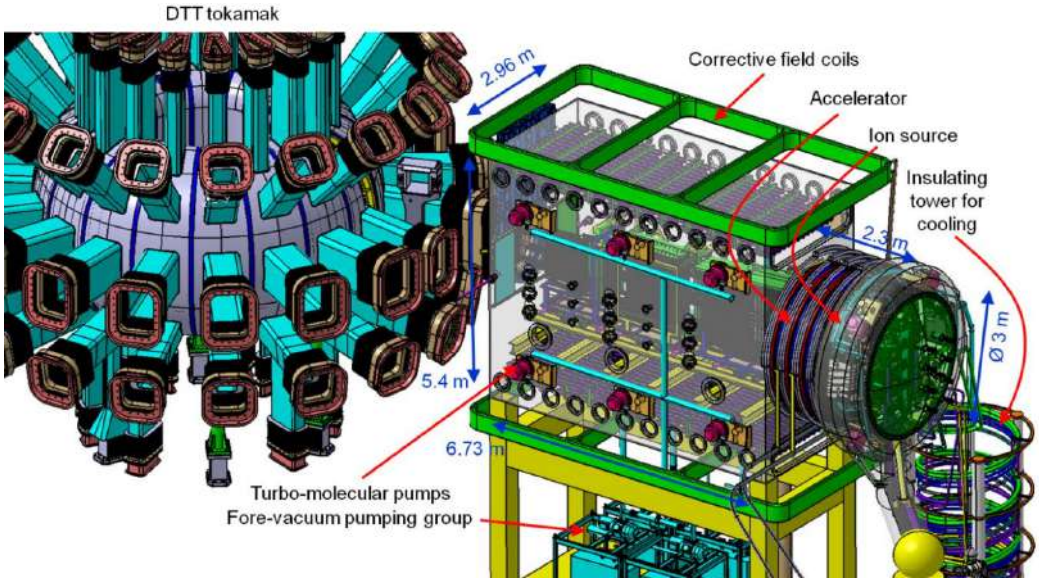

(a) View from the side.

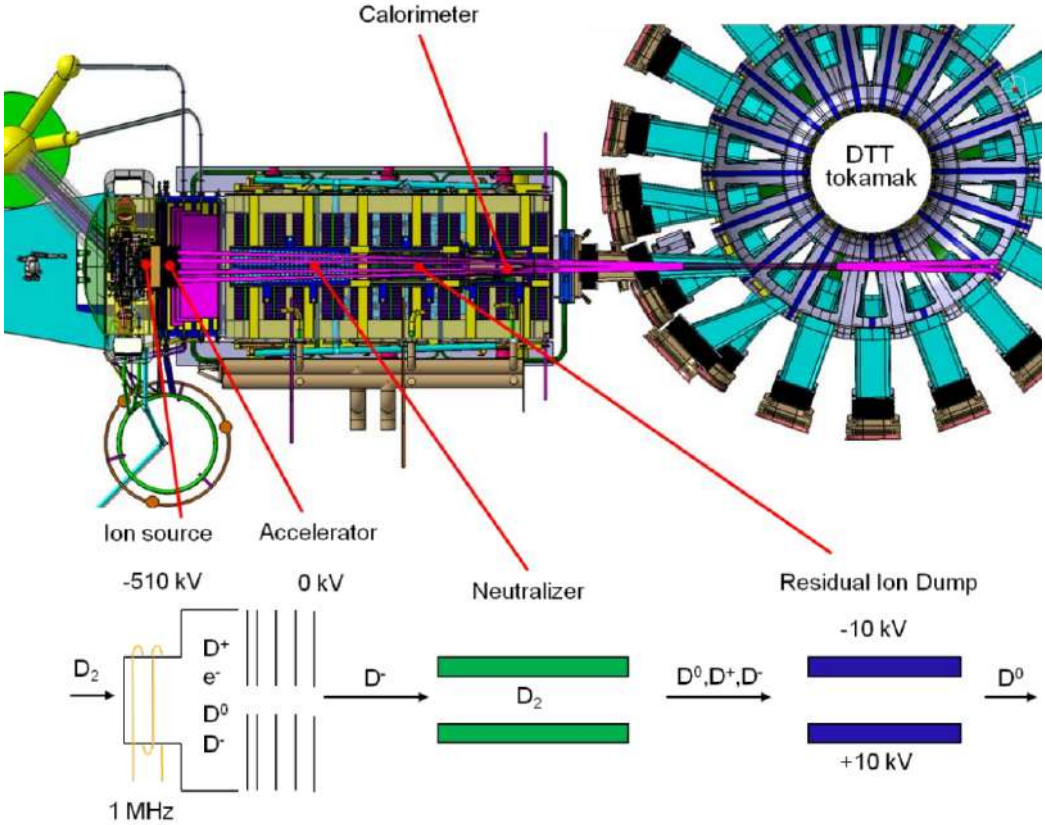

(b) View from above.

Figure 2.7: Sketch of the last DTT NBI design (from [12]).

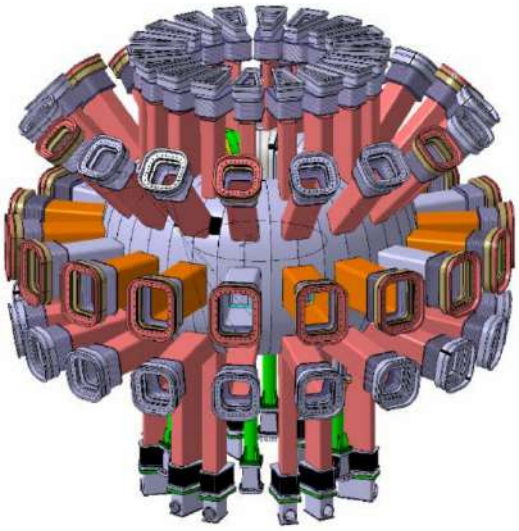

Figure 2.8: Overall view of the DTT vacuum vessel with ports, bellows, and gravity supports (from [12]).

2.6 The DTT structure

The DTT vacuum vessel, whose torus outboard diameter is of 6.9 m, is based on a double wall structure consisting in two separated AISI 316L(N) shells. The assembly of vacuum vessel, ports, bellows, and gravity supports has an height of 9.5 m, a diameter of 11.5 m, and a weight of 174 tons. To enhance its neutron shielding capability with a good safety margin, the double wall cavity is filled with water during low performance plasma operations or borated water (saturated solution of 95 % ^{10}B) during high performance plasma operations.
The vacuum vessel shells are segmented in 15 sectors with a toroidal extension of 20° and 2 sectors with a toroidal extension of 30°. A typical 20° sector present five access ports (enumerated from #1 at the top to #5 at the bottom). Nevertheless, the ports #5 of six 20° sectors are substituted by gravity supports and the ports #5 of other two 20° sectors are substituted by the sixth poloidal field coil inner joints and terminations. Moreover, one of the 20° sector is devoid of whole ports (it presents only 10 half ports). The typical 20° sector presents five access ports and five half ports. Once assembled, the access ports result arranged on 18 slices, as shown in the sketch of the DTT vacuum vessel with ports, bellows, and gravity supports of figure 2.8.
Ports #1 are primarily allocated for fuelling, remote handling operations for the first wall maintenance, and vacuum vessel and first wall cooling pipes. Some diagnostics and the ECRH upper launchers are hosted in ports #2.

Ports #3 are mainly assigned to diagnostics, ECRH equatorial launchers, and ICRH antennas; a single equatorial port is dedicated to the NBI. Ports #4 are designed to allow the divertor commissioning and decommissioning and its remote handling maintenance. In ports #5 diagnostics, pumping, and fuelling systems are housed.

The magnetic system, entirely enclosed in a thermal shield, is fully symmetric with respect to the equatorial plane. It is composed of 18 toroidal field Nb_3Sn coils operating at 42.5 kA with 12 T maximum magnetic field, 6 stacked modules of Nb_3Sn coils making up the 5.2 m high central solenoid, 2 poloidal field Nb_3Sn coils, and 4 poloidal field coils based on NbTi conductor technologies working at lower magnetic field values. The poloidal field coils are employed for plasma shaping and stabilisation. All these coils exploit the technology of Cable–In–Conduit Conductors (CICCs), belonging to the internally cooled conductor family. A forced flow of supercritical helium gas with an inlet temperature of 4.5 K cool down the coils making them superconducting. The central solenoid and the set of toroidal field magnets weight ~ 400 tons and ~ 45 tons respectively.

The first wall consists of sprayed tungsten plasma facing units hosted on specific supports connected to the vacuum vessel. The baseline divertor design foresees an actively cooled conventional bulk tungsten divertor segmented in 54 toroidal cassettes (3 divertor cassettes for each tokamak sector). Each cassette is constituted of a dome, an inner vertical target, and an outer vertical target. This baseline divertor is compatible with different magnetic configurations, including obviously the SN scenario, and is designed to be entirely maintainable via remote handling.

Annual operation scenario

An experimental period of 100 operating days per year is foreseen for DTT. Less than one month and about a month are required for exhausting tritium gas and warming up of the superconducting coils respectively, prior to shut down for maintenance. An annual maintenance period of about 6 months is planned. During this period, beyond the routine inspections of DTT facilities established by the safety regulations, extraordinary maintenance works and installation of new facilities or new diagnostic systems will be carried out. Thanks to the remote handling system, in–vessel components can be inspected or repaired during the warming up and cooling down periods (included in the maintenance interval).

2.7 The neutron budget

During the typical deuterium operations of DTT, a non negligible amount of 2.5 MeV neutrons are produced by $D + D \longrightarrow n + {}^3He + 3.27\,MeV$ fusion reactions. In addition, since tritium is also generated by the fusion channel $D + D \longrightarrow H + T$, a smaller fraction of 14 MeV neutrons is produced as result of $D + T \longrightarrow n + {}^4He + 17.6\,MeV$ reactions (collectively called triton burn–up).

In high performance scenarios, a neutron yield $\leq 1.5 \times 10^{17}$ neutrons/s with about 1 % of 14 MeV neutrons coming from the triton burn–up was assessed. This level of neutron rate can be handled with a good safety margin. Estimations of neutron yields in different scenarios were also carried out by this PhD work, enabling to be confident about the compliance with the required limits.

The neutron maximum performance is expected to be reached 8 years after the operation start–up, with annual DD and DT neutron yields respectively of 1.53×10^{21} neutrons/y and of 1.53×10^{19} neutrons/y.
Assuming an experimental program with DTT operating for 6 months per year and taking into account number of pulses and the emissivity of the planned plasma scenarios, a total DD neutron budget of 3.73×10^{22} after 28 years of operation was evaluated (corresponding to 2.49×10^5 s of operation at DTT full power). For safety purposes, this conservative scenario has been employed for shielding analyses and activation studies.

CHAPTER 3

Transport and modelling

3.1 Transport equations

A complete set of equations describing the particle, momentum, and energy transport of the plasma species σ with mass m_σ, charge q_σ, density n_σ, temperature T_σ, and velocity $\boldsymbol{u}_\sigma$ is the following

$$\begin{cases} \dfrac{\partial n_\sigma}{\partial t} + \boldsymbol{\nabla} \cdot \boldsymbol{\Gamma}_\sigma = S_{\sigma_0} \\ m_\sigma n_\sigma \dfrac{\mathrm{d}\boldsymbol{u}_\sigma}{\mathrm{d}t} = q_\sigma n_\sigma (\boldsymbol{E} + \boldsymbol{u}_\sigma \times \boldsymbol{B}) - \boldsymbol{\nabla} \cdot \underline{\underline{\boldsymbol{P}_\sigma}} + \boldsymbol{R}_{\sigma j} + \boldsymbol{S}_{\sigma_1} \\ \dfrac{3}{2} \dfrac{\partial (n_\sigma T_\sigma)}{\partial t} + \boldsymbol{\nabla} \cdot \left(\boldsymbol{q}_\sigma + \dfrac{5}{2} T_\sigma \boldsymbol{\Gamma}_\sigma \right) = S_{\sigma_2} \end{cases}$$

where $\boldsymbol{\Gamma}_\sigma \coloneqq n_\sigma \boldsymbol{u}_\sigma$ is the particle flux, $\boldsymbol{q}_\sigma$ is the heat flux, $\boldsymbol{R}_{\sigma j}$ represents the variation of the momentum density of the species σ due to the collisions with all other j–th species, S_{σ_0} is the external particle source, $\boldsymbol{S}_{\sigma_1}$ is the external torque source, and S_{σ_2} is the external heat source. The tensor $\underline{\underline{\boldsymbol{P}_\sigma}}$ has the actual pressures as diagonal elements and the viscosity quantities as out–diagonal elements; in an isotropic non–viscous plasma $\boldsymbol{\nabla} \cdot \underline{\underline{\boldsymbol{P}_\sigma}} \approx \boldsymbol{\nabla} p_\sigma$. Since in a single isotope plasma the main ion density n_i can be calculated by the quasi–neutrality relation from the electron and impurity densities, the simplest equation system that governs the plasma particle and heat transport

is

$$\begin{cases} \dfrac{\partial n_e}{\partial t} + \boldsymbol{\nabla} \cdot \boldsymbol{\Gamma}_e = S_{e_0} \\ \dfrac{3}{2}\dfrac{\partial \left(n_e T_e\right)}{\partial t} + \boldsymbol{\nabla} \cdot \left(\boldsymbol{q}_e + \dfrac{5}{2} T_e \boldsymbol{\Gamma}_e\right) = S_{e_2} \\ \dfrac{3}{2}\dfrac{\partial \left(n_i T_i\right)}{\partial t} + \boldsymbol{\nabla} \cdot \left(\boldsymbol{q}_i + \dfrac{5}{2} T_i \boldsymbol{\Gamma}_i\right) = S_{i_2} \end{cases}$$

In first approximation, densities and temperatures depend only on the radial coordinate, since the transport component perpendicular to the toroidal magnetic field is much lower than the parallel component. Thus, the magnitudes of the electron particle flux Γ_e, the electron heat flux intensity q_e, and the ion heat flux intensity q_i can be expressed as a non–linear function of the thermodynamic variables and of their radial gradients as follows

$$\begin{pmatrix} \Gamma_e \\ q_e/n_e \\ q_i/n_i \end{pmatrix} = \underline{\underline{\boldsymbol{V}}} \begin{pmatrix} n_e \\ T_e \\ T_i \end{pmatrix} - \underline{\underline{\boldsymbol{D}}} \begin{pmatrix} \partial n_e/\partial\rho \\ \partial T_e/\partial\rho \\ \partial T_i/\partial\rho \end{pmatrix}$$

where the effective minor radius $\rho := \sqrt{\Phi/\pi B_{\text{tor}}}$ is the radius that a magnetic surface with circular section should have to enclose the same toroidal magnetic flux $\Phi := \int_S \boldsymbol{B} \cdot \mathrm{d}\boldsymbol{S}$ and where the convective and diffusive transport coefficient matrices are respectively

$$\underline{\underline{\boldsymbol{V}}} := \begin{bmatrix} v & a_{12} & a_{13} \\ a_{21} & U_e & a_{23} \\ a_{31} & a_{32} & U_i \end{bmatrix} \qquad \text{and} \qquad \underline{\underline{\boldsymbol{D}}} := \begin{bmatrix} D_e & c_{12} & c_{13} \\ c_{21} & \chi_e & c_{23} \\ c_{31} & c_{32} & \chi_i \end{bmatrix}$$

where v is the electron particle convection, U_e is the electron heat convection, U_i is the ion heat convection, D_e is the electron particle diffusivity, χ_e is the electron heat diffusivity, χ_i is the ion heat diffusivity, and the coupling between the thermodynamic variables is represented by the coefficients a_{ij} and c_{ij}. These transport coefficients depend on local plasma parameters and need to be computed by suitable models, as described in this chapter.

3.2 Classical transport

The classical theory takes only the diffusive component of the transport equations into consideration and also neglects the system geometry, i.e. it assumes isotropic Coulomb collisions between plasma particles. Thus, the diffusion can be described as a random walk–like process characterised by collision frequencies ν between plasma particle species and by mean free

path lengths corresponding to the variations of the mass centre positions of the particle guiding centres $\Delta \boldsymbol{r}_{\mathrm{gc,cm}}$.
The contributions of collisions between particles of the same plasma species to the classical particle diffusion coefficient $D_{\mathrm{class}} \sim \left\langle \boldsymbol{r}^2_{\mathrm{gc,cm}} \right\rangle \nu$ is null, because the mass centre of the particle guiding centres does not move during a collision between two identical particles. Hence, in a single isotope plasma at equilibrium, the classical particle diffusion coefficient is

$$D_{\mathrm{class}} = D_{\mathrm{class}_{ei}} \sim \left\langle \boldsymbol{r}^2_{\mathrm{gc,cm}_{ei}} \right\rangle \nu_{ei} \propto \frac{v^2_{\mathrm{rel}}}{\omega^2_{L_e}} \nu_{ei} \propto \frac{T}{B^2} \frac{n}{T^{3/2}} = \frac{n}{B^2\, T^{1/2}}$$

where ω_{L_e} is the electron Larmor frequency, the relative velocity is approximately equal to the electron thermal velocity $v_{\mathrm{rel}} \approx v_{\mathrm{th}_e} = \sqrt{T_e/m_e}$, the electron–ion collisional frequency is $\nu_{ei} \sim n_e/T^{3/2}$.

The energy diffusion due to the electron–ion collisions is approximately equal to the particle diffusion coefficient $\chi_{\mathrm{class}_{ei}} \approx D_{\mathrm{class}_{ei}}$, since the energy exchange is very inefficient because of the mass difference.
Although the particle diffusion due to the identical species collisions is null, the energy diffusion contributions due to the electron–electron and ion–ion collisions are $\chi_{\mathrm{class}_{ee}} = (v^2_{\mathrm{th}_e}/\omega^2_{L_e})\, \nu_{ee}$ and $\chi_{\mathrm{class}_{ii}} = (v^2_{\mathrm{th}_i}/\omega^2_{L_i})\, \nu_{ii}$ respectively. Particularly, the ion–ion one results the main heat diffusion contribution $\chi_{\mathrm{class}_{ii}} \gg \chi_{\mathrm{class}_{ee}} > \chi_{\mathrm{class}_{ei}}$. From Braginskii detailed calculations [2], it results

$$D_{\mathrm{class}} = D_{\mathrm{class}_{ei}} = 2 \times 10^{-3} \frac{n_{20}}{B^2 \sqrt{T}}\, \mathrm{m}^2/\mathrm{s}$$
$$\chi_{\mathrm{class}} \approx \chi_{\mathrm{class}_{ii}} = 1 \times 10^{-1} \frac{n_{20}}{B^2 \sqrt{T}}\, \mathrm{m}^2/\mathrm{s}$$

with $[n_{20}] = 10^{20}\, \mathrm{m}^{-3}$, $[B] = T$, and $[T] = \mathrm{keV}$.

3.3 Neoclassical transport

The neoclassical theory also takes into account the toroidal geometry, introducing in the transport coefficient calculation the distinction between the passing and trapped particles. Thus, these neoclassical coefficients can be estimated exploiting the passing and trapped particle expressions of displacements due to curvature and magnetic field gradient drifts from the particle reference magnetic surface recalled in section 1.5.2.
The neoclassical particle and heat diffusion coefficients for the passing particles are respectively $D_{\mathrm{NC}_{\mathrm{pass}}} \approx (2\Delta_{\mathrm{pass}})^2 \nu \approx 4q^2 r_L^2 \nu \approx 4q^2 D_{\mathrm{class}} \sim 40 D_{\mathrm{class}}$ and $\chi_{\mathrm{NC}_{\mathrm{pass}}} \approx \chi_{\mathrm{NC}_{\mathrm{pass}_{ii}}} \approx 4q^2 r^2_{L_i} \nu_{ii} \approx 4q^2 \chi_{\mathrm{class}_{ii}} \sim 40\, \chi_{\mathrm{class}}$.

In a collision, a trapped particle may become a passing particle if it gains enough parallel kinetic energy. Hence, in the transport coefficient calculations, an effective frequency $\nu_{\text{eff}} = \nu/\varepsilon$ related to the detrapping time and the trapped particle fraction $f_{\text{trap}} = \varepsilon$ have to be used. Thus, the neoclassical particle and heat diffusion coefficients for trapped particles are $D_{\text{NC}_{\text{trap}}} \approx f_{\text{trap}}\,\Delta^2_{\text{trap}}\,\nu_{\text{eff}} \approx \sqrt{\varepsilon}\,(qr_L/\sqrt{\varepsilon})^2\,(\nu/\varepsilon) \approx (q^2/\varepsilon^{3/2}) D_{\text{class}} \sim 200 D_{\text{class}}$ and $\chi_{\text{NC}_{\text{trap}}} \approx \chi_{\text{NC}_{\text{trap}_{ii}}} \approx (q^2/\varepsilon^{3/2})\,\chi_{\text{class}} \sim 200\,\chi_{\text{class}}$ respectively. Hence, the neoclassical transport is much larger than the classical one and is dominated by the trapped particles, although they are a small fraction of plasma particles.

3.4 Turbulent transport

The turbulent transport theory describes the plasma turbulences, which are the main mechanism responsible for the perpendicular transport with respect to the magnetic field lines.[22, 23]
There are two plasma instability classes: the macro–instabilities (the MHD instabilities) and the micro–instabilities (or drift wave–like instabilities). The scale of the macro–instabilities is in the order of the device size, while the scale of the micro–instabilities is in the order of the Larmor radius.

Ensuring a good MHD stability is crucial to avoid disruptions, i.e. sudden thermal energy losses typically followed by the plasma discharge termination. On the other hand, the drift waves are collective phenomena driven by the quasi–neutrality, the toroidal magnetic geometry, and the spatial non–homogeneity of tokamak plasmas due to non–null pressure gradients.

3.4.1 Drift waves

Independent dynamics of ions and electrons in a magnetically confined plasma may produce collective plasma oscillation modes called drift waves [22, 24, 25]. However, the detachment between electron and ion populations on large spatial scale is hindered by the onset of strong electric fields which restore the quasi–neutrality. Since the early 1960s, the drift modes in magnetically confined plasmas have been attentively studied. In magnetic confinement devices, different drift–type instabilities driven by pressure gradients can take place over a large range of cross–field wavelengths.

Let us study the drift waves under simplifying assumptions, neglecting collisions and working in electrostatic approximation. The axis system is chosen to have the magnetic field $\boldsymbol{B} = B_0\hat{\boldsymbol{z}}$ and the background density gradient $\boldsymbol{\nabla} n_0$ directed as $-\hat{\boldsymbol{x}}$ The subscripts 0 indicate the equilibrium quantities.

The background density gradient leads to a diamagnetic drift. Particularly, the density imbalance in neighboring Larmor circumferences leads to an effective mass flow and hence to a current density $\boldsymbol{J}_*$, called diamagnetic current, perpendicular to the magnetic field. To calculate the diamagnetic current density expression, let us multiply the plasma equilibrium condition (1.2) vectorially by $\boldsymbol{B}$ as follows

$$\begin{aligned}
\boldsymbol{B}\times\boldsymbol{\nabla}P=\boldsymbol{B}\times(\boldsymbol{J}_*\times\boldsymbol{B}) \quad &\Longrightarrow \quad \boldsymbol{B}\times\boldsymbol{\nabla}P=\underbrace{(\boldsymbol{B}\cdot\boldsymbol{B})}_{B_0^2}\boldsymbol{J}_*-\underbrace{\cancelto{0}{(\boldsymbol{B}\cdot\boldsymbol{J}_*)\boldsymbol{B}}}_{\text{since } \boldsymbol{J}_*\perp\boldsymbol{B}} \\
&\Longrightarrow \quad \boldsymbol{J}_*=(\boldsymbol{B}\times\boldsymbol{\nabla}P)/B_0^2 \\
&\Longrightarrow \quad \boldsymbol{J}_*=\frac{\boldsymbol{B}}{B_0^2}\times\left[\boldsymbol{\nabla}\left(n_0T_{e_0}\right)+\boldsymbol{\nabla}\left(n_0T_{i_0}\right)\right] \\
&\qquad\quad \text{with } P=P_{e_0}+P_{i_0}=n_0T_{e_0}+n_0T_{i_0}
\end{aligned}$$

Therefore, the electron diamagnetic current is

$$\boldsymbol{J}_{*e}=\frac{\boldsymbol{B}}{B_0^2}\times\boldsymbol{\nabla}\left(n_0T_{e_0}\right)=\frac{\boldsymbol{B}}{B_0^2}\times\left(T_{e_0}\boldsymbol{\nabla}n_0+n_0\boldsymbol{\nabla}T_{e_0}\right)$$

Assuming isothermal electrons ($\boldsymbol{\nabla}T_{e_0}=0$), we find $\boldsymbol{J}_{*e}=(T_{e_0}/B_0^2)\boldsymbol{B}\times\boldsymbol{\nabla}n_0$. Since a general current density is $\boldsymbol{J}=qn\boldsymbol{v}$, the electron diamagnetic drift velocity is simply

$$\boldsymbol{v}_{*e}=\frac{T_{e_0}}{-e\,n_0B_0^2}\,\boldsymbol{B}\times\boldsymbol{\nabla}n_0 \quad\Longrightarrow\quad \boldsymbol{v}_{*e}=\frac{T_{e_0}}{e\,n_0B_0^2}\,\boldsymbol{\nabla}n_0\times\boldsymbol{B}$$

It can be rewritten in the chosen coordinate system as

$$\boldsymbol{v}_{*e}=\frac{T_{e_0}}{e\,n_0B_0^2}\cdot\frac{\mathrm{d}n_0}{\mathrm{d}x}\,B_0\,(-\hat{\boldsymbol{x}})\times\hat{\boldsymbol{z}} \quad\Longrightarrow\quad \boldsymbol{v}_{*e}=\frac{T_{e_0}}{eB_0}\,\frac{1}{n_0}\,\frac{\mathrm{d}n_0}{\mathrm{d}x}\,\hat{\boldsymbol{y}}$$

This situation is sketched in figure 3.1. In the toroidal geometry, $\hat{\boldsymbol{x}}$ is the radial direction, $\hat{\boldsymbol{y}}$ is the poloidal direction, and $\hat{\boldsymbol{z}}$ is the toroidal direction. Since the variations due to the turbulence are usually faster in the poloidal direction, we assume that the wave vector associated with the perturbation are such as $k_x \ll k_y$ and we neglect k_x in the calculations.
When a little perturbation of the electron density occurs ($n_e = n_0 + \delta n_e$ with $\delta n_e \ll n_0$), an electron and ion flux arise along $\hat{\boldsymbol{y}}$. Being the ions slower than the electrons, this vertical motion leads to a charge separation and hence to a perturbation of the potential ϕ. Starting from the electron dynamics along

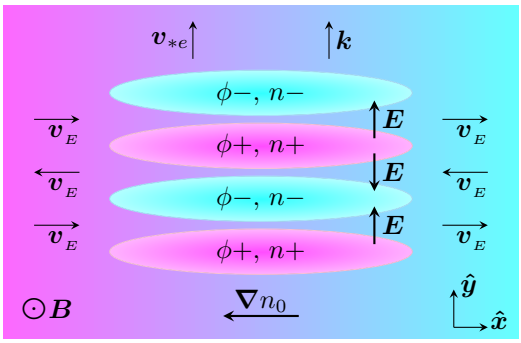

Figure 3.1: Schematic representation of the electron drift wave.

$\hat{\boldsymbol{z}}$ (i.e. parallel to $\boldsymbol{B}$), we find n_e as product between the unperturbed density and a Boltzmann factor

$$\begin{aligned} m_e \frac{\mathrm{d}v_{e_\parallel}}{\mathrm{d}t} = e\frac{\partial\phi}{\partial z} - \frac{1}{n_e}\frac{\partial p_e}{\partial z} \quad &\Longrightarrow \quad e\frac{\partial\phi}{\partial z} - \frac{T_{e_0}}{n_e}\frac{\partial n_e}{\partial z} = 0 \quad \Longrightarrow \\ \int \frac{e}{T_{e_0}}\frac{\partial\phi}{\partial z}\,\mathrm{d}z = \int \frac{1}{n_e}\frac{\partial n_e}{\partial z}\,\mathrm{d}z \quad &\Longrightarrow \quad \frac{e\phi}{T_{e_0}} = \log n_e - \log n_0 \quad \Longrightarrow \\ &\Longrightarrow \quad n_e = n_0 \exp\left(\frac{e\phi}{T_{e_0}}\right) \end{aligned}$$

where $(-e\phi)$ is the potential energy of electrons. If $(-e\phi) \ll T_{e_0}$, then $\exp\big(e\phi/T_{e_0}\big) \approx (1 + e\phi/T_{e_0})$. Therefore the electron density perturbation is

$$\delta n_e := n_e - n_0 \approx n_0\left(1 + \frac{e\phi}{T_{e_0}}\right) - n_0 = \frac{e\phi}{T_{e_0}}\,n_0$$

and the potential perturbation ϕ can be expressed as a function of n_e

$$\phi \approx \frac{\delta n_e}{n_0} \cdot \frac{T_{e_0}}{e} \tag{3.1}$$

The electric field $\boldsymbol{E} = -\boldsymbol{\nabla}\phi$ associated to this potential causes a velocity drift $\boldsymbol{v}_E$ equals to

$$\boldsymbol{v}_E = \frac{\boldsymbol{E}\times\boldsymbol{B}}{B_0^2} = \frac{\boldsymbol{B}}{B_0^2}\times\boldsymbol{\nabla}\phi \approx \frac{\boldsymbol{B}}{B_0^2}\times\boldsymbol{\nabla}\left(\frac{\delta n_e}{n_0}\cdot\frac{T_{e_0}}{e}\right) = \frac{T_{e_0}}{e n_0}\frac{\boldsymbol{B}}{B_0^2}\times\boldsymbol{\nabla}(\delta n_e)$$

which in our coordinate system is

$$\boldsymbol{v}_E \approx \frac{T_{e_0}}{e n_0 B_0}\frac{\partial(\delta n_e)}{\partial y}\,\hat{\boldsymbol{z}}\times\hat{\boldsymbol{y}} \quad \Longrightarrow \quad \boldsymbol{v}_E \approx -\frac{T_{e_0}}{e n_0 B_0}\frac{\partial(\delta n_e)}{\partial y}\,\hat{\boldsymbol{x}}$$

Notice that we are supposing that electrons can move freely in the plasma in order to cancel the charge separation. This hypothesis results in having the electrostatic perturbation in phase with the density perturbation.
The linearised ion continuity equation is

$$\frac{\partial n_i}{\partial t} + \mathrm{v_E}\,\frac{\mathrm{d}n_0}{\mathrm{d}x} = 0$$

Thanks to the quasi–neutrality condition $n_i \simeq n_e \approx n_0(1+e\phi/T_{e_0})$, we obtain

$$n_0\,\frac{\partial}{\partial t}\left(1+\frac{e\phi}{T_{e_0}}\right) - \frac{1}{B_0}\,\frac{\partial\phi}{\partial y}\,\frac{\mathrm{d}n_0}{\mathrm{d}x} = 0 \quad\Longrightarrow\quad \frac{\partial\phi}{\partial t} - \frac{T_{e_0}}{eB_0}\,\frac{1}{n_0}\frac{\mathrm{d}n_0}{\mathrm{d}x}\,\frac{\partial\phi}{\partial y} = 0$$

$$\Longrightarrow\quad \frac{\partial\phi}{\partial t} + v_{*e}\,\frac{\partial\phi}{\partial y} = 0 \quad\Longrightarrow\quad \frac{\cancel{T_{e_0}}}{e\cancel{n_0}}\,\frac{\partial\,\delta n_e}{\partial t} + v_{*e}\,\frac{\cancel{T_{e_0}}}{e\cancel{n_0}}\,\frac{\partial\,\delta n_e}{\partial y} = 0$$

Describing the perturbation as a plane wave $\delta n_e = \tilde{n}\exp\left(i\boldsymbol{k}\cdot\boldsymbol{x} - i\omega t\right)$, where $\omega = \omega_r + i\gamma$, we can rewrite

$$-i\omega\,\delta n_e + v_{*e}\cdot ik_y\,\delta n_e = 0$$

From the dispersion relation

$$\omega = \omega_{*e} \qquad \text{with } \omega_{*e} \coloneqq v_{*e}\,k_y$$

we notice that the propagation velocity of this perturbation is equal to the electron diamagnetic drift velocity v_{*e}.

We supposed that the electrons can move freely in the plasma; in this case the equation (3.1) is fulfilled and the drift wave frequency is purely real. Hence the drift wave is stable and propagates in the plasma without increasing or undergoing damping. If the electrons cannot move freely in the plasma, such as in non–null resistivity plasma, then a phase shift between the density perturbation δn_e and the electric potential ϕ occurs. Therefore the expression (3.1) has to be corrected introducing a phase shift

$$\phi\,(1-i\delta) \approx \frac{\delta n_e}{n_0}\,\frac{T_{e_0}}{e}$$

Thus, the dispersion relation becomes $\omega = \left(v_{*e}\,k_y\right)/\left(1-i\delta\right)$ that for $\delta \ll 1$ can be rewritten as

$$\omega \approx \omega_{*e}\,(1+i\delta)$$

As a result of the phase shift, a drift wave exponential growth $e^{\gamma t}$ follows, where the instability growth rate γ is the imaginary part of the drift wave frequency. Depending on the γ sign, the wave can be damped or can grow

exponentially in time. So the introduction of a non–null plasma resistivity leads to a phase shift between the potential and the electron density which allows the drift wave to extract energy available in the pressure gradient. The turbulent radial heat flux q due to the perturbation, given by the following temporal average

$$q = \left\langle \frac{3}{2}\,\delta p\, v_{E_r} \right\rangle$$

where δp is the pressure oscillation and v_{E_r} is the radial component of $\boldsymbol{v}_E$, is non–null only when δp is out of phase with v_{E_r}.

Generalising the drift waves to the tokamak configuration is a tough task, due to the toroidal geometry and to the non–uniform magnetic field.
The drift due to the magnetic field curvature generates a coupling of density and temperature perturbation that can lead to an instability, even if the electric potential and the density perturbation are in phase. Such instabilities are called interchange instabilities. In the plasma core, where temperatures are very high, the collisionality and hence the resistivity are minimised. Thus, in the tokamak plasma core the interchange instabilities dominate the resistive ones.
With the instability growth, non–linear interaction between modes on different scales occur, leading to the their turbulent saturation.

One of the most important non–linear mechanisms of instability regulation is related to zonal flows (ZFs)[26, 27], which are azimuthally symmetric shear flows excited by all types of micro–instabilities. The ZFs extract energy from the drift waves and so quench them, regulating transport.

There are three ways to classify the drift wave modes: one is based on the wavenumber (low–k modes or high–k modes), one depends on the driving mechanism, and one distinguishes between electron or ion modes.

It is useful to define the characteristic lengths of variation of the thermodynamic variables L_n, L_{T_e}, L_{T_i}, and L_p as follows

$$\boxed{L_n \coloneqq -\frac{n}{\nabla_r, n}} \qquad \boxed{L_{T_e} \coloneqq -\frac{T_e}{\nabla_r\, T_e}} \qquad \boxed{L_{T_i} \coloneqq -\frac{T_i}{\nabla_r\, T_i}} \qquad \boxed{L_p \coloneqq -\frac{p}{\nabla_r\, p}}$$

with $\nabla_r \coloneqq \partial/\partial\rho$.
Let us examine the modes which, being the most unstable, are responsible for the turbulent transport levels in thermonuclear plasmas: the Ion Temperature Gradient modes (ITGs), the Electron Temperature Gradient modes (ETGs), and the Trapped Electron Modes (TEMs).

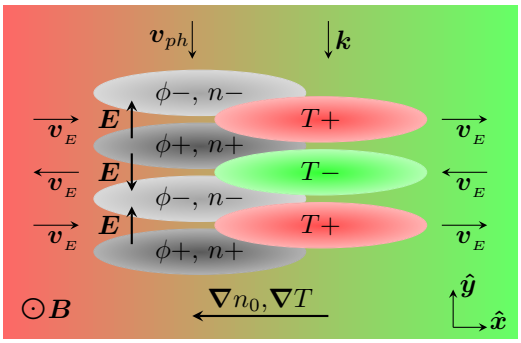

Figure 3.2: Schematic representation of the ITG drift wave (in the LFS).

3.4.2 ITGs

In the tokamak LFS, where the ion temperature gradient has the same direction of the magnetic field gradient, a drift wave due to $\boldsymbol{\nabla}_r T_i$ arises. For understandable reasons, these micro–instabilities are called Ion Temperature Gradient (ITG) modes [28].

Let us consider an initial ion temperature perturbation δT_i in the tokamak LFS, as sketched in figure 3.2. This perturbation causes a velocity drift given both by the magnetic field curvature and by the magnetic field gradient $\mathrm{v}_d \sim v_\parallel^2 + v_\perp^2/2 \sim \left(T_\parallel^2 + T_\perp^2\right)$. Thus, the drift motion is lower in the coldest plasma regions. Hence, a density perturbation arises and in turn produces a potential perturbation, not in phase with the ion temperature perturbation. If we assume that the electrons respond adiabatically, there is no phase shift between potential and density perturbation. An $\boldsymbol{E} \times \boldsymbol{B}$ drift occurs due to the electric field $\boldsymbol{E}$ associated with the potential perturbation. The effect of this drift is to move cold plasma in the coldest region and hot plasma in the hottest region. Hence, the ion temperature perturbation is amplified in the LFS. The compression due to v_d governs the process and the perturbation propagates in the direction of the ion diamagnetic drift.

The ITGs, which develop on a spatial scale of the order of the ion Larmor radius (a relatively large scale amongst the micro–instabilities), fall within the low–k modes, with reference to their wave number.

In order that the ITG modes are driven unstable, R/L_{T_i} has to be larger than an ITG critical threshold [29, 30], that can be expressed as a function of plasma parameters [31] as follows

$$\left.\frac{R}{L_{T_i}}\right|_{\text{crit}}^{\text{ITG}} = \frac{4}{3}\left(1+\frac{T_i}{T_e}\right)\left(1+2\,\frac{s}{q}\right) \qquad \text{for } \frac{R}{L_{T_i}} < 2\left(1+\frac{T_i}{T_e}\right)$$

where q is the safety factor and s is the magnetic shear $s := (r/q)(\mathrm{d}q/\mathrm{d}r)$.

3.4.3 ETGs

The Electron Temperature Gradient (ETG) modes [32, 33] are instabilities driven by the electron temperature gradient $\boldsymbol{\nabla}_r T_e$ and are the electron counterpart of the ITGs. The linear physics of ITG and ETG modes is very similar under the exchange of electrons with ions.
The ETGs, which develop on a spatial scale of the order of the electron Larmor radius (a relatively small scale amongst the micro–instabilities), fall within the high–k modes.

For many years it was believed that the flux driven by the ion–scale modes, like ITGs, would be considerable bigger than the one driven by ETGs, because the gyro–Bohm model predicts a small ratio between the ETG and ITG diffusion coefficients $D_{\mathrm{ETG}}/D_{\mathrm{ITG}} \sim \sqrt{m_e/m_i} \simeq 1/40$.
When the non–linear effects are also considered, the isomorphism between ITGs and ETGs vanishes. Unlike the ITGs, the ETG modes can originate the ETG streamers, thin and radially elongated structures able to carry an electron heat flux amount comparable to the one carried by low–k modes.[32, 34]

Furthermore, intense interactions between high–k and low–k modes was found in recent studies][35, 36, 34]. The ETG streamers can be suppressed by ITG zonal flows, while the ETGs can increase the heat flux carried by ion–scale modes.

The ETG modes are also driven unstable above a critical value of R/L_{T_e}. The expression of the ETG critical threshold [33], based on gyrokinetic simulation studies, is

$$\left.\frac{R}{L_{T_e}}\right|_{\mathrm{crit}}^{\mathrm{ETG}} = \max\left\{\left[0.8\frac{R}{L_n}\right]; \left[(1+\tau)(1-1.5\,\varepsilon)\left(1.33+1.91\,\frac{s}{q}\right)\left(1+0.3\,\varepsilon\,\frac{\mathrm{d}\kappa}{\mathrm{d}\varepsilon}\right)\right]\right\}$$

with $\tau \coloneqq (Z_{\mathrm{eff}}\,T_e/T_i)$, the inverse aspect ratio $\varepsilon \coloneqq r/R_0$, and the plasma elongation $\kappa \coloneqq a/b$, where $a \coloneqq r_{\mathrm{LCFS}}$ is the minor radius of the separatrix in the equatorial mid–plane and b is its vertical counterpart.

3.4.4 TEMs

The trapped and passing electrons respond differently to an electrostatic potential ϕ. Instabilities linked to only the trapped electrons are often responsible of most of the electron heat transport in a tokamak: the Trapped Electron Modes (TEMs) [37].
The TEM development is related to both density gradient $\boldsymbol{\nabla}_r n$ and electron temperature gradient $\boldsymbol{\nabla}_r T_e$.

The Trapped Electron Modes are also driven unstable above a R/L_{T_e} critical threshold [38, 39]

$$\left.\frac{R}{L_{T_e}}\right|_{\text{crit}}^{\text{TEM}} = \frac{0.357\sqrt{\varepsilon}+0.271}{\sqrt{\varepsilon}}\left[4.90 - 1.31\,\frac{R}{L_n} + 2.68\,s + \log\left(1+20\,\nu_{\text{eff}}\right)\right]$$

where the trapped particle fration $f_{\text{trap}} = \sqrt{\varepsilon}$ is taken into account and the effective frequency is $\nu_{\text{eff}} = \nu_{ei}/\omega_{*e}$ with ν_{ei} electron–ion collision frequency. Investigating the TEM critical threshold dependence on (R/L_n) and (T_e/T_i) in more detail, it was found that up to $R/L_n \lesssim 1.3$ TEMs are stabilised for a ratio T_e/T_i increasing, while for $R/L_n \gtrsim 1.3$ the effect is opposite.[40]

3.4.5 Temperature profile stiffness

Summarising, the ITG and TEM micro–instabilities are ion–scale modes, i.e. their characteristic lengths are of the order of the ion Larmor radius, while the ETG micro–instabilities are electron–scale modes, i.e. their characteristic lengths are of the order of the electron Larmor radius. Equivalently, the ITGs and TEMs are low–k modes, while the ETGs are high–k modes.
The ITG and ETG modes are driven by a temperature gradient, ion and electron respectively, while TEMs are driven by both a temperature gradient and the density gradient.

Above the thresholds, these micro–instabilities become unstable and drive electron and ion heat transport. The ion heat transport is mainly due to the ITG modes, which usually dominate over ETGs and TEMs. At low collisionality and dominant electron heating conditions, TEMs dominate the electron heat transport, the ITGs contribute weakly to it, and ETGs are stable.

According to the semi–empirical transport model CGM (Critical Gradient Model), the following expressions can be written for the ion heat flux q_i

$$q_i = q_i^{\text{res}} + n_i q^{\frac{3}{2}}\,\chi_s\,\frac{T_i^2 r_{L_i}}{eBR^2}\frac{R}{L_{T_i}}\left(\frac{R}{L_{T_i}} - \left.\frac{R}{L_{T_i}}\right|_{\text{crit}}\right)\cdot\Theta\left(\frac{R}{L_{T_i}} - \left.\frac{R}{L_{T_i}}\right|_{\text{crit}}\right)$$

and for the electron heat flux q_e

$$q_e = q_e^{\text{res}} + n_e q^{\frac{3}{2}}\,\chi_s\,\frac{T_e^2 \rho_s}{eBR^2}\frac{R}{L_{T_e}}\left(\frac{R}{L_{T_e}} - \left.\frac{R}{L_{T_e}}\right|_{\text{crit}}\right)\cdot\Theta\left(\frac{R}{L_{T_e}} - \left.\frac{R}{L_{T_e}}\right|_{\text{crit}}\right)$$

where q_i^{res} and q_e^{res} are the residual ion heat flux and the residual ion heat flux respectively, q is the safety factor, $\rho_s := c_s/\omega_{L_i}$ is defined as ratio between

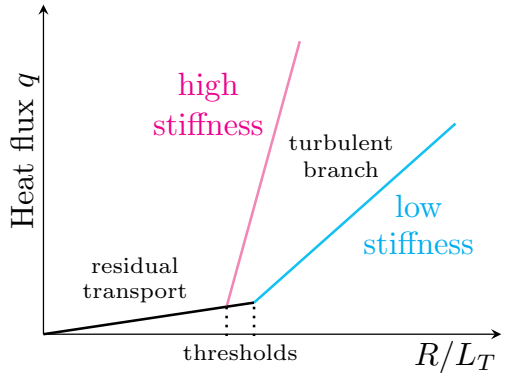

Figure 3.3: Typical trend of the energy flux q as a function of R/L_T.

the ion sound velocity $c_s := T_e/m_i$ and the ion Larmor frequency ω_{L_i}, χ_s (proportional to the heat flux curve slope) quantifies the turbulent transport term, and the Heaviside step–function Θ supplies the threshold effect.

Below $(R/L_T)|_{\text{crit}}$, the heat diffusivity (χ_i or χ_e) is constituted only by a basic level, not necessarily neoclassical, which produces a low residual transport term q^{res}. Above this threshold, a higher level due to the turbulent transport is added to the basic one. In figure 3.3 the typical behaviour of the heat flux q as a function of the logarithmic temperature gradient R/L_T is shown. For high χ_s values, a small increase in R/L_T drives a large increase in χ and heat flux. This implies that it becomes difficult to change significantly the temperature peaking with the level of experimental flux available. As result, temperature profiles are quite stiff, i.e. resilient to change. Thus, χ_s indicates the extent to which the temperature gradient responds to a heat flux variation, i.e. reveals the level of stiffness of temperature profiles. When the heat flux curve above the threshold $(R/L_T)|_{\text{crit}}$ is very steep, we talk about high stiffness of temperature profiles, while if the heat flux curve slope is lower we talk about low stiffness of temperature profiles.

3.5 Gyrokinetic models of transport

3.5.1 Gyrokinetic equations

The temporal evolution of the 6D distribution functions of the plasma particles and of the electromagnetic potentials is entirely described by the kinetic equations, including the collisional Vlasov equation of every species and the coupled Maxwell equations.

The 5D gyrokinetic equations can be derived from the 6D kinetic equations, exploiting some observed turbulent fluctuation features which allows us to average over the Larmor motion.

1. The oscillations are small compared to corresponding background quantities

$$\delta n_\sigma \ll n_{\sigma_0} \qquad \delta \boldsymbol{B} \ll \boldsymbol{B}_0 \qquad e\,\delta\phi_\sigma \ll T_\sigma \qquad \forall\sigma \text{ species}$$

   where $n_\sigma = n_{\sigma_0} + \delta n_\sigma$, $\boldsymbol{B} = \boldsymbol{B}_0 + \delta\boldsymbol{B}$ and $eT_\sigma = T_{\sigma_0} + e\delta\phi_\sigma$.
   For typical plasma parameter, these conditions are fulfilled in the core. The fluctuations at the plasma edge can reach $\sim 10\,\%$ of the background non–fluctuating quantities.

2. The oscillation frequency ω is small compared to the Larmor frequencies

$$\omega \ll \omega_{L_\sigma} \quad \forall\sigma \text{ species}$$

   and therefore the background quantities are assumed constant.

3. The turbulent fluctuations are strongly anisotropic

$$k_\parallel \ll k_\perp$$

Exploiting these properties, we can split each distribution function f_σ in a stationary part and a perturbed part $f_\sigma = F_{\sigma_0} + \delta f_\sigma$ and then average over the gyro–motions. Thus, we find a new set of equations called gyrokinetic equations, whose dimension is reduced. A complete derivation of the gyrokinetic equations is described in [41].

3.5.2 Gyrokinetic transport codes

To evaluate the particle and heat transport, solving the gyrokinetic equations, several numerical codes have been developed over the years from the late sixties. The gyrokinetic (GK) codes constitute the most advanced tool to investigate the turbulent transport.
Most of them are gradient–driven: they calculate the heat flux for a given R/L_T value. Some are flux–driven: for a given flux they calculate the corresponding R/L_T value.

The gyrokinetic problem is intrinsically non–linear (NL), but generally gyrokinetic codes can be also run linearly.
Among the gyrokinetic codes we can distinguish the global codes from the local codes. Although both types require large computing resources, the

former are more resource consuming, because they examine the plasma in its entirety. The local code are also referred to as flux tube codes, because they consider a bundle of magnetic field lines, called flux tube, whose length and radial width are chosen to serve the simulation purposes.

Because of their large computing resource demand, the gyrokinetic codes cannot be used for full plasma simulations over the whole radial profile. Even for runs at single time and spatial position, supercomputers highly parallelised and High Performance Computing (HPC) techniques are required to run the gyrokinetic codes.

3.5.3 The GENE code

GENE (Gyrokinetic Electromagnetic Numerical Experiment) [42, 43], among the gyrokinetic codes, is an open source plasma micro–turbulence code developed by an international group of physicists and computational scientists.
GENE can be used both in the local and in the global operation mode in order to solve the non–linear gyrokinetic equations on a fixed grid in 5D phase space and so compute the oscillations on a gyro–motion scale and the resulting particle and heat transport coefficients in magnetic plasmas.[1]

Specific GENE simulations of DTT scenarios were performed and used as benchmark for the results achieved in this PhD work by the quasi–linear transport models in the integrated modelling.

3.5.4 The GYRO and CGYRO codes

GYRO [44, 45, 46, 47] was the first global electromagnetic solver for the GK equations with kinetic electrons. It was used to calculate the core plasma turbulence. Moving radially toward the pedestal region, the turbulent phenomena change due to the steeper plasma pressure gradients and the larger collisionality. Therefore, the new CGYRO [48, 49, 50, 51] code is an Eulerian GK solver developed to complement GYRO and specifically optimised for electromagnetic, collisional, multi–scale simulations. GYRO and CGYRO provided a transport database for the calibration of reduced transport models.

[1] The GENE code is exploited both in fusion and in astrophysical plasmas.

3.6 Quasi–linear transport models

The quasi–linear (QL) transport models, based on linearised equations, are simpler and hence faster than the gyrokinetic codes. They allow to simulate the whole radial plasma profiles and their time evolution.[2]

The suffix "quasi" indicates that the QL models need a method to calculate some typical NL quantities from the linear ones. Only a gyrokinetic code can calculate the saturated flux of a mode. Hence a quasi–linear model always needs a saturation rule, which is a model feature, to predict the saturated fluxes from linear quantities. A simple saturation rule, called mixing length rule, used in the past in several QL models is $D \approx \sum_k \gamma_{\boldsymbol{k}}/k_\perp^2$, where $\gamma_{\boldsymbol{k}}$ is the growth rate of the mode with wave vector $\boldsymbol{k}$ and $k_\perp^2 = k_x^2 + k_y^2$. Nowadays, more advanced saturation rules are adopted.

For the DTT simulations made in this PhD work, we have always use the most sophisticated QL model available nowadays: TGLF and QuaLiKiz, described in the following sections.

3.6.1 The TGLF model

The TGLF (Trapped Gyro–Landau Fluid) model [52, 53, 54, 55] is a gyro–fluid, local, and electromagnetic quasi–linear model, based on a system of gyro–Landau fluid equations. It considers the kinetic effects such as the gyro–averaging and the Landau damping. The TGLF model, developed after GLF23 [56], improves the finite Larmor radius effects and the trapped particle response compared to its predecessor. To solve equations in shaped geometry with finite aspect ratio, TGLF uses the Miller equilibrium model [57].

TGLF calculates numerically the linear modes and then uses a saturation rule fitted to a large database of nonlinear GK simulations. Over the years, increasingly sophisticated saturation rules have been elaborated: SAT0, SAT1, SAT1–geo, and SAT2.
The former is the original one and is a single scale rule, while the following saturation rules are multi–scale. The SAT1 rule is able to cover both ion–scale and electron–scale micro–instabilities (from the low–k ion modes up to the high–k ETG modes) and was introduced to improve the modelling of the rotation effect, include the Dimits shift effects, and the interactions between different wave numbers. Both the SAT0 and SAT1 rules were benchmarked against GYRO non–linear simulations with kinetic electrons

[2] Calculating a flux level at a given radius in only a temporal instant with a GK code requires about 10^4–10^7 CPU hours, while simulating the whole plasma with a QL code requires some CPU minutes.

and Miller shaped geometry.[3] The SAT1–geo rule, released in November 2019, features an improved description of geometrical effects and calibration against CGYRO non–linear simulations. The last SAT2 rule, released in January 2021, is characterised by a fit of the geometrical coefficients to 3D CGYRO spectra, an improved collision model, and a better agreement with CGYRO non–linear simulations described in [59].

In this PhD work, simulations using both the TGLF implementation in transport solvers and its stand–alone version have been performed. At the beginning of the project, SAT0 and SAT1 were used to predict the plasma profiles of DTT. Then these saturation rules were replaced by the two most recent versions of TGLF. In the thesis, we will refer to the results achieved by the SAT1–geo and SAT2 rules only.

3.6.2 The QuaLiKiz model

The QuaLiKiz model (QLK) [60, 61] is a gyrokinetic and electrostatic QL transport model in circular geometry.

In this thesis, we will present the results of the DTT integrated modelling achieved by the last QLK release [62], which includes an improved TEM treatment through the employment of a revised collision operator.
In addition to this new official version, an ad hoc version of the model with an enhanced TEM electron heat flux was created for DTT and tested, as described in the chapter 4 and in [18]. This ad hoc QLK correction is not intended to be a recommendation of a general prescription, but rather a form of uncertainty quantification by modifying the model to account for known physics deficiencies (regimes strongly dominated by TEMs are still challenging for QLK) for this specific case. The improvements achieved by this specially–made version of QLK were too small to justify its employment in following simulations.

Furthermore, in order to set–up the simulations in a faster way, runs with the QLK Neural Network (QLKNN) [63] model have been also carried out, applying the QLKNN–hyper–10D version. This work has been also useful in testing the proper functioning of the QLKNN in DTT regime conditions.

In this PhD work, the QLK model has been also used both in stand–alone mode and in integrated simulations.

[3] At the beginning, TGLF linear modes were benchmarked against a database constituted by 1800 GKS code [58] linear stability calculations.

3.7 Transport solvers

The transport solvers are very useful tools for predicting new scenarios and for modelling experimental data of plasma discharges. Typically, various transport models are implemented in a single transport solver. The transport modelling can be done following a predictive approach, i.e. computing the plasma kinetic profiles, or an interpretative approach, i.e. fixing density and temperature profiles to calculate other quantities. Several interfaced tokamak physics codes, each performing a specific task, are integrated in these suites and interact to obtain self–consistent simulations.

Different transport solvers have been developed over time. Among them, two codes have been used in this PhD work: ASTRA and JINTRAC, presented in the following sections. We also devised a new iterative ASTRA–JINTRAC scheme for some high complexity DTT cases, as described in section 4.3.2.

At the beginning of the work, the development state of the core transport simulator ETS (European Transport Solver) [64] within the framework of the IMAS (Integrated Modelling & Analysis Suite) [65, 66], adopted by the ITER team, was evaluate not advanced enough to enable the work planned for DTT. Recently, some preliminary exploring studies for a transition to the IMAS environment started.

3.7.1 ASTRA

ASTRA (*Automated System for TRansport Analysis*) [67] is a very flexible transport solver whose first version was born in late eighties at the Kurchatov Institute in Moscow. The ASTRA code uses the realistic flux surface 2D geometry, recalculated self–consistently by the SPIDER [68] equilibrium solver, to solve 1D fluid transport equations. It is subject to continuous developments in order to add new features and to improve its functionality.

ASTRA works in the UNIX C shell, exploiting Fortran/C compilers and X11 graphic libraries. It displays the behaviour in time of the various plasma profiles and through a number of interactive panels it allows the user to intervene during the program execution adjusting the model variables and so conditioning the course of the simulation.

The QuaLiKiz and TGLF quasi–linear models are implemented in ASTRA and can be used to calculate the turbulent transport.
Furthermore, the NBI and ECRH power deposition and current drive can be calculated by specific codes integrated in ASTRA: the beam–tracing code TORBEAM [69, 70] and the RABBIT [71] (Rapid Analytical Based Beam Injection Tool) code.

Unfortunately, ASTRA is not equipped with a module for the self–consistent treatment of the ionisation state distribution of impurities yet.

3.7.2 JINTRAC

The modelling suite JINTRAC (Jet INtegrated TRAnsport Code) is a collection of several physics models integrated together to model tokamak plasmas. JINTRAC includes the transport solver JETTO, a 1.5D core plasma fluid code which can predict the plasma profiles up to the separatrix. The JINTRAC repositories are hosted and managed by a git workflow. The Jet Application Management System (JAMS) is the primary graphical user interface for JINTRAC. From the last JETTO version, released in September 2021, parallel MPI compilation is the default for all compilers.

JETTO can be used for the core modelling setting suitable boundary conditions, as employed in this PhD thesis, or coupled with a SOL code included in JINTRAC.

The QuaLiKiz and TGLF quasi–linear models (included QLKNN) are also implemented in JETTO and can be used to calculate the turbulent transport. The MHD equilibrium can be self–consistently calculated during a run by the equilibrium solver ESCO integrated in the suite.
The ECRH, NBI, and ICRH systems can be respectively modelled by the GRAY [72] code, the PENCIL [73] code, and the PION[74] code.[4]
Moreover, impurity densities and radiation can be modelled (treating separately all ionisation states) by the SANCO [75] code integrated in JETTO, based on the ADAS (Atomic Data and Analysis Structure) database.

[4]The PION code also calculates the synergy effects between ICRH and NBI.

CHAPTER 4

First–principle based multi–channel integrated modelling in support to the design of DTT

This work was published in *I. Casiraghi et al 2021 Nuclear Fusion 61 116068.*

Abstract

An intensive integrated modelling work of main scenarios of the new tokamak DTT (Divertor Tokamak Test facility) with the Single Null divertor configuration has been performed using first–principle quasi–linear transport models, in support to the design of the device and to the definition of its scientific work–programme. First results of this integrated modelling work on DTT ($R_0 = 2.14\,\mathrm{m}$, $a = 0.65\,\mathrm{m}$) are presented here along with outcome of the gyrokinetic simulations used to validate the reduced models in the DTT range of parameters. As a result of this work, the heating mix was defined, the size of device was increased to $R_0 = 2.19\,\mathrm{m}$ and $a = 0.70\,\mathrm{m}$, the use of pellets for fuelling has been advised and reference profiles for diagnostic design, estimates of neutron yields and fast particle losses have become available.

4.1 Introduction

Studying the controlled power and particle exhaust from a fusion reactor is a main research topic in the European Fusion Roadmap[6, 7].

ITER[5] (International Thermonuclear Experimental Reactor) is planned to test a conventional metal divertor operating in a plasma fully detached condition. This baseline approach to the power exhaust problem may not be suitable for extrapolation to the operating conditions of DEMO[76] (DEMOnstration power plant) and future reactors, requiring plasma facing components able to cope with huge power fluxes in the range of 10–20 $\mathrm{MW/m^2}$.

Therefore, studying and developing an alternative exhaust strategy is crucial to mitigate the risk.
This is the main task of the new tokamak DTT (Divertor Tokamak Test facility)[8, 9, 10], whose construction is starting in Frascati, Italy, with the first plasma planned for 2026. The DTT design is in advanced status but will be kept flexible with regard to the choice of the divertor until 2023, when the outcome of the work conducted under the EUROfusion PEX ad hoc group will be available to drive the best choice for the DTT divertor.
For the optimisation of the various aspects of the DTT design, it is of key importance to perform integrated modelling of the foreseen operational scenarios using first principle based transport models and state–of–art modules for heating, fuelling and magnetic equilibrium. Integrated modelling allows to predict main plasma profiles as a result of non–linear interactions between plasma, heating and fuelling, and impurity influxes, as well as amongst different transport channels.

This is the aim of the work describe in this chapter, which reports the first DTT simulations using theory–based transport models, to support the DTT design, and particularly the definition of the heating mix, the design of the neutron shields, the assessment of fast particle losses and the design of diagnostic systems, as well as to help the elaboration of a DTT scientific work–programme.

4.2 The DTT project

The new Italian tokamak DTT is a D–shaped superconducting device, whose construction is starting at the ENEA Research Center in Frascati, Italy. A drawing of the DTT device is shown in figure 4.1.

The characteristics of DTT were chosen to make it ITER and DEMO relevant, so that exhaust solutions could be extrapolated to a reactor–grade plasma. Bearing in mind the requirement of a strong compatibility with the operating conditions in DEMO, DTT is designed to be a bulk–edge integrated experiment with a reactor relevant bulk. Therefore, the DTT dimensionless physical parameters should be as close as possible to the ITER and DEMO ones. It is not possible to simultaneously preserve all these quantities, and hence DTT has been scaled down following the so called "weak scaling" described in [13]. Since the P_{sep}/R parameter, where P_{sep} is the power exiting through the separatrix, is recognised as a key metric for the extent of the exhaust issue in a tokamak, geometry and auxiliary power coupled to the plasma have been chosen to guarantee a value of $P_{\mathrm{sep}}/R = 15\,\mathrm{MW/m}$ similar to those foreseen for ITER and DEMO. So, the power at the divertor in DTT

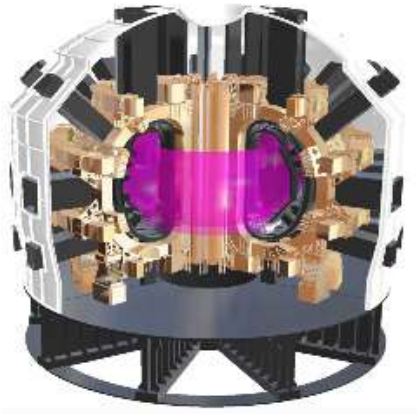

Figure 4.1: DTT device.

and DEMO will be comparable.
Table 4.1 shows rough indications for both dimensional and dimensionless parameters of the DTT configuration simulated in this work compared to ITER and EU DEMO. The collisionality has been calculated as

$$\nu_e^* = 6.92 \times 10^{-18} \, \frac{q R_0 n_e Z_{\text{eff}} \ln \Lambda_e}{T_e^2 \varepsilon^{3/2}}$$

where n_e is expressed in m^{-3}, T_e is expressed in eV, and ε is the inverse aspect ratio.[77]
The superconducting coils allow for pulse length up to 100 s, with plasma current $I_{\text{pl}} \leq 5.5\,\text{MA}$ and with toroidal field coils able to generate an on–axis toroidal magnetic field $B_{\text{tor}} \leq 6\,\text{T}$ at $R = 2.14\,\text{m}$. DTT has an up–down symmetric geometry, major radius $R_0 = 2.19\,\text{m}$, minor radius $a = 0.70\,\text{m}$, elongation $\kappa \leq 1.89$, and average triangularity $\langle\delta\rangle \leq 0.4$. The device size was recently increased from the previous values $R_0 = 2.14\,\text{m}$, $a = 0.65\,\text{m}$. The simulations reported here refer to the 2.14 m device, and have contributed to the decision of its enlargement.
For the reference baseline DTT scenarios, a Greenwald density target value of $\langle n \rangle / n_G \sim 0.45$ (where n_G is the Greenwald fraction defined in [78]), has been chosen in order to have a high operational flexibility, leaving open the possibility to explore in the future scenarios with higher densities.
The plasma shape parameters of the Single Null (SN) configuration are similar to those of the present European design of DEMO ($R_0/a \approx 3.1$, $\kappa_{95} \approx 1.55 - 1.8$, $\delta_{95} \approx 0.3$). The technical description of the DTT vacuum vessel, first wall and baseline divertor, and magnetic system is contained in [8].

Table 4.1: Main parameter comparison between the DTT configuration simulated in this chapter and ITER and EU DEMO future devices.[14, 15, 16, 17]

	DTT	ITER	EU DEMO
R [m]	2.14	6.2	9.1
a [m]	0.65	2.0	2.93
A	3.3	3.1	3.1
I_{pl} [MA]	5.5	15	19.6
B_{tor} [T]	6	5.3	5.7
P_{tot} [MW]	45	150	460
P_{sep} [MW]	32	87	154
P_{sep}/R [MW/m]	15	14	17
λ_q [mm]	0.7	0.9	1.0
Pulse length [s]	100	400	7600
β_N [%]	1.6	1.6	2.6
ν_e^* at $r/a = 0.5$ [10^{-2}]	1.1	1.1	0.5
ρ^* [10^{-3}]	3.3	2.0	1.5
$\langle n \rangle$ [$10^{20}/\mathrm{m}^3$]	1.8	1.0	0.9
$\langle T_e \rangle$ [keV]	6.7	8.5	13
τ_E [s]	0.4	3.6	4.2

To address the particle and power exhaust problem, alternative divertor solutions and improved plasma facing materials will be developed and tested in DTT, thanks to its high flexibility in magnetic configurations and divertor choice. The various divertor solutions and technologies include Liquid Metal Divertors (LMD), based on either capillary porous systems or boxes/pools systems, and advanced divertor configurations such as Double Null (DN), Quasi–SnowFlake (QSF), and single null with Negative Triangularity (NT) scenarios. The reference configuration that we will use in this work is the SN.

DTT will be equipped with three auxiliary heating systems: a Negative ion–based Neutral Beam Injection (NNBI) system, a 60–90 MHz Ion Cyclotron Resonance Heating (ICRH) system, and a 170 GHz Electron Cyclotron Resonance Heating (ECRH) system.
In order to match ITER and DEMO values of P_{SEP}/R, where P_{SEP} is the power flowing through the last closed magnetic surface, a large amount of auxiliary power is needed (~ 45 MW in the full power scenario). The 3 heating systems will be progressively realised and installed on DTT.
The first experimental plasma (day–0 scenario) will be achieved using only 8 MW from second harmonic ECRH (~ 7.2 MW at the plasma) at the half field operational point (plasma current $I_{\mathrm{pl}} = 2$ MA and toroidal magnetic field $B_{\mathrm{tor}} = 3$ T). In a couple of years, the power coupled to the plasma will be increased up to ~ 25 MW in the phase called day–1 scenario, working at $I_{\mathrm{pl}} = 4$ MA and $B_{\mathrm{tor}} = 5.85$ T. The heating mix in this initial phase has been fixed: 16 MW from ECRH (~ 14.4 MW at plasma), 4 MW from ICRH (~ 3 MW at plasma), and 7.0–7.5 MW at plasma from NBI (with a neutral beam injector at 400 keV). Instead, the definitive power mix for the DTT full performance scenario has been rediscussed with respect to the original options proposed in [8], following the simulation results reported in this chapter, and new options have been evaluated, as discussed in section 4.3.6, within the following ranges of power at plasma: 26–36 MW of ECRH, 3–9 MW of ICRH, and 7.5–15 MW of NBI at energies between 200–600 keV.
The amount of heating power is an order of magnitude larger than typical power densities in nowadays tokamaks and foreseen in ITER. This trait, jointly with the cryogenic system needs, forces DTT to be an actively cooled device.

In addition to the main task dedicated to plasma exhaust, DTT will be highly relevant also for tokamak physics integrated studies with reactor relevant parameters. Thanks to the high plasma core performance, DTT is located in a unique operational region, at high density but low collisionality, which is unexplored by present tokamaks (e.g. $n_e \sim (0.6 - 0.8) \times 10^{20}/\mathrm{m}^3$ and $\nu_e^* \approx (2.9 - 4.3) \times 10^{-2}$ at $r/a = 0.5$ in AUG high performance plasmas,

$n_e \sim (0.7 - 0.9) \times 10^{20}/\mathrm{m}^3$ and $\nu_e^* \approx (2.2 - 3.9) \times 10^{-2}$ at $r/a = 0.5$ in JET-ILW baseline discharges).

Therefore, DTT will support the experimental program of ITER, operating in parallel with it, and it will address high priority issues, such as ELM pacing, pellet fuelling, management and avoidance of disruptions, burning plasma energetic particle physics, and plasma control.

4.3 Integrated modelling of SN scenarios

The integrated modelling of various DTT scenarios with SN configuration in H–mode has been performed. These simulations solve the transport equations for heat, particle and momentum using a first principle transport model in a self–consistent magnetic equilibrium, to predict steady–state radial profiles of the electron and ion temperatures, density (both main species and impurity), toroidal rotation, and current density. The heating profiles are also calculated consistently, as well as all non–linear interactions between heating and plasma and between the different transport channels.

As described in detail in section 4.3.2, integrated runs have been primarily done using the JINTRAC[79] suite of codes and in some cases using the ASTRA[67] transport solver with a mixed ASTRA–JINTRAC approach.

4.3.1 General settings

The performed simulations of DTT deuterium plasmas cover the region inside the separatrix. The equilibrium is calculated self–consistently during the run, keeping fixed the boundary, as described in section 4.3.3. Approximately 4 seconds of plasma evolution needs to be simulated until convergence, due to the current diffusion time. The transport equations are solved within $\rho_{\mathrm{tor}} = 0.94$, where $\rho_{\mathrm{tor}} \coloneqq \sqrt{\frac{(\Phi/\pi B_{\mathrm{tor}})}{(\Phi/\pi B_{\mathrm{tor}})_{\mathrm{max}}}}$ is the normalised effective minor radius, i.e. the normalised radius that a magnetic surface with circular section should have to enclose the same toroidal magnetic flux Φ. The values at the top of the edge pedestal are used as boundary condition.
The pedestal pressure has been previously calculated by the Europed code[80] with the EPED1 model[81], which is based on two concepts. The pedestal transport is determined by turbulence driven by the kinetic ballooning modes (KBM) which sets a soft boundary for the gradient. This is implemented in the code via the simple expression width $= 0.076 \times \sqrt{\beta_{\mathrm{pol}}^{\mathrm{ped}}}$, which provides one constraint that determines the gradient. However, once the pedestal reaches the KBM constraint, the pedestal height can still increase via the widening

of the pedestal width. The widening continues till the peeling–ballooning (PB) modes are destabilised and an ELM is triggered. The EPED model determines pedestal height and pedestal width by identifying the intersection between the PB constraint and the KBM constraint.
The prescribed inputs of Europed runs are the magnetic equilibrium, the electron density at the pedestal top n_e^{ped}, the value of β_{pol}, and the temperature and density at the separatrix T_e^{sep} and the relative shift, defined as the distance between position of the pedestal density n_e^{pos} and temperature T_e^{pos}.[82] Note that the separatrix density n_e^{sep} is not an input parameter, but is determined by $n_e^{\mathrm{pos}} - T_e^{\mathrm{pos}}$ and by the density offset applied in the SOL. For the same offset, the increase of the relative shift leads to the increase of n_e^{sep}.[83] The value of n_e^{ped} has been set to achieve a line averaged electron density $\bar{n}_e \sim (0.40 - 0.47)\, n_G$. $T_i = T_e$ has been assumed in the pedestal. Instead, the value of β_{pol} has been chosen, in an iterative way, in order to match the value predicted by JINTRAC run. In the full power simulations, $n_e^{\mathrm{ped}} = 1.4 \times 10^{20}\,\mathrm{m}^{-3}$, $\beta_{\mathrm{pol}} = 0.60$, a relative shift between n_e^{ped} and T_e^{ped} to obtain $n_e^{\mathrm{sep}} \approx 0.25\, n_e^{\mathrm{ped}}$, and $T_e^{\mathrm{sep}} = 100\,\mathrm{eV}$ values have been set and temperature values at the pedestal top of about $T_e^{\mathrm{ped}} \simeq 2.4\,\mathrm{keV}$ have been predicted. A more detailed discussion about the Europed input values is addressed in section 4.3.5.2.

Inside the top of the pedestal, the turbulent heat and particle transport is calculated by Trapped–Gyro–Landau–Fluid (TGLF) [54, 55, 53, 52], which is a gyrofluid and electromagnetic (EM) quasi–linear model with shaped flux surfaces, or by QuaLiKiz (QLK)[60, 61], which is a gyrokinetic and electrostatic (ES) quasi–linear transport model with circular flux surfaces. A large amount of work has been made in the last decade to validate these models against experimental results. A wide overview on progress in understanding core transport in tokamaks is presented in [84], including examples of validation of quasi–linear (QL) models against present experiments. Some recent TGLF validation carried out for DIII–D and AUG plasma discharges are reported in [85, 86, 87, 88], while recent QLK validation works are presented in [89, 60, 90, 91, 92] for hybrid, baseline, and mixed–isotope JET experiments. Bearing in mind that DTT will operate in a $T_e > T_i$ regime, a particularly relevant validation work is the one presented in [93], with results of both TGLF and QLK modelling of an extensive set of experimental results from AUG and JET–ILW in regimes with high T_e/T_i.
In this work, the the two most recent versions of TGLF have been used: TGLF SAT1–geo, released in November 2019, featuring an improved description of geometrical effects and calibration against CGYRO non–linear simulations and TGLF SAT2, released in January 2021, featuring further im-

provements and better agreement with CGYRO as discussed in [94]. In runs with QLK, a recent release of the model [62] with improved TEM treatment thanks to a revised collision operator has been employed. For QLK, in addition to this new official version, an ad hoc version of this model, where the TEM electron heat flux has been multiplied by a factor 2 to match the gyrokinetic simulations described in sect.4.3.5.4, has also been tested. This ad hoc retuning is physically justified by the fact that the region inside mid–radius in DTT is strongly dominated by TEM, which is challenging for QuaLiKiz. The ad–hoc QuaLiKiz correction is not intended here to be a recommended general prescription, but rather a form of uncertainty quantification by modifying the model to account for known physics deficiencies for this specific case. In all QLK runs, the EM stabilisation mock–up[92] has been turned off because of the $T_e \gg T_i$ regime of DTT scenarios, which is outside the regime where the mock–up was developed. For reasons of numerical stability, a small fraction (3 %) of Bohm transport is added to the main turbulent transport.0
For electron heat transport, which has negligible neoclassical component, an additional diffusivity $\chi = 0.5\,\mathrm{m}^2/\mathrm{s}$ has been added in the region $\rho_{\mathrm{tor}} < 0.2$, where the turbulence level tends to vanish.
In order to set–up the runs in a faster way, simulations with the QLK Neural Network (QLKNN)[63] model have been also carried out, applying the QLKNN–hyper–10D version. This work has been also useful to test the proper functioning of QLKNN in the DTT regime conditions.
The neoclassical transport is calculated by the Romanelli–Ottaviani model[95] for impurities and NCLASS[96] for main particles.
The toroidal rotation is predicted using a theory–driven empirical model[97, 98], in which the inward momentum pinch is included in the simulation thanks to the construction of a pinch number RV_φ/χ_φ that has the trend $RV_\varphi/\chi_i \propto -\sqrt{r/R}$ given by [97], is null at the plasma centre, and is ~ 2.5 at $\rho_{\mathrm{tor}} = 0.4$. The choice of those conditions is based on an analysis of some plasma parameters and the experimental pinch number dependence on those parameters found out in [98]. The Prandtl number χ_φ/χ_i is fixed at 0.7, i.e. in the place of a calculated momentum transport coefficient χ_φ the product $0.7\chi_i$ is used, where χ_i is the ion thermal transport coefficient. The choice of 0.7 accounts empirically also for the component of residual stress due to $E \times B$ shearing, which lowers the nominal Prandtl number. The rotation pedestal has been arbitrarily assumed 10 krad/s taking from present devices, in any case we note that the simulation is mainly influenced by the rotation gradient, not by its absolute value.

Heating and current drive are modelled self–consistently in JINTRAC runs with suitable codes, as described in 4.3.4. The particle source from NBI

is also calculated, whilst the edge neutral penetration is negligible inside $\rho_{\text{tor}} = 0.94$.

In our integrated modelling, argon (Ar, $A \simeq 40$, $Z = 18$) and tungsten (W, $A \simeq 184$, $Z = 74$) are included as impurities. argon is a seeding gas used to enlarge the edge radiative dissipation decreasing the divertor power load, while tungsten comes from the divertor.
In JINTRAC runs, impurity densities and radiation are simulated up to the separatrix with SANCO[75]. For both gases, all ionisation states are treated separately by SANCO. In order to conserve the particle number equal to the initial value, escape velocity, neutral influx and recycling factor are set null. A radially constant effective charge equal to $Z_{\text{eff}} = \sum_i Z_i^2 n_i / n_e = 1.7$ (sum over ion species) and a density ratio $n_W / n_{Ar} = 0.05$ are used as initial conditions.

Evaluating the neutron rate is a key point in the tokamak design, because the neutron shields have to be able to withstand the neutron loads. In the JINTRAC simulations, the total neutron number is calculated as sum of neutrons produced by the fusion reactions between two thermal nuclei, between a thermal nucleus and a fast nucleus of the NBI beam, and between a thermal nucleus and a fast nucleus of the ICRH minority species.

Sawteeth and ELMs are not included in the modelling, with the exception of the simulations described in section 4.3.5.3 where a continuous model for ELMs has been used. The absence of sawteeth implies that the profiles presented here would correspond to the saturated recovery after a sawtooth crash.

4.3.2 JINTRAC & ASTRA

The DTT simulations have mainly been carried out with the JINTRAC suite with the JETTO[99] transport solver. The JINTRAC system includes several interfaced tokamak–physics codes (~ 25 modules) and has been used extensively for decades on experimental data of different tokamaks and to predict future devices. The 1.5 D core plasma fluid code JETTO is the central part of JINTRAC, designed to calculate plasma profiles up to the separatrix. The JINTRAC suite has been used for full physics simulations of DTT using QLK or QLKNN, predicting current density and equilibrium, temperatures, densities (main ion and impurities), rotation, and heating, as described in section 5.2.1.

In addition, the ASTRA transport solver has also been used, within an iterative ASTRA–JINTRAC scheme devised for some high complexity cases with TGLF as turbulent transport model, due to the low speed of JINTRAC TGLF runs with DTT parameters. The starting point of this mixed method

is running a JETTO simulation with QLK and use the resulting profiles as inputs for ASTRA. Then, an ASTRA run predicts temperatures and density with fixed current density, heating, toroidal rotation, impurities, and radiative power, taken from JINTRAC. In this run, the equilibrium is solved self–consistently by the SPIDER[68] code. Impurities are included but not evolved in ASTRA; their profiles are set proportional to the electron density n_e with a constant that reflects the JINTRAC settings. The impurity ionisation profiles are the ones provided by JINTRAC. As third step, the ASTRA profiles of density and temperatures are kept fixed in a new JETTO run aimed at recalculating heating and safety factor profiles. The second and the third phases are repeated until convergence.
This mixed ASTRA–JINTRAC approach is quite efficient, because ASTRA TGLF simulations are much faster than JETTO TGLF runs and one iteration usually is enough.

4.3.3 Equilibrium

The expected standard operational points of DTT (with $R_0 = 2.14\,\mathrm{m}$) in terms of on–axis toroidal magnetic field B_{tor} and plasma current I_{pl} are the following:

- full current and full field operational point, with $I_{\mathrm{pl}} = 5.5\,\mathrm{MA}$ and $B_{\mathrm{tor}} = 6\,\mathrm{T}$;
- reduced current and full field operational point, with $I_{\mathrm{pl}} = 4.0\,\mathrm{MA}$ and $B_{\mathrm{tor}} = 6\,\mathrm{T}$;
- reduced current and half field operational point, with $I_{\mathrm{pl}} = 2.0\,\mathrm{MA}$ and $B_{\mathrm{tor}} = 3\,\mathrm{T}$.

For these simulations, reference DTT plasma equilibria with average triangularity $\langle\delta\rangle \simeq 0.3$, major radius $R_0 = 2.14\,\mathrm{m}$, and minor radius $a = 0.65\,\mathrm{m}$ for each of these standard operational points have been provided by the free boundary CREATE–NL[100] solver.

In the JETTO simulations, the MHD equilibrium is self–consistently recalculated 3 times per second by the equilibrium solver ESCO integrated in the suite. The plasma boundary is kept fixed to the CREATE–NL reference one. The plasma shape of the SN DTT scenario at the full current and full field operational point is shown in figure 4.2.
At the flux surface that contains the 95 % of the poloidal flux, performed simulations of DTT full power scenarios returned triangularity values in the range $\delta_{95} = 0.29$–0.31, elongation values in the range $k_{95} = 1.66$–1.69, and safety factor values in the range $q_{95} = 2.6$–2.7.

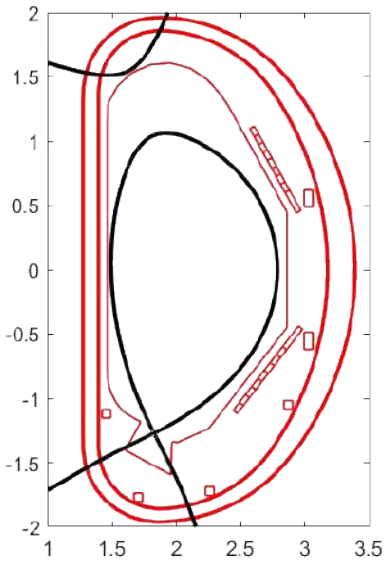

Figure 4.2: Separatrix shape of the SN DTT scenario (wtih $R_0 = 2.14\,\mathrm{m}$).

4.3.4 Heating and Current Drive (HCD)

Since DTT will be equipped with three auxiliary heating systems, the integrated simulations of this device feature high complexity level. The ECRH, ICRH, and NBI power depositions are computed several times during the runs, including the synergy effects.

In the heating configuration of full power option D, which has become the new reference option for the full power scenario, there are 4 ECRH clusters. Each cluster is composed of 8 gyrotrons at 170 GHz, with an installed power of 1–1.2 MW from each gyrotron. Depending on the access port, these 8 gyrotrons are divided into 2 upper (UP) gyrotrons, 3 equatorial top (EQT) gyrotrons, and 3 equatorial bottom (EQB) gyrotrons. A loss factor before launchers of 0.9 is evaluated, leading the ECRH power at plasma to around 30.2 MW.

The ICRH system of DTT is designed to operate in the frequency range 60–90 MHz. In the reference $B_{\mathrm{tor}} = 6\,\mathrm{T}$ scenario, the cyclotron resonances of ^{3}He and H minorities are located on–axis when the ICRH frequency is 60 MHz or 90 MHz respectively. The system is devised in modular units, placed in equatorial ports, and each module is based on a pair of 2–strap antennas. In order to better cope with abrupt coupling changes because of L–H transitions or ELMs, the 2 antennas of a module are fed in parallel. Since the power supplied by each RF antenna is 2 MW, supposing an efficiency of 0.75 (typical

efficiencies for transmission lines and antenna coupling are 80 % and 90 %), the ICRH coupled power is ~ 1.5 MW per antenna. The installation of the first RF module is scheduled for the initial phase. Depending on the full power option choice, an upgrade with one or two modules more may be realised. Particularly, the full power option D heating configuration includes two ICRH modules.

Due to the high DTT densities, to allow a central NBI power deposition during the flat–top plasma discharge phase, a negative ion–based NBI system at high energies $E > 300$ keV must be used in DTT. During early current ramp–up, late current ramp–down, and low current scenarios the employment of the NBI system must be cautiously evaluated, in order to avoid shine–through risks. Moreover, an important feature of the NBI system is its current drive capability and central fuelling. The full power option D heating configuration includes only 1 NBI injector, which provides ~ 10.0 MW of power to the plasma, with a 500 keV deuterium beam. In the day–1 scenario, this injector will be used at reduced energy (~ 400 keV) supplying a NBI power amount ≤ 7.5 MW to the plasma.

The RF antenna, NBI injectors, and ECRH gyrotrons have been configured within the JINTRAC suite.

The ECRH power deposition is calculated every 0.25 s by the GRAY code[72]. Since DTT gyrotrons are too numerous to be included separately in GRAY (the maximum number is 20), they have been grouped in subsets. In the full power option D run, 12 beams are used (2 UP beams, 5 EQT beams, and 5 EQB beams). Each beam is simulated by the sum of one central ray and 160 rays arranged on 10 concentric rings and has a toroidal angle equal to 2°. In simulations of full power and day–1 scenarios all beams are injected in O–mode. Due to the lower magnetic field value, in the day–0 scenario the EC power is expected to be absorbed at second harmonic. Since the O–mode polarisation is known to be less efficient at second harmonic, the ECRH system will be used in X–mode for the day–0 case to maximise the absorption. The poloidal angles have been set in the following ranges: $43° - 44°$ for UP beams, $2° - 6°$ for EQT beams, and (-13°)−(-15°) for EQB beams.

The NBI power deposition is calculated by the PENCIL code[73]. Since the DTT NBI source is composed by negative ions, all beam particles are injected at the nominal energy. Hence, in PENCIL the full energy fraction has been set equal to 1. The total loss of NBI fast particles, considering both prompt and ripple losses, has been assessed at ~ 4 % in [101] and hence has resulted negligible.

The PION[74, 102, 103] code calculates the ICRH power deposition, including the synergy effects with NBI. In the performed simulations Hydrogen

has always been used as minority species with a concentration of 5 % and the RF frequency has been set to 90 MHz. So, the cyclotron resonance is located where the magnetic field is equal to $B \simeq 5.9\,\mathrm{T}$, i.e. at $\rho_{\mathrm{tor}} \sim 0.15$.

4.3.5 Full Power Option D scenario

The so–called option D has been selected as the new reference configuration for the Full Power (FP) scenario. In this configuration, auxiliary heating systems deliver a total power of $\sim 46\,\mathrm{MW}$ to the plasma: $\sim 10.0\,\mathrm{MW}$ from the NBI system, $\sim 6.0\,\mathrm{MW}$ from the ICRH system, and $\sim 30.2\,\mathrm{MW}$ from the ECRH system.

4.3.5.1 Runs with QLK or TGLF of full power option D scenario

The integrated modelling of a steady–state deuterium plasma in the FP option D scenario has been performed using both the standard QLK model and an ad hoc QLK version in a JETTO run and the TGLF SAT1–geo or SAT2 model with the JINTRAC–ASTRA approach.
The electron temperature T_e, ion temperature T_i, electron density n_e, toroidal rotation ω_{tor}, and safety factor q radial profiles obtained by these four runs are shown in figure 4.3. The radial profiles of all power densities and those of the total electron and ion powers are displayed in figure 4.4 (a) and 4.4 (b) respectively, only for the standard QLK simulation. The power density and total power profiles resulting from the other three runs are similar in shape and size. The current density radial profile and its main contribution are shown in figure 4.5.
From figure 4.3, we notice that the profiles of T_e and T_i reach maximum values in the range of 18.0–21.6 keV and in the range of 9.1–10.4 keV respectively. There is a good agreement between TGLF and QLK temperature profiles, which are a bit smaller in the TGLF SAT1–geo run, up to differences of the order of ∼15–20 % at the plasma centre, because of a slight difference in the temperature gradient in the region $0.65 \lesssim \rho_{\mathrm{tor}} \leq 0.94$. Electron densities of the two models present a good agreement for $\rho_{\mathrm{tor}} \gtrsim 0.5$, but a non–negligible discrepancy appears inside. Particularly, n_e has a moderately peaked profile in the TGLF simulation, while the QLK density profile is extremely flat in the inner half of the plasma. Due to a quite different n_e gradient in $0.2 \lesssim \rho_{\mathrm{tor}} \lesssim 0.5$, the maximum n_e value sweeps from $2.0 \times 10^{20}\,\mathrm{m}^{-3}$ to $2.6 \times 10^{20}\,\mathrm{m}^{-3}$.
In order to identify the most reliable prediction and to explain the difference of density peaking between TGLF and QLK, a benchmark work of the two quasi–linear models against the gyrokinetic model GENE[42, 43] in the

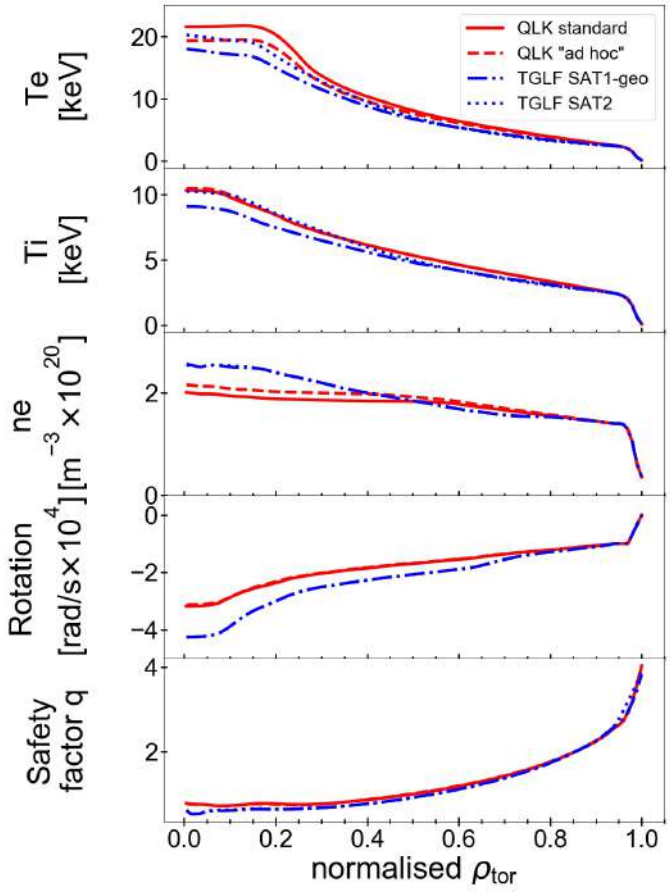

Figure 4.3: Steady–state radial profiles of the electron and ion temperatures, electron density, toroidal rotation, and safety factor of the FP option D scenario, with turbulent transport calculated by TGLF SAT1–geo (blue dash–dot line) or SAT2 (blue dotted line) or by standard QLK (red solid line) or ad hoc QLK with TEM electron heat flux multiplied by a factor 2 (red dashed line).

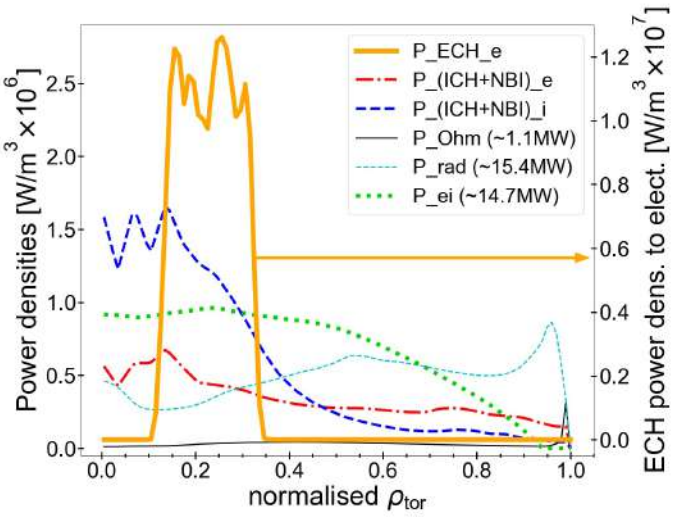

(a) Power densities.

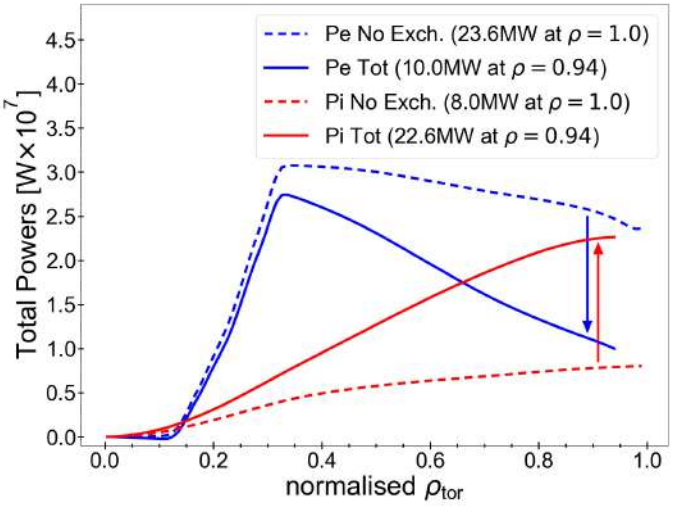

(b) Volume integrated powers.

Figure 4.4: (a) Radial profiles of power densities: ECRH power deposited to electrons $P_{\mathrm{ECH}\,e}$, NBI and ICRH power deposited to electrons $P_{(\mathrm{ICH+NBI})\,e}$, NBI and ICRH power deposited to ions $P_{(\mathrm{ICH+NBI})\,i}$, Ohmic power P_{Ohm}, radiative power P_{rad}, and thermal exchange power between electrons and ions P_{ei}. (b) Radial profiles of electron and ion total powers including or not including the thermal exchange power between species.

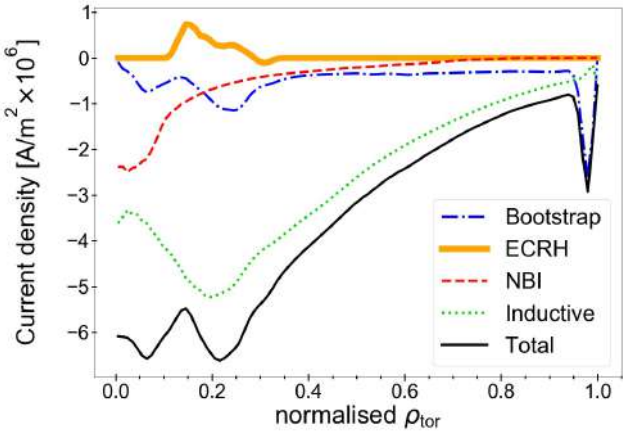

Figure 4.5: Radial profiles of the total current density and of its main contributions.

DTT parameter range has been performed and its results are displayed in section 4.3.5.4.

Comparing the modelling results between the standard QLK version and the QLK version with $2 \times q_{e,\mathrm{TEM}}$, we noticed that the "ad hoc" model introduced small variations in the right direction. Particularly, the density peaking is a bit increased (closer to the TGLF one) in the "ad hoc" QLK density profiles. Nevertheless, these improvements are too small to justify the employment of this QLK version in further simulations.

With both QLK and TGLF models, it turns out that DTT is characterised by T_e significantly larger than T_i, particularly in the inner half of the plasma. This is due to the very large and localised ECH power density ($P_{\mathrm{ECH}\,e} \sim 1.1 \times 10^7\,\mathrm{W/m^3}$), and to the fact that T_e/T_i is a key factor determining the ion critical gradient $(R/L_T)_{\mathrm{crit}}$ [28, 29], lowering it for increasing T_e/T_i. The low ITG threshold in presence of a high ion stiffness then prevents T_i from peaking. This behaviour is in line with several observations in nowadays tokamaks or stellarators with high electron heating, see for example the recent work in [104]. Instead T_e is largely determined by TEMs, which exhibit much lower stiffness and typically higher $\left(R/L_{T_e}\right)$ thresholds, so that a higher T_e peaking can be reached. The ITG modes and TEMs are dominant in these plasmas, while ETG modes[33], which are included in the integrated simulations, do not play an important role, due to the high T_e/T_i. The ETG unimportance resulted evident from both stand–alone runs and profile simulations performed with TGLF and with QLK with/without ETG inclusion. Moreover, the linear gyrokinetic runs carried out with GENE also

confirmed the lack of the ETG contribution.
Locally, in the DTT FP scenario, electron heating dominates in the inner plasma region, as evidenced by figure 4.4(b). Since the ion channel is very stiff and bound to a low critical gradient due to $T_e/T_i > 1$, ions represent a big power sink through collisional exchange. The ion temperature profile results stuck near the threshold irrespective of the large amount of supplied power.
Globally, the core radiated power $P_{\mathrm{rad}} \approx 15.4$–$17.8\,\mathrm{MW}$ is about the 35 % of the total power, the Ohmic power $P_{\mathrm{Ohm}} \approx 1.1\,\mathrm{MW}$ is quite negligible, and a large amount of power ($13.7\,\mathrm{MW} \lesssim P_{ei} \lesssim 14.7\,\mathrm{MW}$) is exchanged from electrons to ions because of the collisional coupling. Therefore, although the external electron power $P_{e\,\mathrm{ext}} \approx 38\,\mathrm{MW}$ is much bigger than the external ion power $P_{i\,\mathrm{ext}} \approx 8\,\mathrm{MW}$, globally the total electron power $P_{e\,\mathrm{tot}} \approx 9.5$–$10.4\,\mathrm{MW}$ is much lower than the total ion one $P_{i\,\mathrm{tot}} \approx 21.8$–$22.6\,\mathrm{MW}$. In DTT, the collisional time is higher than the confinement time, so the collisional exchange is not enough to equilibrate T_e and T_i. As things stand, obtaining an ion temperature profile as high as possible would be beneficial; to achieve this, one would have to find ways of reducing the ion stiffness or increasing the ITG threshold, besides having more central ion power. The choice of the option D as the FP reference scenario has been based on this principle. Particularly, some electromagnetic (EM) stabilisation effects are known to reduce ion stiffness and they can be increased by the presence of fast ions (FI).[105, 106] These considerations have led to the choice of increasing the ICRH power to the maximum technically feasible and increase the NBI energy with respect to the original proposal described in [8].

From figure 4.3, we also note that the safety factor value at the flux surface that contains the 95 % of the poloidal flux is quite low $q_{95} \approx 2.5$–2.6. An increased disruptivity is observed in plasma with such low q_{95}, e.g. [107]. As a consequence, the DTT team decided to enlarge the DTT major radius from $R_0 = 2.14\,\mathrm{m}$ to $R_0 = 2.19\,\mathrm{m}$ and its minor radius from $a = 0.65\,\mathrm{m}$ to $a = 0.70\,\mathrm{m}$, to bring q_{95} nearer to 3.

Within the JINTRAC runs, the contribution of impurities is calculated by SANCO, using neoclassical transport and turbulent transport from QLK. In figure 4.6, the density profiles of impurities and the profile of the effective charge Z_{eff} are displayed for the QLK case with solid lines. The TGLF simulations in ASTRA do not evolve impurity species, but only take into account their effects assuming the n_e profile shape. Nevertheless, it is interesting to get an idea of which argon and tungsten densities would be computed by QLK for T_e, T_i, and n_e values such as those of the TGLF case. Thus, a JETTO run with interpretative T_e, T_i, and n_D profiles equal to the TGLF SAT1–geo case has been performed, including SANCO calculations for impurity densi-

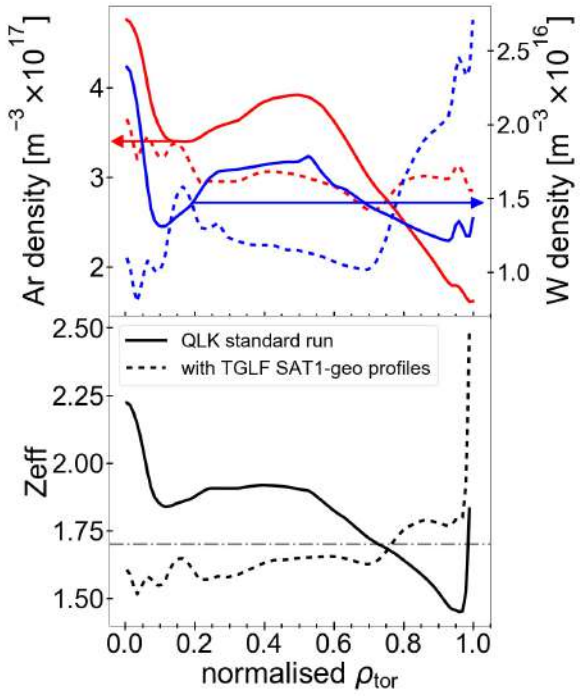

Figure 4.6: Radial profiles of the impurity densities (argon in red, tungsten in blue) and of effective charge Z_{eff}. The standard QLK case results (solid lines) are compared to an assessment of the impurity and Z_{eff} profiles in presence of TGLF SAT1–geo predicted profiles carried out with JETTO/SANCO and QLK (dashed lines).

ties and using QLK as turbulent transport model for the impurities. This allows us to estimate the effect of the TGLF electron density peaking on the impurity profiles, as shown in figure 4.6 with dashed lines.
argon and tungsten densities amount to $n_{\text{Ar}}/n_e \approx 0.28\,\%$ and $n_{\text{W}}/n_e \approx 0.014\,\%$ respectively. We observe some penetration of the impurities into the core with both models.
In future works, other possible seeding gasses will be tested in place of argon to investigate their effect on the edge radiative dissipation.

The largest neutron loads to be coped with obviously occur in the FP scenario. The more challenging prospect in this respect is represented by the TGLF SAT2 FP run, where the maximum value of neutron rate is reached. The total neutron density rate and the radial profiles of its three contributions shown in figure 4.7 refer to the run outcome with TGLF SAT2 profiles. Integrating over all the profile up to the separatrix, the total neutron rate

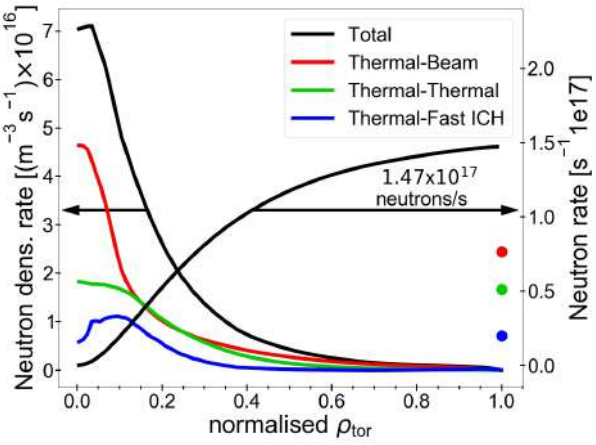

Figure 4.7: Radial profiles of neutron density rates, where neutrons are produced by fusion reactions between: two thermal nuclei (green), between a thermal nucleus and a fast nucleus of the NBI beam (red), and between a thermal nucleus and a fast nucleus of the ICRH minority species (blue), any pair of nuclei (black). The radial profile of the total neutron rate is also displayed (black), with points indicating the three contributions to it. These profiles refer to the TGLF SAT2 FP case.

in this case amounts to 1.47×10^{17} neutrons/s, resulting compatible with the present design of neutron shields with a good safety margin. The neutron density rates obtained from simulations with standard or ad hoc QLK or with TGLF SAT1–geo profiles are a bit lower, but definitely similar in shape, to give total neutron rates in the range of $1.29–1.36 \times 10^{17}$ neutrons/s. In all cases, the largest contribution is given by the fusion reactions between NBI fast deuterium and thermal deuterium, but the thermal–thermal neutrons are also very significant.

In figure 4.8 the density and energy density radial profiles of energetic particles (EP) are shown for the standard QLK run. The EP profiles in the TGLF SAT2, TGLF SAT1–geo, and ad hoc QLK cases present similar shapes. In the FP reference scenario, the energy fraction owned by the EPs amounts to $W_{\mathrm{EP}}/W_{\mathrm{tot}} \approx 6.5–7.7\,\%$.

For the sake of completeness, the table 4.2 presents the main dimensionless physical quantities of this scenario. Particularly, the total radiation from the plasma inside the separatrix can be subtracted or not from the input power when calculating the confinement, yielding the two τ_E values in table.

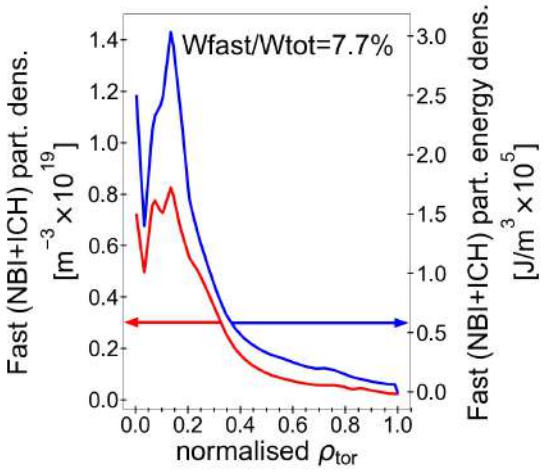

Figure 4.8: Radial profiles of density and energy density of energetic particles due to the both NBI and ICRH systems.

Table 4.2: FP option D scenario dimensionless quantities.

	TGLF SAT1–geo	TGLF SAT2	QLK standard	QLK ad hoc
τ_E $(P = P_{\rm tot})$	0.25	0.27	0.27	0.28
τ_E $(P = P_{\rm sep})$	0.43	0.42	0.41	0.43
H_{98} $(P = P_{\rm sep})$	0.95	1.00	0.99	0.98
$\beta_{\rm N_{therm}}$ [%]	1.39	1.47	1.49	1.51
$\beta_{\rm N_{tot}}$ [%]	1.49	1.57	1.62	1.62
$W_{\rm EP}/W_{\rm tot}$ [%]	6.5	6.7	7.7	6.7
$\langle n_e \rangle / n_G$	0.44	0.44	0.40	0.42

4.3.5.2 Pedestal variations

The core–edge integration is a key point in the DTT integrated modelling work. Since the pedestal points are used as boundary conditions in the JETTO/ASTRA simulations, for the FP scenario we investigated the pedestal height variability depending on the Europed run inputs to examine robustness of the major results of our analysis. Some Europed inputs (such as $I_{\rm pl}$, $B_{\rm tor}$, R_0, ...) are imposed by the selected scenario and by general DTT parameters, therefore we have not performed sensitivity tests on these. We have tested the sensitivity to β vaues in the range $0.4 \lesssim \beta_{\rm pol} \lesssim 0.8$ and verified that the effect is small. Then, the $\beta_{\rm pol}$ value has been selected iteratively to match the JINTRAC predicted value.
It has also been checked that $T^{\rm sep}$ value variations in the range of 100–200 eV did not lead to significant changes in the pedestal values. Substituting argon with an other impurity (for instance with Neon as seeding gas) or varying the $Z_{\rm eff}$ value around the reference value do not impact effectively the pedestal height. All these small $T_e^{\rm ped}$ variations fall back into a typical accuracy of around ±20% of the EPED model when the pedestal is peeling–ballooning limited.[81]

Although modelling the direct effect of the gas on the pedestal is outside the scope of this work, the effect of the gas is expected to increase $n_e^{\rm sep}$ and shift the density position $n_e^{\rm pos}$ outwards, as observed in AUG, JET–ILW, TCV, and DIII–D [108, 82, 109, 110, 111]. Therefore, we have assessed the gas effect on the pedestal by testing the impact of the density position on the predicted $T_e^{\rm ped}$.
A null relative shift ($n_e^{\rm pos} = T_e^{\rm pos}$), is the standard assumption in the basic EPED model and has been used throughout this work. Assuming that the density has the same position as the temperature (corresponding to $n_e^{\rm sep}/n_e^{\rm ped} \approx 0.25$, i.e. to $n_e^{\rm sep} \approx 3.5 \times 10^{19}/{\rm m}^3$), the Europed run predicts $T_e^{\rm ped} \approx 2.2\,{\rm keV}$.

However, relatively recent results shows that typically $n_e^{\rm pos} > T_e^{\rm pos}$, with values of the shift higher than $\approx 0.002\psi_N$.[82, 108] The possible effect of $n_e^{\rm pos} > T_e^{\rm pos}$ has been tested, as displayed in figure 4.9.

By increasing the relative shift, $T_e^{\rm ped}$ decreases till a saturation is reached above the relative shift $\approx 0.01\psi_N$ (corresponding to $n_e^{\rm sep}/n_e^{\rm ped} \approx 0.5$, i.e. to $n_e^{\rm sep} \approx 7 \times 10^{19}/{\rm m}^3$). The saturation is related to the effect of the density position on the pressure position, as discussed in [83]. In DTT $n_e^{\rm sep}/n_e^{\rm ped} \lesssim 0.5$ is expected, and in the main simulations of this work $n_e^{\rm sep}/n_e^{\rm ped} \approx 0.2 - 0.3$. With this value, the EPED model is rather accurate (within 20 %). The most recent results obtained in JET show that the shortfall compared to EPED occurs at relatively high separatrix density (approximately $n_e^{\rm sep}/n_e^{\rm ped} > 0.5$,

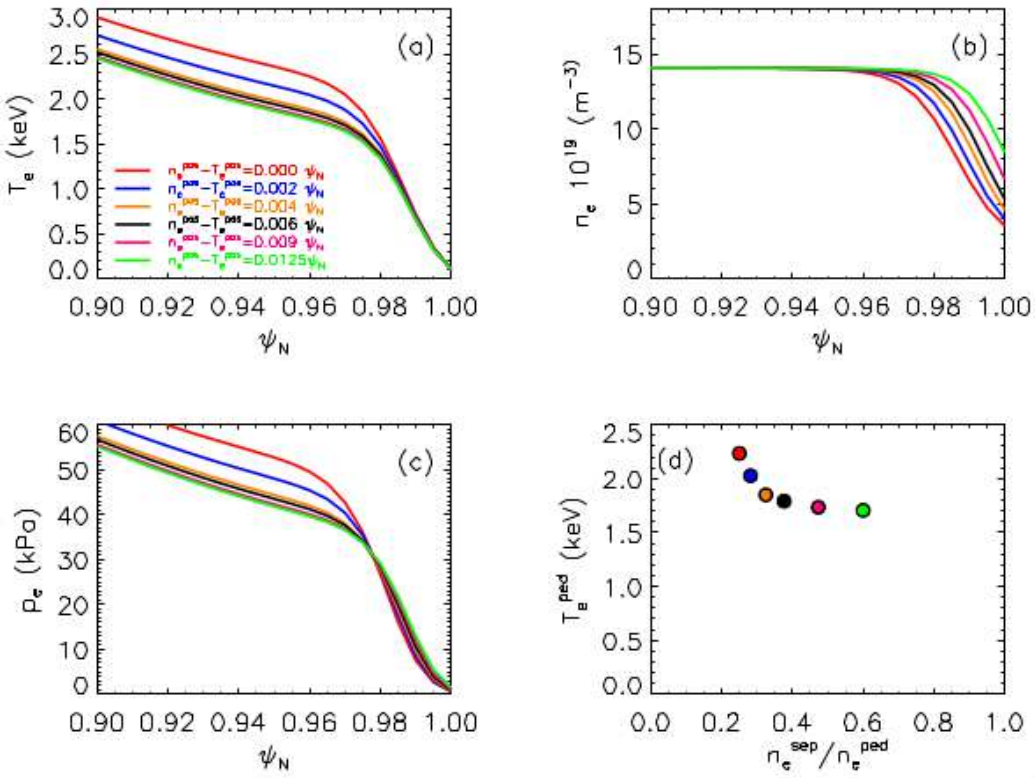

Figure 4.9: Profiles of (a) electron temperature, (b) density, and (c) pressure in the pedestal region for different values of relative shift $(n^{\mathrm{pos}} - T^{\mathrm{pos}})\,(\psi_N)$. (d) Electron temperature at the pedestal top T_e^{ped} as a function of $n_e^{\mathrm{sep}}/n_e^{\mathrm{ped}}$.

with significant discrepancies that occur above 0.6).[112] Nonetheless, to test the effect of possible higher $n_e^{\mathrm{sep}}/n_e^{\mathrm{ped}}$ an Europed simulation has been done also at $n_e^{\mathrm{sep}}/n_e^{\mathrm{ped}} \approx 0.5 - 0.6$. This value is expected to be already relative high for DTT, however not high enough to lead to major problems with the reliability of the EPED predictions.[112] Above $n_e^{\mathrm{sep}}/n_e^{\mathrm{ped}} \approx 0.5-0.6$, there is presently no model to assess reliably the effect of the gas rate on the pedestal. The minimum temperature reached with the highest relative shift of $0.0125\psi_N$ (with $n_e^{\mathrm{sep}} \approx 8 \times 10^{19}\,/\mathrm{m}^3$, i.e. with $n_e^{\mathrm{sep}}/n_e^{\mathrm{ped}} \approx 0.6$) is $T_e^{\mathrm{ped}} \approx 1.7\,\mathrm{keV}$, so approximately 500 eV lower than the reference case.

In order to test the effects of the pedestal variations due to different relative shift values on plasma profiles, we repeated the standard QLK run of the FP reference scenario (with null relative shift) but setting the pedestal points calculated by EPED with a relative shift of $0.0125\psi_N$. Temperature and density radial profiles of these two simulations are compared in figure 4.10. We observe that the temperature value reduction at the top of the pedestal prop-

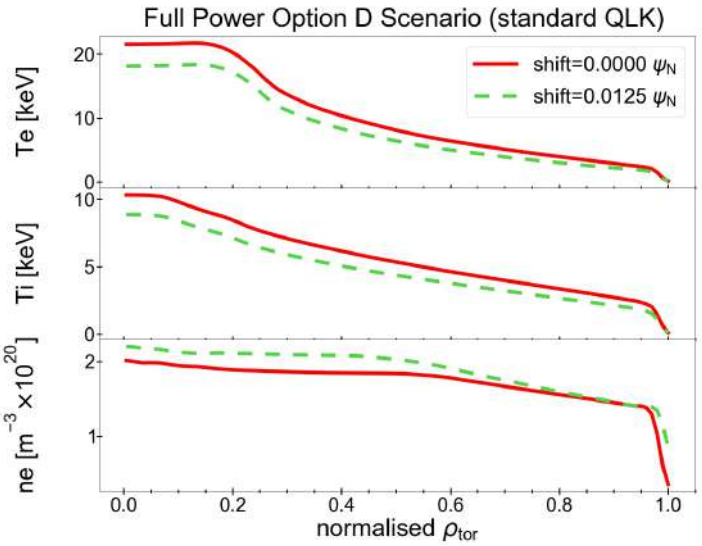

Figure 4.10: Radial profiles of electron temperature, ion temperature, and electron density predicted by JETTO runs using the standard QLK model for different values of relative shift (the red lines correspond to a null shift, while the green lines correspond to a shift of $0.0125\psi_N$).

agates inwards up to the plasma centre, but it is more interesting to notice the increased density peaking as a consequence of a non–null pedestal relative shift.

Overall however the scenario predictions are not significantly affected.

4.3.5.3 Fuelling issues

In order to evaluate whether the predicted density profiles can be sustained by only gas puff or a pellet fuelling system is required, the level of edge neutrals required to operate in the FP option D scenario without pellets has been investigated.
The standard QLK run of section 4.3.5.1 has been extended up to the separatrix by replacing the fixed pedestal externally calculated by Europed with results of a suitable Edge Transport Barrier (ETB) tuned to reproduce the Europed pedestal.

To calculate the neutral source, the FRANTIC[113] code has been included in the simulation, setting a feedback control of gas puffing to reach the electron density value expected at the TOB (Top Of Barrier) with null recycling. The ETB transport coefficients are arranged to obtain the temperature at the top of the pedestal as close as possible to the Europed values,

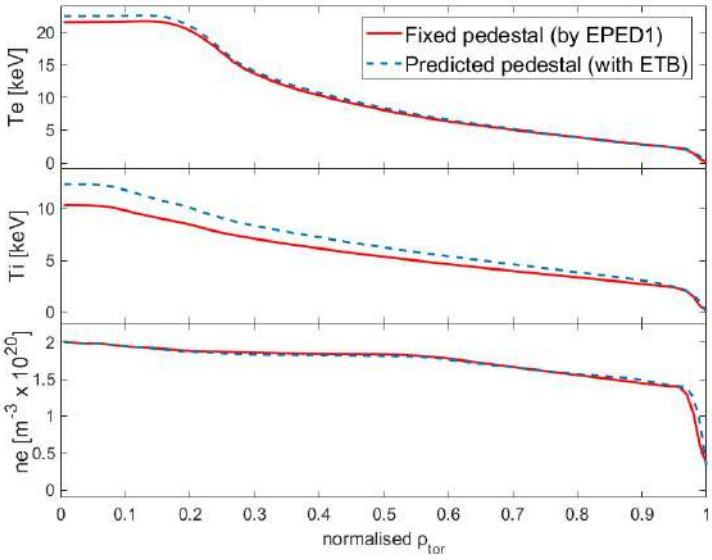

(a) Whole radial profiles.

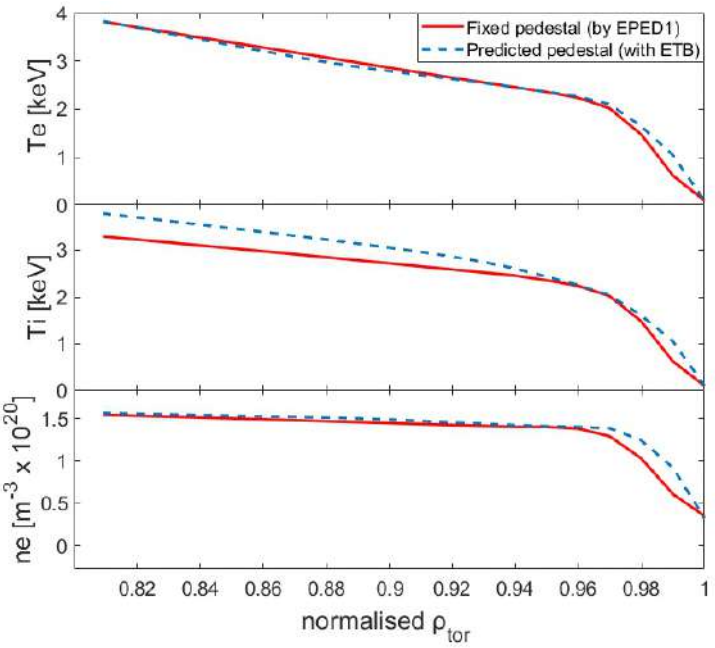

(b) Profile zoom in the pedestal region.

Figure 4.11: Comparison of T_e, T_i, and n_e radial profiles between the standard QLK case with fixed pedestal of section 4.3.5.1 (solid red lines) and the new standard QLK case with the moulded ETB (dashed blue lines).

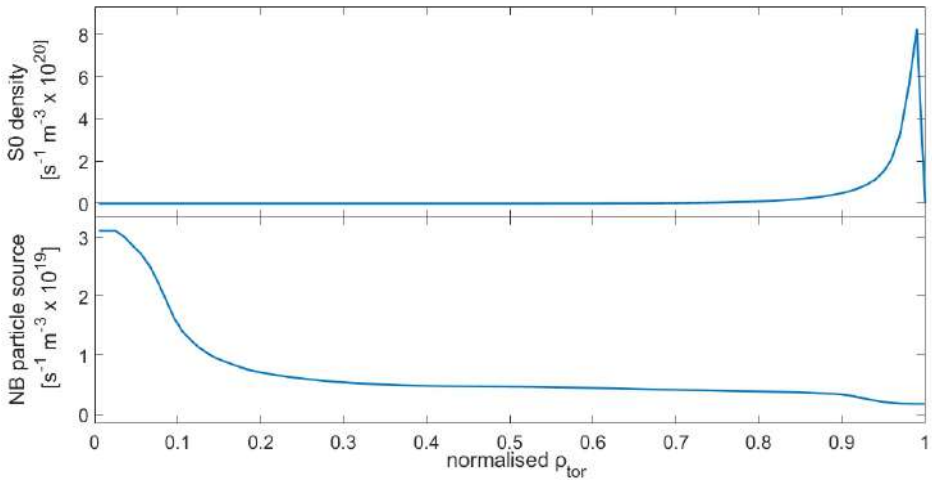

Figure 4.12: Radial profile of the source of neutrals from the edge and radial profile of the NBI particle source.

thanks to a continuous ELM model. In figure 4.11, the T_e, T_i, and n_e radial profiles resulting from this adjustment work are compared to the profiles of the QLK case with fixed pedestal to show the good agreement between them.

The neutral penetration into the plasma evaluated by FRANTIC is adequate for fuelling, since the neutral density rate is up to $\rho_{\text{tor}} \sim 0.8$, as displayed in figure 4.12. The NBI contribution to the neutral source is small. To reach the density value at the TOB which allows to have $\langle n_e \rangle \sim 0.4\, n_G$ in the FP reference scenario, a neutral flux level of about 0.36×10^{22} particles/s at the separatrix is required.
The dependence of neutral penetration across the separatrix as a function of deuterium fuelling was found starting from results obtained in [114] with the edge code SOLEDGE2D–EIRENE[115, 116]. A scan on fuelling was performed starting from a detached case. Results are shown in figure 4.13; particularly, $\sim 5 \times 10^{22}$ particles/s is the deuterium fuelling corresponding to the required neutral flux at the separatrix. This entails that we should need a gas puffing and pumping system capable of supplying and pumping at least $\sim 5 \times 10^{22}$ particles/s, which is near to the feasibility limit.
Due to this marginality, and in order to avoid degrading the edge plasma with extremely high pas puff rates, a pellet injection system is deemed useful as a fuelling method in DTT to minimise the operational risk.

A modelling work of pellets is just started. In addition, a work of core–pedestal–SOL integrated modelling, totally self–consistent in terms of temperature and density profiles, fluxes, and transport coefficients, is envisaged as future development.

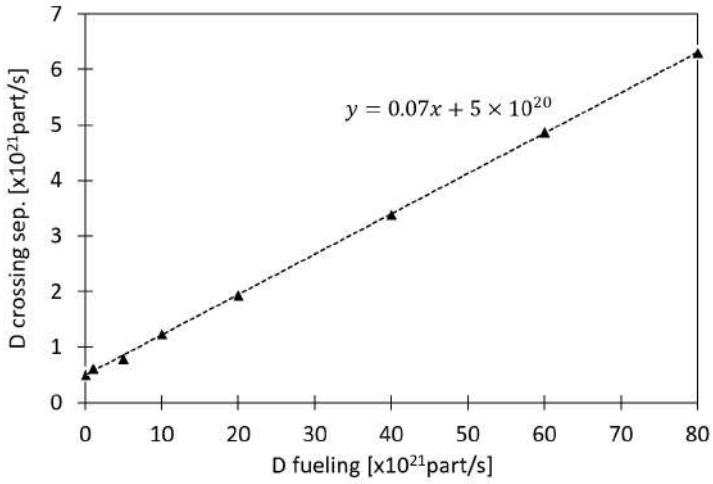

Figure 4.13: Dependence of neutral penetration across the separatrix on deuterium fuelling as derived from SOLEDGE2D–EIRENE simulations.

4.3.5.4 Gyrokinetic simulations to validate QLK and TGLF for DTT full power parameters

Linear and nonlinear gyrokinetic simulations have been performed at the fixed radius $\rho_{\rm tor} = 0.32$, using the flux–tube (radially local) version of the GENE code, in order to characterise the turbulence, compute the particle and heat fluxes and estimate the density peaking, testing the results of the ASTRA–TGLF and JINTRAC–QuaLiKiz predictive runs. This analysis has been carried out with the main goal of understanding which of the two transport simulations gives the more reliable estimate of the density peaking, since they give different results.
The parameters from the end of the ASTRA–TGLF run have been used as GENE inputs. A detailed analysis of this case has been performed, and some parameters have been also replaced with the corresponding ones from the end of the JINTRAC–QuaLiKiz simulation, to investigate their impact on the results. The main simulation parameters (from ASTRA–TGLF) are summarised in table 4.3.

Argon and tungsten impurities with effective charge $Z_{\rm eff} = 1.65$ have been accounted for as kinetic species in the simulations when not differently stated. The normalised radial logarithmic gradients of the f profiles ($f = n, T$) are here defined as $R/L_f = -R\,{\rm d}\ln f/{\rm d}r$, where R and r are the plasma major and minor radii at the selected magnetic surface, respectively. The other parameters are the ion/electron temperature ratio T_i/T_e, the impurity density fractions $n_{\rm imp}/n_e$ (normalised with the electron density), the safety factor q,

Table 4.3: Reference parameters from the end of the ASTRA–TGLF simulation, at the radius of analysis $\rho_{\rm tor} = 0.32$, used as GENE inputs.

R/L_n	R/L_{T_e}	R/L_{T_i}	T_i/T_e	$n_{\rm Ar}/n_e$	$n_{\rm W}/n_e$
2.99	7.8	3.93	0.59	1.5×10^{-3}	7.5×10^{-5}
q	$\hat{s}$	κ	δ	ν_c	β_e
0.76	0.31	1.38	4.9×10^{-2}	5.23×10^{-5}	2.75×10^{-2}

the magnetic shear $\hat{s} = (r/q)\mathrm{d}q/\mathrm{d}r$, the elongation κ, the triangularity δ, the GENE collision parameter $\nu_c = 2.3031 \times 10^{-5} \ln\Lambda \; R[\mathrm{m}] n_e[10^{19}\mathrm{m}^{-3}]/T_e[\mathrm{keV}]^2$, where $\ln\Lambda = 24 - \ln\left(\sqrt{10^{13} n_e[10^{19}\mathrm{m}^{-3}]}/10^3 \, T_e[\mathrm{keV}]\right)$ is the Coulomb logarithm, the ratio of the electron plasma pressure to the magnetic pressure $\beta_e = 2\mu_0 n_e T_e / B_0$, with μ_0 the vacuum permeability and $B_0 = 5.9$ T the vacuum magnetic field on the magnetic axis. All the simulations are run with collisions, using a Landau operator. Since the electron–ion collision rate depends on n_i, which changes depending on the number of considered species (n_i is adapted using quasi–neutrality), the electron–ion thermal collision rate varies depending on the number of considered species and it can be easily evaluated for each case as $\nu_{ei} = 4(n_i/n_e)\sqrt{T_e/m_e}\nu_c/R$.
In the ASTRA–TGLF run the impurities have not been predicted, therefore their density profiles are set proportional to the electron (ion) one. A realistic geometry has been considered, with magnetic equilibrium obtained with the EFIT solver [117, 118], then approximated with a Miller analytic model [119]. Fast ions have been neglected due to their small density fraction $n_{\rm FI}/n_e \sim 2\%$ at the radius of analysis, but their potential effect on the transport should be investigated in the future. Finally, the effect of the $E \times B$ rotation shear has been neglected ($\gamma_E = -(r/q)(\mathrm{d}\Omega_{\rm tor}/\mathrm{d}r)R/c_s = -0.03$, where $\Omega_{\rm tor}$ is the toroidal angular velocity and $c_s \equiv \sqrt{T_e/m_i}$ the ion sound speed), since its effect has been found to be negligible by performing a nonlinear GENE simulation at reference parameters.

To start, the linear k_y spectra of the growth rate γ and angular frequency ω corresponding to the first two most unstable modes have been computed with the GENE eigenvalue solver for reference parameters from the ASTRA–TGLF simulation at $\rho_{\rm tor} = 0.32$, in order to characterise the turbulence regime. The results are collected in figure 4.14.

The growth rate γ (a) and the angular frequency ω (b) are shown versus k_y, comparing simulations where the impurities have been neglected (black squares) with the ones where they have been taken into account (red trian-

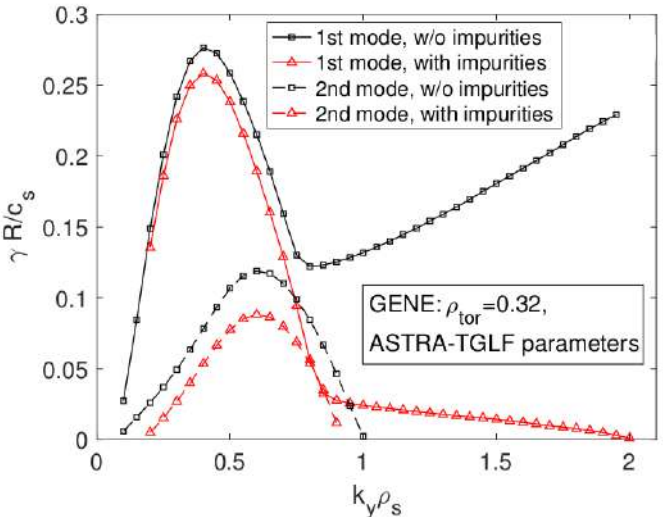

(a) Growth rate γ.

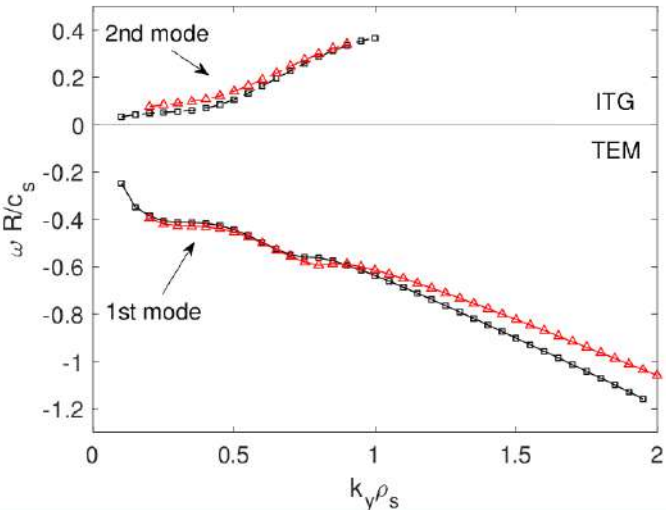

(b) Angular frequency ω.

Figure 4.14: The k_y spectra of the growth rate γ (a) and angular frequency ω (b) of the most unstable linear mode (solid) and of the second unstable linear mode (dashed), neglecting (black) or taking into account (red) the impurities, for ASTRA–TGLF parameters at $\rho_{\rm tor} = 0.32$. Both γ and ω are normalised with c_s/R, while k_y is normalised with $1/\rho_s$.

gles). The growth rate γ and the angular frequency ω are normalised with c_s/R, while k_y is normalised with $1/\rho_s$, where $\rho_s = c_s/\Omega_i$ is the sound Larmor radius, with Ω_i the ion cyclotron frequency. The dominant mode is a Trapped Electron Mode (TEM) at all the wavenumbers, while the second unstable mode is an Ion Temperature Gradient (ITG) mode, corresponding to $\omega < 0$ and $\omega > 0$ respectively, according to GENE conventions. The sub–dominant ITGs are peaked at a larger wavenumber ($k_{y,\text{ITG peak}}\ \rho_s \sim 0.6$) compared to the dominant TEMs ($k_{y,\text{TEM peak}}\ \rho_s \sim 0.4$). As a consequence the ITGs are even more non–linearly sub–dominant, since smaller wavenumbers most contribute to the NL fluxes. Micro Tearing Modes (MTM) are found with the GENE initial value solver for $k_y\rho_s \leq 0.1$, which are destabilised by the finite β_e (they are identified as MTMs looking at the ballooning structures of the electrostatic potential fluctuation $\delta\varphi$ and of the parallel vector potential fluctuation $\delta A_\parallel$). However, they correspond to small growth rates and do not impact the nonlinear (NL) fluxes at reference parameters. Finally, the impurities have a small stabilising effect on the smaller k_y TEM branch, a moderate effect on the subdominant ITGs, while they considerably stabilise TEMs at $k_y\rho_s > 0.8$, as seen comparing the red and black curves in figure 4.15(a).

As a second step, a QL evaluation of the electron particle flux Γ_e spectrum dependence on R/L_n has been pursued using a simple ES "mixing length" model based on GENE linear simulations, following [120, 121]. For each k_y, the QL fluxes are evaluated as $F^{QL} = A_0 \sum_{k_y} w^{QL}(k_y) F^L_{\text{norm}}(k_y)$, where A_0 is a scaling factor associated to the absolute fluctuation amplitude, which is the same for different fluxes $F = \Gamma_e, q_e, q_i$ and cancels out when computing flux ratios, $F^L_{\text{norm}}(k_y)$ represents a properly normalised spectral contribution to the flux which is evaluated with the fields from the corresponding linear eigenmode, and the QL saturation prescriptions $w^{QL}(k_y) = (\gamma/\langle k^2_\perp\rangle)^\xi$ specify the k_y dependence of the relative saturation amplitude levels of the NL electrostatic potential φ. Here $\langle k^2_\perp\rangle$ indicates the flux–surface average of the squared perpendicular wave number, weighted with the $|\varphi|^2$ ballooning structure, considering only $k_x = -\Delta k_x, 0, \Delta k_x$ ($\Delta k_x = 2\pi/L_x$, with L_x the x box size) following [122], and setting $\xi = 2$ (this, a posteriori, gives the best QL–NL spectra agreement). The QL results are summarised in figure 4.15.

Figure 4.15(a) shows the Γ_e spectrum, normalised with the total (summed over k_y) value of $(q_e + q_i)/T_e$, in the $(k_y\rho_s, R/L_n)$ plane.
The "zero–particle–flux" condition $\Gamma_e = 0$ (green line), which is very close to the actual $\Gamma_e = \Gamma_{e,\text{ref.}}$ from ASTRA–TGLF inputs ($\Gamma_{e,\text{ref.}} \sim 1.01\times10^{18}\text{s}^{-1}\text{m}^{-2}$ at the radius of analysis, therefore it is almost negligible), is satisfied for $R/L_n \sim 1.8$, which is smaller than the TGLF SAT1–geo reference value

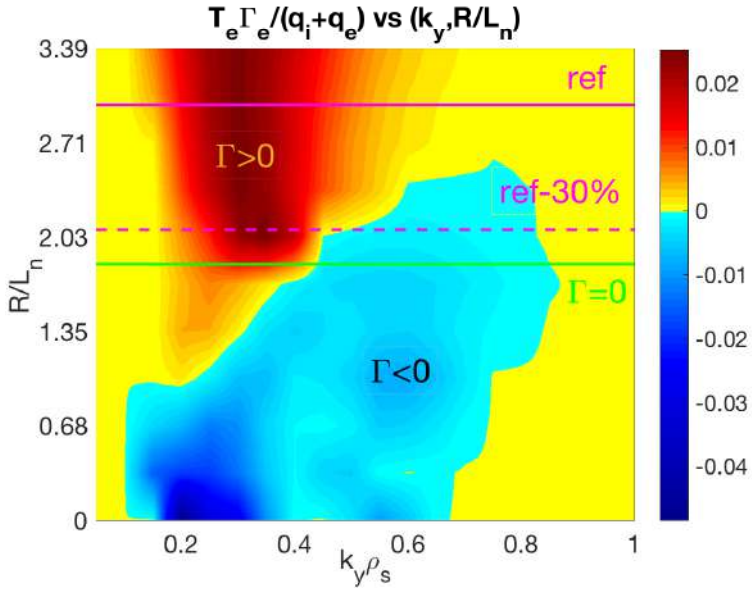

(a)

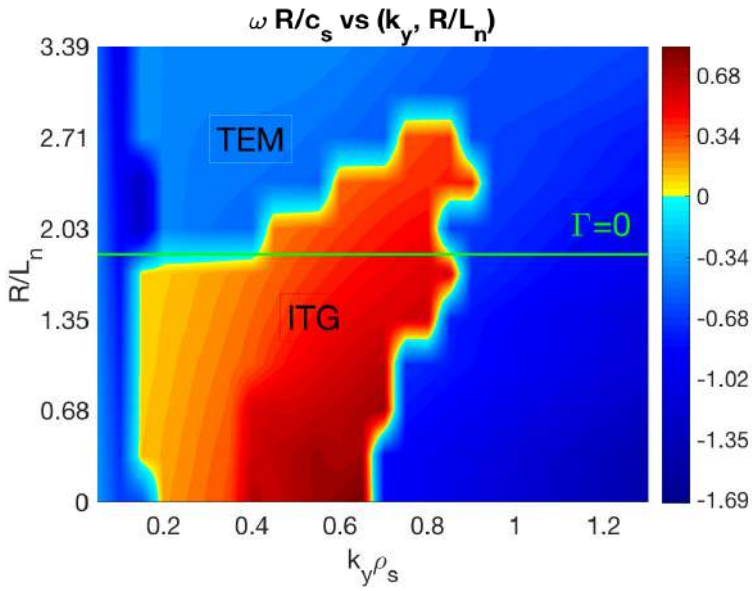

(b)

Figure 4.15: (a) Spectrum of the QL electron particle flux $\Gamma_e(k_y)$ versus R/L_n, normalised with $(q_e+q_i)/T_e$, where q_e and q_i are the total QL electron an ion heat fluxes and $\Gamma_e(k_y)$ satisfies $\Gamma_e = \sum_{k_y} \Gamma_e(k_y)$. (b) k_y spectrum of the growth rate γ of the most unstable linear mode versus R/L_n. The growth rate γ is normalised with c_s/R, while k_y is normalised with $1/\rho_s$.

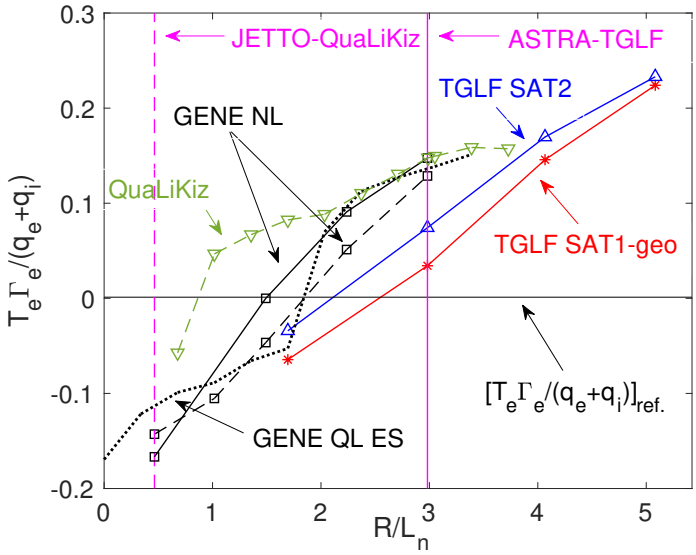

Figure 4.16: Normalised electron particle flux $T_e\Gamma_e/(q_e + q_i)$ vs R/L_n, with parameters from ASTRA–TGLF (solid or dotted) and JINTRAC–QuaLiKiz (dashed) predictive transport simulations, computed with GENE NL (black), GENE QL (black, dotted), TGLF SAT1–geo (red), TGLF SAT2 (blue) and QuaLiKiz (green), where the QL codes have been run using the stand–alone version. The reference values $R/L_n \sim 3$ (ASTRA–TGLF) and $R/L_n = 0.46$ (JINTRAC–QuaLiKiz) are shown by solid and dashed vertical magenta lines, respectively.

$R/L_n \sim 3$ (magenta solid line), below a $\pm 30\%$ error bar. The $\Gamma_e = 0$ condition is obtained from a balance of low–k TEM–driven outward flux with a larger–k ITG–driven inward flux. This correspondence of the TEM and ITG regimes with the Γ_e signs is obtained comparing figure 4.15(a) with figure 4.15(b), which shows the frequency ω in the $(k_y\rho_s, R/L_n)$ plane (> 0 for ITG and < 0 for TEM according to GENE conventions).

R/L_n scans of NL GENE ion–scale local runs have been performed to obtain a GK estimate of the peaking (i.e. the R/L_n that satisfies $\Gamma_e \sim 0$). The GENE results are shown in figure 4.16 by solid black lines, compared with the ones that are obtained running TGLF SAT1–geo (solid/red) and TGLF SAT2 (solid/blue) stand–alone simulations.

An additional R/L_n scan of GENE NL runs (dashed/black) has been performed replacing the values of the temperature logarithmic gradients $R/L_{T_e} = 7.8$, $R/L_{Ti} = 3.93$ (ASTRA–TGLF values) with the ones corresponding to the JINTRAC–QuaLiKiz predictive simulation: $R/L_{T_e} = 9.08$,

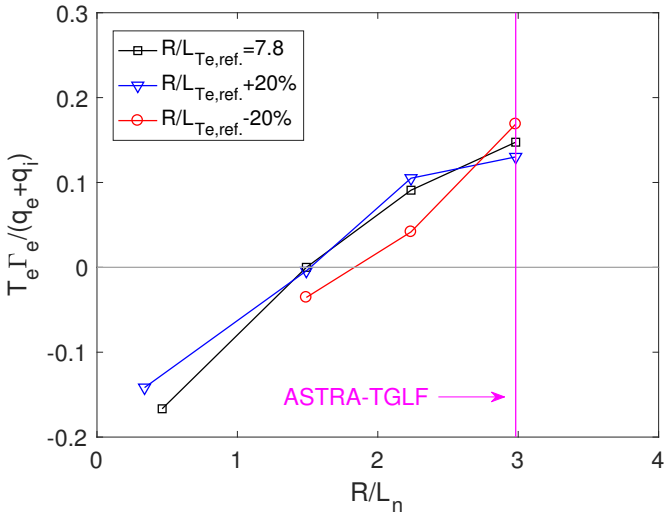

Figure 4.17: Normalised electron particle flux $T_e\Gamma_e/(q_e+q_i)$ vs R/L_n, for the three values $R/L_{T_e} = 7.8, 7.8 \pm 20\%$ of the normalised electron temperature logarithmic gradient.

$R/L_{Ti} = 4.58$, compared with corresponding QuaLiKiz stand–alone simulations (dashed/green). The reference value of $R/L_n \sim 3$ from ASTRA–TGLF is shown by a solid vertical magenta line, while the corresponding value $R/L_n = 0.46$ from JINTRAC–QuaLiKiz by a dashed vertical magenta line. More in detail, figure 4.16 shows the normalised electron particle flux $T_e\Gamma_e/(q_i + q_e)$ vs R/L_n. The predicted density peaking by each code is obtained from figure 4.16(a) at the crossing of the corresponding curve with the horizontal line $\Gamma_e \sim 0$. It follows that GENE prediction ($R/L_n \sim 1.4 - 1.8$) lies in between the QuaLiKiz and TGLF ones, not confirming the "flat n_e" prediction of QuaLiKiz. In particular, even replacing the ASTRA–TGLF $R/L_{Te,i}$ values with those from JINTRAC–QuaLiKiz, GENE still predicts a peaked n_e, with even slightly larger R/L_n.

The sensitivity of the GENE estimate of the electron density peaking to changes in R/L_{T_e}, which is the main driver of the TEM–dominant turbulence regime, has been tested by repeating the nonlinear R/L_n scans, increasing and decreasing the reference ASTRA–TGLF value $R/L_{T_e} = 7.8$ by $\pm 20\%$. The results, shown in figure 4.17, indicate that the effect of changing R/L_{T_e} within a $\pm 20\%$ error bar has a small/moderate effect on the peaking, which increases by $\sim 20\%$ when R/L_{T_e} is decreased.
However, a similar sensitivity test in QuaLiKiz indicated a significant increase in zero–particle–flux R/L_{n_e} with decreasing R/L_{T_e}. Zero–particle–flux

at $R/L_{n_e} = 1.5$ (the GENE value) was attained with only a $\sim 15\,\%$ decrease in R/L_{T_e}. The zero–flux boundary in QuaLikiz is extremely sensitive to the ITG–TEM transition in this regime, and occurs here rapidly over multiple wavenumbers with stiff TEM heat flux, also meaning that the ad–hoc TEM electron heat flux model tested here was less effective than expected in reducing the power–balance R/L_{T_e}. The self–organised $R/L_n - R/L_T$ state that leads to flat n_e profiles in the QuaLiKiz simulations for $\rho_{\text{tor}} < 0.4$ in this specific regime thus likely arises from discrepancies in the ITG–TEM instability boundary in $R/L_n - R/L_T$ space compared to higher–fidelity gyrokinetic models. This will be explored in future work.

Summing up, the very flat profile predicted by JINTRAC–QuaLiKiz in the inner region is not validated by a comparison of QuaLiKiz stand–alone with GENE. Also, the amount of n_e peaking predicted by ASTRA–TGLF turns out to be a bit overestimated when compared with GENE, although qualitatively nearer to the gyrokinetic prediction. Both models should then be taken with care in the region inside $\rho_{\text{tor}} = 0.4$, which is characterised by high power density, TEM dominance and q values below 1, with sawteeth not yet accounted for.

4.3.6 FP scenario heating mixes

Prior to this modelling work, the heating mix of the full power scenario was not established. One of the purposes of this work was to optimise the choice of power distribution amongst the 3 systems and of the NBI energy. In addition to the three heating mix options proposed in [8], other possible candidates have been suggested within the DTT physics group. The various options are listed in table 4.4.
In order to assist the heating mix choice, each of these 9 SN FP H–mode scenarios has been simulated both in a JETTO run with the standard QLK model and with a JINTRAC–ASTRA approach with TGLF SAT1–geo model.

For the sake of clarity, some radial profiles of only the 3 most salient options, obtained from TGLF SAT1–geo runs are shown in figure 4.18. Main parameters of these 3 cases are displayed in table 4.5. In all the FP options, the characteristic behaviour of the main plasma profiles seen in section 4.3.5.1 recurs. Particularly, the electron density has a moderately peaked profile reaching maximum values in the range of $(1.9\text{–}2.7)\times 10^{20}\,\text{m}^{-3}$ and in the central plasma region the electron temperature $T_e \approx 15\text{–}27\,\text{keV}$ is much higher than the ion temperature $T_i \approx 8\text{–}12\,\text{keV}$.

Table 4.4: Heating mix options (power values at plasma) evaluated for DTT full power scenarios.

Option	ECRH	ICRH	NBI
A	$\sim 28.8\,\mathrm{MW}$ (32 gyr.$\times 1\,\mathrm{MW}$)$\times 0.9$	$\sim 3\,\mathrm{MW}$ (2 antennas in 1 module)	$\sim 15\,\mathrm{MW}$ 2 inj.$\times$(7.5 MW at 400 keV)
B	$\sim 36.0\,\mathrm{MW}$ (16 gyr.$\times 1\,\mathrm{MW}$ + 20 gyr.$\times 1.2\,\mathrm{MW}$)$\times 0.9$	$\sim 3\,\mathrm{MW}$ (2 antennas in 1 module)	$\sim 7.5\,\mathrm{MW}$ 1 inj.$\times$(7.5 MW at 400 keV)
C	$\sim 28.8\,\mathrm{MW}$ (32 gyr.$\times 1\,\mathrm{MW}$)$\times 0.9$	$\sim 9\,\mathrm{MW}$ (6 antennas in 3 modules)	$\sim 7.5\,\mathrm{MW}$ 1 inj.$\times$(7.5 MW at 400 keV)
D	$\sim 30.2\,\mathrm{MW}$ (24 gyr.$\times 1\,\mathrm{MW}$ + 8 gyr.$\times 1.2\,\mathrm{MW}$)$\times 0.9$	$\sim 6\,\mathrm{MW}$ (4 antennas in 2 modules)	$\sim 10\,\mathrm{MW}$ 1 inj.$\times$(10 MW at 500 keV)
E	$\sim 28.8\,\mathrm{MW}$ (32 gyr.$\times 1\,\mathrm{MW}$)$\times 0.9$	$\sim 3\,\mathrm{MW}$ (2 antennas in 1 module)	$\sim 15\,\mathrm{MW}$ 1 inj.$\times$(10 MW at 500 keV) + + 1 inj.$\times$(5.0 MW at 200 keV)
F	$\sim 28.8\,\mathrm{MW}$ (32 gyr.$\times 1\,\mathrm{MW}$)$\times 0.9$	$\sim 3\,\mathrm{MW}$ (2 antennas in 1 module)	$\sim 10\,\mathrm{MW}$ 1 inj.$\times$(10 MW at 600 keV)
G	$\sim 30.2\,\mathrm{MW}$ (24 gyr.$\times 1\,\mathrm{MW}$ + 8 gyr.$\times 1.2\,\mathrm{MW}$)$\times 0.9$	$\sim 6\,\mathrm{MW}$ (4 antennas in 2 modules)	$\sim 7.5\,\mathrm{MW}$ 1 inj.$\times$(7.5 MW at 400 keV)
H	$\sim 30.2\,\mathrm{MW}$ (24 gyr.$\times 1\,\mathrm{MW}$ + 8 gyr.$\times 1.2\,\mathrm{MW}$)$\times 0.9$	$\sim 6\,\mathrm{MW}$ (4 antennas in 2 modules)	$\sim 10\,\mathrm{MW}$ 1 inj.$\times$(10 MW at 400 keV)
I	$\sim 26.3\,\mathrm{MW}$ (16 gyr.$\times 1\,\mathrm{MW}$ + 11 gyr.$\times 1.2\,\mathrm{MW}$)$\times 0.9$	$\sim 9\,\mathrm{MW}$ (6 antennas in 3 modules)	$\sim 10\,\mathrm{MW}$ 1 inj.$\times$(10 MW at 500 keV)

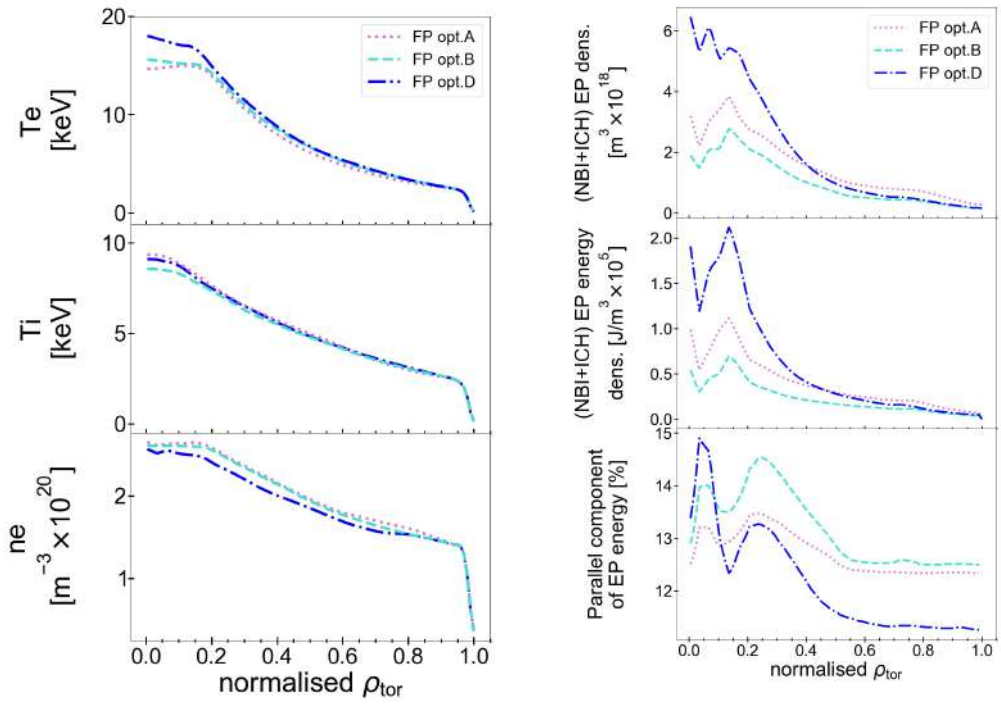

(a) (b)

Figure 4.18: Comparison of radial profiles among the most salient options of the FP scenario. (a) Profiles of electron temperatures, ion temperatures, and electron densities. (b) Profiles of energetic particle densities, energetic particle energy densities, and parallel components of the energetic particle energies.

Table 4.5: Main parameters of a sub–set of heating options for the DTT FP scenario using TGLF SAT1–geo.

Heating Option	τ_E [s] ($P = P_{\rm tot}$)	τ_E [s] ($P = P_{\rm sep}$)	H98Y	$\beta_{\rm N_{therm}}/\beta_{\rm N_{tot}}$	$W_{\rm EP}/W_{\rm tot}$ [%]	T_{e_0}/T_{i_0} [keV/keV]	$\langle n_e \rangle / n_G$	Neutron rate
A	0.25	0.45	0.95	1.40/1.49	5.7	14.6/9.3	0.47	1.24×10^{17} s
B	0.26	0.44	0.95	1.42/1.46	3.3	15.6/8.5	0.46	0.85×10^{17} s
D	0.25	0.43	0.95	1.39/1.49	6.5	18.0/9.1	0.44	1.29×10^{17} s

In order to achieve more central NBI deposition as well as to minimise the collisionless ripple fast particle losses[123] and allow resonant excitation of Alfvénic waves[124], the higher NBI energy has been preferred to the higher NBI power option, in addition to opting for the largest possible injection angle.
Given the need of trying to equilibrate T_e and T_i, the option B with 40 MW of ECH power has been discarded, and the missing NBI power has been replaced by ICH power, which has the double advantage of providing central ion heating and a fast particle population that could help lowering the high ion stiffness observed by TGLF and QLK[105]. From the power deposition calculations, the synergy effects between ICRH and NBI proved to be very relevant, leading to a maximised energetic particle content in option D.

With the state–of–the–art in quasi–linear models, differences between the various options are not large. However, the non–linear effects linked with thermal and suprathermal pressure gradients not included in the QL models could play an important role on the ion temperature profile.

From the physics point of view, the option D is the best compromise between technical feasibility, need to heat ions, and creation of suitable EP population.

4.3.7 Day 1 scenario

In the day–1 phase (with $B_{\mathrm{tor}} = 6\,\mathrm{T}$ and $I_{\mathrm{pl}} = 4.0\,\mathrm{MA}$), the power coupled to the plasma ($\sim 25\,\mathrm{MW}$) will be shared among the heating systems as described in the section 4.2. The integrated modelling of a steady–state deuterium plasma in the day–1 scenario has been performed using both the standard QLK model in a JETTO run and the TGLF SAT1–geo model with the JINTRAC–ASTRA approach.
The simulation settings widely described from the beginning of section 5.2.1 up to the end of section 4.3.4 has been also employed in these day–1 scenario modelling work.

Since the density value at the top of the pedestal has not been reduced with respect to the full power case, the Greenwald fraction increased to $\langle ne \rangle \sim 0.5\, n_G$, still well within safety margins. The pedestal parameters predicted by Europed for day–1 scenario are very similar to the full power case ones.

The electron temperature T_e, ion temperature T_i, electron density n_e, toroidal rotation ω_{tor}, and safety factor q radial profiles obtained by QLK and TGLF SAT1–geo runs are displayed in figure 4.19. According both models, the density peaking results less pronounced in day–1 phase than in the reference FP scenario, leading to a lower central value $n_{e_0} \approx 2.0 \times 10^{20}\,/\mathrm{m}^3$.

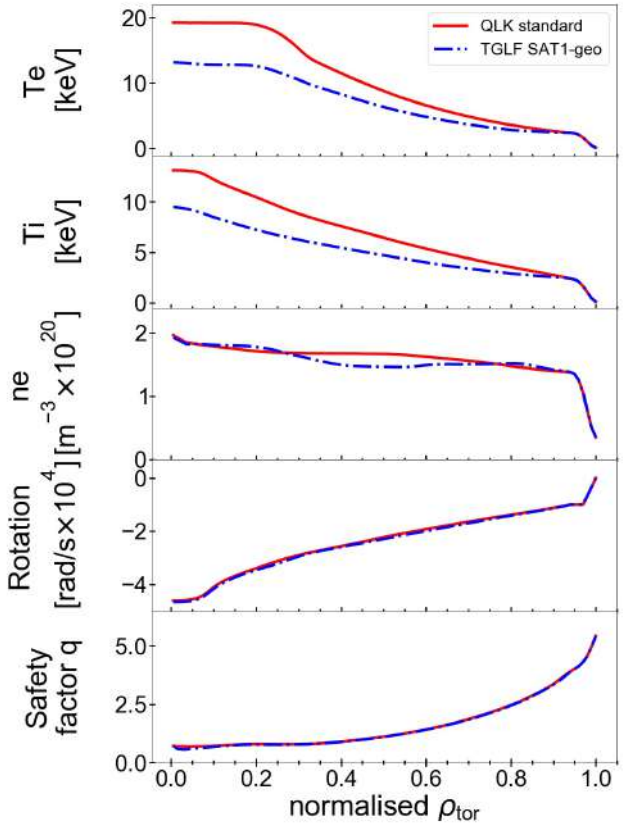

Figure 4.19: Steady–state radial profiles of the electron and ion temperatures, electron density, toroidal rotation, and safety factor of the day–1 scenario, with turbulent transport calculated by TGLF SAT1–geo (blue dash–dot line).

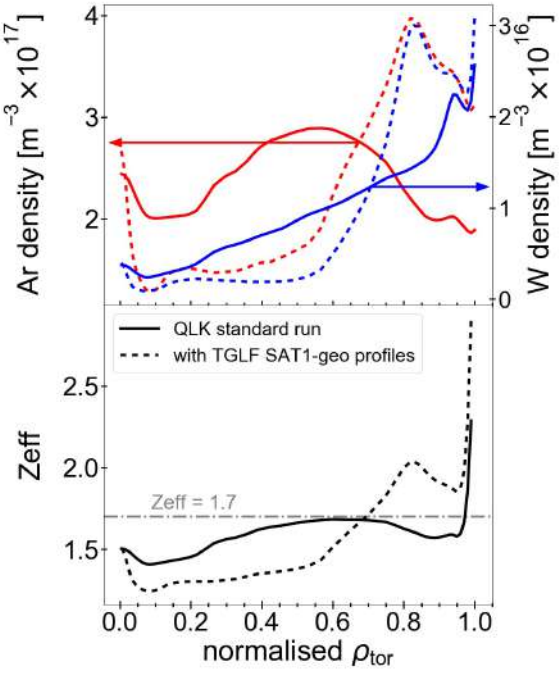

Figure 4.20: Radial profiles of the impurity densities (Ar in red, W in blue) and of effective charge in the day–1 scenario for the TGLF SAT1–geo case. The standard QLK case results (solid lines) are compared to an assessment of the impurity and Z_{eff} profiles in presence of TGLF SAT1–geo predicted profiles carried out with JETTO/SANCO and QLK (dashed lines).

We notice some discrepancies between QLK and TGLF temperature profiles. In the day–1 case, the electron temperature is estimated rather similar in the QLK run with respect to the full power case, while is significantly reduced in the TGLF run. For both models, the T_i values are similar in day–1 and FP scenarios, in spite of having half the injected power. This may be ascribed both to the increased ITG threshold with lower T_e/T_i and to the high ion stiffness, which makes a factor 2 difference in power rather ineffective in terms of T_i profiles (although crucial for divertor studies).

In figure 4.20, there are impurity densities and effective charge radial profiles for the standard QLK run (solid lines) compared to an assessment of the impurity and Z_{eff} profiles in presence of TGLF SAT1–geo predicted profiles carried out with JETTO/SANCO and QLK (dashed lines). We note that the impurities feature less central accumulation than in the full power case.

For the TGLF case, shown in figure 4.21(a), the neutron rate is reduced

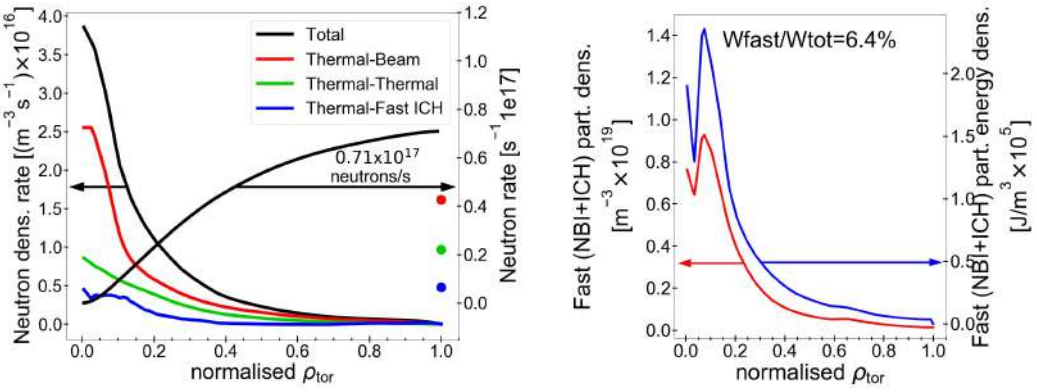

(a) (b)

Figure 4.21: (a) Radial profiles of neutron density rates (neutrons from thermal nuclei in green, from a thermal nucleus and a fast NBI nucleus in red, and from a thermal nucleus and a fast ICRH nucleus in blue). The radial profile of the total neutron rate is also displayed (black). (b) Radial profiles of density and energy density of EPs due to the both NBI and ICRH systems.

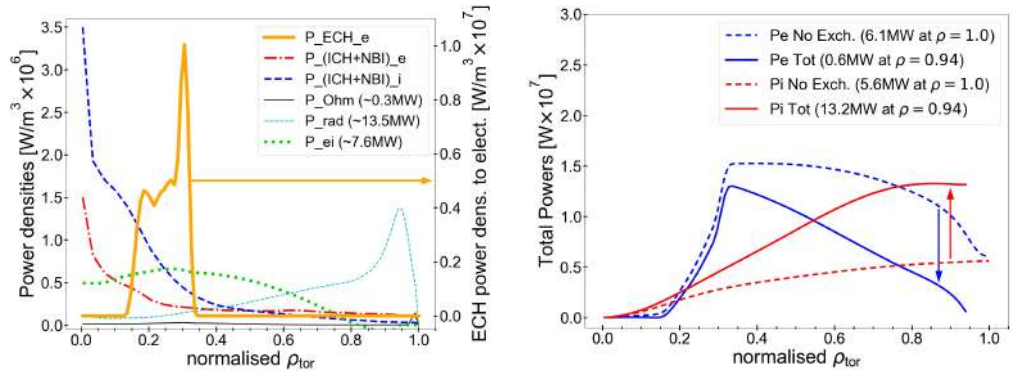

(a) (b)

Figure 4.22: (a) Radial profiles of power densities in the day–1 scenario: ECRH power deposited to electrons $P_{\mathrm{ECH}\,e}$, NBI and ICRH power deposited to electrons $P_{(\mathrm{ICH+NBI})\,e}$, NBI and ICRH power deposited to ions $P_{(\mathrm{ICH+NBI})\,i}$, Ohmic power P_{Ohm}, radiative power P_{rad}, and thermal exchange power between electrons and ions P_{ei}. (b) Radial profiles of electron and ion total powers including or not including the thermal exchange power between species in the day–1 scenario.

to 7.1×10^{16} neutrons/s. In figure 4.21(b) the EP contents are shown for the TGLF SAT1–geo case.

In figure 4.22(a) the radial profiles of all power densities and those of the total electron and ion powers are shown in figure 4.22 (b), only for the standard QLK simulation.

4.3.8 Day 0 scenario

The day–0 phase (with $B_{\text{tor}} = 3\,\text{T}$ and $I_{\text{pl}} = 2.0\,\text{MA}$) features only 8 MW of ECH power in second harmonic X–mode (coupling to the plasma $\sim 7.2\,\text{MW}$ of power), as described in section 4.2. The integrated modelling of a steady–state deuterium plasma in the day–0 scenario has been performed using the TGLF SAT1–geo model with the JINTRAC–ASTRA approach. We do not show QLK results for this case, as this purely electron heated case is the one where QLK validity is most affected by the dominant TEM regime.
The simulation settings widely described in the initial sections of 4.3 has been also used in this day–0 scenario modelling work. While maintaining the same relative impurity mix of Ar and W used in FP runs, in the day–0 simulation has been set a flat $Z_{\text{eff}} = 1.4$ profile as initial condition in SANCO. The density at the pedestal top has been reduced with respect to the full power case, to have approximately a Greenwald fraction of about 0.36.

In figure 4.23(a), the radial profiles of T_e, T_i, n_e, and q predicted by the TGLF SAT1–geo run of day–0 phase are shown. The reduced pedestal density with respect to the full power case and the slightly peaked n_e profile lead to a lower central density value of about $n_{e_0} \approx 0.7 \times 10^{20}\,/\text{m}^3$.
T_e is much larger that T_i ($T_{e_0} \approx 12\,\text{keV}$ and $T_{i_0} \approx 4\,\text{keV}$), due to having only electron heating and low density. The toroidal rotation is not shown as there is no NBI torque, so it reduces to intrinsic rotation, with edge values difficult to estimate but expected small.

In figure 4.23(b), impurity densities and effective charge radial profiles are shown for an assessment of the impurity and Z_{eff} profiles in presence of TGLF SAT1–geo predicted profiles carried out with JETTO/SANCO and QLK (dashed lines). We note that the impurities show much less core penetration in the day–0 case.

For the sake of completeness, in figure 4.22 the radial profiles of all power densities and those of the total electron and ion powers are shown in figure 4.24 (a) and 4.24 (b) respectively.

A neutron rate of $\sim 4 \times 10^{14}$ neutrons/s has been estimated for the day–0 scenario.

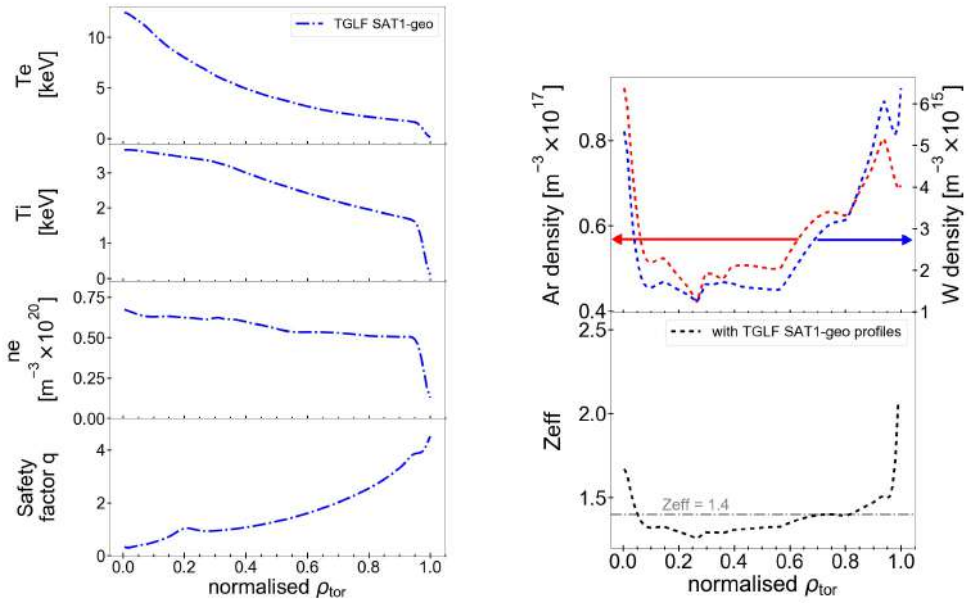

(a) (b)

Figure 4.23: (a) Steady–state radial profiles of the electron and ion temperatures, electron density, and safety factor of the day–0 scenario, with turbulent transport calculated by TGLF SAT1–geo (blue dash–dot line). (b) Radial profiles of the impurity densities (argon in red, tungsten in blue) and of effective charge Z_{eff} in the day–0 scenario in presence of TGLF SAT1–geo predicted profiles carried out with JETTO/SANCO and QLK (dashed lines)

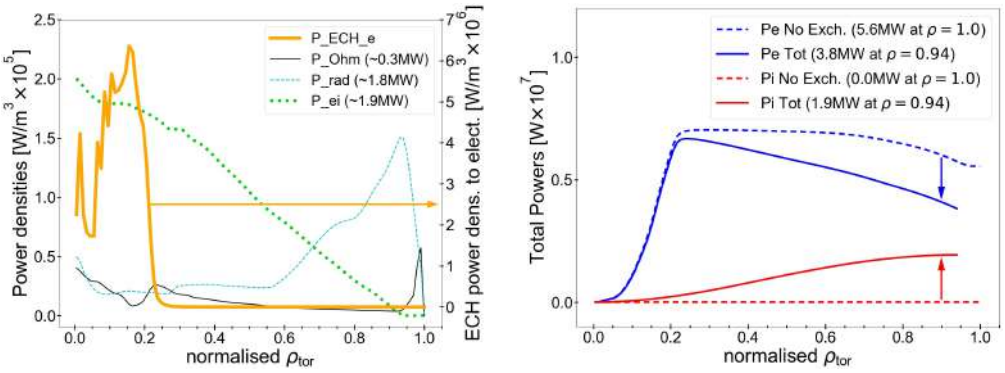

(a) (b)

Figure 4.24: (a) Radial profiles of power densities in the day–0 scenario: ECRH power deposited to electrons $P_{\mathrm{ECH}\,e}$, Ohmic power P_{Ohm}, radiative power P_{rad}, and thermal exchange power between electrons and ions P_{ei}. (b) Radial profiles of electron and ion total powers including or not including the thermal exchange power between species in the day–0 scenario.

4.4 Conclusions

The first–principle multi–channel integrated modelling of the main DTT baseline scenarios using quasi–linear transport models (TGLF, QLK) has started and is key to support the design of the device and to help the elaboration of a DTT scientific work–programme. Particularly, this work has been crucial to define the reference heating mix for the full power scenario among 9 possible options. Moreover, results from this modelling led to the decision to enlarge the device up to $R_0 = 2.19\,\mathrm{m}$ and $a = 0.70\,\mathrm{m}$. Reference profiles in different scenarios are now available for diagnostic system design, as well as estimates of neutron yields and fast particle losses. In addition, a preliminary risk evaluation of a fuelling via gas puffing without the pellet support has been done, suggesting a beneficial impact of incorporating pellet fuelling in addition to gas puff. Some validation of the quasi–linear models used against gyrokinetic simulations in the specific DTT range of parameters has been performed, as an essential procedure to improve the reliability of such predictions.

CHAPTER 5

Core–edge–SOL integrated modelling for the Divertor Tokamak Test facility scenarios

This work has been submitted to *Plasma Physics and Controlled Fusion.*

Abstract

Deuterium plasma discharges of the Divertor Tokamak Test facility (DTT) in different operational scenarios have been predicted by a comprehensive first–principle based integrated modelling activity using state–of–art quasi–linear transport models. The results of this work refer to the updated DTT configuration, which includes a device size optimisation (enlargement to $R_0 = 2.19\,\mathrm{m}$ and $a = 0.70\,\mathrm{m}$) and upgrades in the heating systems. Special attention was paid to the consistency with the edge parameters required to achieve divertor plasma detachment. The compatibility of these physics–based predicted scenarios with the electromagnetic coil system capabilities was then verified. In addition, first estimates of DTT sawteeth and of DTT ELMs were achieved.

5.1 Introduction

To align the research priorities towards the electricity production from thermonuclear fusion energy, a list of eight challenges to be faced was defined in the European Fusion Roadmap[6, 7]. Finding a reliable solution for the problem of the controlled exhaust of energy and particles from a fusion reactor is the second mission goal. All plasma–facing components must withstand the large particle and heat fluxes of a fusion reactor (up to 10–20 $\mathrm{MW/m^2}$). The baseline strategy of employing a conventional metal divertor in Single Null (SN) configuration operating in partially detached plasma conditions, adopted in ITER[5], could not be directly extrapolated to DEMO[76] and

future commercial fusion power plants, so alternative strategies need to be explored. In this framework, a new tokamak facility dedicated to study power exhaust is under construction in Italy: the Divertor Tokamak Test facility (DTT)[8, 9, 10].
The DTT machine is a D–shaped superconducting tokamak, under construction at the ENEA Research Center in Frascati, whose parameters have been optimised to be as similar as possible with the operating conditions in DEMO. A detailed description of the DTT project is reported in [18], where the main parameters of DTT are compared to those of ITER and EU DEMO.
In DTT ($R_0 = 2.19\,\mathrm{m}$, $a = 0.70\,\mathrm{m}$, tungsten first wall and divertor, superconducting coils, pulse length $\leq 100\,\mathrm{s}$, vacuum toroidal field $B_{\mathrm{tor}} \leq 5.85\,\mathrm{T}$, plasma current $I_{\mathrm{pl}} \leq 5.5\,\mathrm{MA}$, equipped with ECRH, NBI, and ICRH systems for a total auxiliary heating $\leq 45\,\mathrm{MW}$) improved plasma–facing materials and different divertor solutions will be developed and tested, including advanced magnetic configurations (such as double null, quasi–snowflake, and SN with negative triangularity scenarios) and liquid metal divertors.

In order to minimise risks and reduce costs, a first–principle based integrated modelling as comprehensive as possible of plasma discharges in different operational scenarios is a fundamental tool for designing a new tokamak. Therefore, main DTT scenarios were simulated for the initial machine configuration with $R_0 = 2.14\,\mathrm{m}$, as reported in [18]. This work led to the optimisation of the device size, increased to $R_0 = 2.19\,\mathrm{m}$, and of the reference heating mix, as widely described in [18].
After this initial work, it became evident that the core simulations needed to be consistent with the requirements to achieve divertor plasma conditions compatible with current technologies. Particularly, Scrape–Off Layer (SOL) and divertor plasma simulations [114] performed with the 2D edge numerical code SOLEDGE2D–EIRENE [115, 116] estimated the minimum separatrix density required to obtain sustainable conditions in full power operations. Therefore a new thread of simulations was started for the machine configuration $R_0 = 2.19\,\mathrm{m}$, in which particular attention was paid to the integration of the core and pedestal runs with the SOL modelling.

In this chapter, the latest results for the new machine configuration with $R_0 = 2.19\,\mathrm{m}$ of the multi–channel integrated simulations based on state–of–art first–principle quasi–linear (QL) transport models of the DTT baseline scenarios are presented. The modelling is now updated to the current DTT configuration, including the machine enlargement and the consequent auxiliary heating system upgrades. This work provides reference profiles for diagnostic system design, estimates of neutron yields, calculations of fast particle losses, fuelling requirements, MHD evaluations, and other tasks.

Great efforts have been made to obtain plasma scenarios compatible with

divertor and first wall power handling capability and tungsten influx. To avoid the tungsten melting, the heat loads should be lower than $20\,\mathrm{MW/m^2}$ to the divertor, $7.5\,\mathrm{MW/m^2}$ to the internal first wall, and $1\,\mathrm{MW/m^2}$ to the external wall.[12] To avoid the erosion and the consequent high tungsten influx and core accumulation, the plasma temperature should not exceed the value of 5 eV at both the divertor and the wall.[12] Therefore, DTT should operate with plasma in partially and fully detached states with the latter that could be more relevant for DEMO. Edge modelling indicates that the detachment conditions require a strong radiation by impurity seeding and high separatrix density values, which at the end affects pedestal properties.[125] These requirements have been taken into account in the core simulations by setting suitable values at the separatrix as boundary conditions. Different seeding gases have also been tested.

The consistency between the control coil system capabilities and plasma profiles has been checked too.

In addition, an analysis of sawteeth in DTT using the Porcelli model [126] has been carried out for the first time and some considerations on the possible impact of Edge Localised Modes (ELMs) have been made based on existing scalings [127, 128, 129, 130].

5.2 The DTT integrated modelling

An extensive modelling work of DTT scenarios has been conducted for the last three years. The baseline scenarios with the SN configuration with positive triangularity in H–mode during the flat–top phase are now available for the new DTT design. These integrated simulations predict radial profiles of the electron and ion temperatures, density (both main species and impurity), toroidal rotation, and current density, calculating consistently the magnetic equilibrium, the heating profiles, and the non–linear interactions between the different transport channels and between heating and plasma.
With respect to the configurations previously studied in [18] and reported in the previous chapter, the latest changes of the baseline scenarios are included in this chapter. To this day, the planned DTT scenarios with the SN magnetic configuration are called A1, B1, C1, D1, and E1. These reference scenarios are characterised by the values of plasma current, toroidal magnetic field, and auxiliary heating system powers listed in table 5.1. The scenarios A1–B1–C1 are foreseen in the period 2028–2032, whilst D1 and E1 from 2032 onwards.

To enhance the reliability of our modelling predictions, matching as well

Table 5.1: DTT scenarios with the SN configuration.

Phase	I_{pl} [MA]	B_{tor} [T]	ECH installed power [MW]	ICH installed power [MW]	NBI installed power [MW]
A1	2.0	3.0	8.0	0.0	0.0
B1	2.0	3.0	16.0	4.0	0.0
C1	4.0	5.85	16.0	4.0	0.0
D1	5.5	5.85	16.0	4.0	10.0
E1	5.5	5.85	32.0	8.0	10.0

as possible the key parameters between core and SOL simulations is an essential aspect. Firstly, an investigation work about the edge parameter ranges in existing tokamaks (C–mod and JET), described in [131], was done to establish the best settings for DTT.
Several SOL simulations, whose details are also reported in [125], were performed with the SOLEDGE2D–EIRENE code in order to define the detachment conditions in the main DTT baseline scenarios: the A1 scenario (the first plasma scenario), the C1 scenario, and the E1 scenario (the full power scenario with positive triangularity).
Then, we proceeded iteratively with a work of adjustment of the simulation settings, operating on both sides. Particularly, the results of the DTT edge modelling entails strenuous requirements in the simulations discussed in this chapter in terms of impurity concentrations and pedestal parameters to reach detachment conditions, as specified in the following sections for each analysed scenario.

5.2.1 General settings of simulations

This work concerns the integrated modelling of DTT scenarios with the SN configuration with positive triangularity.
The simulations of DTT deuterium plasmas during the flat–top phases were mainly performed using the JETTO[99] transport solver included in the JINTRAC[79] suite of codes and in some cases using the ASTRA[67] transport solver with a mixed ASTRA–JINTRAC approach discussed in [18].
Although these runs cover the region inside the separatrix, the transport equations for heat, particle, and momentum are solved only within the top of the pedestal.

The neoclassical heat and particle transport is calculated by the NCLASS [96] model, while the turbulent transport is either calculated by trapped–gyro–Landau–fluid (TGLF) [54, 59], a gyrofluid and electromagnetic QL model with shaped flux surfaces, or by QuaLiKiz (QLK)[61, 62], a gyrokinetic and electrostatic QL transport model with circular flux surfaces. Specifically, we employed the most recent. versions of the models: TGLF SAT2, characterised by a fit of the geometrical coefficients to 3D CGYRO spectra and by an agreement with CGYRO non–linear simulations described in [59], and the last release of QLK, featuring enhancements in the trapped electron mode (TEM) treatment described in [62]. In addition to the main turbulent transport, a small contribution (3 %) of Bohm transport is used to ensure the numerical stability to the computation. Furthermore, since the neoclassical electron heat transport contribution results rather insignificant close to the plasma centre, an additional electron diffusivity of $\chi = 0.5\,\mathrm{m}^2\,\mathrm{s}$ is added within $\rho_{\mathrm{tor}} = 0.2$, where the normalised effective minor radius $\rho_{\mathrm{tor}} := \sqrt{(\Phi/\pi B_{\mathrm{tor}})/(\Phi/\pi B_{\mathrm{tor}})_{\mathrm{sep}}}$ is the normalised radius that a magnetic surface with circular section should have to enclose the same toroidal magnetic flux Φ.

In the pedestal region, the kinetic profiles of the two main species are kept fixed, using the pedestal top values of temperatures and densities as boundary conditions of our core simulations, and $T_e = T_i$ is assumed. The pedestal profiles were previously determined by specific runs of Europed code [80] using the EPED1 model [81], for each scenario.
A good agreement between edge and core steady–state simulations ensures a high confidence level in the modelling results. Hence, properly defining all simulation settings and all parameters to use for the pedestal characterisation in order to be compatible with detachment conditions imposed by the SOL calculations [114, 125] has been crucial.

For every Europed simulation, we prescribed a certain seeding gas and we set input values in agreement with the edge requirements for the effective charge $Z_{\mathrm{eff}} = \sum_i Z_i^2 n_i/n_e$ in the pedestal, the temperature at the separatrix T_e^{sep}, and the relative shift defined as the distance between the positions of the pedestal temperature and density ($T_e^{\mathrm{pos}} - n_e^{\mathrm{pos}}$).
Moreover, in the pedestal modelling, the magnetic equilibrium is specified, the electron density at the pedestal top n_e^{ped} is set to obtain a Greenwald fraction of $\bar{n}_e/n_{\mathrm{Gr}} \approx (0.45 - 0.55)$ in the core runs, and a tuned β_{pol} value is used to match with the JINTRAC predictions.

In the core modelling, two impurities are always included: a seeding gas (argon, neon, or nitrogen), used to increase the edge radiative dissipation reducing the divertor power load, and tungsten (W, $A \approx 184$, Z = 74) coming from the first wall and the divertor. In the JINTRAC runs, the SANCO

code [75] calculates impurity densities and radiation up to the separatrix, treating all ionisation states separately. To conserve the particle number during the simulation, we set the recycling factor, the escape velocity, and the neutral influx as null; the decay lengths are set equal to $\lambda_n = \lambda_T = 1.0\,\mathrm{cm}$, in agreement with the edge simulations. Setting a radially constant effective charge Z_{eff} and an impurity density ratio $n_{\mathrm{W}}/n_{\mathrm{seed.gas}}$ as SANCO initial conditions entails certain concentrations of the seeding gas and tungsten during the run, tuned to be compatible with typical values in tokamaks operating in full detachment [132] and with SOL modelling predictions.

During the JINTRAC simulations, the equilibrium solver ESCO updates the MHD equilibrium three times per second, keeping fixed the plasma boundary to the reference shape described in [133] and provided by the free boundary solver CREATE–NL [100].

A theory–driven empirical model [97, 98] has been employed to predict the toroidal rotation. Based on the pinch number dependence on some plasma parameters discussed in [98], we built a pinch number RV_φ/χ_φ null at the plasma centre, equals to ~ 2.5 at $\rho_{\mathrm{tor}} = 0.4$, and with the trend $RV_\varphi/\chi_i \propto -\sqrt{r/R}$ to include the inward momentum pinch. The momentum transport coefficient χ_φ is substituted by the product between the ion thermal transport coefficient χ_i and a Prandtl number value $\chi_\varphi/\chi_i = 0.7$ lower than the unit to consider the residual stress due to $E \times B$ shearing. In the pedestal region, the rotation has been arbitrarily supposed to move from zero up to $|\omega_{\mathrm{tor}}| = 10\,\mathrm{krad/s}$, that is a reasonable assessment based on measurements in present tokamaks. Anyway, the simulation is not significantly affected by this assumption, but rather by the rotation gradient.

The implementations in JINTRAC of the ECRH (Electron Cyclotron Resonance Heating), ICRH (Ion Cyclotron Resonance Heating), and NBI (Neutral Beam Injector) systems have been updated to their new set–up designed for the present DTT configuration, so that the heating and current drive systems as well as the NBI particle source could be simulated self–consistently during the JETTO runs, accounting also for the synergy effects.

The ECRH system includes up to 32 gyrotrons at 170 GHz, split in 4 clusters, with an installed power of 1 MW from each gyrotron. Every cluster is composed by two upper (UP) gyrotrons, three equatorial top (EQT) gyrotrons, and three equatorial bottom (EQB) gyrotrons, depending on the access port. The ECRH power deposition is calculated four times per second by the GRAY code [72], considering at the most 20 different beams and modelling each beam as sum of one central ray and 160 rays arranged on 10 concentric rings evenly distributed between the beam axis and the beam radius, at which the wave electric field amplitude is $1/e$ times the on–axis value.

DTT will also be equipped with a negative ion based NBI system with a single injector able to inject up to 10 MW of power into the plasma. The deuterium beam is designed to reach an energy ≤ 510 keV, to operate effectively ad high densities.[134] The injector installation is planned for the 2032. The NBI system is modelled by the PENCIL code [73], setting all beam particles injected at the nominal energy due to the negative ion source. As described in detail in [101], the sum of prompt and ripple NBI fast particle losses is $\sim 4\,\%$ only and we could neglect them in our modelling work.

Every module of the ICRH system is composed by a pair of three–strap RF antennas located in an equatorial port and operating in the frequency range 60–90 MHz, with an installed power of 2 MW from each antenna. Up to 2 ICRH modules, i.e. up to 4 RF antennas, will be installed on DTT. The ICRH power deposition and the synergy effects with NBI are computed by the PION code [74] in the performed runs. In the simulations with ICRH of this chapter, a RF frequency of 90 MHz and a concentration of 5 % hydrogen as minority species are always set, so that the cyclotron resonance is placed where the magnetic field is $B_{\text{tor}} \approx 5.9$ T.

The total neutron rate, which is due to the sum of neutron production from fusion reactions between two thermal nuclei, between a thermal nucleus and a fast nucleus of the NBI beam, and between a thermal nucleus and a fast nucleus of the ICRH minority species, is also computed during the JETTO runs. This assessment is useful to guarantee that the designed neutron shields will be able to cope with DTT neutron loads.

For the first time, an investigation of the sawteeth in DTT has been carried out using the Porcelli model [126]. These simulations are described in section 5.3.2. In the other sections, the simulations do not include sawteeth and hence their profiles have to be interpreted as related to the saturated recovery after a sawtooth crash.

ELMs are not included in the modelling yet, but first estimations of their impact on the full power scenario predictions through suitable scalings [127, 128, 129, 130] are discussed in 5.3.3.

5.3 The E1 scenario

The E1 scenario works at the full current and full field operational point, i.e. with plasma current of $I_{\rm pl} = 5.5\,\mathrm{MA}$ and vacuum toroidal magnetic field of $B_{\rm tor} = 5.85\,\mathrm{T}$.
The reference heating option selected in [18] for the DTT E1 scenario, corresponding to the full power scenario, foresees:

- 32 gyrotrons to provide a total ECRH power to the plasma of about 28.8 MW (as a result of 32 MW of installed power and an estimated loss factor before launchers of 0.1), injecting beams in O–mode;
- 4 RF antennas split in 2 modules to provide a total ICRH power to the plasma of about 6.0 MW (as a result of 9 MW of installed power and an efficiency of 0.75 due to transmission lines and antenna coupling);
- 1 neutral beam injector with 510 keV to provide a total NBI power to the plasma of about 10.0 MW.

Being too numerous to be modelled separately, the 32 gyrotrons have been assembled into subsets: 12 different ECRH beams are simulated by GRAY. In relation to the EC launcher positioning of [135], the toroidal angles have been set in the following ranges: $(-5.0°) - (-4.5°)$ for UP beams, $(-4.0°) - (+0.5°)$ for EQT beams, and $(+1.0°) - (+2.5°)$ for EQB beams. The poloidal angles have been set in the following ranges: $(+42.5°) - (+44.5°)$ for UP beams, $(-5.5°) - (-1.0°)$ for EQT beams, and $(-2.5°) - (+2.5°)$ for EQB beams. With these angle settings, a high ECRH power density is deposited in the central region $0.1 \leq \rho_{\rm tor} \leq 0.35$ of the plasma, as shown in figure 5.2(a).

For the E1 scenario, a comparative analysis between two possible seeding gases (argon or neon) has been done with both core and edge [114] modelling. In JETTO simulations with argon (Ar, $A \approx 40$, Z = 18), we set $Z_{\rm eff} = 1.8$ and $n_{\rm W}/n_{\rm Ar} = 0.01$ as SANCO initial conditions, while in runs with neon (Ne, $A \approx 20$, Z = 10) we set $Z_{\rm eff} = 2.2$ and $n_{\rm W}/n_{\rm Ne} = 0.04$.

Obviously, the Europed modelling has been also doubled to obtain the pedestal pressures with argon and with neon, setting the same values of effective charge used in SANCO as initial conditions. Temperatures at the separatrix of $T_e^{\rm sep} = T_i^{\rm sep} = 130\,\mathrm{eV}$, a pedestal top density of $n_e^{\rm ped} = 1.4 \times 10^{20}\,\mathrm{m}^{-3}$, a value of $\beta_{\rm pol} = 0.55$, and a relative shift of $(T_e^{\rm pos} - n_e^{\rm pos}) = 0.0125\psi_N$ in order to have $n_e^{\rm sep} \approx 0.8 \times 10^{20}\,\mathrm{m}^{-3}$ have been set as inputs of these E1 Europed runs, predicting pedestal top temperatures of about 1.6 keV and 1.7 keV in the cases with argon and with neon respectively.
The $\langle n_e \rangle_{\rm sep} \approx 0.8 \times 10^{20}\,\mathrm{m}^{-3}$ is the minimum density that allows sustainable

steady–state divertor conditions in the E1 scenario with reasonable values of the effective charge at the separatrix $\langle Z_{\rm eff}\rangle_{\rm sep}$.

Thus, the core integrated modelling of the E1 scenario has been performed with both argon and neon as seeding gas and using both TGLF and QLK as turbulent transport model. For the E1 runs, the transport equations have been always solved solved within $\rho_{\rm tor} = 0.94$.

Table 5.2 shows the main modelling settings and results of edge and core modelling of the E1 scenario: the effective charge at the pedestal top $Z_{\rm eff}^{\rm ped}$, the effective charge at the separatrix $Z_{\rm eff}^{\rm sep}$, the electron density at the pedestal top $n_e^{\rm ped}$, the seeding gas concentration at the pedestal top $C_{\rm seed.gas}^{\rm ped} = n_{\rm seed.gas}^{\rm ped}/n_{\rm D}^{\rm ped}$, the tungsten concentration at the pedestal top $C_{\rm W}^{\rm ped} = n_{\rm W}^{\rm ped}/n_{\rm D}^{\rm ped}$, and the amount of power radiated within the region $0.85 < \rho_{\rm tor} < 1.0$.
Some discrepancies between core and edge simulations are due to the different modelling approaches and to the numerous input parameters. However, a good compatibility is obtained between edge and core simulations of the E1 scenario, taking into account that the core simulations include two impurities whilst the SOL simulations include only the seeded impurity. The uncertainty on tungsten concentration leads to uncertainty on the power crossing the separatrix with a given main impurity concentration; this could lead to different divertor plasma states. Other differences may be given by the transport model used, the tuning of transport parameters, the inclusion of pinches, and the treatment of impurity transport.
We also notice from table 5.2 that argon requires slightly lower effective charge and lower power radiated within the separatrix than neon to obtain detached divertor plasma. Nevertheless, with both seeded impurities it is possible to obtain detached condition with more than 20 MW crossing the separatrix which is a condition for H–mode operations. A work on core–pedestal–SOL integrated modelling, totally self–consistent in terms of temperature and density profiles, fluxes, and transport coefficients, can be envisaged as future development.

The radial profiles of electron temperature T_e, ion temperature T_i, electron density n_e, toroidal rotation $\omega_{\rm tor}$, safety factor absolute value $|q|$, seeding gas density $n_{\rm seed.gas}$, tungsten density $n_{\rm W}$, effective charge $Z_{\rm eff}$, radiative power density $Q_{\rm rad}$, and radiative power $P_{\rm rad}$ obtained by the four core runs are shown in figure 5.1. In figures 5.2(a) and (b), there are respectively the radial profiles of all power densities and of the total electron and ion powers, only for the TGLF case with argon since the power density and total power profiles related to the other three simulations are similar in shape and size.

We note from figure 5.1(b) that impurities do not accumulate in the

Table 5.2: Comparison between edge and core modelling main results for the E1 scenario.

	Edge modelling	Edge modelling	Core modelling TGLF	Core modelling QLK	Core modelling TGLF	Core modelling QLK
Seeding Gas	Ne	Ar	Ne	Ne	Ar	Ar
$Z_{\text{eff}}^{\text{ped}}$	2.6 – 3.2	2.2 – 3.0	1.7	2.4	1.4	2.0
$Z_{\text{eff}}^{\text{sep}}$	3.0 – 4.2	2.0 – 3.6	2.3	3.9	2.0	3.5
n_e^{ped} $[10^{20}/\text{m}^3]$	1.5 – 1.7	1.5 – 2.1	1.4	1.4	1.4	1.4
$C_{\text{seed.gas}}^{\text{ped}}$ $[10^{-2}]$	4.0 – 15.6	0.5 – 2.9	1.6	3.9	0.4	1.2
$C_{\text{W}}^{\text{ped}}$ $[10^{-5}]$	–	–	5.0	1.0	2.4	6.0
P_{rad} [MW] $0.85 < \rho_{\text{tor}} < 1.0$	6.5 – 8.8	5.3 – 10.0	4.5	8.8	3.0	6.4

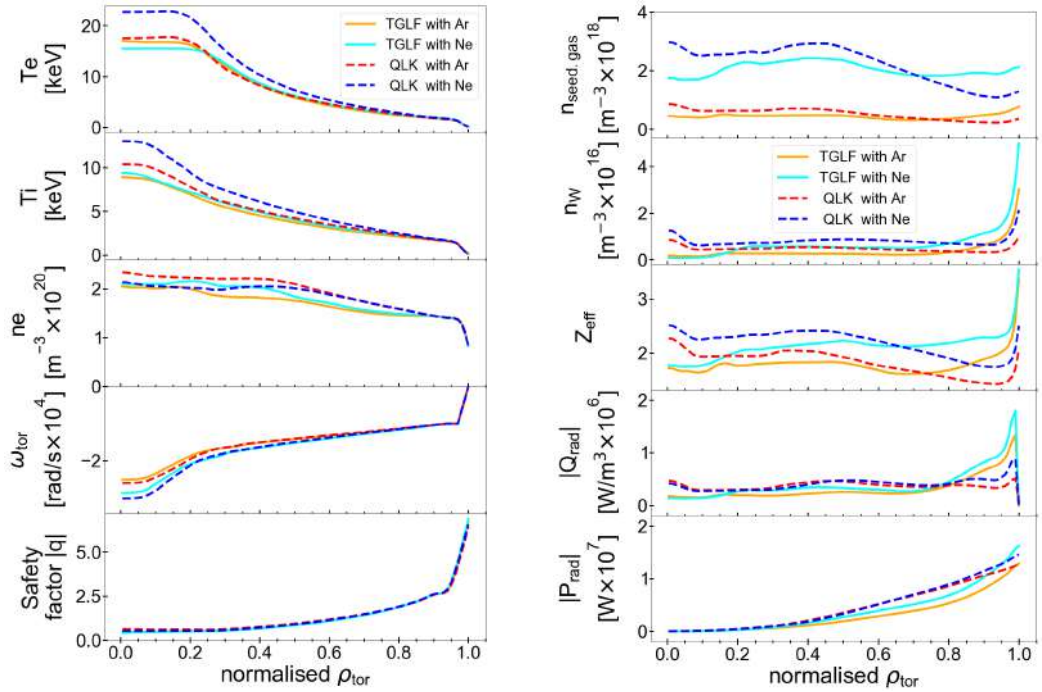

(a) (b)

Figure 5.1: Radial profiles (a) of the electron and ion temperatures, electron density, toroidal rotation, and safety factor absolute value and (b) of the seeding gas and tungsten densities, effective charge, radiative power density, and radiative power for the E1 scenario flat–top phase, with turbulent transport calculated by TGLF SAT2 (solid lines) or by QLK (dashed lines) with argon (reddish lines) or with neon (blueish lines).

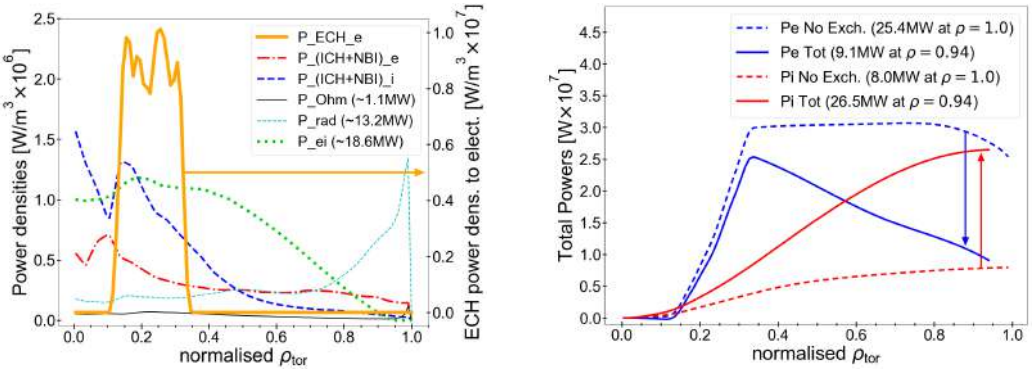

(a) Power densities. (b) Volume integrated powers.

Figure 5.2: (a) Radial profiles of power densities: ECRH power deposited to electrons $P_{\mathrm{ECH}\,e}$, NBI and ICRH power deposited to electrons $P_{(\mathrm{ICH+NBI})\,e}$, NBI and ICRH power deposited to ions $P_{(\mathrm{ICH+NBI})\,i}$, Ohmic power P_{Ohm}, radiative power P_{rad}, and thermal exchange power between electrons and ions P_{ei}. (b) Radial profiles of electron and ion total powers including or not including the thermal exchange power between species.
All these profiles of E1 scenario refer to the TGLF case with argon.

centre significantly. Nonetheless, the effect of differences in electron and deuterium profiles according to the used transport model reflects on the impurity densities considerably. As discussed before, the effective charge values listed in table 5.2 ($Z_{\mathrm{eff}}^{\mathrm{ped}} = 1.4 - 2.4$ and $Z_{\mathrm{eff}}^{\mathrm{sep}} = 2.0 - 3.9$) cover a broad range and are quite compatible with the SOL modelling values.

From figure 5.1(a), we notice that the temperature profiles are quite in good agreement, with the exception of the QLK run with neon. Some discrepancies arise in the density profiles, due to both the differences in the impurity profiles and the change of turbulent transport model. The different predictions in electron density profiles by QLK and by TGLF are a known question, already dealt with for the old DTT configuration, as extensively discussed in [18]. Especially the excessive n_e flatness in the inner region of the plasma, such as in the present QLK run with neon, is not validated, as found by a comparison of QLK stand–alone runs with gyrokinetic results obtained by the GENE code [42, 43] reported in [18]. Although the TGLF results should be more reliable, both QL models should be approached with care inside $\rho_{\mathrm{tor}} = 0.4$, where the power density is very high and the $|q|$ profile is quite lower than 1 in these simulations without sawteeth. Excluding the unlikely case with QLK and neon, $T_{e_0} \approx 15.5$–$19.0\,\mathrm{keV}$, $T_{i_0} \approx 8.9$–$11.7\,\mathrm{keV}$, and $n_{e_0} \approx (2.05 - 2.35) \times 10^{20}/\mathrm{m}^3$ values are reached at the plasma centre.

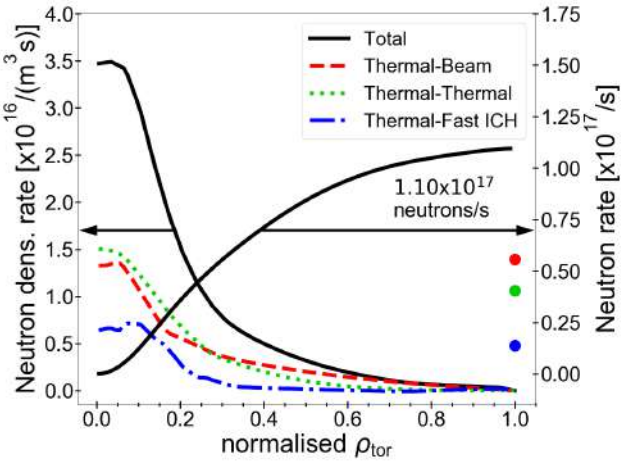

Figure 5.3: Radial profiles of neutron density rates, where neutrons are produced by fusion reactions between: two thermal nuclei (green), between a thermal nucleus and a fast nucleus of the NBI beam (red), and between a thermal nucleus and a fast nucleus of the ICRH minority species (blue), any pair of nuclei (black). The radial profile of the total neutron rate is also displayed (black), with points indicating the three contributions to it. These profiles of the E1 scenario refer to the QLK case with argon.

In any case, the electron temperature results much larger than the ion temperature over almost all plasma radius. Notwithstanding the high thermal exchange power due to the collisional coupling P_{ei} flowing from electrons to ions, the ion temperature profile is unable to grow, because the ion temperature gradient mode (ITG) threshold is low for $T_e/T_i > 1$ and a strong ion stiffness is predicted by the turbulent transport model. We highlight that the E1 scenario has been found to be dominated by the ITG modes over all the radial profile. Raising the electron density in order to strengthen the collisional coupling could be an attempt to balance more T_e and T_i, although limited by the ECRH cut–off at $n_e = 3.58 \times 10^{20}\,\mathrm{m}^3$. Nevertheless, since the ITG threshold is weakly dependent on the temperature ratio when $T_e/T_i > 1$, this would lead to a decrease of T_e rather than a T_i gain.

As shown in figure 5.2, we notice that the ohmic power is quite negligible $P_{\mathrm{Ohm}} \approx 0.8 - 1.1\mathrm{MW}$, the core radiated power $P_{\mathrm{rad}} \approx 12.8 - 16.1\mathrm{MW}$ is around the 29–36% of the total power, and a huge amount of collisional power $P_{ei} \approx 18.6 - 21.9\mathrm{MW}$ flows from electrons to ions.

In figure 5.3, the radial profiles of the neutron density rate and of its three contributions as well as of the integrated neutron rate are displayed

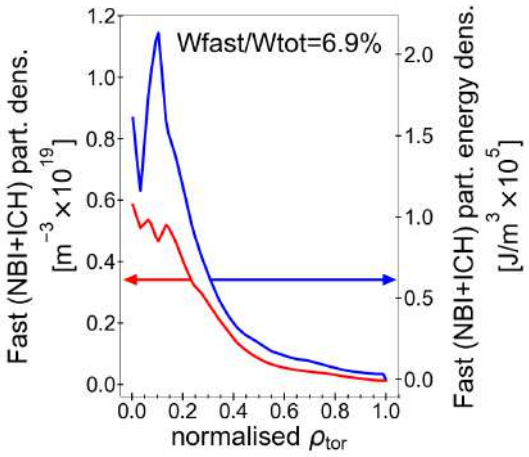

Figure 5.4: Radial profiles of density and energy density of energetic particles due to the NBI and ICRH systems. These profiles of the E1 scenario refer to the TGLF case with argon.

for the QLK case with argon. Similar trends of neutron contributions can be observed in all E1 simulations: in any case, the thermal–thermal and the thermal–beam components are dominant. The total neutron rate results in the range $(0.9 - 1.3) \times 10^{17}$ neutrons/s. This order of neutron loads can be easily withstood by the neutron shields currently planned for DTT.

In figure 5.4, radial profiles of the particle and energy densities of the energetic ions are displayed for the run with TGLF and argon. Similar profile shapes has been found for the other E1 cases. The energetic particles, which are due to the NBI and ICRH systems, own an energy amount in the range of 5–7 % of the total plasma energy.

The radial profiles of current densities are shown in figure 5.5. They refer to the run with TGLF and argon, but all other cases exhibit alike profiles. The total current density J is mainly due to the inductive contribution.

In the examined core simulations of the E1 scenario, triangularity values in the range $\delta_{95} = 0.31 - 0.33$, elongation values in the range $\kappa_{95} = 1.62 - 1.64$, and safety factor values in the range $|q_{95}| = 2.8 - 2.9$ have been calculated at the flux surface which contains the 95 % of the poloidal flux. In the present DTT configuration the $|q_{95}|$ value is close to 3, larger than in the previous machine design [18], reducing therefore the disruption risk [107].

Furthermore, for these E1 simulations, an energy confinement time and an H–factor (with $P = P_{\mathrm{sep}}$) respectively equal to $\tau_E = (0.3 - 0.5)$ s and $H_{98} = 0.8 - 1.1$ have been calculated.

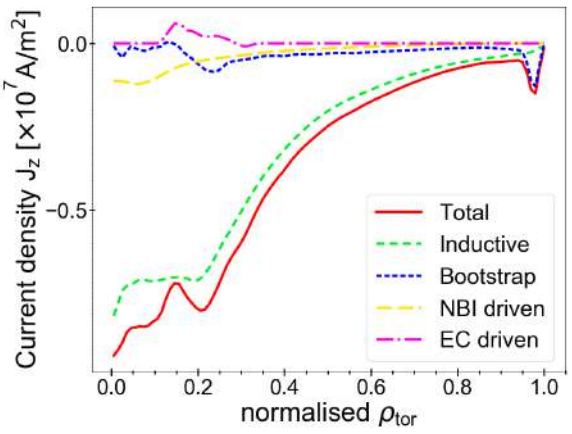

Figure 5.5: Radial profiles of current densities in the SN E1 scenario: total curren J, inductive current J_{ind}, bootstrap current J_{BS}, NBI drive current J_{NB}, and EC drive current J_{EC}.

5.3.1 EC current drive and power deposition

The safety factor radial profiles of the E1 scenario flat top phase are characterised by $|q| = 1$ located in the outer half of the plasma ($\rho_{\text{tor}} \approx 0.53 - 0.58$) and by inner values of $|q|$ pretty lower than 1 (with $|q_0| \approx 0.5$), as observed in figure 5.1(a). Such profiles indicate strong $n = 1$ $m = 1$ ideal MHD activity and as such sawtooth crashes would likely take place before these conditions are reached. It would affect a wide plasma region, and then the whole plasma evolution. Therefore, from one side we started to integrate the sawteeth evolution in the DTT E1 scenario simulations, as described in section 5.3.2, and, on the other side, we performed an initial study regarding the tailoring of the q profile by varying the EC current drive (ECCD) and the EC power deposition localisation, as discussed in this section. The aim of the analysis here reported is to investigate the possibility of lowering the $|q| = 1$ radial location ρ_1 and guarantee that it does not exceed $\rho_{\text{tor}} = 0.5$, thus reducing the crash extension and improving the scenario against the effect of the sawtooth oscillations. In order to achieve such purpose, the EC current can be driven to increase the q values in the plasma region characterised by $|q| < 1$, or to decrease the q values outside ρ_1, lowering then the slope of the q profile in the inner region.

Exploiting the wide flexibility of the EC system, we tested different angle sets for DTT gyrotrons, included some drastic cases (e.g. with depositing the whole power extremely outside), in order to investigate how much

ECRH&ECCD could affect the safety factor in this scenario. Thus, simulations have been carried out setting the EC launching angles in order to test both inner EC localisation ($\rho_{\rm tor} < 0.5$) with counter–ECCD, with the aim of increasing the q values in the inner half of the plasma, and outer EC deposition with co–ECCD, in order to lower the q gradient in the region outside the $|q| = 1$ location.
The ECCD effects on q profile resulted negligible with a counter–current inside $\rho_{\rm tor} = 0.5$ and quite small with a co–current outside $\rho_{\rm tor} = 0.5$. It is not surprising, since the EC current and the other non–inductive currents are significantly lower than total current, as displayed in figure 5.5. The major impact is actually due to the power deposition location, which deeply modifies the electron temperature gradient and the conductivity. However, a co–ECCD with EC localisation outside $\rho_{\rm tor} = 0.5$ has been found to be only slightly beneficial on $|q| = 1$ placement.

After a trade–off work, we selected a feasible and reasonable set of EC launching angles which guarantees pretty high performance with a better q profile.
In relation to the EC launcher positioning of [135], the toroidal angles have been set in the following ranges: $-25.0°$ for UP beams, $(+17.0°) - (+25°)$ for EQT beams, and $(+14.5°) - (+24.5°)$ for EQB beams. The poloidal angles have been set in the following ranges: $(+40.0°) - (+42.0°)$ for UP beams, $(-15.0°) - (-8.0°)$ for EQT beams, and $(-10.0°) - (-6.0°)$ for EQB beams. With these settings, the ECRH power density is spread between $0.05 \leq \rho_{\rm tor} \leq 0.7$, as shown in figure 5.6.

The electron density and the ion temperature profiles are barely affected in a small region close to the plasma centre by this EC deposition displacement.
The electron temperature instead is considerably reduced within $\rho_{\rm tor} \approx 0.3$, although the central value $T_{e0} \sim 10\,\text{keV}$ is still high. Thanks to this new ECH distribution, the $|q| = 1$ location moves inward of about $\Delta\rho_{\rm tor} \approx 0.05$ (from $\rho_{\rm tor} \approx 0.53$ to $\rho_{\rm tor} \approx 0.48$). Although it is a small improvement, actually it impacts significantly and positively on the sawteeth and, hence, on the plasma stability.

In addition, such spread EC power deposition implies relevant advantages for the fuelling efficiency of the DTT pellets, as examined in [136].

On the other hand, an outer ECRH power deposition could lead to a risky tungsten accumulation in the plasma centre and hence should be handled carefully. As shown in figure 5.7, we verified that for the new gyrotron settings the central W density does not grow too much.

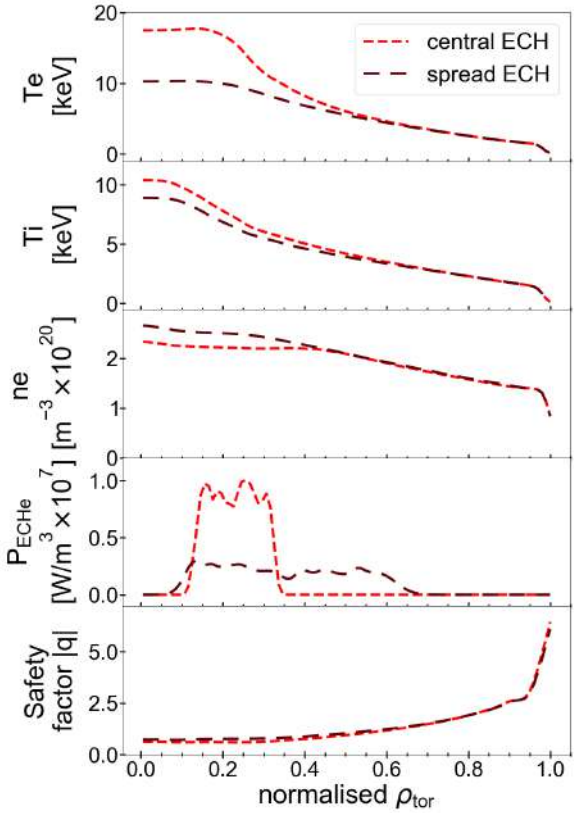

Figure 5.6: Comparison of electron temperature, ion temperature, electron density, ECRH power density, and safety factor radial profiles using different gyrotron angles. These profiles refer to the QLK cases with argon.

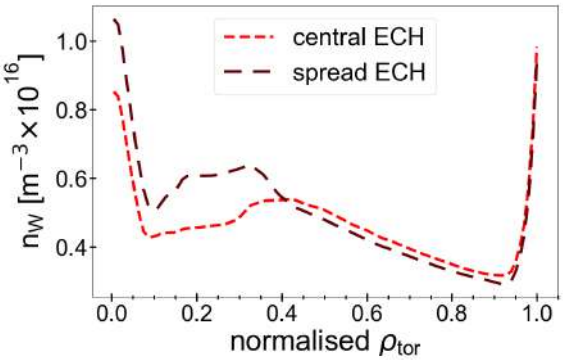

Figure 5.7: Comparison of tungsten density radial profile using different gyrotron angles. These profiles refer to the QLK cases with argon.

5.3.2 Sawteeth

An analysis of the sawtooth impact on the E1 scenario kinetic profiles and on the safety factor has been carried out for the first time in DTT. Specifically, sawteeth have been included into the JETTO simulation with QLK as turbulent transport model, with argon as seeding gas and with a spread ECRH power deposition, described in the previous section 5.3.1.

In spite of the safety factor enhancement due to the new set of gyrotron angles described in section 5.3.1, the low value of $|q_{95}|$ and the $|q|$ profiles shown in figure 5.6 suggest an important sawtooth activity.

The Porcelli sawtooth crash trigger model discussed in [126], and integrated in the code suite, has been used for the identification of the instability onset. The coefficients related to the four implemented stability criteria have been set to the default values $C_f = C^* = C_\rho = 1$ and $C_h = 0.4$. Particularly, C_f multiplies the contribution of fast ion energy, C_ρ is a numerical factor multiplying the thermal Larmor radius in the ion–kinetic regime, C^* quantifies the role of the ion and electron diamagnetic frequency in the ST stabilisation associated to the kink growth rate, and finally C_h quantifies the role of the fast ion energy on the ST stabilisation with respect to the core plasma potential energy.

Initially, the Kadomtsev complete reconnection model [137, 138] has been employed to predict the relaxed temperature, density, and $|q|$ profiles after a sawtooth crash. Therefore, the relaxed $|q|$ profile flattens to unity up to the mixing radius $\rho_{\text{mix}} \approx 0.55$, which describes the portion of plasma involved in the reconnection process and which is somewhat larger than $\rho_1 \approx 0.45$, as shown in figure 5.8(a). The electron temperature evolution, displayed in figure 5.8(b), shows clearly sawtooth oscillations.
This simulation with a complete reconnection foresees a long sawtooth period of about 0.72 s (i.e. $f_{\text{ST}} \approx 1.4$ Hz) because of the stabilising effect of the fast particles coming from the ICRH and NBI heating systems. With a complete reconnection, the predicted crash amplitude of ~ 5.1 keV is also quite large, with a drop of the central temperature of 44 %. This result was expected since a ρ_1 close to $\rho_{\text{tor}} = 0.5$ entails a mixing radius ρ_{mix} in the outer half of the plasma, which means a very large portion of the plasma involved in the reconnection process.

On the other hand, it is well known that the complete flattening of the $|q|$ profiles described by the basic Kadomtsev reconnection model does not always occur experimentally, and $|q_0|$ can stay below 1 after the crash. The large $|q| = 1$ radius predicted for the E1 scenario in the previous section is an indication that the same could happen for DTT [139, 140].

Such situation can be modelled considering a very simple “incomplete”

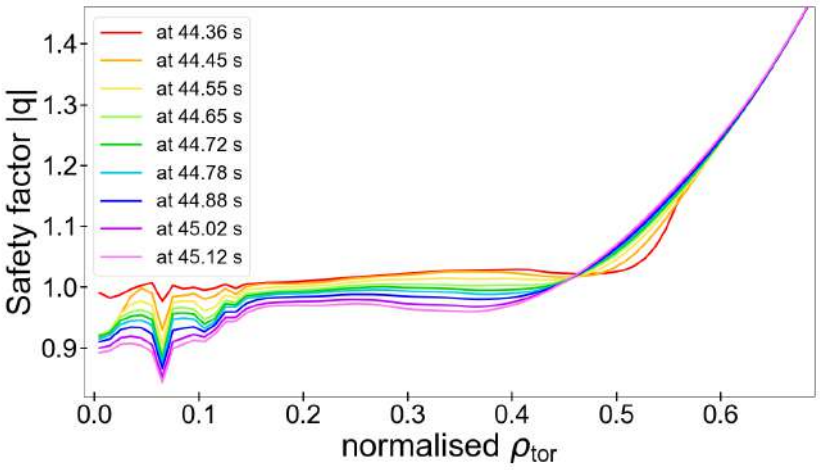

(a) Relaxation of the $|q|$ profile.

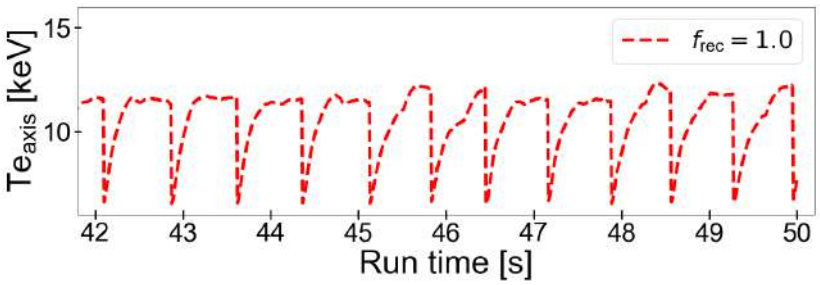

(b) Time evolution of T_{e_0}.

Figure 5.8: Time evolution (a) of the $|q|$ profile after a sawtooth crash and (b) of the electron temperature at the plasma centre T_{e_0}, using a complete reconnection model (i.e. with $f_{\text{rec}} = 1.0$).

Kadomtsev reconnection, where the relaxed profile is a weighted average between the pre–crash and the completely reconnected post–crash profiles. The weight is the reconnection fraction parameter f_{rec}, where a complete reconnection corresponds to $f_{\mathrm{rec}} = 1$.

Therefore, we repeated the simulation described so far, but employing an incomplete reconnection with a value of $f_{\mathrm{rec}} = 0.8$.

From figure 5.9(a), where the $|q|$ profile relaxation after a sawtooth crash predicted is shown, we notice that the q_0 value remains always below 1 in this new run, as expected. Figure 5.9(b) displays the electron temperature evolution for this case with $f_{\mathrm{rec}} = 0.8$, resulting in a sawtooth period of 0.59 s (i.e. $f_{\mathrm{ST}} \approx 1.7\,\mathrm{Hz}$) and a crash amplitude of 4.2 keV. The effect of the incomplete reconnection relaxation on the sawtooth activity predictions is a shortening of the sawtooth period and a reduction of the crash amplitude, however, the central temperature drop is still about 35 %.

In summary, this first analysis predicts an important sawtooth activity for the described E1 scenario flat–top phase, mainly due to the large ρ_1. The mixing radius larger than half radius also suggests that an incomplete reconnection is likely to take place as relaxation process. The incomplete reconnection changes the sawtooth impact increasing its frequency, so predicitng plasma scenario less prone to the onset of MHD instability as the neoclassical tearing modes which can lead to loss of confinement [141]. Describing the incomplete reconnection relaxation by a more accurate reconnection model could also obtain a beneficial reduction of the ρ_1 during sawtooth oscillations. Therefore, simulations considering a more accurate incomplete reconnection model, like the one discussed in [126], are planned for the future.

5.3.3 Edge Localised Modes

In this section, the main features of type–I ELMs are derived for the reference DTT E1 scenario using existing scalings. This will serve as guideline for future edge and plasma wall–interaction studies which are strongly impacted by type–I ELMs in H–mode.
Plasma profiles and values of the TGLF simulation with argon and central ECRH reported in section 5.3 were used here as reference case. Since the employed scalings only depend on pedestal parameters, the choice of a specific run actually does not affect the results. To evaluate the impact of type–I ELMs on DTT, the approach in [142] is followed. Type–I ELMs decrease the plasma energy by typically $\Delta W_{\mathrm{ELM}}/W_{\mathrm{ped}} = 3 - 20\%$, where W_{ped} is the the pedestal energy, in timescales of few hundred μs in present divertor

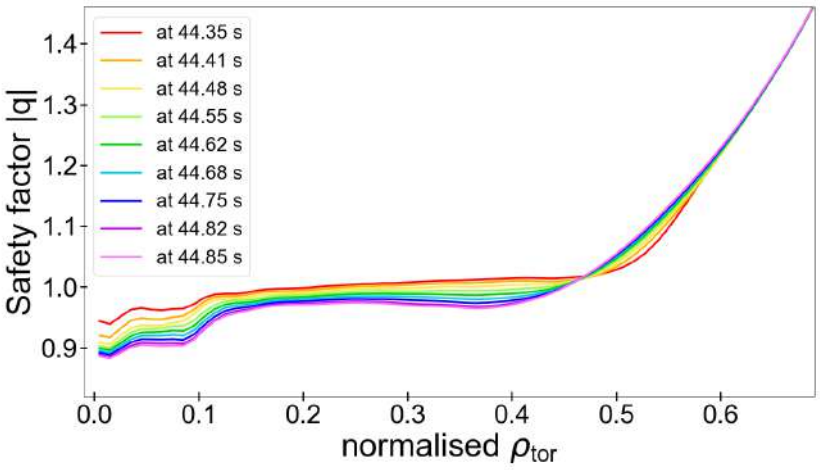

(a) Relaxation of the $|q|$ profile.

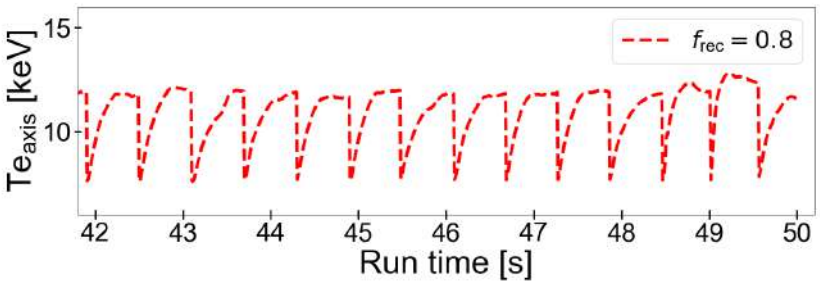

(b) Time evolution of T_{e_0}.

Figure 5.9: Time evolution (a) of the $|q|$ profile after a sawtooth crash and (b) of the electron temperature at the plasma centre T_{e_0}, using an incomplete reconnection model with $f_{\text{rec}} = 0.8$.

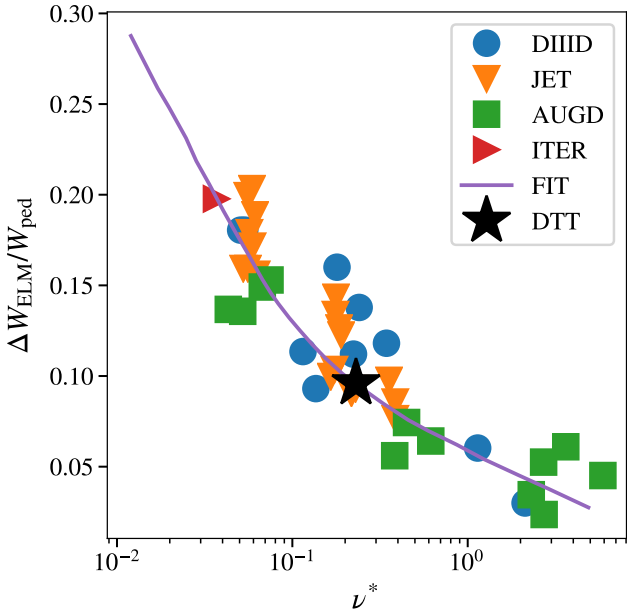

Figure 5.10: Multi–machine scaling of the relative energy loss $\Delta W_{\mathrm{ELM}}/W_{\mathrm{ped}}$ during type–I ELMs as a function of the normalised pedestal collisionality ν^*.

tokamaks. ΔW_{ELM} and W_{ped} are defined as follows

$$\Delta W_{\mathrm{ELM}} = \left(3\left\langle n_{\mathrm{ped}}\right\rangle \Delta T_{\mathrm{ped,ELM}} + 3\left\langle T_{\mathrm{ped}}\right\rangle \Delta n_{\mathrm{ped,ELM}}\right) V_{\mathrm{ELM}}$$
$$W_{\mathrm{ped}} = 3 n_{\mathrm{ped}} T_{\mathrm{ped}} V_{\mathrm{plasma}}$$

where V_{ELM} is the volume of plasma affected by the ELM, $\Delta n_{\mathrm{ped,ELM}}$ and $\Delta T_{\mathrm{ped,ELM}}$ are the density and temperature drops at the pedestal top caused by the ELMs, and V_{plasma} the total plasma volume. A multi–machine scaling shows that $\Delta W_{\mathrm{ELM}}/W_{\mathrm{ped}}$ is a function of the normalised pedestal collisionality $\nu^* \approx 0.46\, q_{95}\, R[\mathrm{m}]/T[\mathrm{keV}]$ (see figure 5.10) [127]. The reference E1 scenario of DTT has a normalised pedestal collisionality (at $\rho_{\mathrm{tor}} = 0.94$) of about $\nu^*_{\mathrm{DTT}} = 0.23$ and hence $\Delta W_{\mathrm{ELM}}/W_{\mathrm{ped}} \approx 9.6\%$. Given $W_{\mathrm{ped}} = 3.56\,\mathrm{MJ}$, $\Delta W_{\mathrm{ELM}} = 0.34\,\mathrm{MJ}$.

The relative energy loss during type–I ELMs is then used to determine the maximum energy fluence to the outer divertor $\varepsilon_{\parallel}^{\mathrm{peak}}$ in $\mathrm{MJ/m^2}$ using the scaling proposed in [128], expressing $n_{e,\mathrm{ped}}$ in $[10^{20}\mathrm{m}^{-3}]$, $T_{e,\mathrm{ped}}$ in [keV], ΔW_{ELM} in [%], and R_{geo} in [m]:

$$\varepsilon_{\parallel}^{\mathrm{peak}} = 0.28 \pm 0.14 \cdot n_{e,\mathrm{ped}}^{0.75\pm0.15} T_{e,\mathrm{ped}}^{0.98\pm0.1} \Delta W_{\mathrm{ELM}}^{0.52\pm0.16} R_{\mathrm{geo}}^{1\pm0.4}$$

which results for DTT to be $\varepsilon_{\parallel}^{\mathrm{peak,DTT}} = 2.10\,\mathrm{MJ/m^2}$ (figure 5.11).

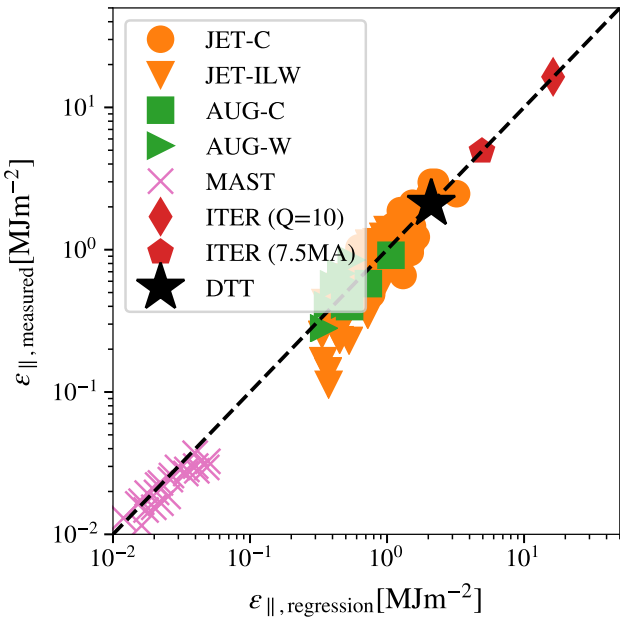

Figure 5.11: Multi–machine scaling of the maximum energy fluence during type–I ELMs [128].

Finally, the time scales of the ELM heat load is approximated by a triangular waveform with a decay time $\tau_{\mathrm{decay}} = 2\,\tau_{\mathrm{ELM}}$ in line with the free–streaming–particle models [129] (figure 5.12). The rise time τ_{ELM} is well correlated with the time for the ion transport from the pedestal to the divertor $\tau_{\parallel} = 2\pi R q_{95}(1 + (3/2)^{0.5}\nu^{*})/C_{s,\mathrm{ped}}$ where $Cs, \mathrm{ped} \approx \sqrt{kT_e/m_i}$ is the ion sound speed.
The results for DTT are $\tau_{\parallel,\mathrm{DTT}} = 250\,\mu\mathrm{s}$ and hence $\tau_{\mathrm{ELM,DTT}} = 591\,\mu\mathrm{s}$.

The ELM power deposition can be calculated in time using the Free Streaming Model (FSM)[143] as follows [144]:

$$q_{\parallel,\mathrm{FS}}(t) = \Gamma_{\parallel,\mathrm{FS}}(t) T_e^{\mathrm{ped}} \left[\left(\frac{\tau}{t} \right)^2 + 1 \right]$$

where $q_{\parallel,\mathrm{FS}}$ and

$$\Gamma_{\parallel,\mathrm{FS}}(t) = \frac{2\, n_e^{\mathrm{ped}}\, c_s^{\mathrm{ped}}}{L_{\parallel}/L_{\mathrm{ELM}}} \left(\frac{\tau}{t} \right)^2 \exp\left[- \left(\frac{\tau}{t} \right)^2 \right]$$

are the parallel heat flux and the parallel ion flux at the divertor target surface location respectively. The resulting evolution of the parallel heat flux in DTT can be seen in figure 5.13.

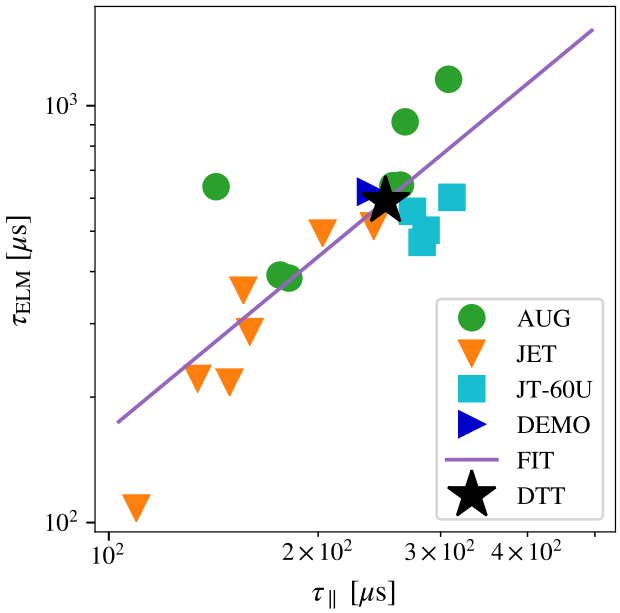

Figure 5.12: ELM–rise time τ_{ELM} as a function of time for the ion transport from the pedestal to the divertor $\tau_{\|}$.

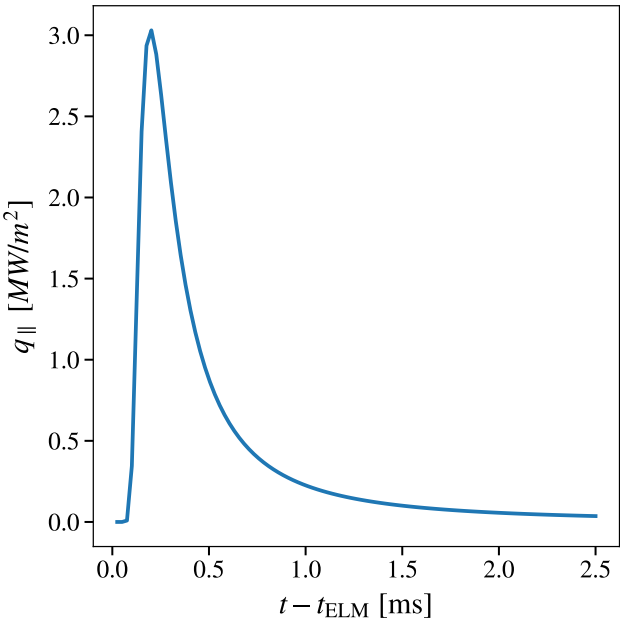

Figure 5.13: Type–I ELM evolution of the parallel heat flux $q_{\|}$ in DTT.

More modelling work will be needed to assess the possible ELM frequency, since simple scalings such as reported in [130] are known to largely underestimate the ELM frequency in present devices.

As a final remark, since the density values at the separatrix are quite high ($n_e^{\text{sep}} \approx 0.8 \times 10^{20}\,\text{m}^{-3}$), we could suspect the DTT E1 scenario to be in a type–II or small ELM regime [145]. Thus, a more detailed analysis on ELM stability and their inclusion in the integrated modelling are envisaged for the future, but beyond the goal of this work.

5.3.4 EM configuration consistency

To ensure the reliability of our modelling predictions, a key aspect is to guarantee the consistency between the electromagnetic configuration and plasma profiles calculated by transport models. Thus, a validation work of the coupling between the CREATE–NL and JETTO has been carried out for the SN flat–top configuration in the E1 scenario.
CREATE–NL is a 2D Finite Element Method (FEM) code able to solve numerically Grad–Shafranov equation under the axisymmetric hypothesis. CREATE–NL is able to work both with "bell–shaped" plasma current profiles [146] and with generic profiles for what concerns poloidal current function f and plasma pressure p.

The plasma boundary, as mentioned above, and the product between the major radius R_0 and the vacuum toroidal field value B_0 at the plasma centre provided by CREATE–NL calculations are used as settings for the integrated core simulations. In turn, the CREATE–NL runs require plasma profiles as input. Particularly, the starting reference DTT E1 SN plasma equilibria supplied by CREATE–NL were obtained assuming hypothetical bell–shape plasma profiles. Clearly, the integrated modelling work treated in the previous sections led to quite different profiles, as pointed out by the comparison figure 5.14. Therefore, an external feedback from CREATE–NL was essential to verify the configuration feasibility with the computed transport profiles.

A recalculation of the currents in the Central Solenoid (CS) and Poloidal Field (PF) coils required to achieve the desired plasma shape and the flat–top plasma boundary flux with the profiles determined by JETTO has been performed. Particularly, this consistency check between the control coil system capabilities and JETTO plasma profiles has been carried out for three simulations of the E1 scenario: the TGLF case with argon and central ECRH shown in figure 5.1, the QLK case with argon and central ECRH shown in figure 5.1 and in figure 5.6, and the QLK case with argon and spread ECRH shown in figure 5.6.

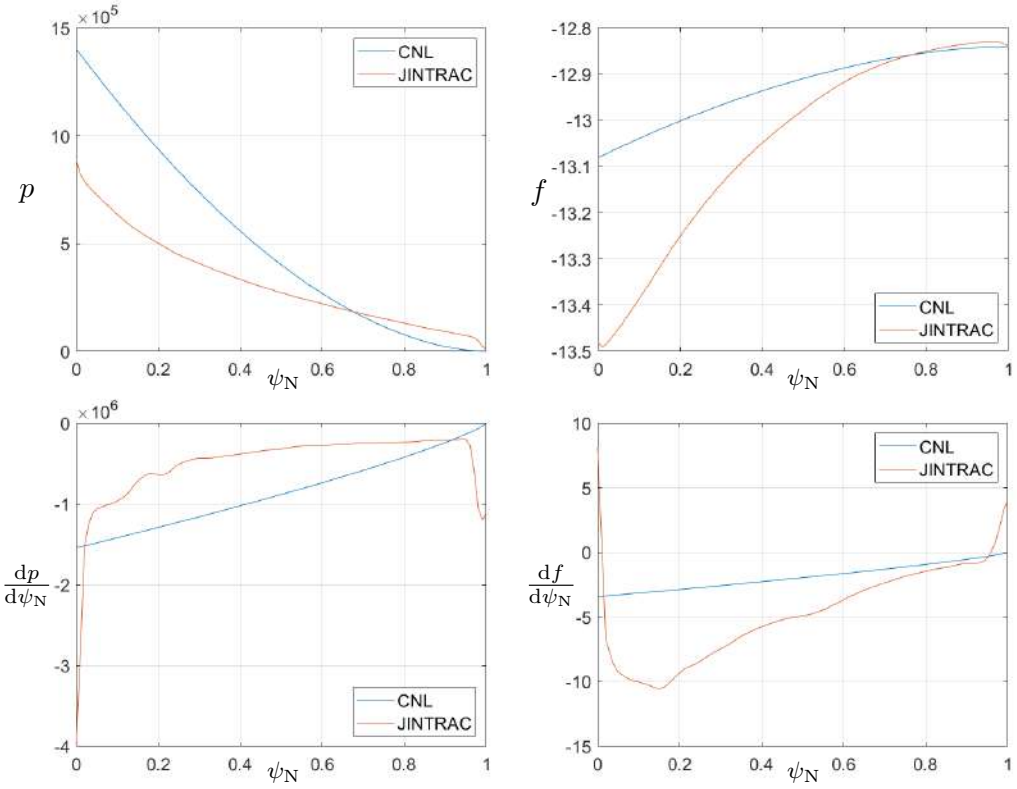

Figure 5.14: Comparison between CREATE–NL (CNL) and JETTO radial profiles of the pressure p, the f function, the pressure gradient $\mathrm{d}p/\mathrm{d}\psi_\mathrm{N}$, and the f gradient $\mathrm{d}f/\mathrm{d}\psi_\mathrm{N}$ for the E1 scenario during the flat–top phase. Bellshape plasma profiles are used as input in the CREATE–NL run. JETTO profiles refer to the QLK case with spread ECRH deposition.

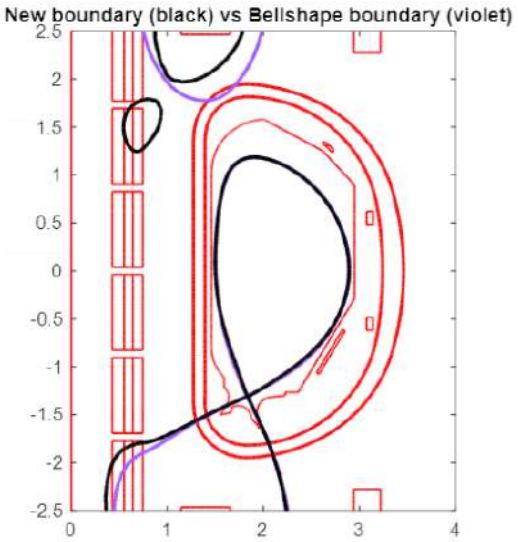

Figure 5.15: Comparison of the plasma boundary between the starting reference equilibrium calculated by CREATE–NL assuming bellshape plasma profiles (in violet) and the equilibrium recalculated by CREATE–NL in order to obtain the desired plasma shape assuming the JETTO plasma profiles (in black).

In all these cases, the same plasma shape with the JETTO plasma profiles has been recovered with good agreement, as displayed in figures 5.15 for an example case. For every plasma profile set, significant variations of both the CS and PF coil currents are needed, as shown in figure 5.16.
Nevertheless, even though these current changes are remarkable, they lie in a feasible range.

Finally, the validation of the output profiles coming from this new iteration in CREATE–NL with the JETTO inputs against the JETTO profiles has been also done to guarantee the goodness of the procedure, as reported in figure 5.17 for an example case.

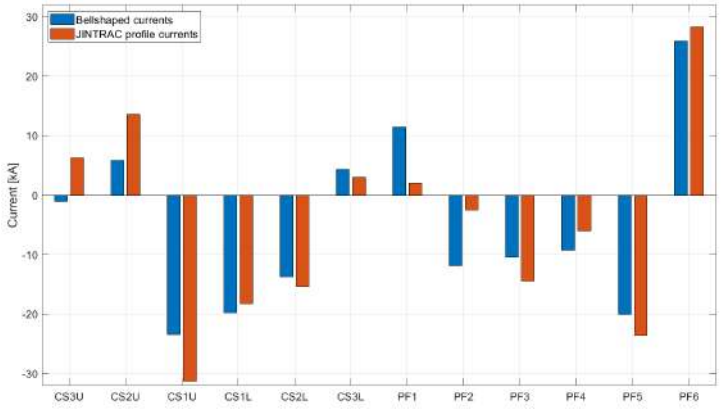

(a) JETTO run: TGLF case with Ar and central ECRH.

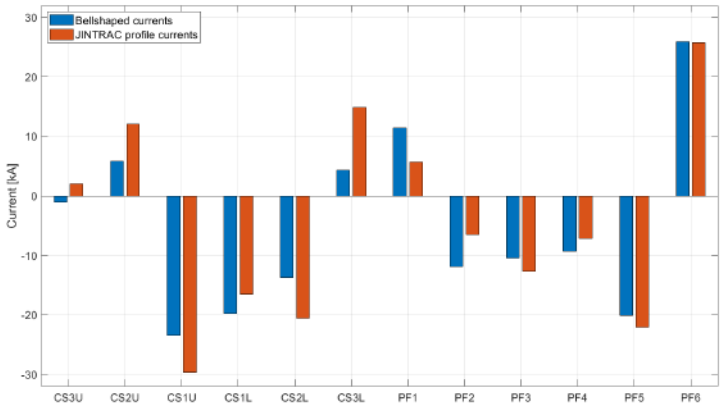

(b) JETTO run: QLK case with Ar and central ECRH.

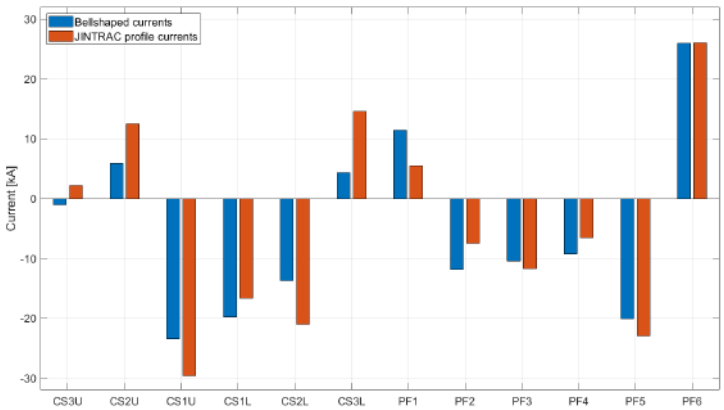

(c) JETTO run: QLK case with Ar and spread ECRH.

Figure 5.16: Comparison of the CS/PF currents between the starting reference equilibrium calculated by CREATE–NL assuming bellshape plasma profiles (in blue) and the equilibrium recalculated by CREATE–NL in order to obtain the desired plasma shape assuming the JETTO plasma profiles (in red), for three different JETTO runs.

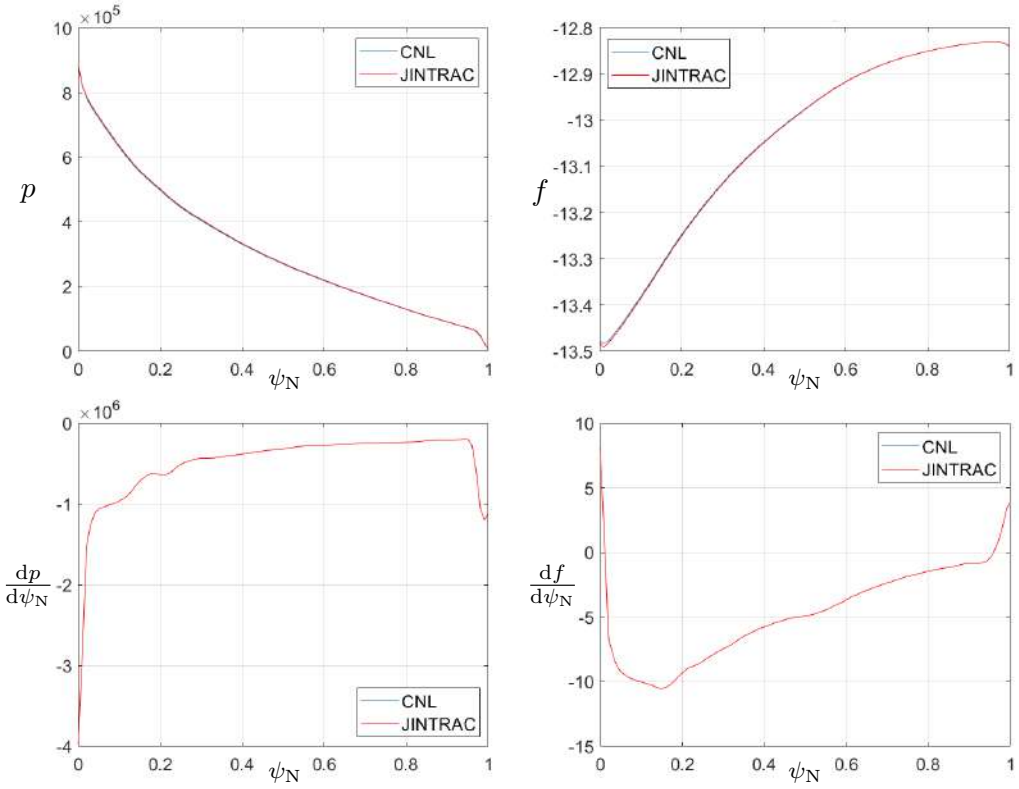

Figure 5.17: Comparison between JETTO radial profiles of the pressure p, the f function, the pressure gradient $\mathrm{d}p/\mathrm{d}\psi_\mathrm{N}$, and the f gradient $\mathrm{d}f/\mathrm{d}\psi_\mathrm{N}$ for the E1 scenario during the flat–top phase and CREATE–NL (CNL) profiles achieved with recalculated coil currents. JETTO profiles refer to the QLK case with spread ECRH deposition.

5.4 The C1 scenario

The C1 scenario works with full vacuum toroidal magnetic field equal to $B_{\text{tor}} = 5.85\,\text{T}$, but with plasma reduced current $I_{\text{pl}} = 4.0\,\text{MA}$.
In the C1 scenario, the auxiliary heating includes:

- 16 gyrotrons to provide a total ECRH power to the plasma of about 14.4 MW with beams in O–mode;
- 1 module with 2 RF antennas to provide a total ICRH power to the plasma of about 3.0 MW.

The ICRH heating profiles have been calculated by PION with the general settings described before, while a prescribed ECRH power deposition equal to the corresponding profile foreseen in [18] has been included.

The C1 pedestal has been calculated by a specific Europed modelling using in input temperatures at the separatrix of $T_e^{\text{sep}} = T_i^{\text{sep}} = 100\,\text{eV}$, a pedestal top density of $n_e^{\text{ped}} = 1.4 \times 10^{20}\,\text{m}^{-3}$, a value of $\beta_{\text{pol}} = 0.65$, a relative shift of $(T_e^{\text{pos}} - n_e^{\text{pos}}) = 0.006\psi_N$ in order to have $n_e^{\text{sep}} \approx 0.45 \times 10^{20}\,\text{m}^{-3}$, neon as impurity, and an effective charge of Z_{eff}, obtaining a temperature of 2.3 keV at the pedestal top ($\rho_{\text{tor}} = 0.89$).

In the C1 scenario core simulation, performed using the TGLF SAT2 model only, neon as seeding gas and tungsten have been modelled, setting $Z_{\text{eff}} = 1.4$ and $n_{\text{W}}/n_{\text{Ne}} = 0.03$ as initial conditions.

All these settings make the core modelling predictions compatible with radiation and impurity content values in edge simulations convergent to a detached state. In table 5.4, the main modelling settings and results of edge and core modelling of the DTT first plasma are listed.

The C1 scenario, such as the full power one, has been found to be ITG dominant at all radii. Figure 5.18 shows the radial profiles of the electron temperature, ion temperature, electron density, and safety factor achieved in this TGLF simulation of the C1 scenario.
Although the ECRH power deposition is quite central, the ratio T_e/T_i and the density peaking are much lower than those of the TGLF case with neon and central ECH deposition in the E1 scenario. It was expected due to the reduced ECH power and to the lack of the NBI particle source. The Greenwald density fraction $\bar{n}_e/n_{\text{Gr}} \approx 0.52$ (still well within safety margins) is similar to values of the E1 scenario, since the n_e profile flatness offsets the effect of using the same pedestal top density of the E1 case at a reduced plasma current. The total neutron rate is about 1.7×10^{16} neutrons/s in the C1 scenario.

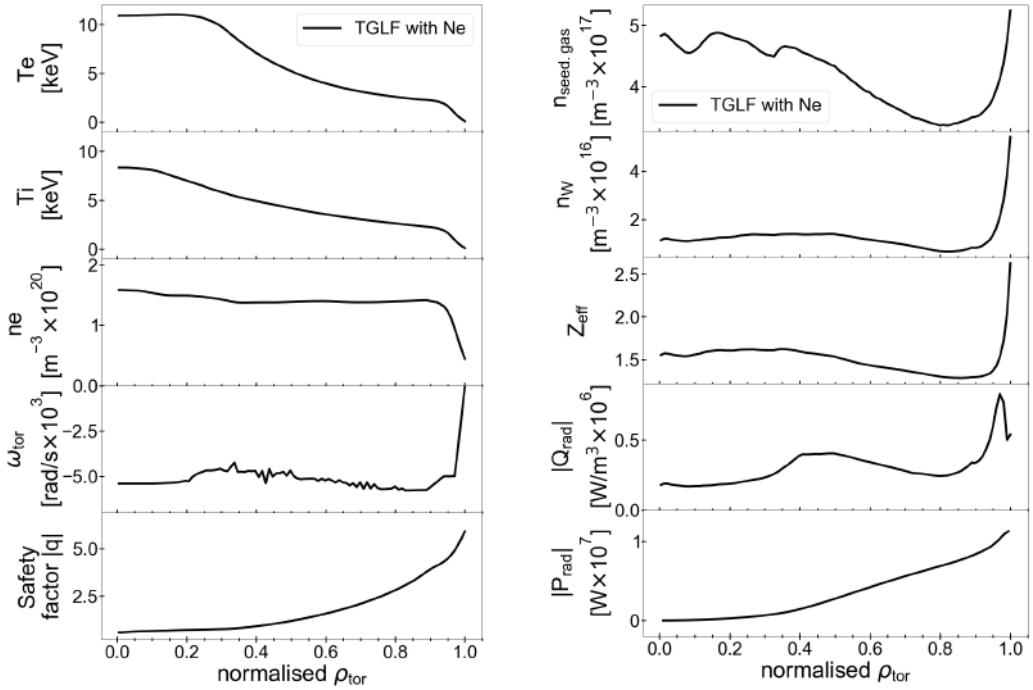

(a) (b)

Figure 5.18: Radial profiles (a) of the electron and ion temperatures, electron density, toroidal rotation, and safety factor absolute value and (b) of the seeding gas and tungsten densities, effective charge, radiative power density, and radiative power for the C1 scenario flat–top phase.

Table 5.3: Comparison between edge and core modelling main results for the C1 scenario.

Run	Edge	Core TGLF
Seeding Gas	Ne	Ne
$Z_{\text{eff}}^{\text{ped}}$	1.5 – 3.3	1.3
$Z_{\text{eff}}^{\text{sep}}$	2.3 – 4.0	2.6
n_e^{ped} $[10^{20}/\text{m}^3]$	1.3 – 1.4	1.4
$C_{\text{seed.gas}}^{\text{ped}}$ $[10^{-2}]$	0.4 – 3.8	0.25
$C_{\text{W}}^{\text{ped}}$ $[10^{-5}]$	–	6.0
P_{rad} [MW] $0.85 < \rho_{\text{tor}} < 1.0$	2.8 – 4.0	9.9

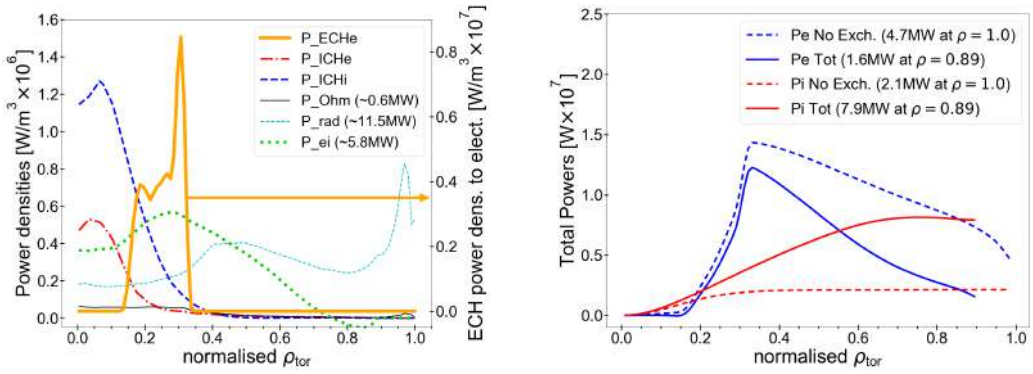

(a) Power densities.

(b) Volume integrated powers.

Figure 5.19: (a) Radial profiles of power densities: ECRH power deposited to electrons $P_{\text{ECH}\,e}$, ICRH power deposited to electrons $P_{\text{ICH}\,e}$, ICRH power deposited to ions $P_{\text{ICH}\,i}$, Ohmic power P_{Ohm}, radiative power P_{rad}, and thermal exchange power between electrons and ions P_{ei} for the C1 scenario. (b) Radial profiles of electron and ion total powers including or not including the thermal exchange power between species for the C1 scenario.

For the C1 scenario, the energy confinement time and the H–factor (with $P = P_{\rm sep}$) resulted respectively $\tau_E \approx 1.3\,{\rm s}$ and $H_{98} \sim 1.6$.

5.5 The A1 scenario

The DTT first experimental plasma is the A1 scenario and will operate at half magnetic field $B_{\rm tor} = 3\,{\rm T}$ and at reduced current $I_{\rm pl} = 2.0\,{\rm MA}$.
The auxiliary heating is provided only by a cluster of gyrotrons, coupling to the plasma about 7.2 MW of ECH power in second harmonic X–mode (resulting above the L–H transition power, according to both the ITPA 2008 L–H threshold scaling [147] and the ITPA 2018 L–H threshold scaling for metallic wall devices [148, 149]). In the JETTO runs, the ECRH beams have been modelled by the GRAY code.
In relation to the EC launcher positioning of [135], the toroidal angles have been set in the following ranges: $+45.0°$ for UP beams, $(-6.0°) - (-0.5°)$ for EQT beams, and $(-13.0°) - (-5.0°)$ for EQB beams. The poloidal angles have been set in the following ranges: $+22.5°$ for UP beams, $+25°$ for EQT beams, and $(+21.5°) - (+25.0°)$ for EQB beams. With these angle settings, the ECRH power density is deposited in the inner half of the plasma, precisely in the region $0.03 \leq \rho_{\rm tor} \leq 0.47$.

For the A1 scenario, nitrogen (N, $A \approx 14$, Z = 7) has been selected as suitable seeding gas. Nitrogen and tungsten densities have been calculated by SANCO during the JETTO runs, setting $Z_{\rm eff} = 2.5$ and $n_{\rm W}/n_{\rm N} = 0.001$ as initial conditions.

To obtain the pedestal pressure for the A1 scenario, proper Europed simulations with the EPED model have been performed. Temperatures at the separatrix of $T_e^{\rm sep} = T_i^{\rm sep} = 100\,{\rm eV}$, a value of $\beta_{\rm pol} = 0.25$, a pedestal top density of $n_e^{\rm ped} = 0.50 \times 10^{20}\,{\rm m}^{-3}$, a relative shift of $(T_e^{\rm pos} - n_e^{\rm pos}) = 0.020\psi_N$ in order to obtain an electron density at the separatrix of $n_e^{\rm sep} \approx 0.34 \times 10^{20}\,{\rm m}^{-3}$, and an effective charge of $Z_{\rm eff} = 3.5$ have been set as inputs of the reference A1 pedestal run, predicting pedestal top temperatures of about 1.2 keV. The pedestal top density has been chosen to have a Greenwald fraction of about 0.47. With these settings, the electron density stays cautiously far from the second harmonic ECRH cut–off ($n_e = 1.79 \times 10^{20}\,{\rm m}^3$).

The A1 scenario core modelling has been carried out using TGLF SAT2 as turbulent transport model and solving the transport equations up to the pedestal top ($\rho_{\rm tor} = 0.92$).

All these settings make the core modelling predictions compatible with the edge requirements in terms of radiation and impurity content to operate in fully detached state. In table 5.4, the main modelling settings and results of

Table 5.4: Comparison between edge and core modelling main results for the A1 scenario.

Run	Edge	Core TGLF
Seeding Gas	N	N
$Z_{\text{eff}}^{\text{ped}}$	3.3	2.4
$Z_{\text{eff}}^{\text{sep}}$	2.9 – 4.1	3.7
$n_e^{\text{ped}}\,[10^{19}/\text{m}^3]$	6.9 – 7.8	5.0
$C_{\text{seed.gas}}^{\text{ped}}\,[10^{-2}]$	8.0 – 10.0	3.2
$C_{\text{W}}^{\text{ped}}\,[10^{-5}]$	–	3.3
P_{rad} [MW] $0.85 < \rho_{\text{tor}} < 1.0$	0.65 – 0.68	1.2

edge and core modelling of the DTT first plasma are listed. Notwithstanding some inevitable differences between core and edge modelling values, a good compatibility is reached also for the A1 scenario.
The C1 scenario is dominated by TEMs within $\rho_{\text{tor}} = 0.6$, while returns to be ITG dominant outside ($\rho_{\text{tor}} > 0.6$). The radial profiles of electron temperature T_e, ion temperature T_i, electron density n_e, and safety factor $|q|$, nitrogen gas density $n_{\text{seed.gas}}$, tungsten density n_{W}, effective charge Z_{eff}, radiative power density Q_{rad}, and deposited ECRH power density Q_{ECHe} of the A1 scenario are shown in figure 5.20.
We notice that T_i is much lower than T_e inside $\rho_{\text{tor}} \sim 0.7$ (with $T_{e_0} \approx 8.8\,\text{keV}$ and $T_{i_0} \approx 3.3\,\text{keV}$), due to having low density ($n_{e_0} \approx 0.81 \times 10^{20}\,/\text{m}^3$) and only electron heating. The impurities do not accumulate in the centre significantly as shown in figure 5.20(b) and the total radiative power is $P_{\text{rad}} \approx 1.5\,\text{MW}$.
Figure 5.21 shows the radial profiles of the total electron and ion powers, with and without thermal coupling.

For the A1 scenario, a neutron rate of about 2×10^{14} neutrons/s is assessed. The energy confinement time and the H–factor (with $P = P_{\text{sep}}$) are respectively $\tau_E \approx 0.36\,\text{s}$ and $H_{98} \approx 1.2$ in the A1 scenario of DTT.

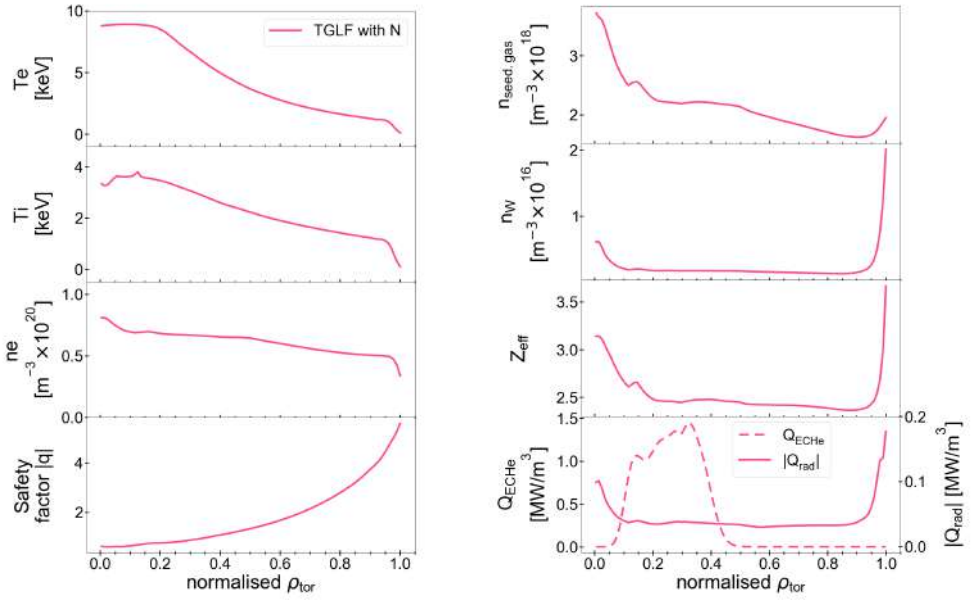

(a) (b)

Figure 5.20: Radial profiles of the A1 scenario referred to a TGLF run with nitrogen. (a) Profiles of electron and ion temperatures, electron density, and safety factor. (b) Profiles of impurity densities, effective charge, radiative power, and ECRH power density.

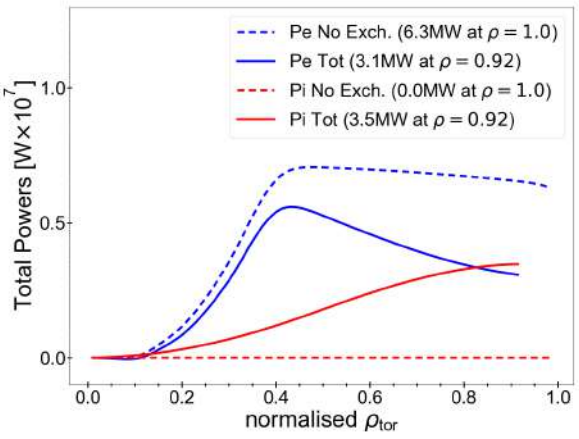

Figure 5.21: Radial profiles of electron and ion total powers including or not including the thermal exchange power between species for the A1 scenario.

Table 5.5: Main parameters of different DTT scenarios.

Scen.	β_p	H_{98} $(P = P_{\rm sep})$	τ_E [s]	$W_{\rm pl}$ [MJ]
A1	~ 0.6	~ 1.2	~ 0.36	~ 2.3
C1	~ 0.5	~ 1.6	~ 1.3	~ 8.8
E1	$0.35 - 0.5$	$0.7 - 1.1$	$0.3 - 0.5$	$9 - 16$

5.6 Conclusions

The main baseline scenarios of the Divertor Tokamak Test facility during the flat–top phase were extensively studied for the new device configuration, including the machine enlargement and the additional heating system upgrades. In this first–principle multi–channel integrated modelling work, theory based quasi–linear transport models (QuaLiKiz [61, 62] and TGLF SAT2 [54, 59]) were used to ensure the highest fidelity currently achievable. Moreover, a long iterative work of key parameter adjustment led to a good agreement between core and SOL simulations, improving the the reliability of our modelling predictions. In addition, the consistency of the plasma profiles calculated by transport models with the electromagnetic configuration achievable by the control coil system were also checked for the E1 scenario. A summary table 5.5 indicates the main results of the reference DTT scenarios. In this updated modelling of the E1 scenario with the new DTT configuration, in order to fulfill the SOL requirements, a density value at the separatrix $n_e^{\rm sep} \approx 0.8 \times 10^{20}\,{\rm m}^{-3}$ was set. This is much larger than typical values of plasma discharges in existing tokamaks and than values in previous DTT simulations [18]. This choice entailed a change in the relative shift of density and temperature pedestals ($T_e^{\rm pos} - n_e^{\rm pos}$) and a very high density gradient in the pedestal, harder to be handled. The present choice for the full power scenario of a Greenwald fraction of about $\bar{n}_e/n_{\rm Gr} \approx 0.5$, implies $T_e \gg T_i$ over almost the whole plasma radius. Raising the Greenwald fraction will be possible, leading to a better balance between T_e and T_i, but mostly via a T_e reduction, because high ion stiffness binds the T_i profile tightly to the ITG critical gradient. Such high stiffness is also consistent with the observation that the E1 scenario has very similar T_i profiles to the C1 scenario, in spite of roughly double additional power. Possible ways of reducing ion stiffness through fast ions have been reported in literature[150, 151, 152, 153], but including these effects in integrated simulations requires an upgrade of existing quasi–linear transport models. Although the electron density is moderately

peaked in the E1 scenario, the tungsten does not accumulate in the plasma centre. In the C1 and A1 scenarios a flatter density profile has been found, as expected due to the lack of the neutral beam injector.
For the first time the sawteeth were included in DTT E1 scenario simulations and a wide analysis for optimising EC launching angles with the aim of improving the E1 safety factor profile was done. The Porcelli and Kadomtsev models have been used respectively to trigger the sawteeth and to predict the relaxed temperature, density, and $|q|$ profiles after a crash. The ST frequency with a complete reconnection is $f_{\mathrm{ST}} \approx 1.4\,\mathrm{Hz}$, while with an incomplete reconnection with a fraction of $f_{\mathrm{rec}} = 0.8$ is $f_{\mathrm{ST}} \approx 1.7\,\mathrm{Hz}$. Furthermore, first estimations of the DTT ELMs in the E1 scenario were performed through suitable scalings. The calculated loss of plasma energy due to one ELM is about 10 % of the pedestal energy in the reference E1 scenario.

CHAPTER 6

Further works

In this chapter, a brief overview of further studies to which this PhD thesis contributed is reported. For every topic, a specific and more detailed paper has been published or submitted. At the beginning of each section, the related reference is indicated.

6.1 Benchmark of QL models against GK runs in JET D and T plasmas with high β

The complete work is widely described in the published paper [154] titled "*Benchmark of quasi–linear models against gyrokinetic single scale simulations in deuterium and tritium plasmas for a JET high beta hybrid discharge*".

Nowadays, the fusion research community devotes big efforts to enhance the quasi–linear models, adding to them an increasing number of physics ingredients and validating their predictions with results of gyrokinetic non–linear simulations and with experimental data.

In this work, a benchmark of the QL models QLK and TGLF against the GK code GENE was carried out for a JET high performance hybrid pulse in deuterium.

The QL models presented some difficulties in high β advanced tokamak scenarios [155, 84, 156, 157, 158, 159, 92, 160]. It is partially due to the lack of NL electromagnetic stabilisation mechanisms [161, 150, 162, 106], even if

some attempt to introduce these effects into QL models has been done [163]. Particularly, TGLF includes linear EM stabilisation effects, but it does not include non–linear EM ones. QLK is an electrostatic (ES) model, but approximate QLK fluxes in the EM regime can be obtained using an EM mock–up, added to the ES results.[1]

The transport dependence on the ion isotope mass has also been investigated in this work, by repeating the benchmark changing the ion isotope to tritium. Experimentally, heavier isotopes have generally been found to have better confinement time and performances than lighter ones [164, 165, 166, 167]. This is in contrast with early theoretical predictions of the gyro–Bohm (gB) mass scaling, according to which turbulent fluxes $\propto \sqrt{m_i}$, where m_i is the ion mass.[2] Gyrokinetic simulations also predicted anti–gB trends due to different mechanisms depending on the specific considered cases: parallel dynamics of non–adiabatic electrons [168, 169], collisions [170], EM effects [171, 172], $\boldsymbol{E} \times \boldsymbol{B}$ flow shear [171, 173], and different impact of fast particles [159, 174].
Further studies on the QL models are recommended to figure out whether they are equipped with the necessary physics to model the isotope dependence correctly.

The goal of this work is to investigate the turbulent transport dependencies both on the EM effects due to high β and on the ion isotope mass from D to T, comparing QL and GK predictions. Therefore, the high β JET hybrid pulse #94875 in deuterium has been modelled by QLK, TGLF SAT1–geo, and GENE codes, to evaluate the capability of QL models to reproduce the physics effects contained in the high fidelity GK codes. In this work, the flux–tube version of GENE has been employed. TGLF features Miller geometry [119] while QLK uses a shifted–circle geometry $(s-\alpha)$ [175]. GENE simulations have been repeated with both the more realistic Miller equilibrium and the simpler $(s-\alpha)$ model.

The analysis has been performed at $\rho_{\text{tor}} = 0.36$ and $\rho_{\text{tor}} = 0.60$ to test the impact of various effects at inner and outer radii. At both radii, the QLK and TGLF linear eigenvalues and heat fluxes have been compared with the results of linear and non–linear GENE simulations, considering both ES and EM regimes to single out the impact of linear EM stabilisation.

The reference parameters were taken from the end of a previous predictive JETTO run in D with QLK, described in detailed in [176]. The magnetic

[1] The EM mock–up consists in running a R/L_{T_i} scan of QLK simulations in the ES regime and then rescaling R/L_{T_i} multiplying it by the radially local ratio $\beta_{\text{thermal}}/\beta_{\text{total}}$ (including FI contribution) [155].

[2] This scaling is based on modelling ITG–driven turbulence within an adiabatic electron, electrostatic approximation in the collisionless regime.

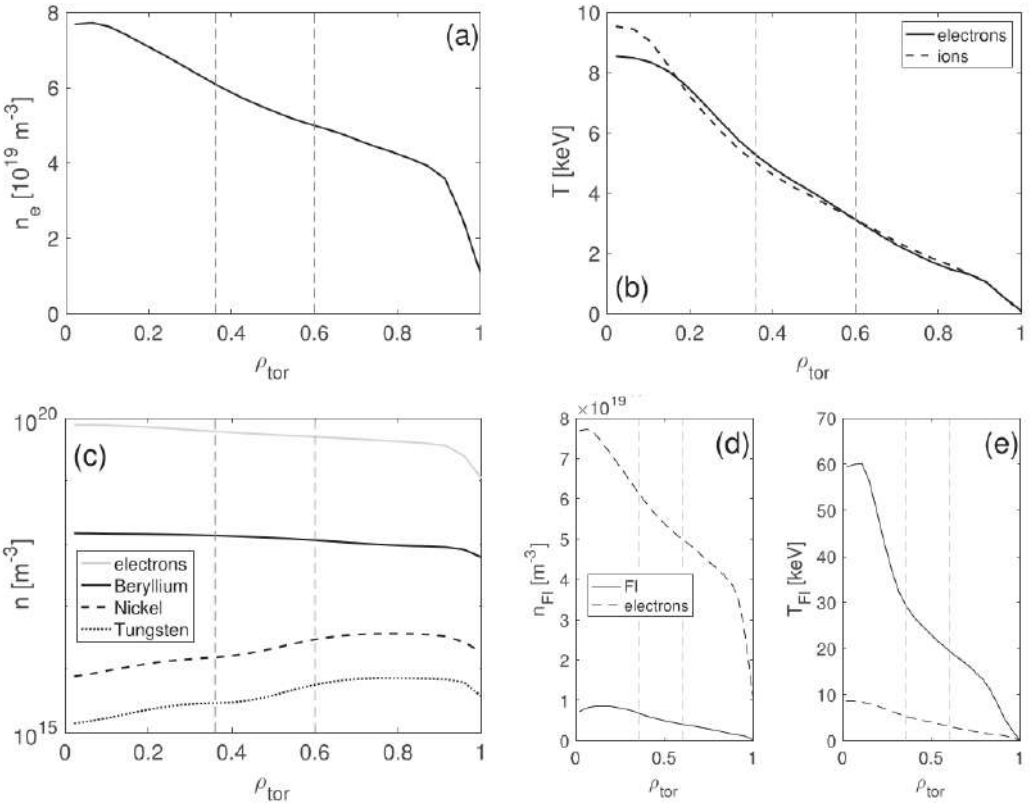

Figure 6.1: Main plasma parameter profiles at the end of the JETTO–QLK run: (a) electron density, (b) electron and main ion (deuterium) temperatures, (c) impurities density profiles compared with n_e in lin–log scale, (d) fast ion density compared to electron one, and (e) fast ion temperature compared to electron one. The vertical lines indicate the two radii of analysis.

equilibrium has been reconstructed with the EFIT equilibrium solver [117, 118]: $\kappa = 1.21$ and $\delta = 0.03$ at $\rho_{\rm tor} = 0.36$, while $\kappa = 1.31$ and $\delta = 0.08$ at $\rho_{\rm tor} = 0.60$. Figure 6.1 shows the reference density and temperature profiles. Impurities (Be, Ni, and W) have been considered as kinetic species in all the simulations.[3] The fast ions (FI) coming from both NBI and ICRH are here considered as a single species, and their temperature distribution is approximated with a Maxwellian. In both GENE and TGLF runs the FI have been considered as a kinetic species, while in QLK they enter only through the EM mock–up.

The rotation shear effects due to NBI injection have been considered at both radii in all the TGLF and NL GENE simulations, but only at $\rho_{\rm tor} = 0.6$

[3]Beryllium, nickel, and tungsten come from the ITER–like wall installed on JET.

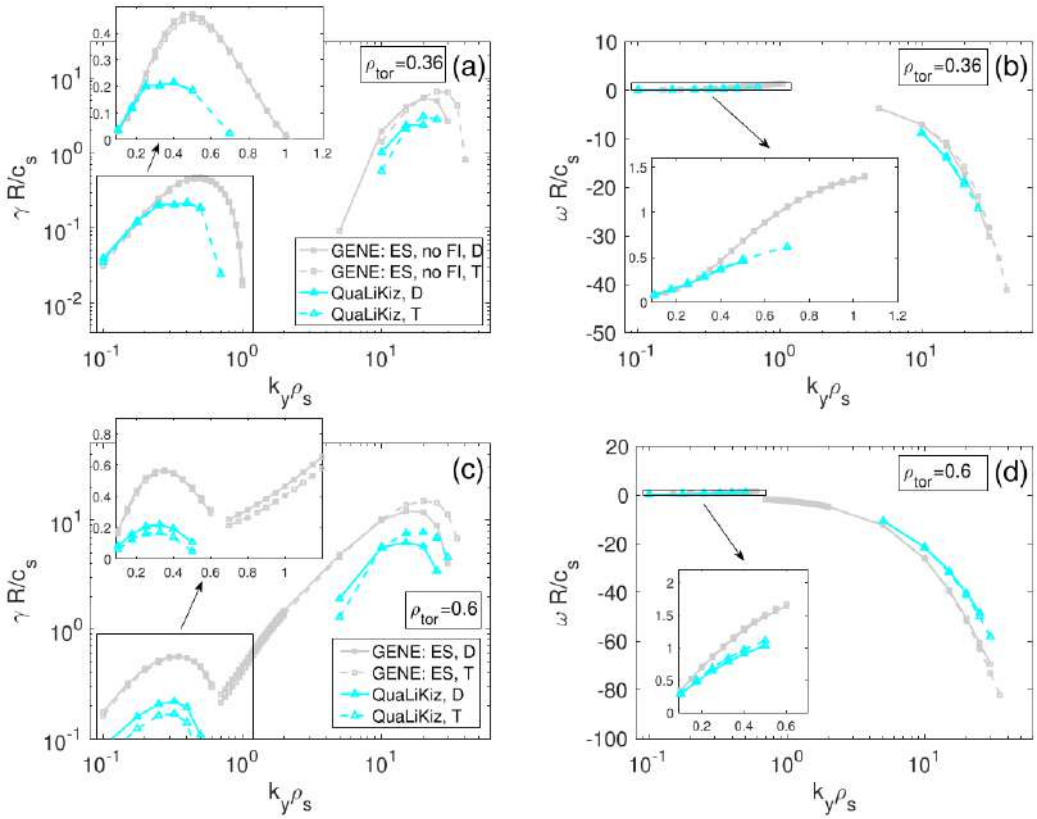

Figure 6.2: Comparison between QLK and GENE k_y spectra of (a)–(c) the growth rate γ and of (b)–(d) the frequency ω of the first unstable linear mode, at (a)–(b) $\rho_{\text{tor}} = 0.36$ and at (c)–(d) $\rho_{\text{tor}} = 0.60$. GENE has been run only in the ES regime with $s-\alpha$ geometry, as well as without FI at the inner radius, to better compare with QLK.

in the QLK runs, since the impact of $\boldsymbol{E} \times \boldsymbol{B}$ stabilisation is neglected in QLK for $\rho_{\text{tor}} < 0.5$ due to the systematic underprediction of parallel velocity gradient destabilisation in that region in the QLK model [155].

Let us start from the linear analysis results, both in D and in T.
In figure 6.2, k_y spectra of the growth rate γ and of the frequency ω of the first unstable linear mode calculated by QLK and by GENE are compared in ES regime. Fast ions have not been considered in these stand–alone QLK simulations. For consistency with the QLK runs, in these cases GENE has been run in $(s-\alpha)$ geometry, in ES regime, and without FI at the inner radius where their content is higher.
We notice that at both radii QLK underestimates amplitude and k_y of growth rate peaks. On the other hand, frequency spectra show a qualitative agree-

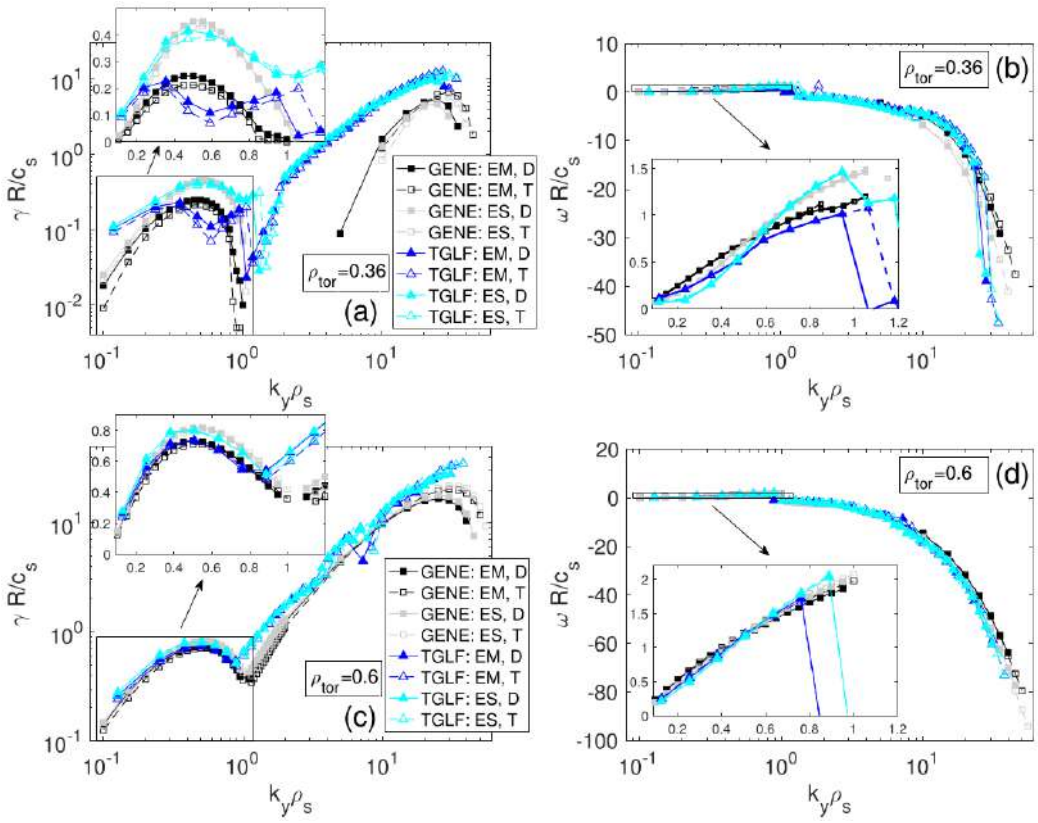

Figure 6.3: Comparison between TGLF SAT1–geo and GENE k_y spectra of (a)–(c) the growth rate γ and of (b)–(d) the frequency ω of the first unstable linear mode, at (a)–(b) $\rho_{\rm tor} = 0.36$ and at (c)–(d) $\rho_{\rm tor} = 0.60$.

ment between QLK and GENE on identifying ITGs and ETGs as dominant turbulences in ion–scale and electron–scale respectively. At $\rho_{\rm tor} = 0.36$ the ITG and ETG regimes are separated by a gap, while at $\rho_{\rm tor} = 0.6$ a continuous TEM–ETG branch fills the intermediate region, due to the variation in T_e gradient (from $R/L_{T_e} \approx 6$ at $\rho_{\rm tor} = 0.36$ to $R/L_{T_e} \approx 10$ at $\rho_{\rm tor} = 0.6$) leading to TEM destabilisation.

In figure 6.3, k_y spectra of the growth rate γ and of the frequency ω of the first unstable linear mode calculated by TGLF SAT1–geo and by GENE are compared in both ES and EM regime. For consistency with the TGLF runs, in these cases GENE has been run with Miller geometry.
We notice that TGLF is in very good agreement with GENE on growth rates for the ES case at both radii and for the EM case at $\rho_{\rm tor} = 0.6$. The frequencies ω calculated by GENE and TGLF are in very good agreement for all the cases and identify ITG and ETG modes as dominant turbulences for

both ES and EM cases at both radii. In addition, comparing the ES and EM runs of GENE, we observe a much stronger linear EM stabilisation at the inner radius with both the two isotopes. Focusing on the isotope comparison, we notice that D growth rates are moderately higher than T ones at the lower wavenumbers which mostly contribute to the fluxes, especially in the EM regime at $\rho_{\rm tor} = 0.36$. Finally, since $(\gamma/k_y)_{\rm max,ETG}/(\gamma/k_y)_{\rm max,ITG} \lesssim 50\,\%$ has been found for all the GENE, QLK, and TGLF simulations, ETGs are not expected to cause significant heat transport and impact the NL fluxes.[4]

Let us analyse now the GENE NL ion–scale simulations, performed both in ES and in EM regime, at both radii, and with both D and T.
For the GENE–QLK benchmark, both the ES and EM cases have been compared and GENE has been run in $(s-\alpha)$ geometry. The ES GENE case at the inner radius does not include FI to be consistent with the corresponding QLK case. For the GENE–TGLF benchmark, only the EM case has been considered, including kinetic FI in all runs.
Since R/L_{T_i} is the main driver of the ITG modes, previously found to be the dominant instability at both radii, we performed scans in R/L_{T_i} of the ion and electron heat fluxes $q_{i_{\rm gB}}$ and $q_{e_{\rm gB}}$.[5] These scans are shown in figure 6.4 for the deuterium simulations. Firstly, observing the GENE results, we notice that the EM stabilisation is much stronger at the inner radius than at the outer radius and the fluxes in the EM cases do not grow with increasing R/L_{T_i} at both radii. This slope variation in the $q_{\rm gB}$ vs R/L_{T_i} curve at $\rho_{\rm tor} = 0.6$ in the EM regime is not reproduced by the TGLF and QLK models. The linear EM effects are not sufficient to fully explain this lack of R/L_{T_i} stiffness, but NL EM effects are required to produce this kind of flattening of the $q_{\rm gB}$ vs R/L_{T_i} curves. Moreover, at $\rho_{\rm tor} = 0.6$ the GENE simulations exhibit a reversed q_i/q_e ratio in the EM regime due to an EM contribution to the electron heat flux of about 30 %. QLK and TGLF fail to predict this reversal effect.
Comparing GENE and QLK results, we find a good agreement on fluxes for the electrostatic cases. The EM mock–up of QLK fails to reproduce the strong EM stabilisation of GENE at $\rho_{\rm tor} = 0.36$, but correctly predicts up–shift of the transport R/L_{T_i} threshold. TGLF is in better quantitative agreement with GENE than QLK at both radii, but at the inner radius still cannot predict the strong NL EM stabilisation effect.
The GENE NL EM simulation with reference parameters has been repeated removing fast ions, showing that the FI effect on fluxes is negligible.

To evaluate the isotope effect on the heat transport, the heat flux scans in

[4] A detailed analysis on the ETG relevance in this JET pulse is presented in [176].
[5] Here, fluxes are expressed in gB units, i.e. $q_{e,i_{\rm gB}} = q_{e,i} \cdot (e^2 R^2 B_0^2)/(\sqrt{m_i} n_e T_e^{5/2})$.

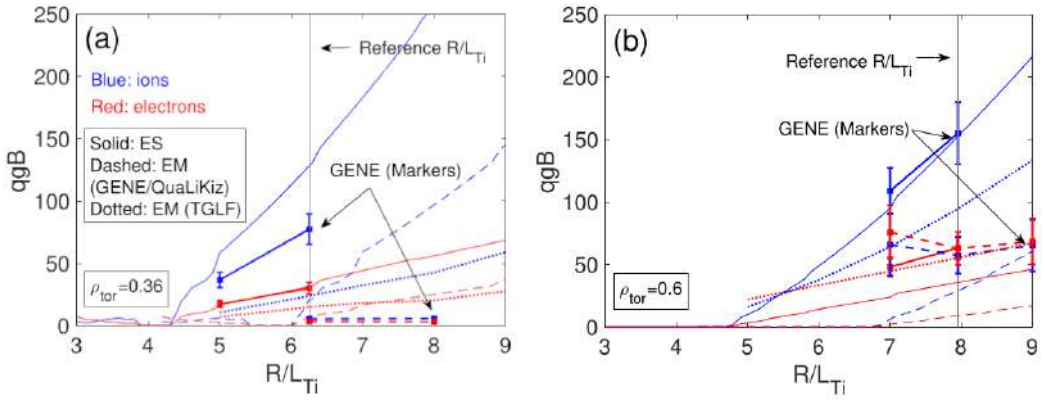

Figure 6.4: Scans in R/L_{T_i} of electron (red) and ion (blue) heat fluxes in gB units, for a deuterium plasma. The GENE NL fluxes are compared with QLK and TGLF QL fluxes, at (a) $\rho_{\rm tor} = 0.36$ and (b) $\rho_{\rm tor} = 0.6$. The ES and EM cases are shown by solid and dashed lines, respectively, except for TGLF in the EM regime, that is indicated by dotted lines to differentiate it from QLK. GENE is marked with squares, and the corresponding error bars represent the standard deviation of the fluxes time traces over the same time interval that has been considered to compute their averages.

R/L_{T_i} have been repeated with tritium. The comparison between D and T results is shown in figure 6.5. A pure gB scaling predicts a ratio between heat fluxes of $q(\mathrm{T})/q(\mathrm{D}) = \sqrt{3/2} \approx 1.22$. In ES regime, GENE and QLK agree on predicting a almost negligible anti–gB effect ($1 \lesssim q(\mathrm{T})/q(\mathrm{D})[R/L_{T_{i\mathrm{ref}}}] \lesssim 1.2$) at $\rho_{\rm tor} = 0.36$ and a small anti–gB effect ($0.8 \lesssim q(\mathrm{T})/q(\mathrm{D}[R/L_{T_{i\mathrm{ref}}}]) \lesssim 1$) at $\rho_{\rm tor} = 0.6$ for both ions and electrons. In EM regime GENE and QLK agree on predicting a negligible anti–gB effect ($1.1 \lesssim q(\mathrm{T})/q(\mathrm{D})[R/L_{T_{i\mathrm{ref}}}] \lesssim 1.2$) at $\rho_{\rm tor} = 0.36$ and a not small anti–gB effect ($0.4 \lesssim q(\mathrm{T})/q(\mathrm{D})[R/L_{T_{i\mathrm{ref}}}] \lesssim 0.9$) at $\rho_{\rm tor} = 0.6$. The TGLF EM runs predicts a small anti–gB effect at both radii ($q(\mathrm{T})/q(\mathrm{D})[R/L_{T_{i\mathrm{ref}}}] \sim 0.8$ at $\rho_{\rm tor} = 0.36$ and $q(\mathrm{T})/q(\mathrm{D})[R/L_{T_{i\mathrm{ref}}}] \sim 1.1$ at $\rho_{\rm tor} = 0.6$). In addition, from figure 6.5 we notice that the GENE runs in tritium also present a flattening of the $q_{\rm gB}$ vs R/L_{T_i} curves, as found for deuterium cases.

Summarising, TGLF agrees better with GENE on the linear spectra and the absolute level of heat fluxes, but concerning the isotope dependence only QLK reproduces the GENE radial trend of a basically gB scaling at inner radii and instead an anti–gB trend at outer radii for the considered case. Further analysis will be carried out in the future to span a larger parameter region compatible with hybrid cases of interest and to compare the QL and GK results with the experimental measurements of the JET campaign in T.

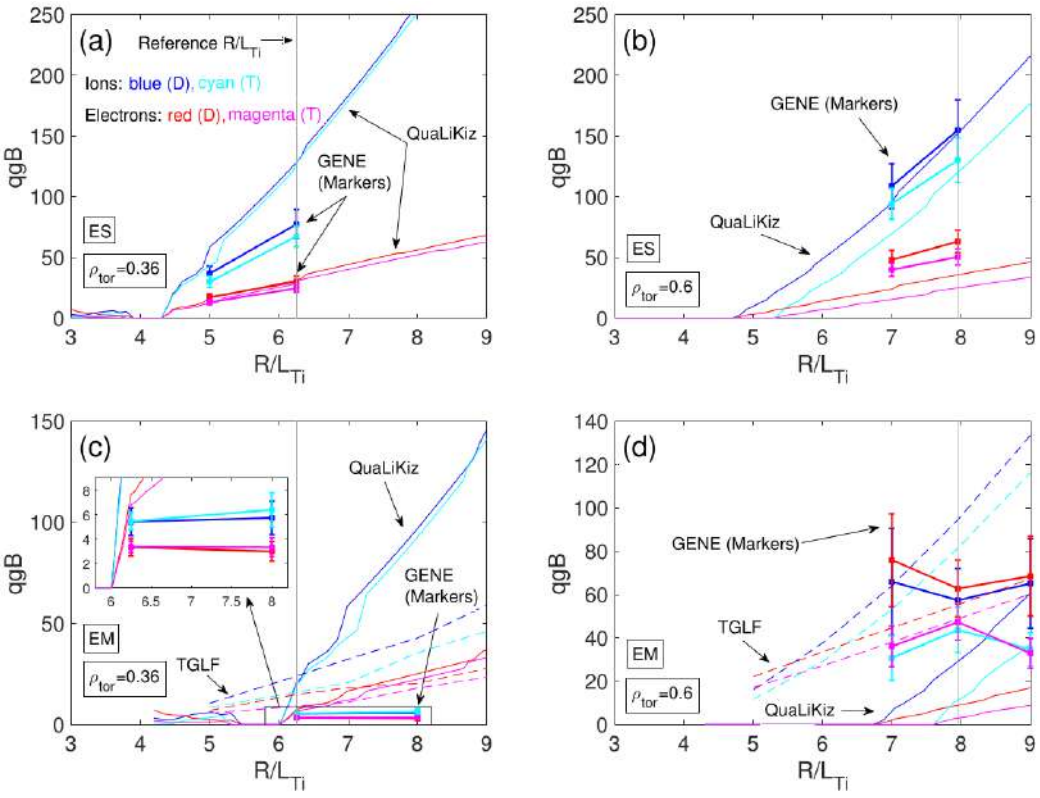

Figure 6.5: Isotope dependence of electron heat fluxes. GENE NL fluxes compared with QLK and TGLF QL fluxes in gB units vs R/L_{T_i} , in D (blue and red correspond to ions and electrons, respectively) and T (cyan and magenta correspond to ions and electrons, respectively). The first and second row correspond to ES and EM simulations, respectively, while the first and second column to $\rho_{\text{tor}} = 0.36$ and $\rho_{\text{tor}} = 0.6$, respectively. GENE is distinguished by QLK (both shown by solid lines) using square markers. TGLF is dashed.

6.2 Deuterium fuelling in view of DTT design

The complete work is widely described in the submitted paper [136] titled "*Predictive simulations of deuterium fuelling in view of DTT design*".

The study described in section 4.3.5.3 highlighted the need for a thorough analysis of the DTT deuterium fuelling, updated to the new device configuration of DTT ($R_0 = 2.19\,\mathrm{m}$, $a = 0.70\,\mathrm{m}$).
Plasma density and temperature profile evolution in the DTT SN full power scenario has been calculated in case of two different fuelling methods: gas puff and pellet injection. Furthermore, these studies have been repeated changing the seeded impurity (argon or neon). The integrated simulations of the E1 scenario of section 5.3 have been used as reference point for the activity described here. Initially, we focused on the QLK runs with a quite central and peaked ECRH deposition. As done in section 4.3.5.3 for the previous DTT configuration, the transport prediction in JETTO has been extended up to the separatrix, modelling the pedestal self–consistently with the plasma core. It allows to optimise the fuelling required to reproduce the transport barrier predicted by the Europed runs.
Since quasi–linear transport models such as QLK and TGLF are unsuitable to emulate the edge physics within the Edge Transport Barrier (ETB), we exploited the simplest ELM model integrated in JETTO to include an additional transport term. This ELM empirical description is based on adjusting transport coefficients in the pedestal region when the normalised pressure gradient exceeds a critical threshold α_c, beyond which ELM crashes occur.[177] In these simulations, α_c has been used as free parameter.

Initially, to tune the pedestal parameters without considering the fast pellet dynamics, gas puff has been investigated as the only deuterium fuelling system. As in section 4.3.5.3, FRANTIC has been used to calculate the neutral source, setting a feedback control of gas puffing to reach the electron density value expected of $1.4 \times 10^{20}\,\mathrm{m}^{-3}$ at the TOB (Top Of Barrier) with null recycling. A good agreement between simulations with fixed and reproduced pedestal is reached in both argon and neon cases, as shown in figure 6.6. Even with the new DTT configuration, the neutral penetration into the plasma has been evaluated adequate for fuelling, but an average neutral flux of 1×10^{22} particles/s has been found to be required at the separatrix to sustain the pedestal. Since this value corresponds to a nominal gas puff rate of $\sim 0.9 \times 10^{23}$ particles/s which is above the feasibility limits for the pumping system, a pellet injection system is mandatory for fuelling the reference DTT full performance scenario.

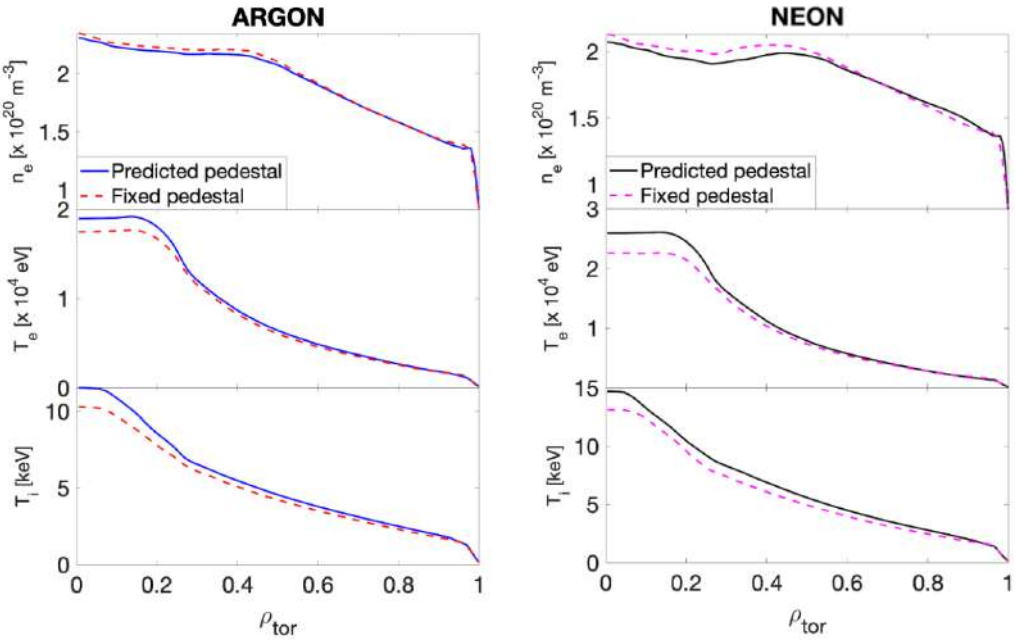

Figure 6.6: Density and temperature radial profiles calculated by JETTO with fixed pedestal (dashed line) and predicted pedestal (solid line), using both argon (left) and neon (right) as seeding gas.

Therefore we investigated the DTT fuelling via pellet injection. The gas puff fuelled plasma profiles has been used as starting point and reference for modelling the plasma response to pellet injection. The ETB parameters optimised in the first part of this work have been reused here.
The HPI2 (Hydrogen Pellet Injection) code [178, 179] has been included in our JETTO simulations to estimate the pellet ablation process and the following density perturbation. It has been used in feedback, injecting a pellet whenever the density level drops below a given value. From a previous stand–alone pellet analysis [180], the Oblique High Field Side (OHFS) injection was identified as the best option to have a high fuelling efficiency (up to 95 %) and feasible technological requirements. Hence the OHFS pellet injection configuration has been employed in this integrated modelling.
Figure 6.7 shows the time evolution of the density profile during a single pellet cycle. We notice that pellet deposition is located in the outer plasma region in the range of $0.65 \lesssim \rho_{\text{tor}} \lesssim 1.0$. The pedestal is well sustained by pellets of radius $r = 1\,\text{mm}$ injected into the plasma at a velocity of $v = 516\,\text{m/s}$ with a frequency of $\sim 18\,\text{Hz}$. These values lie in feasibility ranges.

Unfortunately, after several pellet cycles the plasma density results characterised by a hollow region $0.2 \lesssim \rho_{\text{tor}} \lesssim 0.4$, as shown in figure 6.8. Thus, the

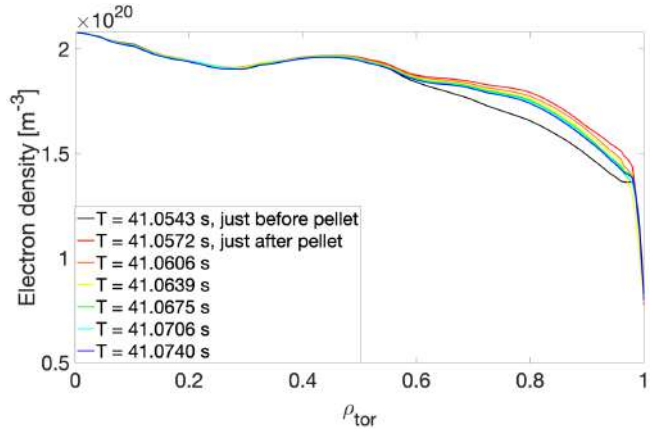

Figure 6.7: Density evolution with during a single pellet cycle (Ne case).

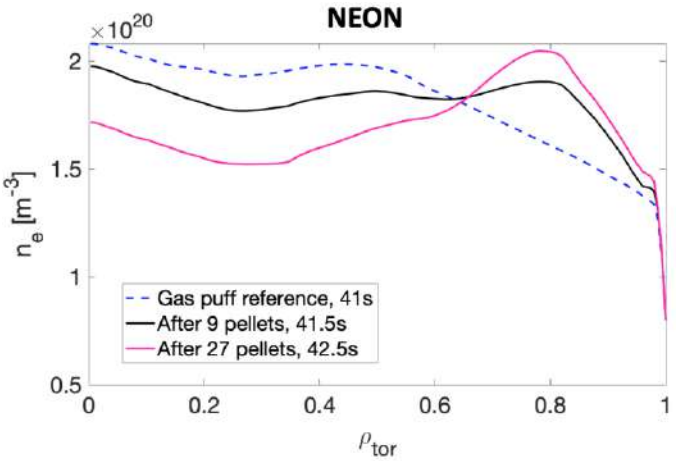

Figure 6.8: Density evolution after several pellet cycles.

inner core is progressively emptied, a pile–up effect raises around $\rho_{\text{tor}} = 0.8$, and a steady–state condition cannot be achieved.
A deep analysis, widely described in [136], has been performed to understand the cause of this behaviour. It is due to an outward convection in the region $0.2 \lesssim \rho_{\text{tor}} \lesssim 0.4$ predicted by the QLK model which empties the core and prevents the pellet from penetrating, driving the density profile hollow. In addition, within $0.6 < \rho_{\text{tor}} < 0.75$ the particle flux is very small just before a pellet injection and a huge inward turbulent flux is predicted by QLK just after the ablated material is deposited in the plasma. In this region, the compensation between the outward diffusive flux and the inward convective flux is no longer guaranteed leading to a net inward anomalous flux. This behaviour has been observed in both neon and argon simulations, but the ar-

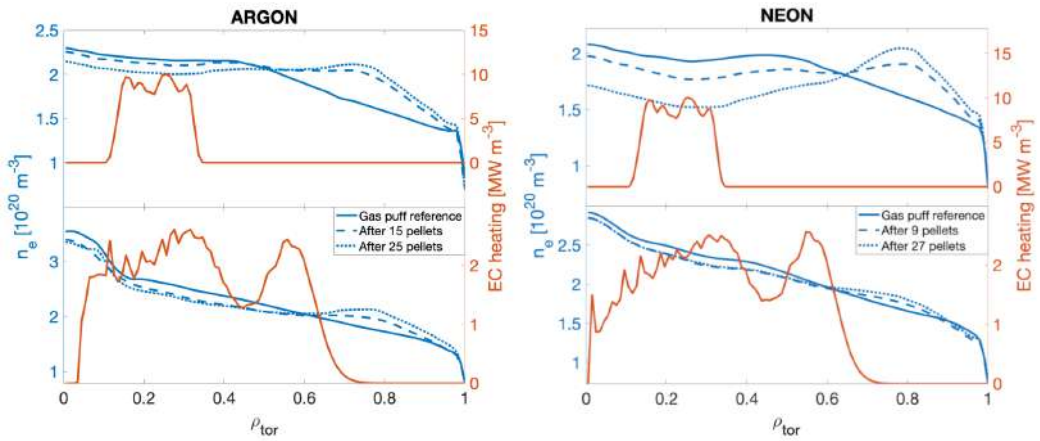

Figure 6.9: Density evolution with pellet fuelling, changing seeded impurity (argon or neon) and changing ECRH power deposition (peaked or spread).

gon case presents outward turbulent fluxes and hence the density pump–out greatly reduced with respect to the Ne case.

In these simulations, a large amount of EC power is deposited in a limited region $0.1 < \rho_{\rm tor} < 0.3$. The well known EC–induced density pump–out, which is typically exploited to avoid the the heavy impurities accumulation in the plasma core, may also drive the hollowness of the main ion profile. A wider ECRH deposition profile should mitigate the pump–out effect. Thus, we repeated the analysis (with both gas puffing and pellet injection), but using a spread EC power deposition as the one of section 5.3.1.
Figure 6.9 compares the electron density evolution between cases with peaked and spread EC power density (both with Ar and Ne). We found that a wider ECH deposition effectively prevents the progressive emptying of the inner plasma core and allows to reach steady–state conditions. In other words, the whole profile is sustained by pellet injection, if a spread ECRH is used.
The total turbulent ion flux predicted by QLK is considerably reduced with respect to values of the peaked EC cases. This is due to a transition within $\rho_{\rm tor} \simeq 0.4$ in the turbulence regime from TEM–dominant to ITG–dominant, which leads to an inversion of the thermo–diffusive contribution to the particle flux from outward to inward. Further details are reported in [136].
Finally, from figure 6.9 we notice that a pellet cycle is characterised by a maximum perturbation of only $\sim 10\,\%$ located in $\rho_{\rm tor} \approx 0.8$. The optimal pellet injection frequency has been found to be about 20 Hz, well in line with today's injectors.

6.3 DTT edge transport multi–code estimate

The complete work is widely described in the published paper [131] titled "*Multi–code Estimation of DTT Edge Transport Parameters*".

To define the operational space of power exhaust relevant parameters, a DTT edge modelling as accurate as possible is needed. To predict power exhaust performances, 2D edge numerical codes such as SOLPS–ITER [181], SOLEDGE2D–EIRENE [115, 116], and U–EDGE [182] are typically used. These codes are not equipped with self–consistent transport treatment methods, but transport parameters are imposed as run inputs. Hence, the particle and energy transport coefficients to be used must be accurately evaluated.

In the first DTT edge modelling [114], uniform transport parameters were assumed as initial step. In the present work, described in [131], a transport profile set has been derived and validated for DTT following two approaches: from modelling of existing tokamaks or from first–principle DTT modelling. For the first validating approach, we looked for machine pulses compatible with the DTT SN full power scenario. Since DTT is a tokamak with unique characteristics (high–field compact machine with high plasma density, current, collisionality, and auxiliary heating power), there is not a single device operating under "DTT–like" conditions. Hence two tokamaks were selected for opposite reasons: Alcator C–Mod (high–field machine with high core and separatrix density, pulse with similar Greenwald fraction) and JET (much more similar to DTT in terms of dimensions, plasma current, q_{cyl}, and auxiliary input power). One C–Mod pulse (#1160729008) and four JET pulses (#96482, #96139, #95946, and #92436) with different impurity seeding (none, nitrogen, or neon) were selected for the analysis. Two JET cases present a high LFS radiation due to a large tungsten content (and hence the edge modelling inner boundary is placed outside of the radiative volume), while the other two JET pulses have low core and higher X–point radiation. All these pulses have been modelled by SOLEDGE2D–EIRENE and two of the JET pulses have been also modelled by SOLPS–ITER to single out possible prediction discrepancies. These simulations are benchmarked with experimental data. Transport parameters are derived for flat–top inter–ELM modelling of DTT, therefore JET and C–Mod experimental data are taken in steady–state inter–ELM time windows. The C–Mod pulse modelling is accurately described in [183], while the JET pulse modelling has been performed following the same methodology used in [184]. In these simulations a good agreement between predicted plasma profiles and experimental data and between SOLEDGE2D and SOLPS predictions was found. Further details of

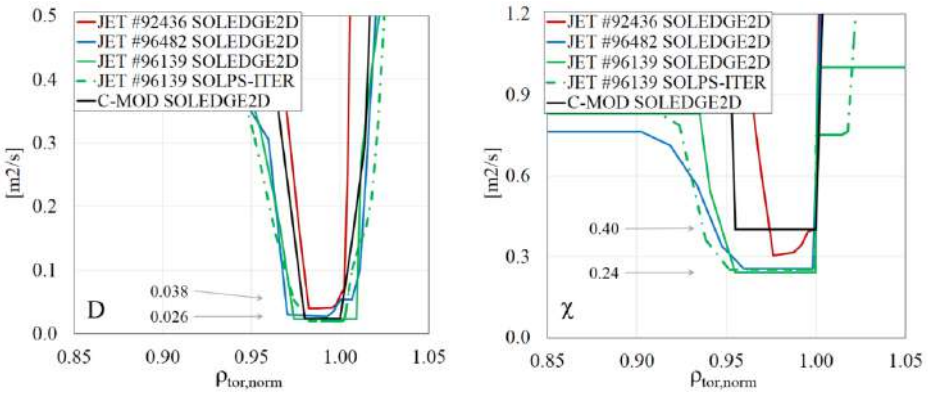

Figure 6.10: Profiles of (a) particle and (b) heat transport coefficients obtained from edge modelling of JET and C–MOD pulses.

the edge runs, presented in [131], are beyond the scope of this section.
The predicted particle transport coefficients D have very similar profiles for all the examined pulses, as shown in figure 6.10(a), and they are in the range $D_{\text{ped}} = 0.32 \pm 0.06\,\text{m}^2/\text{s}$ in the pedestal region. The predicted particle heat coefficients χ are spread over a wider range in the pedestal region, as shown in figure 6.10(b), due to different values of the heat flux decay length λ_q.

Since the Eich scaling [185] predicts a lower λ_q for DTT than for existing tokamaks, the heat transport parameter χ values calculated for the JET and C–Mod pulses have been properly re–scaled to DTT. Particularly, the heat transport coefficient scaling factor is defined as $S_{\text{machine}} := \chi^{\text{Eich}}_{\text{DTT}}/\chi^{\text{Eich}}_{\text{machine}}$, where $\chi^{\text{Eich}}_{\text{machine}}$ is obtained by substituting all parameters from machine scenarios and λ_q from the Eich scaling in the χ expression as a function of λ_q given by the two–point model [186, 187]. The heat transport coefficient scaling factors used here for JET and C–mod pulses are respectively $S_{\text{JET}} \approx 0.34$ and $S_{\text{C–Mod}} \approx 0.44$. The DTT heat transport coefficients derived from JET and C–Mod edge modelling re–scaled according to this method lie in a range of $\chi_{\text{ped}} = 0.12 \pm 0.02\,\text{m}^2/\text{s}$ in the pedestal region, as shown in figure 6.11.

The second approach for validating a suitable transport parameter set consists in deriving them from first–principle DTT simulations of the plasma core. It has been done using the DTT core modelling of the SN full power scenario performed by JETTO with a fixed pedestal previously calculated by EPED, as widely described in section 5.3.
Ion and electron heat transport coefficients χ_i and χ_e are calculated separately in JETTO, as shown in figure 6.11 where they are compared to the χ values from existing tokamak edge modelling re–scaled to DTT. We notice that a quite good agreement between the two approaches is reached in the

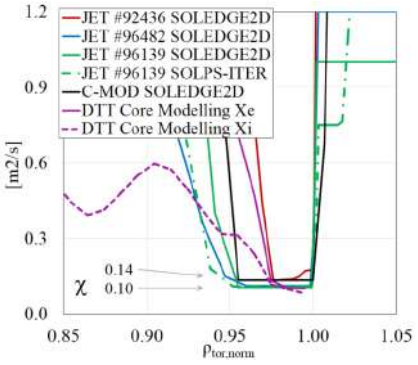

Figure 6.11: Heat transport profiles derived from edge modelling of JET and C–Mod pulses re–scaled to DTT. The χ_e and χ_i profiles derived from core modelling are plotted in purple dashed and solid lines respectively.

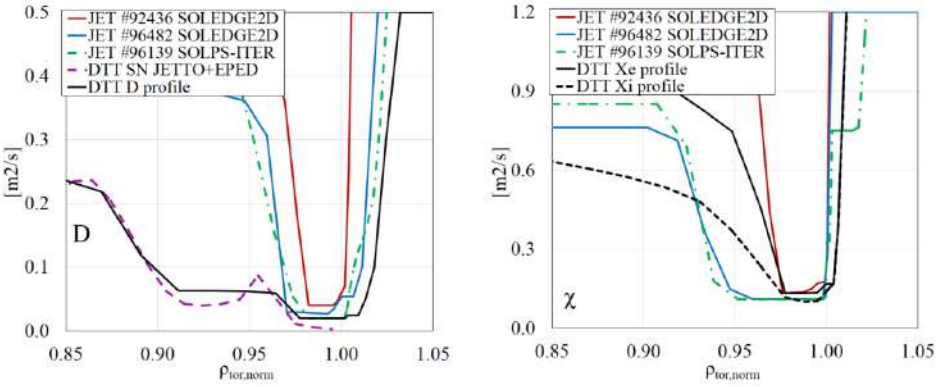

Figure 6.12: Profiles of (a) particle and (b) heat transport coefficients. The black lines refer to the selected DTT reference transport parameters.

pedestal region. To also include, if relevant, the internal pinch effect, an effective particle transport D_{eff} has been derived from the JETTO modelling and compared to the D values obtained by the C–Mod and JET modelling.

Finally, by averaging the pedestal transport profiles derived with different methodologies, we define a reference set of transport parameters for DTT SN simulations. The reference transport profiles were taken from the core modelling inside the pedestal, since the physics–based modelling is more accurate in that region. For the same reasons, transport profiles in the far–SOL and below the X–point were taken from the present machine edge modelling: $D_{\text{far SOL}} = 0.5\,\text{m}^2/\text{s}$ and $\chi_{\text{far SOL}} = 1.0\,\text{m}^2/\text{s}$. The resulting reference particle and heat transport coefficients are plotted in figure 6.12.
This validated set of transport parameters is currently being used for DTT divertor design [125] and scenario development.

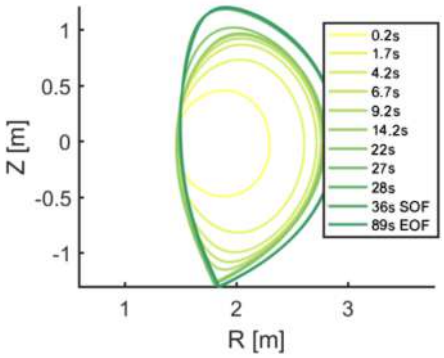

Figure 6.13: Plasma shapes of the DTT SN full power scenario during the ramp–up and the flat–top phases, calculated by CREATE–NL.

6.4 DTT time–dependent 0.5 D modelling

> The complete work is widely described in the published paper [188] titled "*Exploring Divertor Tokamak Test (DTT) operation space and plasma scenarios through time–dependent 0.5D integrated modelling*".

For the first time, a time–dependent modelling of a DTT plasma discharge was performed to design the time evolution of plasma parameters during transient phases, as described in [188]. Particularly, the ramp–up and flat–top phases of the reference SN full power scenario with the present DTT configuration ($R_0 = 2.19\,\mathrm{m}$, $a = 0.70\,\mathrm{m}$) were simulated through the simplified transport code METIS [189]. This 0.5 D numerical code combines 0 D heat and particle transport scaling–laws with 1 D current diffusion modelling and 2 D equilibria. The SN FP plasma boundaries during the ramp–up phase from 0.2 s to 36.0 s (with the X–point formation in the 9–14 s range after the start of the discharge) and during the flat–top phase, shown in figure 6.13, were provided by free boundary CREATE–NL solver.

The flat–top METIS predictions were validated towards JINTRAC results with a quite good agreement, as shown in figure 6.14.

In figure 6.15 the time evolution of 50 s from the plasma discharge start of plasma current, of densities, and of auxiliary heating system powers used in the METIS modelling are displayed. It represents a possible plasma evolution depending on the plasma density waveform, the heating input timings, and displacement of off/on–axis the ECRH deposition. The current ramp–rate of $\sim 200\,\mathrm{kA/s}$ is set in these modelling; the flat–top I_{pl} value is reached at $t = 27\,\mathrm{s}$ with a linear current increase. With the auxiliary heating system

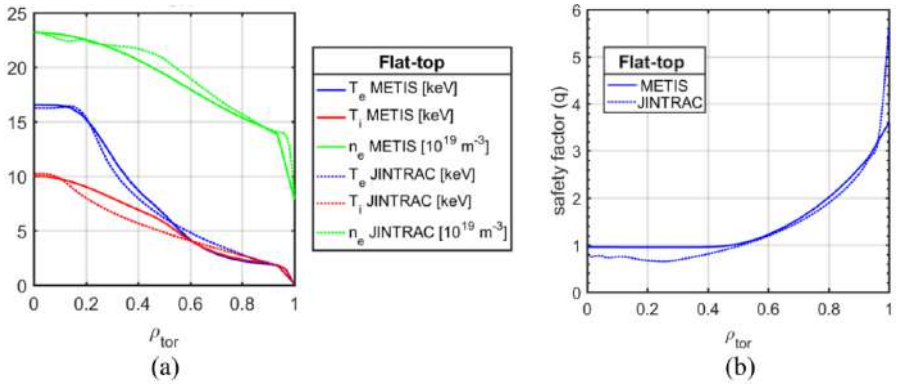

Figure 6.14: Flat–top plasma kinetic (a) and safety factor (b) profiles calculated by METIS compared to those calculated by JINTRAC.

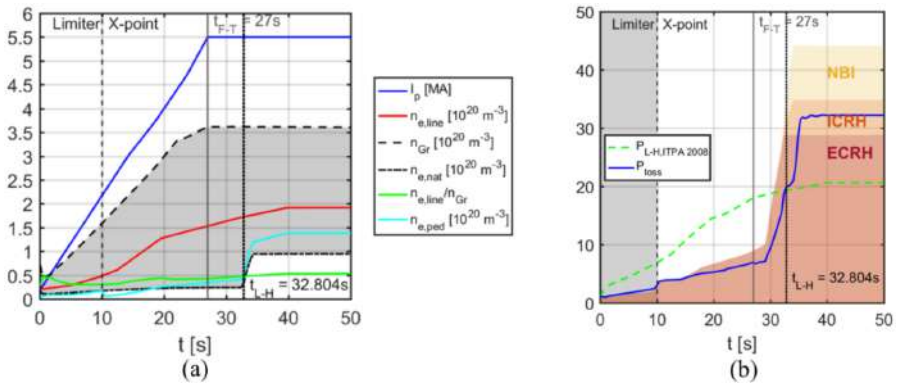

Figure 6.15: Time evolution during the DTT FP ramp–up of (a) plasma current (solid blue), line–averaged electron density (solid red), Greenwald density (black dashed), Greenwald fraction (solid green), n_e^{ped} (solid cyan), and of (b) the auxiliary heating system power used in the METIS modelling.

power trends used in this METIS run, the L–H transition occurs when the power leaving the plasma P_{loss} overcomes the threshold power given by the ITPA 2008 scaling [147]. It happens at around 33 s, i.e. in the current flat–top before of the stationary phase, which starts at 36 s (SOF) and ends at 84–89 s (EOF).

This modelling work presented in [188] is the first step of an ongoing activity aiming to reach an optimal ramp–up trajectory with a convergence between the EM scenarios and transport simulations.

6.5 DTT NBI beamline conceptual design

The complete work is widely described in the published paper [190] titled "*Conceptual Design of the Beamline for the DTT Neutral Beam Injector following a Double Beam Source Design Approach*".

The conceptual design of the beamline for the DTT Neutral Beam heating system was a crucial task. When this PhD work started, the reference solution foresaw two beams of 400 keV supplying a power of 7.5 MW each, as mentioned in chapter 4. Then, several options have been investigated, testing different beam energy and power values and number of beams.
The main NBI beamline components have been optimised to reach a good compromise among various physics and engineering requirements. Comparing results of a set of simulations performed with different codes and suites allowed to gain in reliability and to drive the choice of the most suitable NBI system design.

In addition to the more complex ASTRA and JETTO modelling described in the chapter 4, METIS fast tokamak simulator [189] has been exploited to achieve simulations of the DTT reference single null plasma scenario at full performance, changing the NBI settings.
Particularly, a single injector with an injection angle of 35°, corresponding to a tangency radius of $R_t = 1.91$ m, has been tested with different energies from 100 keV to 500 keV and different powers from 2 MW to 10 MW.
In figures 6.16(a) and 6.16(b), the NBI power density deposition and current drive profiles are shown for these cases to compare them. We notice that the largest energy and power case is beneficial in terms of central heating and notable current drive requirements, as expected.
The option with $E_{\text{beam}} = 500$ keV and $P_{\text{NBI}} = 10$ MW was examined more in detail; figure 6.16(c) shows how the deposited NBI power density is split between plasma electrons and ions. It has been useful to compare these profiles with those calculated by PENCIL in the JETTO simulations: a good agreement was found.

As assessed in chapters 4 and 5, the current reference full power scenario includes a single neutral beam injector operating at 510 keV to supply about 10 MW of NBI power to the plasma. JETTO, ASTRA, and METIS simulations supported this choice. A careful optimisation of the injection angle, which took into account the impact on the ripple losses as described in section 6.7 and on the shine–through losses in the reference DTT high–density plasma scenario, led to the choice of $\alpha_{\text{inj}} = 35°$.

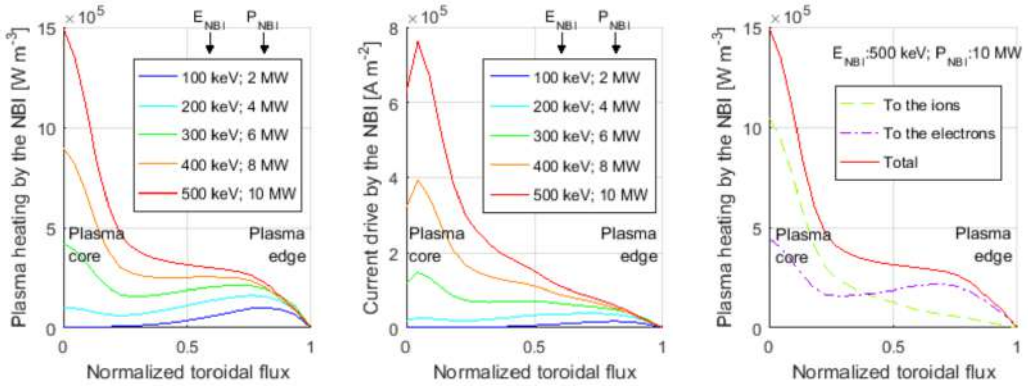

(a) NBI power density. (b) NBI current drive. (c) NBI current drive.

Figure 6.16: Radial profiles of (a) NBI plasma heating and (b) NBI current drive for different values of beam energy and power, according METIS code runs. (c) NBI heating to the ions and electrons of the plasma evaluated using the METIS and ORBIT codes, for the case with $E_{\text{beam}} = 500\,\text{keV}$ and $P_{\text{NBI}} = 10\,\text{MW}$. Figures from [190].

In addition to focusing on the plasma response, the conceptual design of the beamline for the DTT NBI has been also based on maximising the RAMI indexes (Reliability, Availability, Maintainability, and Inspectability) and reducing as much as possible system complexity and costs.
Furthermore, the experience gained from existing experiments provided suitable guidelines to the NBI project.

The adoption of an air–insulated beam source for the DTT neutral beam, following the example of NBI systems of JT60 [191] and LHD [192], increases the Reliability and Availability indexes, by eliminating the requirement of a single large bushing to connect the VV to the transmission line and by improving the accessibility to the beam source.
The BLCs (the neutralizer, the residual ion dump, and the calorimeter) and the RF source of the DTT NBI system will be ITER–like, but differently from ITER on the VV there will be only small flanges for BLC supplies, pumping, and diagnostics. To access to the BLCs for maintenance works, it will be needed to remove the beam sources.
Turbomolecular pumps placed on the VV side walls and NEG pumps placed on the upper and lower vessel surfaces constitute the vacuum pumping system.

The conceptual design of the DTT NBI follows the double beam source approach, as shown in figure 6.17(a). Each of these 2 beam sources accelerate 20 A of negative ions D^- (for a total of 40 A) to an energy of 510 keV, thanks

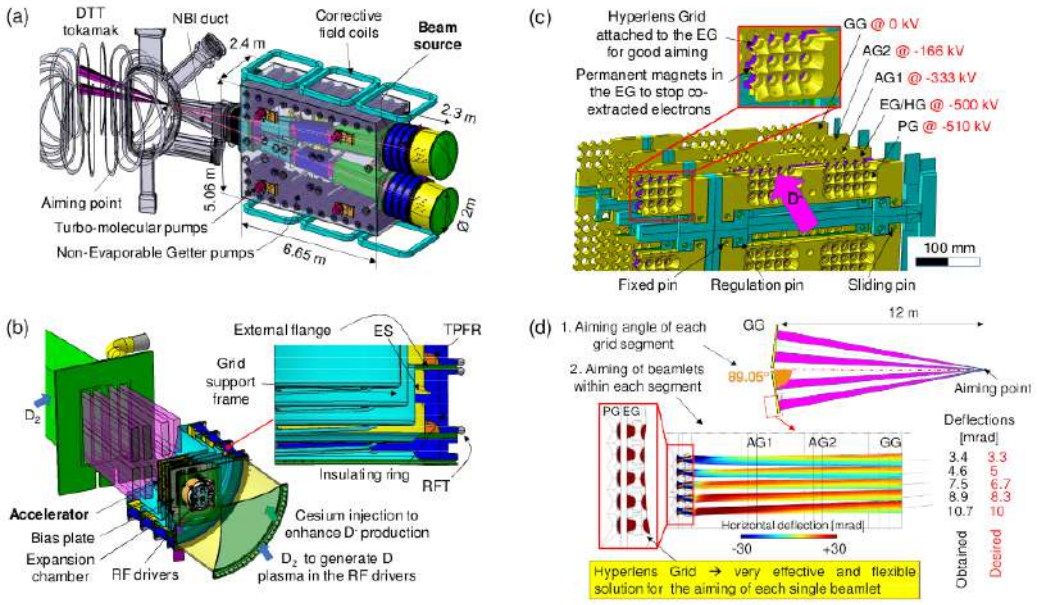

Figure 6.17: Conceptual design of the beamline for DTT NBI: (a) overall view, (b) beam source section view, and (c) accelerator section view. (d) Aiming strategy of the accelerator.

to a set of grids, shown in figure 6.17(c), biased at different potentials:

- a plasma grid (PG) operating at −510 kV,
- an extraction grid (EG) operating at −500 kV,
- a hyperlens grid (HG) operating also at −500 kV,
- a first acceleration grid (AG1) operating at −333 kV,
- a second acceleration grid (AG2) operating at −166 kV,
- and a grounded grid (GG) operating at ground potential.

Four assembled copper segments constitute each grid to achieve a better beam aiming, as shown in figure 6.17(d).
The extraction gap with a thickness of about 6 mm is followed by 3 acceleration gaps of about 100 mm each. The potential difference of about between the PG and the EG, which actually is variated around 10 kV to improve the beam optics for different ion density, allows to extract the D^- ions from the plasma source. To stop all the co–extracted electrons, which would generate

excessive heat loads on the following grids, the EG is equipped with permanent magnets that deflects them onto the grid surface. To maximise the D^- extraction while minimising the co–extracted electrons, the same strategies adopted in SPIDER[193], MITICA[194], and ITER NBI are employed for the PG design: using an enhanced upstream surface shape, operating the grid at high temperature $\sim 150°C$, covering it with a mono–layer of cesium, and applying a high current flow vertically through the grid.

Every grid segment has two matrices of 19 apertures each for a total of 190 apertures per grid segment, i.e. 760 apertures per grid. It is equivalent to say that there are 760 apertures per beam source. Thus, being a double beam NBI system, a total of 1520 beamlets passing through these apertures are extracted and accelerated to form the D^- global beam. This layout is derived from the MITICA geometry, but with around 18 % more apertures to reduce the D^- current density requirement, enhancing the Availability index. To minimise the divergence of beamlets and focus them onto the aiming point located in the plasma at about 12 m from the GG, an optimised inclination of the grid segments is exploited. Furthermore, an effective solution to steer the beamlets is to use the HG attached to the downstream side of the EG. As displayed in figure 6.17(d), the desired values of beamlet deflection and those obtained by first simulations are in good agreement.

The optimisation of the design of the NBI BLCs is still ongoing.
To cope with the extremely high heat loads, all NBI plasma source components and acceleration grids are equipped with high performance cooling systems. Several holes cover the flat surface of the grid frames to allow the particles (electrons, neutrals D^0, and positive particles D^+ and $D_2{}^+$) flow towards the NEG and turbo–molecular pumps.

The procedure to align the NBI accelerator and BLCs significantly impacts the RAMI indexes. After investigating different options, it was chosen to place an alignment target in the beamline downstream of the calorimeters and to equip each grid segment with two optical laser pointers. The tracks of these optical lasers passing through a calibrated hole in the GG are observed by 2 visible cameras mounted on the vessel. Thanks to 2 alignment bars, the whole set of PG, EG, AG1, AG2, and GG segments can be moved in the correct placement. Then, the position of every grid segment is adjusted and blocked by means of regulation screws in specific regulation pins shown in figure 6.17(c). These regulation screws can be reached and tightened also when the whole accelerator is mounted, allowing a fine–tuning of the beam aiming a posteriori. The BLCs can be moved by specific supports to align them with the beamline, exploiting the same optical lasers. During the beam–on operations, a carbon target could replace the alignment target and absorb the beam for periods of the order of some seconds. Substituting the visible

cameras with 2 thermo–cameras, the beam footprint can be checked in the beam–on operations. This alignment procedure strongly enhances the Availability, Maintainability, and Inspectability indexes, reducing the production and operation costs of the DTT NBI beamline.

6.6 NBI interaction with DTT plasma

> The complete work is widely described in the submitted paper [134] titled "*Interaction of high–energy neutral beams with Divertor Tokamak Test plasma*".

Since the DTT NBI is designed to operate at full performance at 510 keV of energy, it represents the highest–energy NBI system after ITER.[6] The injection energy strongly impacts on interaction between plasma and beam fast particles. This work concerns an analysis of the beam–plasma interaction in the full performance scenario of DTT by examining the present DTT NBI design (negative–ion source, tangency radius $R_t \approx 1.95$ m, 510 keV, 10 MW). This analysis has been done using for the first time in DTT the orbit–following Monte Carlo code ASCOT [195] (Accelerated Simulation of Charged particle Orbits in Toroidal devices), a European state–of–the–art code for fast particle studies.[7] Although ASCOT can work with real 3D geometry of the machine and of the magnetic fields, we ran ASCOT only with 2D first wall. The high–energy beam is described in real geometry beamlet by beamlet thanks to the BBNBI code [196] (Beamlet–Based NBI–model), integrated with ASCOT, to better evaluate beam ionisation. Particularly, the trajectories of the 1360 beamlets of the DTT NBI ion source with a single beamlet divergence of 6 mrad have been imported in ASCOT. This detailed description allows to estimate the heat load on the first wall from non–ionised particles, i.e. the shine–through losses.

The analysis has been carried out for the reference DTT SN full power scenario during the flat–top phase. Reference CREATE–NL plasma equilibria has been directly used for ASCOT runs. The plasma density and temperature profiles are taken from the integrated simulation with spread ECRH deposition described in section 5.3.1. Argon and tungsten density profiles are also used by ASCOT to calculate the beam ionisation and the fast ion slowing down. In this work two electromagnetic scenarios in SN

[6] Thanks to grid optic optimisation, a linear decrease of power with energy is estimated about in the range 250–510 keV.

[7] ASCOT is implemented also in the IMAS infrastructure.

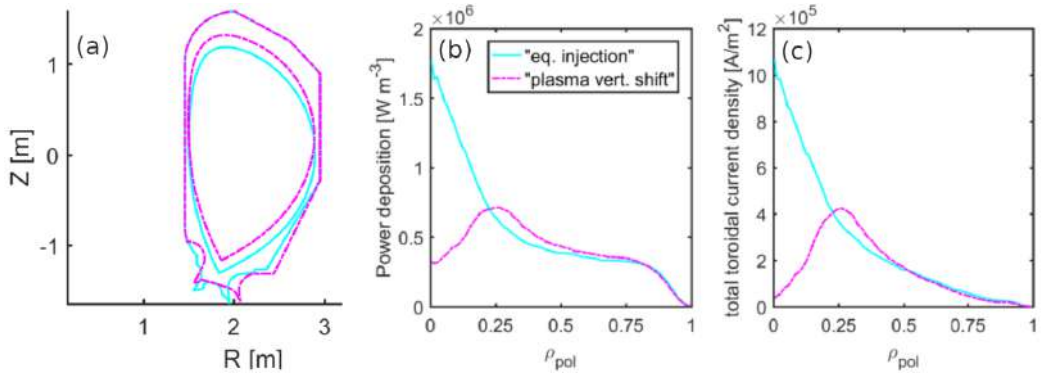

Figure 6.18: (a) First wall and LCFS of the two analysed plasma configurations. (b) NBI deposited power density and (c) driven toroidal current density profiles for these two configurations.

configuration have been analysed: the CREATE–NL equilibrium presented in [197] used as reference in section 5.3 for which the beam is injected on the equatorial plane, and a recent variation with the plasma rigidly shifted upwards by $\sim 15\,\mathrm{cm}$ for which the beam is injected below the equatorial plane. This new configuration allows to accommodate a different divertor concept, as depicted in figure 6.18(a).

The beam penetration beyond plasma edge region and the beam ionisation resulted very effective, respectively thanks to its high–energy and the high plasma density. The orbit losses are minimised by the co–current tangential beam injection and the shine–through losses resulted negligible in the DTT FP scenario. About 60 % of the fast ion energy is deposited to thermal ions and the NBI current drive contributes to the plasma current by about 5 %. All these results are found with both equilibria, although the ionisation cloud is vertically shifted and slightly modified. The plasma vertical position change does not significantly impact the volume–integrated quantities, but has a non–negligible effect on the NBI power density and current density radial profiles, as shown in figure 6.18(b) and (c). The NBI power deposition peak is on–axis when the beam is injected on the equatorial plane, while it results off–axis (peaked around $\rho_{\mathrm{pol}} = 0.25$) in the up–shifted configuration.

Finally, a sensitivity scan on plasma density was performed to verify the coupling of beam power at lower densities, because a partial beam ionisation would result in shine–through losses that may cause harmful first wall heat loads. Since the NBI footprint on the DTT FW, where the shine–through power is concentrated, is a relatively small area of about $\sim 0.25\,\mathrm{m}^2$, the first wall can cope with a low amount of shine–through losses. The limit for safe NBI operations in DTT could be set equal to $\sim 1\,\%$. This preliminary

study showed an exponential increase of shine–through losses for decreasing line–average density from the full power reference values of $2.05 \times 10^{20}\,\mathrm{m}^{-3}$ to $0.26 \times 10^{20}\,\mathrm{m}^{-3}$, regardless of the magnetic configuration. At an halved value of line–averaged density $\bar{n}_e = 1.03 \times 10^{20}\,\mathrm{m}^{-3}$, the fraction of NBI power lost to the first wall for shine–through is about 0.35 %, still within the safety limit. For $\bar{n}_e < 0.7 \times 10^{20}\,\mathrm{m}^{-3}$, the NBI energy and hence power has to be reduced to limit the shine–through. As future development, 3D wall simulations can be envisaged.

6.7 DTT fast ion losses due to field ripple

The complete work is widely described in the published paper [123] titled "*Collisionless losses of fast ions in the divertor tokamak test due to toroidal field ripple*".

The toroidal magnetic field, being produced by a discrete coil system, presents a ripple. In DTT, where only 18 toroidal field coils are foreseen as stated in section 2.6, the magnetic ripple can be non–negligible. Its interaction with fast ions is a well known issue.[8] In the paper [123], the first performed analysis of the effect of the DTT toroidal field ripple on the NBI fast ion losses in the single null full power scenario is reported.

When this work started, the standard equilibrium was based on an earlier version of the DTT design described in [8] with $R_0 = 2.08\,\mathrm{m}$, $B_0 = 6.07\,\mathrm{T}$, $I_{\mathrm{pl}} = 5.54\,\mathrm{MA}$, and $\Delta = 6.6\,\mathrm{cm}$ of Shafranov shift. The poloidal map of the magnetic field ripple in DTT was calculated for this equilibrium, as displayed on the left in figure 6.19. The field ripple increases moving from the plasma centre to the separatrix, as expected, and reaches the maximum values close to the equatorial plane. Particularly, the maximum ripple in the HFS is about 0.42 % of B_0, while in the LFS it reaches 0.22 % of B_0 at the most.[9] Then, the ripple map was recalculated for the full performance scenario in the new reference equilibrium with $R_0 = 2.19\,\mathrm{m}$, $B_0 = 5.894\,\mathrm{T}$, $I_{\mathrm{pl}} = 5.5\,\mathrm{MA}$, and $\Delta = 6.3\,\mathrm{cm}$ of Shafranov shift, as shown on the right in figure 6.19. With this new configuration, the ripple is maximum in the LFS with a value of 0.44 % of B_0 (almost double than before because of a greater closeness to the TF magnetic coils), while in the HFS it reaches 0.23 % of B_0 at the most.

The stochastic loss of trapped particles [199] due to the fast ion interaction with the TF ripple can be reduced by lowering the trapped particle fraction,

[8] For instance, JET is equipped with 32 toroidal field coils.

[9] In JET the ripple at the separatrix is about 0.08 %.[198]

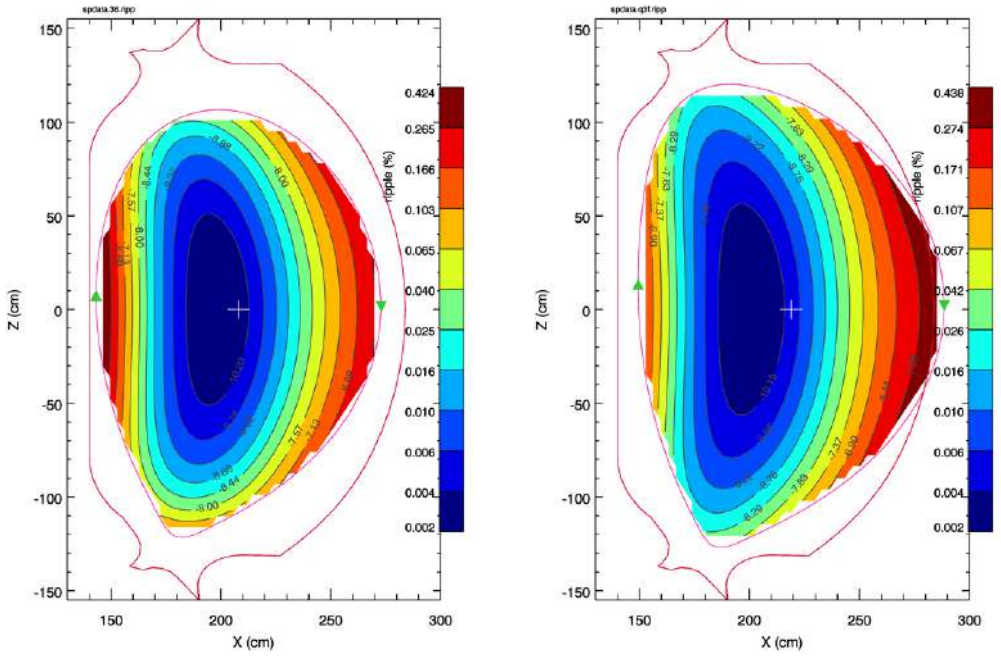

(a) (b)

Figure 6.19: Ripple map (a) for the old DTT configuration with $R_0 = 2.08\,\mathrm{m}$ and (b) for the current DTT reference configuration with $R_0 = 2.19\,\mathrm{m}$. The pink solid line represents the separatrix ($\psi_p = 1$). The first wall (drawn with a solid red line) refers to the old DTT design with $R_0 = 2.08\,\mathrm{m}$, an earlier version of the one described in [8].[123]

which depends on both the NBI injection angle and the beam energy. For the old $R_0 = 2.08\,\mathrm{m}$ configuration of DTT, the guiding centre code ORBIT [200] has been used to calculate fast ion trajectories and their losses due to the field ripple. Four beam energies $E_{\mathrm{NBI}} = 300, 400, 500, 800\,\mathrm{keV}$ and four injection angles $\alpha_{\mathrm{inj}} = 20°, 30.2°, 38.6°, 47°$ have been tested (4×4 runs). The NBI injection geometry is shown in figure 6.20. To assess the field ripple effect, these scans have been repeated for two equilibria: one with ripple and another without ripple. Thus, we can distinguish between the prompt losses or first–orbit losses [201] which occur quickly (< 10 toroidal turns) and the losses of particles with a well–defined pitch $\lambda := v_{\parallel}/v$ due to the magnetic field ripple. In each of these 32 ORBIT runs, the trajectories of 10^4 monoenergetic deuterons are evolved until they cross the separatrix. Since the ORBIT run duration is much smaller than the shortest collision period, we can reasonably assume that the fast ion losses are collisionless.

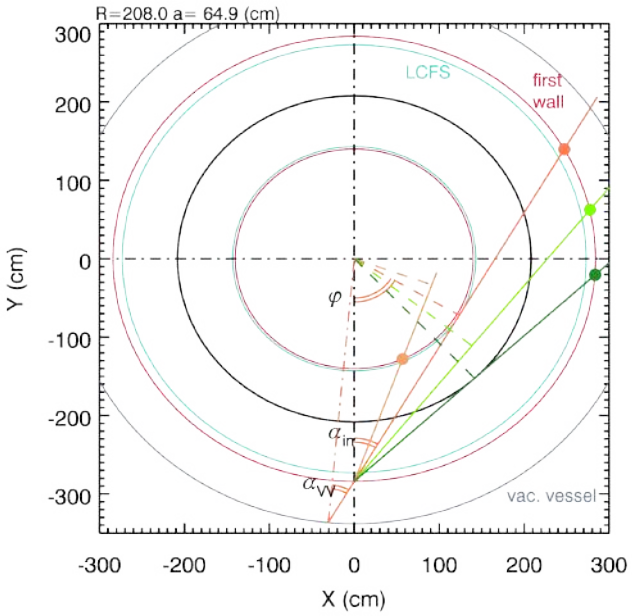

Figure 6.20: The four considered NBI geometries are schematically sketched viewing DTT from above. The chord impact parameters R_t are represented by dashed lines perpendicular to the four chords corresponding to different NBI injection angles α_{inj}. The vacuum vessel, first wall, and the LCFS are drawn with a grey, a red, and a cyan circles respectively.

In figure 6.21, fast ion losses with ripple (in green) and without ripple (in black) are shown for all cases of the scans. We notice that the injection angle effect dominates over the energy impact (more ionised particles in the core). At large injection angles and high beam energies the ripple contribution to the particle losses tends to vanish. Selecting an NBI system design with $R_t \geq 1.77\,\text{m}$ and $E \geq 500\,\text{keV}$ would be the best choice to minimise ripple losses, but also to achieve a better beam penetration and current drive [101]. To limit costs and engineering issues, it was decided to opt for a NBI with an injection angle at the first wall of $\alpha_{\text{inj}} = 38.6°$, corresponding to $R_t = 1.77\,\text{m}$, and with an energy of $E_{\text{beam}} = 400\,\text{keV}$. In this case ($R_0 = 2.08\,\text{m}$, $E_{\text{beam}} = 400\,\text{keV}$, $\alpha_{\text{inj}} \approx 40°$), prompt losses and ripple losses amount to 3.85 % and 0.15 % respectively. The ion birth mainly occurs in the region $\rho \sim 0.9$ close the equatorial plane.

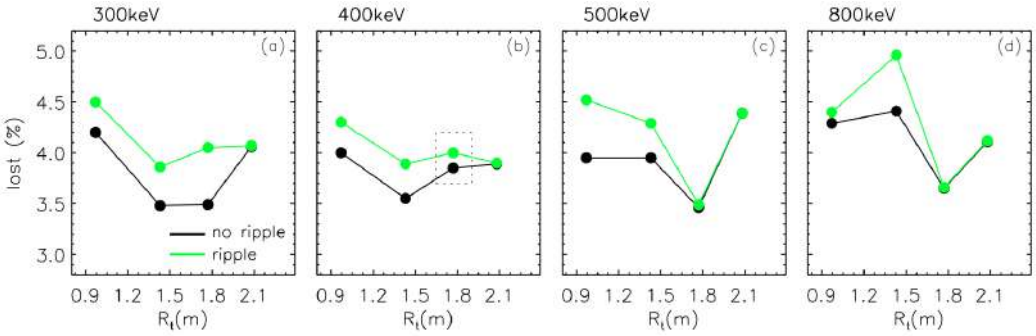

Figure 6.21: Fast ion losses (in percentage) plotted as a function of the tangency radius R_t. Each frame corresponds to a DTT NBI energy from 300 to 800 keV and presents injection angle scans with and without ripple. These results refer to the old $R_0 = 2.08$ m configuration. The dashed box indicates the configuration selected for NBI engineering [101] at the time.[123]

For the new DTT configuration with $R_0 = 2.19$ m, an analogous case with $E_{\text{beam}} = 400$ keV and $R_t = 1.83$ m has been also analysed, but energy and angle scans have not been repeated. To refine the initial ion distribution calculation of initial positions for this new equilibrium, simulations with the code TRANSP [202] has been performed using the plasma profiles of the SN full power scenario with $R_0 = 2.14$ m and with the heating option A simulated with the JINTRAC suite as reported in the chapter 4. Resulting ripple losses $\sim 0.12\,\%$ are similar to those calculated with the earlier geometry although the magnetic ripple has almost doubled, and prompt losses are drastically reduced to a value of about 0.03 %.

Summarising, with both DTT configurations the collisionless losses due to the field ripple have been found to be in an acceptable range 0.12–0.15 %. The first–orbit losses practically vanish if the 3D initial ion positions are calculated properly by TRANSP and JINTRAC runs.
For the $R_0 = 2.19$ m configuration, the NBI design has been updated to a system proving 10 MW to the plasma, with a beam energy of $E_{\text{beam}} = 510$ keV and with a tangency radius $R_t = 1.95$ m. The analysis of the fast ion losses in DTT proceeded and a new paper including all last updating of the NBI system, of the device configuration, and of the full power scenario is going to be submitted soon.

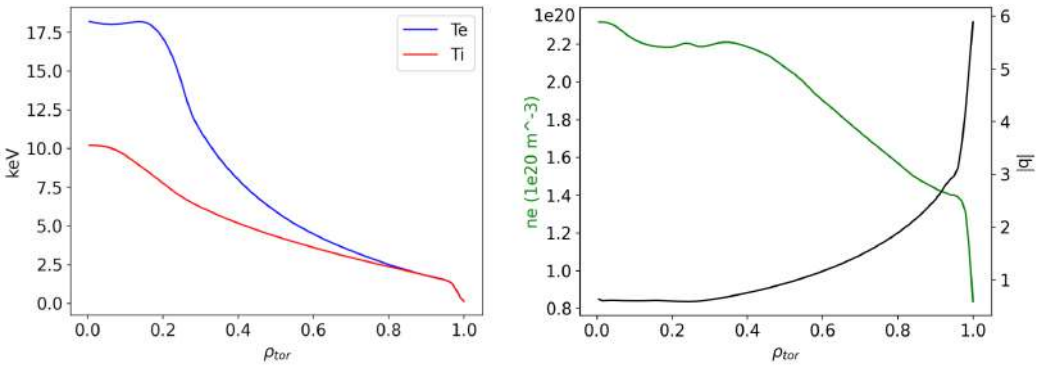

Figure 6.22: Profiles of the electron temperature T_e (blue), the ion temperature T_i (red), the electron density n_e (green), and the safety factor $|q|$ (black) as function of the normalised toroidal ρ_{tor} coordinate, for the DTT reference full power scenario suppressing the ICRH power contribution.

6.8 Investigation of the ICRH physics in DTT

> The complete work is widely described in the published paper [203] titled "*Numerical Investigation of the Ion Cyclotron Resonance Heating (ICRH) Physics in DTT*".

A predictive analysis of features and performances of the DTT ICRH system has been carried out for the reference full power scenario.
A first investigation was performed for a previous (currently outmoded) scenario of DTT, as reported in [204]. Then, more accurate and extensive studies of ICRH system the have been done for the new DTT configuration with $R_0 = 2.19\,\text{m}$ and $a = 0.70\,\text{m}$ in the full field and full current operational point ($B_{\text{tor}} = 5.85\,\text{T}$ and $I_{\text{pl}} = 5.5\,\text{MA}$).

As starting point of this updated and deeper analysis, the integrated modelling work of the full power scenario flat–top phase described in 5 was repeated with the JINTRAC suite of codes, but excluding the ICRH contribution to the plasma heating (with 28.8 MW and 10 MW respectively supplied by the ECRH and NNBI auxiliary heating systems). These new kinetic profiles were provided as input for this work, where the effect of the ICRH source on the plasma is calculated singly by specific theory–based wave codes. Figure 6.22 displays the radial profiles of the electron and ion temperatures, the electron density, and the absolute value of the safety factor predicted by JINTRAC.
The DTT plasma in this scenario has a paramagnetic effect on the vacuum

toroidal magnetic field which increases the field value at the geometric centre up to about 6 T, but this weak effect has not been considered here.

Advanced numerical tools have been used to calculate the ICRH propagation and absorption in the selected scenario: DISEMAG [205] solves the full dispersion relation in the complex wavenumber domain, while FELICE [206] and TORIC [207] solve the integro–differential equation to correctly assess the ICRH power absorption respectively in a slab plasma (1D) and in the tokamak equilibrium configuration (2D).[10] Wave–plasma interaction and wave damping mechanisms can be described and investigated using properly the different codes. In the FELICE and TORIC codes, the conceptual design of the ICRH antennas was incorporated. The current released design of the RF antennas of the DTT ICRH system, whose frequency can be continuously varied in the range of 60–90 Hz, is described in section 2.5.2. More details are reported in [203, 208, 209].

Firstly, power spectra have been calculated firstly by the FELICE code and then by the TORIC code for the ^{3}He minority heating scenario with the RF antenna at 60 MHz. With both codes, power spectra resulted symmetric in the toroidal wavenumber n_φ with the peak localised on $n_\varphi = \pm 25$.

Then, several parametric studies have been performed: the absorption on electrons, majority ions, and minority ions has been calculated as a function of the parallel wavenumber $n_\parallel := \frac{c}{2\pi f(R_0+a)}\, n_\varphi$ (equivalent to n_φ), the minority concentration, and the IC frequency.

The $n_\parallel$ scans tested both the helium–3 minority scheme with the RF injection frequency at $f = 60$ MHz and the hydrogen minority scheme with the RF injection frequency at $f = 85$ MHz. They have been carried out both with DISEMAG and with TORIC and have been repeated to test three different minority concentration values $(1, 3, 5\,\%)$. The absorption trends predicted by TORIC and DISEMAG resulted in very good agreement, with the fraction of absorbed power strongly depending on the parallel wavenumber. For any investigated minority concentration and for both minority species, the absorption trends are preserved by both codes in the $n_\parallel$ scans.

To investigate more deeply the dependence of the power absorption on

[10] DISEMAG (DISpersion ElectroMAGnetic) solves the wave dispersion relation at all orders terms for finite Larmor radius effects in slab geometry in the complex domain of the wave–vector.

FELICE (Finite Element Ion Cyclotron Evaluation) solves the 1D integro–differential wave equation in all plasma domain together with the relevant boundary conditions, and can give useful information about the coupled spectrum of IC antenna in outward radiation conditions or in full cross section mode.

TORIC (TORoidal Ion Cyclotron) solves the 3D integro–differential wave equation in a flux surface coordinate system. It describes the IC waves propagation and absorption in the whole plasma region.

the minority concentration, dedicated scans have been carried out both with TORIC and DISEMAG, both using ^{3}He with $f = 60\,\mathrm{MHz}$ and using ^{1}H with $f = 85\,\mathrm{MHz}$, fixing the toroidal wavenumber at power peak $n_\varphi = 25$. TORIC calculations show maximum absorbed power by ions at 6 % of ^{3}He ($\sim 50\,\%$) and at 2 % of ^{1}H ($\sim 65\,\%$). Unfortunately, DISEMAG is not able to catch this slope changes: the extremely low dependence of the absorbed power on the minority concentration foreseen by DISEMAG is presently under investigation.

In addition, to investigate the dependence of the power absorption on the ICRH frequency, dedicated scans have been carried out varying f in the range 55–95 MHz, using both ^{3}He and ^{1}H as minority species and fixing $n_\varphi = 23$ and a minority concentration of 3 %. A good agreement between the TORIC and DISEMAG trends has been found: the ion absorption is maximised at frequencies of 75–80 MHz both with ^{3}He (totally due to the majority species) and with ^{1}H (mainly due to the minority species) with absorption location around $r/a = (0.4 - 0.5)$.

Finally, a new promising ICRH heating scheme based on a mixture of three ions has been proposed for DTT. Exploiting a second minority species with a concentration lower than 1 % and with the fundamental cyclotron resonance close to the fast wave L–cutoff between the fundamental cyclotron resonances of the main ions and the first minority ion species, this second minority is very efficiently heated by the ICRH system. This scheme was successfully developed and tested in JET [4], Alcator C–Mod [210], and ASDEX Upgrade [211] tokamaks.[212, 213]
Thus, a preliminary study for DTT of the three–ion scenario with $n_\parallel = 8$ and $f = 60\,\mathrm{MHz}$ has been carried out based on the profiles foreseen by JINTRAC and shown in figure 6.22, involving a plasma composed by $\sim 66\,\%$ of H, $\sim 33\,\%$ of D, and 0.1 % of ^{3}He.
About 80 % of the injected power is absorbed by the helium ions, accelerating them up to $\sim 1\,\mathrm{MW}$. Hence, this new three–ion scheme will be useful also for generating fast ions.

Details of all these numerical investigations of the ICRH physics in DTT, reported in [203], are beyond the scope of this PhD thesis.

6.9 Neutron detector design for DTT

The complete work is widely described in the published paper [214] titled "*Conceptual design of a collimated neutron flux monitor and spectrometer for DTT*".

An intense neutron rate is expected in DTT during the high performance operations. The neutron emissivity ε is due to the 2.45 MeV DD neutrons for the most part and also to the 14.1 MeV DT neutrons, produced respectively by first and second fusion reactions reported in (1.1).
DTT will be equipped with several neutron diagnostic systems. Amongst them, a horizontal multi–channel collimated neutron flux monitor (also referred to as neutron camera) and a 2.45 MeV Time–Of–Flight (TOF) neutron spectrometer for DTT were designed. The neutron camera is dedicated to provide the neutron emissivity profile and can contribute to the plasma position real–time control. The neutron spectrometer, based on the design of TOFOR [215], is aimed at providing information on the plasma core performances in terms of T_{i_0}, n_D/n_e, and n_T/n_e measurements.

Their performance analysis has been based on the day–1 scenario and the full power option A scenario (the first reference FP scenario), described in the chapter 4. The PENCIL code, used in the JINTRAC simulations, has a simplified beam geometry description and tends to produce more peaked neutron profiles. In addition, the neutron emissivity contribution due to the DT reactions is not calculated in the JINTRAC runs. Therefore, to obtain a more realistic modelling of the fast ions deposition, interpretative runs of FP option A and day 1 scenarios were performed with TRANSP [202], using NUBEAM [216] to calculate the distribution functions of the slowing down NNBI fast ions, of the ICRH accelerated D ions and of the fusion products as a function of space, energy, and pitch. All plasma profiles were taken from the JINTRAC runs, whilst the heating was recalculated by TRANSP. Then the DRESS (Directional RElativistic Spectrum Simulator) code [217] was used to calculate neutron emissivities and energy spectra using non–isotropic and fully relativistic kinematics cross sections.
In the TRANSP–NUBEAM runs, the impurity densities are taken from the JINTRAC calculations, assuming that argon is fully stripped and tungsten has an average ionisation stage of 52. TRANSP then calculates the deuterium density and the effective charge imposing the quasi–neutrality condition. The implementation of the NNBI in NUBEAM is based on the preliminary system design described in [101] with two sources located at two adjacent toroidal sectors above and below the equatorial plane with a tan-

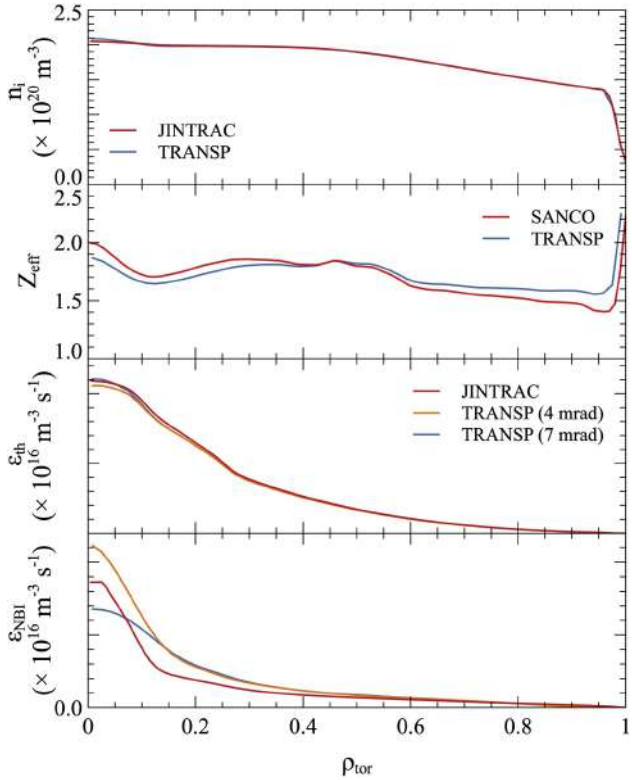

Figure 6.23: Radial profiles of the ion density, effective charge, the thermal–thermal component of the neutron emissivity $\varepsilon_{\mathrm{th}}$, and the beam–thermal component of the neutron emissivity $\varepsilon_{\mathrm{NBI}}$ in the SN FP scenario calculated by JINTRAC and by TRANSP using a NBI divergence of 4 mrad and 7 mrad.

gency radius of 1.77 m. Two beam divergences of 4 mrad and 7 mrad have been tested.

As shown in figure 6.23, the n_i and Z_{eff} profiles calculated by JINTRAC and TRANSP are in good agreement. The difference of code or of NBI divergence has a minimal impact on the thermal–thermal neutron emissivity. The beam–thermal neutron emissivity profiles are quite different: the TRANSP case with a NBI divergence of 4 mrad (closer to the zero divergence used in PENCIL) presents a $\varepsilon_{\mathrm{NBI}}$ radial profile similar to the JINTRAC one, the TRANSP case with a NBI divergence of 7 mrad (representative of typical NBI systems) presents a broader $\varepsilon_{\mathrm{NBI}}$ profile.

Figure 6.24 displays the temporal evolution of the neutron rate Y_n contributions and the triton burn–up ratio $Y_{\mathrm{DT}}/Y_{\mathrm{DD}}$ in the FP scenario calculated by TRANSP–NUBEAM. In agreement with the JINTRAC run outcomes, TRANSP found the thermal–beam (BT) contribution be dominant, followed

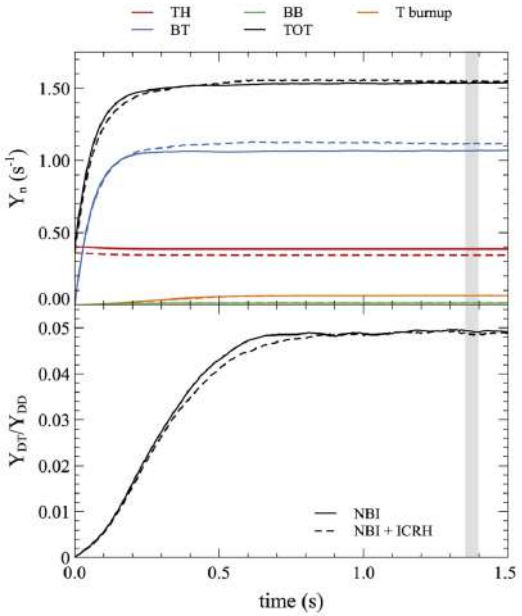

Figure 6.24: Neutron rates, split in the different components, calculated in TRANSP for the FP option A scenario using a NNBI divergence of 4 mrad with NBI only (solid lines) and NBI plus ICRH (dashed lines), and the triton burn–up ratio. The shaded area indicates the time interval used to generated the fast ion distribution and neutron emissivities used in the neutron diagnostic design.

by the thermal–thermal (TH) one. The beam–beam (BB) component is definitely negligible. The neutron rate due to the triton burn–up is in the range of 4–5 % for both FP and day–1 scenarios. If the ICRH heating and the related minority species (5 % of H) are removed from the TRANSP run, the thermal deuterium density increases and thermal–thermal neutron emission grows, but the beam–thermal component decreases due to the lack of the ICRH–accelerated D ions. Thus, the total neutron rate results approximately unchanged.
Compared to the JINTRAC evaluations, the total neutron rates predicted by TRANSP–NUBEAM are higher by ~ 6 % for the day–1 scenario and by ~ 13 % for the FP scenario; about 6 % of this discrepancy is due to the triton burn–up contribution (not included in JINTRAC).

The neutron detectors have been designed based on these results, on the corresponding neutron energy spectra calculated by DRESS, and on the estimates of the scattered neutron contribution by the MCNP (Monte Carlo N–Particle) code [218] as described in [219]. The neutron detector design, described in detail in [214], is beyond the scope of this PhD thesis.

6.10 GEM–based SXR plasma imaging in DTT

The complete work is widely described in the published paper [220] titled "*Development of 2D GEM–based SXR plasma imaging for DTT device: Focus on readout structure*".

A global plasma Soft X–ray (SXR) 2D imaging technique based on a Gas Electron Multiplier (GEM) detector has been designed, focusing on the readout anode. The GEM detector was adapted to register the SXR radiation coming from a tokamak plasma and particularly the tungsten and seeded impurity emission. The possibility of adopting this technology as a DTT divertor view diagnostic was verified. Particularly, the electron temperature, electron density, and impurity profiles of the full power option A scenario described in the chapter 4 were exploited to obtain the integrated emissivity of the SXR spectrum along the detector LOS (Lines Of Sight). Details of this SXR detector design are reported in [220].

CHAPTER 7

Conclusions and future works

The first physics–based multi–channel simulations of the main baseline operational scenarios of the new Divertor Tokamak Test facility during the flat–top phases were performed. This integrated modelling work, progressively improved including a growing number of aspects and refining run settings, both guided and followed the machine design evolution in the last three years.

These simulations are based on first–principle transport models. Several neoclassical (NCLASS, Romanelli–Ottaviani) and turbulent (QLKNN, QLK, QLK ad hoc version, TGLF SAT0, TGLF SAT1, TGLF SAT1–geo, TGLF SAT2) transport models were employed. The comparison among analogous simulations with different quasi–linear transport models made us confident in the reliability of the predicted plasma profiles and allowed us to identify the weak points of the models in the various DTT operational regimes. Some preliminary tests to use the drift kinetic code NEO [221] as impurity neoclassical model were done in order to properly consider the impact of poloidal asymmetries on tungsten transport.
A validation of the quasi–linear models against the GENE gyrokinetic simulations in the specific DTT range of parameters was also performed.

Initially, the full power scenario (with $\sim 45\,\mathrm{MW}$ of total auxiliary heating power supplied by the ECRH, NBI, and ICRH systems to the plasma), the intermediate phase Day–1 at about half power, and the first plasma Day–0 scenario were modelled in the previous DTT configuration ($R_0 = 2.14\,\mathrm{m}$, $a = 0.65\,\mathrm{m}$, vacuum toroidal field $B_{\mathrm{tor}} \leq 6.0\,\mathrm{T}$). To select the optimal power distribution amongst the three auxiliary heating systems and the neutral beam energy, the full performance scenario was tested with nine different

heating mix options. This analysis led to the new reference heating mix consisting of 32 MW of ECRH installed power, 8 MW of ICRH installed power, and 10 MW of NBI installed power with the NBI system operating at 510 keV. The low value of the safety factor value at the flux surface that contains the 95 % of the poloidal flux, which is typically associated with a higher disruptivity risk, alarmed the DTT team that decided to enlarge the machine.
The new DTT configuration ($R_0 = 2.19\,\mathrm{m}$, $a = 0.70\,\mathrm{m}$, vacuum toroidal field $B_{\mathrm{tor}} \leq 5.85\,\mathrm{T}$) was then remodelled including the updates of magnetic equilibria and heating systems. Particularly, simulations of the full power scenario, the intermediate scenario with about half power, and the first plasma scenario (respectively renamed E1, C1, and A1 scenarios) were performed.

The prediction accuracy has been improved recursively by matching the core and SOL simulation boundary conditions to ensure the core–edge–SOL consistency. This iterative work of key parameter adjustment was repeated for all the examined scenarios and for different seeded impurities (argon, neon, nitrogen). A work of core–pedestal–SOL integrated modelling, totally self–consistent in terms of temperature and density profiles, fluxes, and transport coefficients, can be envisaged as future development, using COCONUT [222] which properly combines the JETTO and EDGE2D codes within the JINTRAC suite.

In the E1 scenario updated modelling, to fulfill the SOL requirements, a density value at the separatrix $n_e^{\mathrm{sep}} \approx 0.8 \times 10^{20}\,\mathrm{m}^{-3}$ was set. This is much larger than typical values of plasma discharges in existing tokamaks and than values in previous DTT simulations. It entailed a change in the relative shift of density and temperature pedestals and a very high density gradient in the pedestal, harder to be handled. The present choice for the full power scenario of a Greenwald fraction of about $\bar{n}_e/n_{\mathrm{Gr}} \approx 0.5$, implies $T_e \gg T_i$ over almost the whole plasma radius. Raising the Greenwald fraction will be possible, leading to a better balance between T_e and T_i, but mostly via a T_e reduction, because high ion stiffness binds the T_i profile tightly to the ITG critical gradient. Such high stiffness is also consistent with the observation that the E1 scenario has very similar T_i profiles to the C1 scenario, in spite of roughly double additional power. Possible ways of reducing ion stiffness through fast ions have been reported in literature[150, 151, 152, 153], but including these effects in integrated simulations requires an upgrade of existing quasi–linear transport models. Although the electron density is moderately peaked in the E1 scenario, the tungsten does not accumulate in the plasma centre. In the C1 and A1 scenarios a flatter density profile has been found, as expected due to the lack of the neutral beam injector.

An analysis of the required fuelling system performance to sustain the high density profiles in the full power scenario proved that using only the gas

puffing system would be insufficient and that deuterium pellets are needed for the DTT fuelling. The pellet features (frequency, pellet size, injection point) have been optimised to fuel DTT; results will be published in [136].

Neutron rates were evaluated and found compatible with the present design of the neutron shields.

All these integrated simulations of the DTT plasma profiles have been carried out using the JINTRAC suite with the JETTO transport solver or using an iterative ASTRA–JINTRAC scheme, specifically devised for some high complexity cases.
The prospect of adopting the IMAS (Integrated Modelling & Analysis Suite) infrastructure as standard database for DTT has been considered in order to be aligned with the ITER team choice. Since in the last year JETTO has been enriched by the option of using IDS (Interface Data Structure) of the IMAS environment for input and/or output file, it simplifies the potential transition to IMAS. Some preliminary exploring studies in this regard started.

To guarantee the consistency between the electromagnetic configuration achievable by the control coil system and plasma profiles predicted by the integrated simulations, a weak coupling between CREATE–NL and JETTO was set–up and applied to the SN flat–top configuration in the full power scenario. Particularly, a recalculation of the currents in the central solenoid and poloidal field coils needed to achieve the desired plasma shape and the flat–top plasma boundary flux with the profiles determined by JETTO was performed. Although significant coil current variations were found to be required, they lie in a feasible range.

The DTT Edge Localised Modes were estimated for the first time through suitable scalings. The calculated loss of plasma energy due to one ELM is about 10 % of the pedestal energy in the reference full power scenario. A more detailed analysis on ELM stability and their inclusion in the integrated modelling are planned for the near future.

The sawteeth were recently included in DTT full power scenario simulations and a wide analysis for optimising EC launching angles to improve the safety factor profile was done. The Porcelli and Kadomtsev models have been used respectively to trigger the sawteeth and to predict the relaxed temperature, density, and $|q|$ profiles after a crash. The ST frequency with an incomplete reconnection with a fraction of $f_{\mathrm{rec}} = 0.8$ is $f_{\mathrm{ST}} \approx 1.7\,\mathrm{Hz}$. As further development, a more accurate incomplete reconnection relaxation model could be tested in order to better calculate the $|q| = 1$ position during sawtooth oscillations with expected beneficial effects.

Following the decision to move upwards the plasma by about 15 cm to accomodate a new divertor design, new magnetic equilibria have been recently made available. Therefore, the integrated modelling will be updated soon,

even though no significant changes are expected in the core plasma profiles.

To characterise the ramp–up and ramp–down phases of the reference DTT full power scenario, specific time–dependent ASTRA simulations using the TGLF SAT2 model are scheduled. A first preliminary time–dependent modelling work of the ramp–up L–mode phase was already performed, in collaboration with the Max–Planck Institut für Plasmaphysik (IPP). To also include the evolving H–mode phase in the ramp–up modelling, ASTRA simulation are planned to be coupled with IMEP [223] (Integrated Model of tokamak plasma confinement based on Engineering Parameters) for the pedestal calculation.

In parallel to the analysis of the DTT SN scenarios with Positive Triangularity (PT), a SN full power scenario with Negative Triangularity (NT) has also been designed. Both quasi–linear and gyrokinetic runs were carried out to assist its development. In addition to the modelling activity, dedicated experiments in view of DTT NT scenario design were done in the AUG and TCV tokamaks, within the EUROfusion WPTE (Work Package Tokamak Exploitation) under the Research Topic RT07. This PhD project has dealt with the first QL simulations of the NT scenario, and more work is planned on this front.

Finally, the simulations developed in this PhD thesis, and further work of integrated modelling planned for the future, will be a key tool for the development of the DTT Research Plan, an activity that has been recently started within an international framework of scientific collaboration.

List of publications, conference proceedings, workshops, and international meeting presentations

My ORCID page is: https://orcid.org/0000-0002-1719-6682.

Papers and conference proceedings

- I. Casiraghi et al., *Core integrated simulations for the Divertor Tokamak Test facility scenarios towards consistent core–pedestal–SOL modelling* (submitted to Plasma Physics and Controlled Fusion).
- I. Casiraghi et al., *Scenario modelling for the Divertor Tokamak Test facility*, Il Nuovo Cimento 45 C 162, 2022.
- I. Casiraghi et al., *First–principle based multi–channel integrated modelling in support to the design of the Divertor Tokamak Test facility*, Nuclear Fusion 61 116068, 2021.
- I. Casiraghi, P.Mantica et al., *First–principle based multi–channel integrated modelling in support to the design of the Divertor Tokamak Test facility*, IAEA–TH–743 (28th IAEA Fusion Energy Conference 2020 proceedings), 2021.
- I. Casiraghi et al., *Integrated modelling of the main Divertor Tokamak Test facility scenarios*, 47th EPS Conference on Plasma Physics 2021–June 525–528, 2021.
- A. Mariani et al., *Benchmark of quasi–linear models against gyrokinetic single scale simulations in deuterium and tritium plasmas for a JET high beta hybrid discharge*, Nuclear Fusion 61 066032, 2021.

- M. Chernyshova et al., *Development of 2D GEM–based SXR plasma imaging for DTT device: Focus on readout structure*, Fusion Engineering and Design 169 112443, 2021.
- P. Agostinetti et al., *Conceptual Design of the Beamline for the DTT Neutral Beam Injector following a Double Beam Source Design Approach*, Plasma and Fusion Research 16 2405080, 2021.
- G. Spizzo et al., *Collisionless losses of fast ions in the Divertor Tokamak Test due to toroidal field ripple*, Nuclear Fusion 61 116016, 2021.
- M. Cecconello et al., *Conceptual design of a collimated neutron flux monitor and spectrometer for DTT*, Fusion Engineering and Design 167 112382, 2021.
- P. Vincenzi et al., *Exploring Divertor Tokamak Test (DTT) operation space and plasma scenarios through time–dependent 0.5D integrated modelling*, 47th EPS Conference on Plasma Physics 2021–June 677–680, 2021.
- L. Balbinot et al., *Multi–code Estimation of DTT Edge Transport Parameters*, Nuclear Materials and Energy 101350, 2022.
- A. Cardinali et al., *Numerical Investigation of the Ion Cyclotron Resonance Heating (ICRH) Physics in DTT*, Journal of Physics: Conference Series 2397 012017, 2022.
- P. Vincenzi, *Interaction of high–energy neutral beams with Divertor Tokamak Test plasma*, proceeding of the 32nd Symposium on Fusion Technology, 18 – 23 September 2022.
- B. Baiocchi, L. Aucone et al., *Predictive studies of deuterium fuelling strategies in the Divertor Tokamak Test facility* (submitted to Plasma Physics and Controlled Fusion).

Posters presented to international conferences

- I. Casiraghi et al., *Theory based simulations to predict the plasma profiles of the Divertor Tokamak Test facility baseline scenarios*, FuseNet PhD event, 4–6 July 2022.
- I. Casiraghi, P. Mantica et al., *First–principle based multi–channel integrated modelling in support to the design of the Divertor Tokamak Test facility*, 28th IAEA Fusion Energy Conference, 10 – 15 May 2021.

- I. Casiraghi et al., *First principle scenario modelling of the Divertor Tokamak Test facility*, 29th International Toki Conference on Plasma and Fusion Research (ITC29), 27 – 30 October 2020.
- I. Casiraghi et al., *First principle scenario modelling of the Divertor Tokamak Test facility*, 4th Asia–Pacific Conference on Plasma Physics (AAPPS–DPP), 26 – 31 October 2020.
- I. Casiraghi et al., *Integrated scenario modelling in tokamak devices using first principle based transport models. Application to the design of the new Italian tokamak DTT.*, FuseNet PhD event, 23 – 24 November 2020.
- P. Vincenzi, *Interaction of high–energy neutral beam with Divertor Tokamak Test plasma*, 32nd Symposium on Fusion Technology, 18 – 23 September 2022.
- L. Aucone et al., *Predictive simulations of deuterium fuelling in the Divertor Tokamak Test facility plasmas*, FuseNet PhD event, 4–6 July 2022.
- A. Mariani et al., *Transport analysis of a DTT negative triangularity scenario*, 48th EPS conference on Plasma Physics, 27 June – 1 July 2022.
- L. Balbinot et al., *Multi–code Estimation of DTT Edge Transport Parameters*, International Conference on Plasma Surface Interaction in Controlled Fusion Devices (PSI–25), 13 – 17 June 2022.
- P. Vincenzi et al., *Exploring Divertor Tokamak Test (DTT) operation space and plasma scenarios through time–dependent 0.5D integrated modelling*, 47th EPS Conference on Plasma Physics, 21 – 25 June 2021.
- P. Martin et al., *Divertor Tokamak Test Facility: Science Basis and Status of the Project*, 28th IAEA Fusion Energy Conference, 10 – 15 May 2021.

Oral contributions to international conferences

- I. Casiraghi et al., *Predict–first scenario modelling in support of the design of the Divertor Tokamak Test facility*, 48th EPS conference on Plasma Physics, 27 June – 1 July 2022.

- I. Casiraghi, *First–principle integrated modelling of the main scenarios of the new Divertor Tokamak Test facility*, 107° Congresso Nazionale della Società Italiana di Fisica, 13 – 17 September 2021.

- I. Casiraghi et al., *Overview on the first–principle integrated modelling of the main scenarios of the new Divertor Tokamak Test facility*, 25th Joint EU–US Transport Task Force meeting, 6 – 10 September 2021.

- I. Casiraghi et al., *The new Divertor Tokamak Test facility: main scenario integrated modelling*, FuseNet 8–bit PhD event, 2021.

- N. Bonanomi et al., *From L–mode to the L–H transition, experiments on ASDEX Upgrade, gyrokinetic simulations and full-radius transport modeling*, 48th EPS conference on Plasma Physics, 27 June – 1 July 2022.

- M. Chernyshova et al., *Development of 2D GEM–based SXR plasma imaging for DTT device: Focus on readout structure*, 31st Symposium on Fusion Technology (SOFT2020), 20 – 25 September 2020.

- A. Romano, *Il contributo Italiano al programma mondiale sulla fusione termonucleare controllata: il progetto Divertor Tokamak Test*, 106° Congresso Nazionale della Società Italiana di Fisica (SIF 2021), 14 – 18 September 2020.

- P. Martin et al., *The new Divertor Tokamak Test Facility*, 61st APS Annual Meeting of the Division of Plasma Physics, 21 – 25 October 2019.

Participations to workshops

- Spanish fusion HPC (High Performance Supercomputing) workshop (1st edition), 27 November 2020.

- ETS (European Transport Solver) training workshop, 23 November – 4 December 2020.

Seminars

- I. Casiraghi, *IMEP: an Integrated Model of tokamak plasma confinement based on Engineering Parameters*, based on the TTF meeting talk of T. Luda (2021).

Works as referee

- Nuclear Fusion $\longrightarrow$ 2 published papers + 1 rejected paper.
- Journal of Instrumentation $\longrightarrow$ 1 published paper.

Acknowledgements

I sincerely thank Paola Mantica for the great support, the trust, and the accurate suggestions she has given me during these years. Her inexhaustible passion for our work and her unflinching dedication are inspiring. She is a force of nature!

I am also grateful to Florian Koechl, Alberto Mariani, and Benedetta Baiocchi for their simulation work, but especially for answering exhaustively my many questions, demonstrating a disarming patience every time.

I am grateful to Gary Staebler and Jonathan Citrin for providing advice on the use of the TGLF and QLK models respectively and I thank Giovanni Tardini for his help with the ASTRA simulations.

This work was carried out in the frame of the DTT design activity. I am very grateful to all the colleagues involved in the DTT project for their precious contribution and for welcoming me into the group.
Particularly I would like to thank Lorenzo Frassinetti, Paolo Innocente, Luca Balbinot, Lorenzo Aucone, Silvana Nowak, Tommaso Barberis, Roberto Ambrosino, Antonio Castaldo, Marco Cavedon, Lorenzo Figini, Piero Agostinetti, Pietro Vincenzi, Alessandro Cardinali, Silvio Ceccuzzi, Mattia Dicorato, Piero Martin, Gregorio Vlad, Fulvio Zonca, Gustavo Granucci, and Marco Valisa for their valuable help and advices.

Many thanks go to all the CNR–ISTP staff for the kindness and hospitality shown during these years. I am very lucky to have coffee breaks with a group of unusual and funny people that I really like.

I would like to thank EUROfusion for providing numerical tools required for this modelling work.

A grant financed by ENEA supported my PhD project.

Bibliography

[1] John Wesson. *Tokamaks*. Oxford science publications, 2011. 4th edition.

[2] Jeffrey P. Freidberg. *Plasma Physics and Fusion Energy*. Cambridge University Press, 2007.

[3] Grafik of C. Brandt. *Max-Planck-Institut f¨ur Plasmaphysik, IPP Bilddatenbank*, 2011.

[4] JET EFDA Contributors. Special Issue on Joint European Torus (JET). *Fusion Science Technology*, 53(4):861–1227, 2008.

[5] `https://www.iter.org/`.

[6] EFDA 2012 Fusion electricity – A roadmap to the realisation of fusion energy (2012), `https://www.euro-fusion.org/fileadmin/user_upload/Archive/wp-content/uploads/2013/01/JG12.356-web.pdf`.

[7] EUROfusion 2018 European research roadmap to the Realisation of Fusion Energy, `https://www.euro-fusion.org/fileadmin/user_upload/EUROfusion/Documents/2018_Research_roadmap_long_version_01.pdf`.

[8] R. Martone, R. Albanese, F. Crisanti, P. Martin, and A. Pizzuto. Divertor Tokamak Test Facility: Interim Design Report (Green Book). *ENEA Internal Report (ENEA Frascati Research Center)*, 2019.

[9] G. Granucci et al. *Fusion Engineering and Design*, 122:349–355, 2017.

[10] `https://dtt-project.enea.it/`.

[11] DTT-Divertor Tokamak Test facility. Project Proposal (Blue Book). 2015.

[12] *DTT Plant Integration Document (DTT PID), version 3.2 (last update 07/07/2022).* Currently this document is not public, but information and clarifications can be requested to info@dtt-project.it.

[13] A. Pizzuto et al. *Nuclear Fusion*, 50:095005, 2010.

[14] *ITER Organization 2018 ITER Research Plan within the Staged Approach (Level III – Provisional Version), report ITR-18-003.*

[15] B. Baiocchi and P. Mantica. *Physics-based transport modelling of main species particle and energy transport in the core plasma of ITER reference scenarios during stationary phases and post-pellet transients.* third report.

[16] A.S. Kukushkin et al. *Nuclear Fusion*, 43:716, 2003.

[17] R. Wenninger et al. *Nuclear Fusion*, 57:016011, 2017.

[18] I. Casiraghi et al. *Nuclear Fusion*, 61:116068, 2021.

[19] S. Ishida et al. *Nuclear Fusion*, 51:094018, 2011.

[20] P. Agostinetti et al. *Nuclear Fusion*, 51:063004, 2011.

[21] P. Agostinetti et al. *Nuclear Fusion*, 56:016015, 2016.

[22] W. Horton. Drift waves and transport. *Reviews of Modern Physics*, 71:735–778, Apr 1999.

[23] X. Garbet and P. Mantica et al. Physics of transport in tokamaks. *Plasma Physics and Controlled Fusion*, 46(12B):B557–B574, nov 2004.

[24] J. Weiland. Collective Modes in Inhomogeneous Plasma IOP. 2000.

[25] A. Hirose. *Drift Instabilities in Magnetically Confined Plasmas: A Brief Overview.* Autumn College on Plasma Physics, International Centre for Theoretical Physics, Trieste, Italy. Plasma Physics Laboratory, University of Saskatchewan, Canada, 2005.

[26] P.H. Diamond et al. Zonal flows in plasma — a review. *Plasma Physics and Controlled Fusion*, 47(5):R35–R161, 2005.

[27] K. Itoh et al. Physics of zonal flows. *Physics of Plasmas*, 13(5):055502, 2006.

[28] F. Romanelli and F. Zonca. *Physics of Fluids B*, 5:4081–9, 1993.

[29] Romanelli F. *Physics of Fluids B*, 1:1018–25, 1989.

[30] P. Mantica et al. Experimental Study of the Ion Critical–Gradient Length and Stiffness Level and the Impact of Rotation in the JET Tokamak. *Physical Review Letters*, 102:175002, 2009.

[31] S.C. Guo and F. Romanelli. The linear threshold of the ion temperature gradient driven mode. *Physics of Fluids B: Plasma Physics*, 5(2):520–533, 1993.

[32] F. Jenko, W. Dorland, M. Kotschenreuther, and B.N. Rogers. Electron temperature gradient driven turbulence. *Physics of Plasmas*, 7(5):1904–1910, 2000.

[33] F. Jenko, W. Dorland, and G.W. Hammett. *Physics of Plasmas*, 8:4096–104, 2001.

[34] T. Görler and F. Jenko. Scale Separation between Electron and Ion Thermal Transport. *Physical Review Letters*, 100:185002, 2008.

[35] N.T. Howard et al. Synergistic cross-scale coupling of turbulence in a tokamak plasma. *Physics of Plasmas*, 21(11):112510, 2014.

[36] S. Maeyama et al. Cross-Scale Interactions between Electron and Ion Scale Turbulence in a Tokamak Plasma. *Physical Review Letters*, 114:255002, 2015.

[37] B.B. Kadomtsev and O.P. Pogutse. Trapped particles in toroidal magnetic systems. *Nuclear Fusion*, 11(1):67–92, 1971.

[38] A.G. Peeters et al. Linear gyrokinetic stability calculations of electron heat dominated plasmas in ASDEX Upgrade. *Physics of Plasma*, 12(2):022505, 2005.

[39] F. Ryter et al. Experimental Study of Trapped–Electron–Mode Properties in Tokamaks: Threshold and Stabilization by Collisions. *Physical Review Letters*, 95:085001, 2005.

[40] A. Casati et al. Temperature ratio dependence of ion temperature gradient and trapped electron mode instability thresholds. *Physics of Plasmas*, 15(4):042310, 2008.

[41] A.J. Brizard and T.S. Hahm. Foundations of nonlinear gyrokinetic theory. *Reviews of Modern Physics*, 79:421–468, 2007.

[42] T. Görler, X. Lapillonne, S. Brunner, T. Dannert, F. Jenko, F. Merz, and D. Told. The global version of the gyrokinetic turbulence code GENE. *Journal of Computational Physics*, 230:7053–71, 2011.

[43] `http://genecode.org/`.

[44] J. Candy and E.A. Belli. GYRO Technical Guide. *General Atomics Technical Report*, 2010.

[45] J. Candy and R.E. Waltz. Anomalous transport scaling in the DIII–D tokamak matched by supercomputer simulation. *Physical Review Letters*, 91:045001, 2003.

[46] J. Candy and R.E. Waltz. An Eulerian gyrokinetic-Maxwell solver. *Journal of Computational Physics*, 186:545, 2003.

[47] J. Candy, R.E. Waltz, and W. Dorland. The local limit of global gyrokinetic simulations. *Physics of Plasmas*, 11:L25, 2004.

[48] E.A. Belli and J. Candy. Implications of advanced collision operators for gyrokinetic simulation. *Plasma Physics and Controlled Fusion*, 59:045005, 2017.

[49] E.A. Belli and J. Candy. Impact of centrifugal drifts on ion turbulent transport. *Physics of Plasmas*, 25:032301, 2018.

[50] J. Candy E.A. Belli and R.V. Bravenec. A high-accuracy Eulerian gyrokinetic solver for collisional plasmas. *Journal of Computational Physics*, 324:73, 2016.

[51] J. Candy, I. Sfiligoi, E. Belli, K. Hallatschek, C. Holland, N. Howard, and E.D'Azevedo. Multiscale-optimized plasma turbulence simulation on petascale architechtures. *Computers & Fluids*, 188:125, 2019.

[52] G.M. Staebler, J.E. Kinsey, and R.E. Waltz. *Physics of Plasmas*, 12:102508, 2005.

[53] G.M. Staebler, J.E. Kinsey, and R.E. Waltz. *Physics of Plasmas*, 14:055909, 2007.

[54] G.M. Staebler, J. Candy, N.T. Howard, and C. Holland. *Physics of Plasmas*, 23:062518, 2016.

[55] J.E. Kinsey et al. The first transport code simulations using the trapped gyro–Landau–fluid model. *Physics of Plasmas*, 15(5):055908, 2008.

[56] R.E. Waltz et al. A gyro-Landau-fluid transport model. *Physics of Plasmas*, 4(7):2482–2496, 1997.

[57] W.M. Stacey and Cheonho Bae. Representation of the plasma fluid equations in "miller equilibrium" analytical flux surface geometry. *Physics of Plasmas*, 16(8):082501, 2009.

[58] A. Peeters et al. The nonlinear gyro-kinetic flux tube code GKW. *Computer Physics Communications*, 180:2650–2672, 2009.

[59] G.M. Staebler et al. *Plasma Physics and Controlled Fusion*, 63:015013, 2021.

[60] J. Citrin et al. *Plasma Physics and Controlled Fusion*, 59:124005, 2017.

[61] C. Bourdelle, J. Citrin, B. Baiocchi, A. Casati, P. Cottier, X. Garbet, and F. Imbeaux. *Plasma Physics and Controlled Fusion*, 58:014036, 2016.

[62] C.D. Stephens et al. *Journal of Plasma Physics*, 87(4):905870409, 2021.

[63] K.L. van de Plassche, J. Citrin, C. Bourdelle, Y. Camenen, F.J. Casson, V.I. Dagnelie, F. Felici, A. Ho, and Van S. Mulders. *Physics of Plasmas*, 27:022310, 2020.

[64] D.P. Coster et al. The European Transport Solver. *IEEE Transactions on Plasma Science*, 38(9), 2010.

[65] F. Imbeaux et al. Design and first applications of the ITER integrated modelling & analysis suite. *Nuclear Fusion*, 55(12):123006, 2015.

[66] M. Schneider et al. Simulation of heating and current drive sources for scenarios of the ITER research plan. *Nuclear Fusion*, 61(12):126058, 2021.

[67] G.V. Pereverzev and P.N. Yushmanov. ASTRA automated system for transport analysis in a tokamak IPP Report 5/98. *Max-Planck-Institut für Plasmaphysik*, 2002.

[68] A.A. Ivanov. *32nd EPS Conf. on Plasma Physics—Terragona 29C (ECA), P-5.063*, 2005.

[69] E. Poli, A.G. Peeters, and G.V. Pereverzev. TORBEAM, a beam tracing code for electron–cyclotron waves in tokamak plasmas. *Computer Physics Communications*, 136(1):90–104, 2001.

[70] E. Poli et al. TORBEAM 2.0, a paraxial beam tracing code for electron–cyclotron beams in fusion plasmas for extended physics applications. *Computer Physics Communications*, 225:36–46, 2018.

[71] M. Weiland et al. RABBIT: Real–time simulation of the NBI fast–ion distribution. *Nuclear Fusion*, 58(8):082032, 2018.

[72] D. Farina. *Fusion Science and Technology*, 52:154 –60, 2007.

[73] C.D. Challis, J.G. Cordey, H. Hamnén, P.M. Stubberfield, J.P. Christiansen, E. Lazzaro, D.G. Muir, D. Stork, and E. Thompson. *Nuclear Fusion*, 29:563, 1989.

[74] L.-G. Eriksson, T. Hellsten, and U. Willen. *Nuclear Fusion*, 33:1037, 1993.

[75] L. Taroni. *21st EPS Conf. Contr Fus Plas Phys—Montpellier 102 I*, 1994.

[76] `https://euro-fusion.org/programme/demo/`.

[77] D.M. Thomas, A.W. Leonard, T.H. Osborne, R.J. Groebner, W.P. West, and Burrell K.H. *Plasma Physics and Controlled Fusion*, 48:A183, 2006.

[78] M. Greenwald. *Plasma Physics and Controlled Fusion*, 44:R27, 2002.

[79] M. Romanelli et al. *Plasma and Fusion Research*, 9:3403023, 2014.

[80] S. Saarelma, C.D. Challis, L. Garzotti, L. Frassinetti, C.F. Maggi, M. Romanelli, and C. Stokes. Integrated modelling of H–mode pedestal and confinement in JET–ILW. *Plasma Physics and Controlled Fusion*, 60(1):014042, 2018.

[81] P.B. Snyder, R.J. Groebner, J.W. Hughes, T.H. Osborne, M. Beurskens, A.W. Leonard, H.R. Wilson, and X.Q. Xu. *Nuclear Fusion*, 51:103016, 2011.

[82] E. Stefanikova et al. *Nuclear Fusion*, 58:056010, 2018.

[83] L. Frassinetti et al. *Nuclear Fusion*, 61:016001, 2021.

[84] P. Mantica, C. Angioni, N. Bonanomi, J. Citrin, B.A. Grierson, F. Koechl, A. Mariani, and G.M. Staebler. *Plasma Physics and Controlled Fusion*, 62:014021, 2020.

[85] S. Mordijck et al. *Nuclear Fusion*, 60:066019, 2020.

[86] B.A. Grierson, G.M. Staebler, W.M. Solomon, G.R. McKee, C. Holland, M. Austin, A. Marinoni, L. Schmitz, and R.I. Pinsker. *Physics of Plasmas*, 25:022509, 2018.

[87] E.J. Doyle et al. *(FEC) 2012 IAEA Fusion Energy Conf. EX/P3-26.*

[88] C.Angioni, E. Fable, F. Ryter, P. Rodriguez-Fernandez, and T. Pütterich. *Nuclear Fusion*, 59:106007, 2019.

[89] A. Ho, J. Citrin, F. Auriemma, C. Bourdelle, F.J. Casson, H.-T. Kim, P. Manas, G. Szepesi, and H. Weisen. *Nuclear Fusion*, 59:056007, 2019.

[90] M. Marin, J. Citrin, C. Bourdelle, Y. Camenen, F.J. Casson, A. Ho, F. Koechl, and M. Maslov. *Nuclear Fusion*, 60:046007, 2020.

[91] M. Marin et al (JET Contributors). *Nuclear Fusion*, 61:036042, 2021.

[92] F.J. Casson et al. *Nuclear Fusion*, 60:066029, 2020.

[93] C.K. Kiefer, C. Angioni, G. Tardini, N. Bonanomi, B. Geiger, P. Mantica, T. Pütterich, E. Fable, and P.A. Schneider. *Nuclear Fusion*, 61:066035, 2021.

[94] G.M. Staebler, J. Candy, E.A. Belli, J.E. Kinsey, N. Bonanomi, and B. Patel. *Plasma Physics and Controlled Fusion*, 63:015013, 2021.

[95] M. Romanelli and M. Ottaviani. *Plasma Physics and Controlled Fusion*, 40:1767, 1998.

[96] W.A. Houlberg, K.C. Shaing, S.P. Hirshman, and M.C. Zarnstorff. *Physics of Plasmas*, 4:3230, 1997.

[97] A.G. Peeters, C. Angioni, Y. Camenen, F.J. Casson, W.A. Hornsby, A.P. Snodin, and D. Strintzi. *Physics of Plasmas*, 16:062311, 2009.

[98] A.G. Peeters et al. *Nuclear Fusion*, 51:094027, 2011.

[99] G. Cenacchi and A. Taroni. *ENEA-RT-TIB 88-5 ENEA*, 1988.

[100] R. Albanese, R. Ambrosino, and M. Mattei. *Fusion Engineering and Design*, 96-97:664–7, 2015.

[101] P. Agostinetti et al. *Fusion Engineering and Design*, 146:441–446, 2019.

[102] T. Hellsten and L.-G. Eriksson. *Nuclear Fusion*, 29:2165, 1989.

[103] T. Hellsten and L. Villard. *Nuclear Fusion*, 28:285, 1988.

[104] M. Beurskens et al. *(IAEA FEC) 2020 IAEA-CN-EX/6-3 International Atomic Energy Agency.*

[105] A. Di Siena, T. Görler, H. Doerk, E. Poli, and R. Bilato. *Nuclear Fusion*, 58:054002, 2018.

[106] A. Di Siena, T. Görler, E. Poli, A.B. Navarro, A. Biancalani, and F. Jenko. *Nuclear Fusion*, 9:124001, 2019.

[107] A.M. Garofalo et al. *Fusion Engineering and Design*, 89:876–81, 2014.

[108] M.G. Dunne et al. *Plasma Physics and Controlled Fusion*, 59:025010, 2017.

[109] L. Frassinetti et al. *Nuclear Fusion*, 59:076038, 2019.

[110] U.A. Sheikh et al. *Plasma Physics and Controlled Fusion*, 61:014002, 2019.

[111] H.Q. Wang et al. *Nuclear Fusion*, 58:096014, 2018.

[112] L. Frassinetti. *28th IAEA Fusion Energy Conf. (FEC 2020) EX/2-2*, 2020.

[113] S. Tamor. *Journal of Computational Physics*, 40:104, 1981.

[114] L. Balbinot, G. Rubino, and P. Innocente. *Nuclear Materials and Energy*, 27:100952, 2021.

[115] H. Bufferand et al. Near wall plasma simulation using penalization technique with the transport code SOLEDGE2D–EIRENE. *Journal of Nuclear Materials*, 438:S445–S448, 2013.

[116] H. Bufferand et al. Numerical modelling for divertor design of the WEST device with a focus on plasma–wall interactions. *Nuclear Fusion*, 55(5):053025, 2015.

[117] L.L. Lao, H. St. John, R.D. Stambaugh, A.G. Kellman, and W. Pfeiffe. *Nuclear Fusion*, 25:1611, 1985.

[118] M. Brix, N.C. Hawkes, A. Boboc, V. Drozdov, and S.E. Sharapov. *Review of Scientific Instruments*, 79:10F325, 2008.

[119] R.L. Miller, M.S. Chu, J.M. Greene, Y.R. Lin-Liu, and R.E. Waltz. *Physics of Plasmas*, 5:973, 1998.

[120] A. Mariani, S. Brunner, J. Dominski, A. Merle, G. Merlo, O. Sauter, T. Görler, F. Jenko, and D. Told. *Physics of Plasmas*, 25:012313, 2018.

[121] A. Mariani, S. Brunner, G. Merlo, and O. Sauter. *Plasma Physics and Controlled Fusion*, 61:064005, 2019.

[122] F. Jenko, T. Dannert, and C. Angioni. *Plasma Physics and Controlled Fusion*, 47:B195, 2005.

[123] G. Spizzo et al. Collisionless losses of fast ions in the divertor tokamak test due to toroidal field ripple. *Nuclear Fusion*, 61:116016, 2021.

[124] L. Chen L. and F. Zonca. *Reviews of Modern Physics*, 88:015008, 2016.

[125] P. Innocente et al. *Nuclear Materials and Energy*, 33:101276, 2022.

[126] F. Porcelli et al. *Plasma Physics and Controlled Fusion*, 38:2163, 1996.

[127] A. Loarte et al. *Phys. Scripta*, 128:222—228, 2007.

[128] T. Eich et al. *Nuclear Materials and Energy*, 12:84–90, 2017.

[129] T. Eich et al. *Journal of Nuclear Materials*, 390-391:760–763, 2009.

[130] A. Loarte et al. *Plasma Physics and Controlled Fusion*, 45(9):1549–1569, 2003.

[131] L. Balbinot et al. *Nuclear Materials and Energy*, page 101350, 2022.

[132] A. Huber et al. *Physica Scripta*, 2020:014055, 2020.

[133] A. Castaldo et al. *Energies*, 15:1702, 2022.

[134] P. Vincenzi et al. Interaction of high–energy neutral beams with Divertor Tokamak Test plasma. *Submitted to Fusion Engineering and Design.*

[135] S. Garavaglia et al. *Fusion Engineering and Design*, 168:112678, 2021.

[136] B. Baiocchi and L. Aucone et al. "Predictive studies of deuterium fuelling strategies in the Divertor Tokamak Test facility". *Submitted to Plasma Physics and Controlled Fusion.*

[137] B.B. Kadomtsev. *Fiz. Plazmy*, 1:710–715, 1975.

[138] B.B. Kadomtsev. *Sov. Tech. Phys. Lett.*, 2:389, 1976.

[139] J. O'Rourke. *Plasma Physics and Controlled Fusion*, 33:289, 1991.

[140] F.M. Levinton and S.H. Batha. *Physics of Fluids B: Plasma Physics*, 5:2554, 1993.

[141] O. Sauter et al. *Physical Review Letters*, 88:105001, 2002.

[142] Y. Igitkhanov and B. Bazylev. *IEEE Transactions on Plasma Science*, 42(9):2284–2290, 2014.

[143] W. Fundamenski et al. *Plasma Physics and Controlled Fusion*, 48:109, 2006.

[144] T. Abrams et al. *Nuclear Materials and Energy*, 17:164–173, 2018.

[145] G.F. Harrer et al. *Nuclear Fusion*, 58 11:112001, 2018.

[146] J.L. Luxon and B.B. Brown. *Nuclear Fusion*, 22:813, 1982.

[147] Y.R. Martin et al. *Journal of Physics: Conference Series*, 123:012033, 2008.

[148] E. Delabie et al. Overview and interpretation of L–H threshold experiments on JET with the ITER-like wall. *25th IAEA Fusion Energy Conference P5–24 (St Petersburg, Russia, 13–18 October 2014).*

[149] E. Delabie et al. Status of TC-26: L-H/H-L scaling in the presence of Metallic walls. *ITPA Transport & Confinement meeting Fall (2018).*

[150] J. Citrin et al. *Physical Review Letters*, 111:155001, 2013.

[151] A. Di Siena et al. *Nuclear Fusion*, 58:054002, 2018.

[152] A. Di Siena et al. *Nuclear Fusion*, 59:124001, 2019.

[153] A. Di Siena et al. *Physical Review Letters*, 127:025002, 2021.

[154] A. Mariani et al. Benchmark of quasi-linear models against gyrokinetic single scale simulations in deuterium and tritium plasmas for a JET high beta hybrid discharge. *Nuclear Fusion*, 61:066032, 2021.

[155] J. Citrin et al. *Plasma Physics and Controlled Fusion*, 59:034007, 2017.

[156] N. Bonanomi et al. *Nuclear Fusion*, 58:026028, 2018.

[157] P. Mantica. *Invited Talk at 58th APS DPP Meeting (October 31 – November 4 2016 S. Jose, CA),* `https://meetings.aps.org/Meeting/DPP16`.

[158] P. Mantica. *Poster at 23rd EU-US Transport Task Force Meeting (September 11–14 2018 Sevilla, ES),* `http://www.psft.eu/ttf2018`.

[159] N. Bonanomi et al. *Nuclear Fusion*, 59:096030, 2019.

[160] G.M. Staebler et al. *Nuclear Fusion*, 58:115001, 2018.

[161] J. Citrin et al. *Plasma Physics and Controlled Fusion*, 57:014032, 2015.

[162] J. Garcia et al. *Nuclear Fusion*, 55:053007, 2015.

[163] G.G. Whelan, M.J. Pueschel, and P.W. Terry. *Physical Review Letters*, 120:175002, 2018.

[164] M. Bessenrodt-Weberpals et al. *Nuclear Fusion*, 33:1205, 1993.

[165] C.W. Barnes et al. *Physics of Plasmas*, 3:4521, 1996.

[166] C.F. Maggi et al. *Plasma Physics and Controlled Fusion*, 60:014045, 2018.

[167] P.A. Schneider et al. *Nuclear Fusion*, 57:066003, 2017.

[168] B.D. Scott. *Phys. Fluids B*, 4:2468, 1992.

[169] E.A. Belli, J. Candy R.E, and Waltz. *Physical Review Letters*, 125:015001, 2020.

[170] M. Nakata, M. Nunami, H. Sugama, and T.H. Watanabe. *Physical Review Letters*, 118:165002, 2017.

[171] J. Garcia, T. Görler, F. Jenko, and G. Giruzzi. *Nuclear Fusion*, 57:014007, 2017.

[172] P. Manas et al. *Nuclear Fusion*, 59:014002, 2019.

[173] X. Garbet and R.E. Waltz. *Physics of Plasmas*, 3:1898, 1996.

[174] P.A. Schneider. *Nuclear Fusion*, 61:036033, 2021.

[175] J.W. Connor, R.J. Hastie, and J.B. Taylor. *Physical Review Letters*, 40:396, 1978.

[176] J. Citrin et al. *Nuclear Fusion*, 62:086025, 2022.

[177] L. Garzotti et al. Simulations of density profiles, pellet fuelling and density control in ITER. *Nuclear Fusion*, 52(1):013002, 2012.

[178] B. Pégourié, V. Waller, R.J. Dumont, L-G. Eriksson, L. Garzotti, A. Géraud, and F. Imbeaux. Modelling of pellet ablation in additionally heated plasmas. *Plasma Physics and Controlled Fusion*, 47(1):17, 2005.

[179] F. Koechl, B. Pégourié, A. Matsuyama, H. Nehme, V. Waller, D. Frigione, L. Garzotti, G. Kamelander, V. Parail, and JET EFDA contributors. Modelling of Pellet Particle Ablation and Deposition: The Hydrogen Pellet Injection code HPI2. *EFDA–JET–PR(12)57.*

[180] B. Pégourié and E. Geulin. Final report PEX/DTT, Topic 4 – CEA–01 (Deliverable PMI–2.3–T011–D001), EUROfusion. 2020.

[181] S. Wiesen et al. The new SOLPS–ITER code package. *Journal of Nuclear Materials*, 463, 2015.

[182] T.D. Rognlien, J.L. Milovich, M.E. Rensink, and G.D. Porter. A fully implicit, time dependent 2–D fluid code for modeling tokamak edge plasmas. *Journal of Nuclear Materials*, 196-198:347–351, 1992.

[183] C. Meineri et al. Preliminary assessment of neon impact on DTT power exhaust with alcator C–Mod transport coefficients. *Offshore Mediterranean Conference*, OM–2021:191, 2021.

[184] G. Rubino et al. Assessment of scrape-off layer and divertor plasma conditions in JT–60SA with tungsten wall and nitrogen injection. *Nuclear Materials and Energy*, 26:100895, 2021.

[185] T. Eich et al. Scaling of the tokamak near the scrape–off layer H–mode power width and implications for ITER. *Nuclear Fusion*, 53(9):093031, 2013.

[186] C.S. Pitcher and P.C. Stangeby. Experimental divertor physics. *Plasma Physics and Controlled Fusion*, 39(6):779, 1997.

[187] P.C. Stangeby. *The Plasma Boundary of Magnetic Fusion Devices*. CRC Press, 2000. 1st edition.

[188] P. Vincenzi et al. Exploring Divertor Tokamak Test (DTT) operation space and plasma scenarios through time-dependent 0.5D integrated modelling. *47th EPS Conference on Plasma Physics*, 2021–June:677–680, 2021.

[189] J.F. Artaud et al. Metis: a fast integrated tokamak modelling tool for scenario design. *Nuclear Fusion*, 58:105001, 2018.

[190] P. Agostinetti et al. Conceptual Design of the Beamline for the DTT Neutral Beam Injector following a Double Beam Source Design Approach. *Plasma and Fusion Research: Regular Articles*, 16:2405080, 2021.

[191] A. Kojima et al. Progress in long-pulse production of powerful negative ion beams for jt-60sa and iter. *Nuclear Fusion*, 55:063006, 2015.

[192] Y. Takeiri et al. High performance of neutral beam injectors for extension of lhd operational regime. *Fusion Science and Technology*, 58:482, 2010.

[193] P. Agostinetti et al. Physics and engineering design of the accelerator and electron dump for spider. *Nuclear Fusion*, 51:063004, 2011.

[194] P. Agostinetti et al. Detailed design optimization of the mitica negative ion accelerator in view of the iter nbi. *Nuclear Fusion*, 56:016015, 2016.

[195] E. Hirvijoki et al. ASCOT: Solving the kinetic equation of minority particle species in tokamak plasmas. *Computer Physics Communications*, 185(4):1310–1321, 2014.

[196] O. Asunta et al. Modelling neutral beams in fusion devices: Beamlet–based model for fast particle simulations. *Computer Physics Communications*, 188:33–46, 2015.

[197] R. Ambrosino. *Fusion Engineering and Design*, 167:112330, 2021.

[198] V.G. Kiptily et al. *Nuclear Fusion*, 49:065030, 2009.

[199] R.B. White. *The Theory of Toroidally Confined Plasmas (chapter 9, pages 402–414)*. London: Imperial College Press, 2014. 3rd edition.

[200] R.B. White and M.S. Chance. Hamiltonian guiding center drift orbit calculation for plasmas of arbitrary cross section. *Physics of Fluids*, 27:10 2455, 1984.

[201] Y.B. Zhu, W.W. Heidbrink, and L.D Pickering. *Nuclear Fusion*, 50:084024, 2010.

[202] R. Hawryluk. *Physics of Plasmas Close to Thermonuclear Conditions. An empirical approach to tokamak transport.* 1980. Vol 1 ed B. Coppi et al (Brussels: CEC) pp 19–46.

[203] A. Cardinali et al. *Journal of Physics: Conference Series*, 2397:012017, 2022.

[204] A. Cardinali et al. *Plasma Physics and Controlled Fusion*, 62:044001, 2020.

[205] A. Cardinali et al. *Nuclear Fusion*, 42:427, 2002.

[206] M. Brambilla et al. *Plasma Physics and Controlled Fusion*, 41:1, 1999.

[207] M. Brambilla et al. *Nuclear Fusion*, 34:1121, 1994.

[208] G.S. Mauro et al. *Proc. 32 nd Symposium on Fusion Technology (SOFT) at Dubrovnik, Croatia*, 2022.

[209] S. Ceccuzzi et al. *Proc. 24 th RF Topical Conference on Radio-frequency Power in Plasmas at Annapolis, USA*, 2022.

[210] M. Greenwald et al. *Physics of Plasmas*, 21:110501, 2014.

[211] B. Streibl et al. Chapter 2: Machine Design, Fueling, and Heating in ASDEX Upgrade. *Fusion Science and Technology*, 44(3):578–592, 2003.

[212] Y.O. Kazakov et al. *Nat. Phys.*, 13:973, 2017.

[213] Y.O. Kazakov et al. *Physics of Plasmas*, 28:020501, 2020.

[214] M. Cecconello et al. *Fusion Engineering and Design*, 167:112382, 2021.

[215] M.G. Johnson et al. The 2.5–MeV neutron time–of–flight spectrometer TOFOR for experiments at JET. *Nuclear Instruments and Methods in Physics Research Section A: Accelerators, Spectrometers, Detectors and Associated Equipment*, 591(2):417–430, 2008.

[216] A. Pankin, D. McCune, R. Andre, G. Bateman, and A. Kritz. The tokamak Monte Carlo fast ion module nubeam in the national transport code collaboration library. *Computer Physics Communications*, 159(3):157–184, 2004.

[217] J. Eriksson, S. Conroy, E. Andersson Sundén, and C. Hellesen. Calculating fusion neutron energy spectra from arbitrary reactant distributions. *Computer Physics Communications*, 199:40–46, 2016.

[218] `https://mcnp.lanl.gov/`.

[219] R. Villari et al. Nuclear design of Divertor Tokamak Test (DTT) facility. *Fusion Engineering and Design*, 155:111551, 2020.

[220] M. Chernyshova et al. Development of 2d gem-based sxr plasma imaging for dtt device: Focus on readout structure. *Fusion Engineering and Design*, 169:112443, 2021.

[221] E. Belli and J. Candy. *Plasma Physics and Controlled Fusion*, P50:095010, 2008.

[222] A. Taroni et al. *Proc. 16th IAEA Int. Conf. on Fusion Energy (Montreal, Canada, 7–11 Oct 1996)*, 2:477.

[223] T. Luda et al. *Nuclear Fusion*, 60:036023, 2020.

[224] I. Casiraghi. Experimental investigation and modelling of isotope effects on transport in the JET tokamak in view of the upcoming D–T campaign. *Master thesis*, 2019.

[225] B. Coppi and F. Pegoraro. Theory of the ubiquitous mode. *Nuclear Fusion*, 17(5):969–993, 1977.

[226] P.I. Strand et al. Comparisons of anomalous and neoclassical contributions to core particle transport in tokamak discharges. *European Physical Society (2004)*, 28.

[227] J. Weiland. *Collective Modes in Inhomogeneous Plasmas: Kinetic and Advanced Fluid Theory*. CRC Press, 1999. 4th edition.

[228] Y. Feng et al. Recent improvements in the EMC3-EIRENE code. *Contributions to Plasma Physics*, 54, 2014.

[229] H. Bufferand et al. Progress in edge plasma turbulence modelling–hierarchy of models from 2D transport application to 3D fluid simulations in realistic tokamak geometry. *Nuclear Fusion*, 61(11):116052, 2021.

[230] Francis F. Chen. *Introduction to Plasma Physics and Controlled Fusion*. Springer International Publishing, 2016. 3rd edition.

[231] Roberto J. Goldston and Paul H. Rutherford. *Introduction to Plasma Physics*. Taylor & Francis Group, 1995.

Nomenclature

AC Alternating Current.

ADAS Atomic Data and Analysis Structure.

AG Acceleration Grid.

ALCATOR ALto CAmpo TORo.

ASCOT Accelerated Simulation of Charged particle Orbits in Toroidal devices.

ASDEX Axially Symmetric Divertor EXperiment.

ASTRA Automated System for TRansport Analysis.

AUG ASDEX UpGrade.

BBNBI Beamlet–Based NBI–model.

BLC Beam Line Component.

CD Current Drive.

CEA Commissariat à l'Énergie Atomique et aux énergies alternatives.

CGM Critical Gradient Model.

CICC Cable–In–Conduit Conductor.

CNL CREATE–NL.

CNR Consiglio Nazionale delle Ricerche.

CREATE Consorzio di Ricerca per l'Energia, l'Automazione e le Tecnologie dell'Elettromagnetismo.

CRPP Centre de Recherches en Physique des Plasmas.

CS Central Solenoid.

DEMO DEMOnstration power plant.

DIFFER Dutch Institute For Fundamental Energy Research.

DISEMAG DISpersion ElectroMAGnetic.

DN Double Null.

DRESS Directional RElativistic Spectrum Simulator.

DTT Divertor Tokamak Test facility.

ECCD EC Current Drive.

ECRH Electron Cyclotron Resonance Heating.

EDWM Extended Drift Wave Model.

EFIT Equilibrium FITting.

EG Extraction Grid.

ELM Edge Localised Mode.

EM ElectroMagnetic.

ENI Ente Nazionale Idrocarburi.

EOF End Of Flat–top.

EP Energetic Particles.

EPFL École Polytechnique Fédérale de Lausanne.

EQB EQuatorial Bottom.

EQT EQuatorial Top.

ES ElectroStatic.

ETB Edge Transport Barrier.

ETG Electron Temperature Gradient mode.

ETS European Transport Simulator.

FELICE Finite ELement Ion Cyclotron Evaluation.

FEM Finite Elements Method.

FI Fast Ions.

FOM stichting Fundamenteel Onderzoek der Materie.

FP Full Power.

FW Fisrt Wall.

gB gyro–Bohm.

GEM Gas Electron Multiplier.

GENE Gyrokinetic Electromagnetic Numerical Experiment.

GG Grounded Grid.

GK GyroKinetic.

H–mode High confinement mode.

HCD Heating and Current Drive.

HFS High–Field Side.

HG Hyperlens Grid.

HPC High Performance Computing.

HPI Hydrogen Pellet Injection.

HVPS High Voltage Power Supply.

ICRH Ion Cyclotron Resonance Heating.

IDS Interface Data Structure.

ILW ITER–Like Wall.

IMAS Integrated Modelling & Analysis Suite.

INFN Istituto Nazionale di Fisica Nucleare.

IPP Institut für PlasmaPhysik.

IPPLM Institute of Plasma Physics and Laser Microfusion.

IRFM Institut de Recherche sur la Fusion par confinement Magnétique.

ITER International Thermonuclear Experimental Reactor.

ITG Ion Temperature Gradient mode.

ITPA International Tokamak Physics Activity.

JAMS JET Application Management System.

JET Joint European Torus.

JINTRAC JET INtegrated TRAnsport Code suite.

JT60–SA Japan Torus–60 Super Advanced.

KBM Kinetic Ballooning Mode.

KIT Karlsruhe Institute of Technology.

L–mode Low confinement mode.

LCFS Last Close Flux Surface.

LFS Low–Field Side.

LHD Large Helical Device.

LMD Liquid Metal Divertors.

LOS Lines Of Sight.

MAST Mega Ampere Spherical Tokamak.

MCNP Monte Carlo N–Particle.

MHD Magneto–HydroDynamics.

MISE MInistero dello Sviluppo Economico.

MITICA Megavolt ITER Injector and Concept Advancement.

MIUR Ministero dell'Istruzione, Università e Ricerca.

MTM Micro Tearing Modes.

NBI Neutral Beam Injector.

NEG Non–Evaporable Getter.

NL Non–Linear.

NT Negative Triangularity.

O–mode Ordinary mode.

OHFS Oblique High Field Side.

PB Peeling–Ballooning.

PEX Plasma EXhaust assessment panel.

PF Poloidal Field.

PFC Plasma–Facing Component.

PG Plasma Grid.

PT Positive Triangularity.

QL Quasi–Linear.

QLK QuaLiKiz.

QLKNN QLK Neural Network.

QSF Quasi–SnowFlake.

RABBIT Rapid Analytical Based Beam Injection Tool.

RAMI Reliability, Availability, Maintainability, and Inspectability.

RF Radio Frequency.

RFX Reversed Field eXperiment.

RT Research Topic.

SN Single Null.

SOF Start Of Flat–top.

SOL Scrape–Off Layer.

SPIDER Source for the Production of Ions of Deuterium Extracted from a Radio frequency plasma.

ST sawteeth.

SXR Soft X–Ray.

TCV Tokamak à Configuration Variable.

TEM Trapped Electron Mode.

TF Toroidal Field.

TGLF Trapped Gyro–Landau Fluid.

TL Transmission Line.

TOB Top Of Barrier.

TOF Time–Of–Flight.

TORIC TORoidal Ion Cyclotron.

UKAEA UK Atomic Energy Authority.

UP UPper.

VV Vacuum Vessel.

WPTE Work Package Tokamak Exploitation.

X–mode eXtraordinary mode.

ZF Zonal Flow.